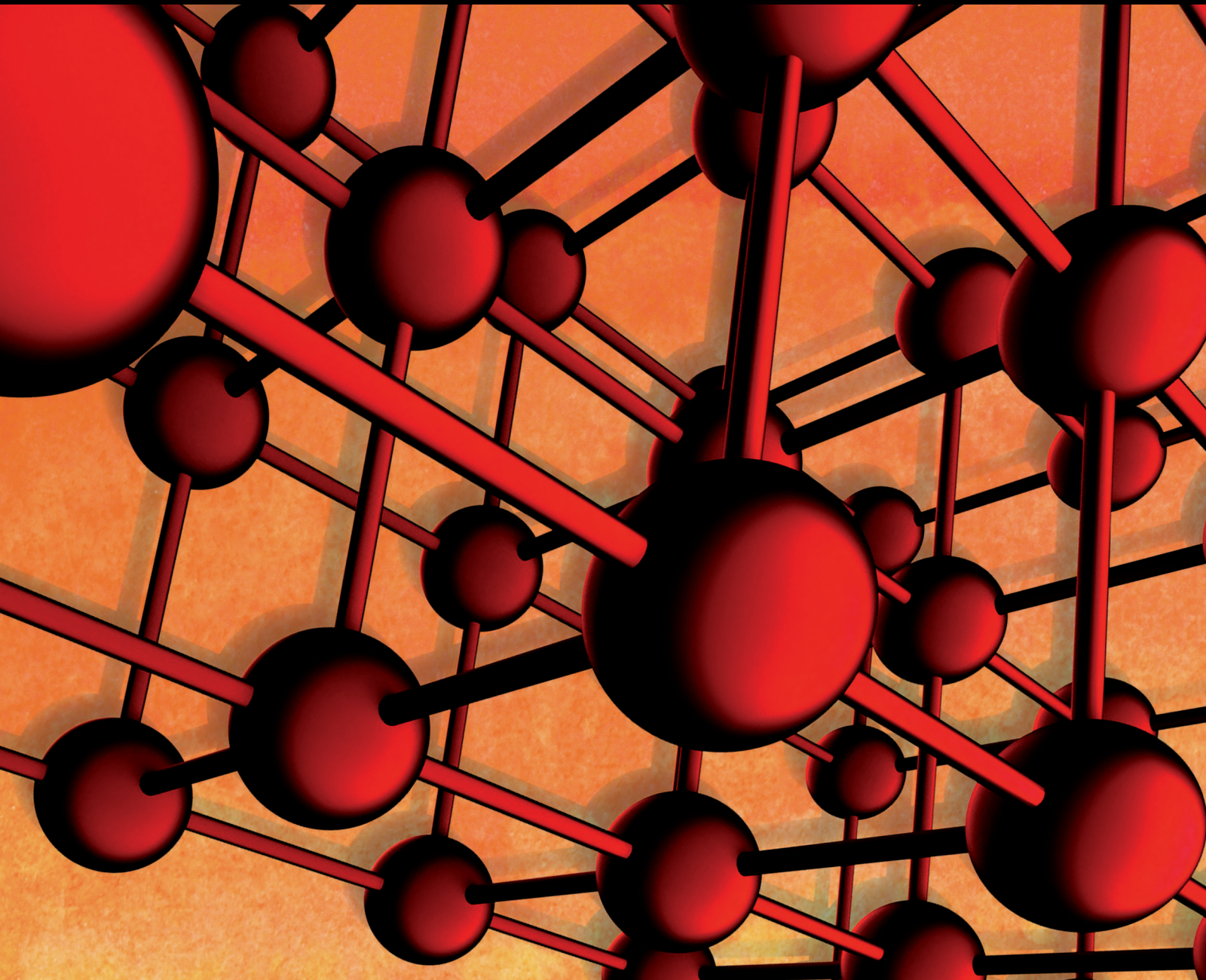


Advances in Materials Science and Engineering

Novel Technologies and Applications for Construction Materials

Guest Editors: Gonzalo Martínez-Barrera, Osman Gencel, João Marciano Laredo dos Reis, and Juan José del Coz Díaz





Novel Technologies and Applications for Construction Materials

Advances in Materials Science and Engineering

Novel Technologies and Applications for Construction Materials

Guest Editors: Gonzalo Martínez-Barrera, Osman Gencel,
João Marciano Laredo dos Reis, and Juan José del Coz Díaz



Copyright © 2014 Hindawi Publishing Corporation. All rights reserved.

This is a special issue published in “Advances in Materials Science and Engineering.” All articles are open access articles distributed under the Creative Commons Attribution License, which permits unrestricted use, distribution, and reproduction in any medium, provided the original work is properly cited.

Editorial Board

- Dimitrios G. Aggelis, Belgium
K. G. Anthymidis, Greece
Amit Bandyopadhyay, USA
Arun Bansil, USA
Zoe Barber, UK
Massimiliano Barletta, Italy
Jozef Bednarcik, Germany
Jamal Berakdar, Germany
Alessandra Bianco, Italy
Susmita Bose, USA
Heinz-Gunter Brokmeier, Germany
Steve Bull, UK
Peter Chang, Canada
Daolun Chen, Canada
Manish U. Chhowalla, USA
Sanjeeviraja Chinnappanadar, India
Chi-Wai Chow, Taiwan
Narendra B. Dahotre, USA
Jie Dai, Singapore
Joo P. Davim, Portugal
Francesco Delogu, Italy
Seshu B. Desu, USA
Yong Ding, USA
Kaveh Edalati, Japan
Gilbert Fantozzi, France
Sergi Gallego, Spain
Lian Gao, China
Santiago Garcia-Granda, Spain
Filippo Giannazzo, Italy
Hiroki Habazaki, Japan
Joke Hadermann, Belgium
Richard Hennig, USA
Rui Huang, USA
Shyh-Chin Huang, Taiwan
Baibiao Huang, China
Jacques Huot, Canada
Maarit Karppinen, Finland
Katsuyuki Kida, Japan
Jaehwan Kim, Republic of Korea
Jae-Ho Kim, Republic of Korea
Akihiko Kimura, Japan
Takayuki Kitamura, Japan
Sridhar Komarneni, USA
Hongchao Kou, China
Prashant Kumta, USA
Jui-Yang Lai, Taiwan
Pavel Lejcek, Czech Republic
Cristina Leonelli, Italy
Markku Leskela, Finland
Bin Li, China
Feng Li, China
Ying Li, USA
Yuanhua Lin, China
Zhimin Liu, China
Meilin Liu, Georgia
Wei Liu, France
Ying Liu, USA
Jun Liu, China
Yunqi Liu, China
Haiming Lu, China
Fernando Lusquios, Spain
Peter Majewski, Australia
Philippe Miele, France
Hossein Moayedi, Malaysia
Paul Munroe, Australia
Luigi Nicolais, Italy
Hiroshi Noguchi, Japan
José L. Ocaña, Spain
Tsutomu Ohzuku, Japan
Xiaoqing Pan, USA
Bart Partoens, Belgium
Ganapathiraman Ramanath, USA
Manijeh Razeghi, USA
Antonio Riveiro, Spain
Pascal Roussel, France
Fawzy H. Samuel, Canada
Jainagesh A. Sekhar, USA
Jiangbo Sha, China
Liyuan Sheng, China
Fridon Shubitidze, USA
You Song, China
Charles C. Sorrell, Australia
Costas M. Soukoulis, USA
Sam-Shajing Sun, USA
Weihua Tang, China
Kohji Tashiro, Japan
Philippe Thomas, France
Somchai Thongtem, Thailand
Achim Trampert, Germany
Vladimir Tsukruk, USA
Filip Tuomisto, Finland
Stuart Turner, Belgium
Krystyn Van Vliet, USA
Rui Vilar, Portugal
Holger von Wenckstern, Germany
Rong Wang, USA
Min Wang, China
Rui Wang, China
Qiang Wang, China
Lu Wei, China
Jörg M K Wiezorek, USA
Wei Wu, USA
Gongnan Xie, China
Aiguo Xu, China
Hemmige S. Yathirajan, India
Jianqiao Ye, UK
Wenbin Yi, China
Jinghuai Zhang, China
Tao Zhang, China
Bin Zhang, China
Jun Zhang, China
Jian Zhang, Singapore
Kai Zhang, China
Kai Zhang, China
Jing Zhang, China
Li Zhang, China
Ming-Xing Zhang, Australia
Wei Zhou, China

Contents

Novel Technologies and Applications for Construction Materials, Gonzalo Martínez-Barrera, Osman Gencil, João Marciano Laredo dos Reis, and Juan José del Coz Díaz
Volume 2014, Article ID 960541, 2 pages

Strengthening Reinforced Concrete Beams with CFRP and GFRP, Mehmet Mustafa Önal
Volume 2014, Article ID 967964, 8 pages

The Mechanical Behavior of Fiber Reinforced PP ECC Beams under Reverse Cyclic Loading, Yaw ChiaHwan and Han JianBo
Volume 2014, Article ID 159790, 9 pages

Investigation of Soil Liquefaction Potential around Efteni Lake in Duzce Turkey: Using Empirical Relationships between Shear Wave Velocity and SPT Blow Count (N), Ali Ateş, İnan Keskin, Ermedin Totiç, and Burak Yeşil
Volume 2014, Article ID 290858, 15 pages

Crack Extension Resistance of Normal-Strength Concrete Subjected to Elevated Temperatures, Jing Chen and Zhoudao Lu
Volume 2014, Article ID 683756, 12 pages

Impact of High Temperature on the Compressive Strength of ECC, Xingyan Shang and Zhoudao Lu
Volume 2014, Article ID 919078, 7 pages

Application of Interfacial Propagation and Kinking Crack Concept to ECC/Concrete Overlay Repair System, Yaw ChiaHwan and Li Wei
Volume 2014, Article ID 623467, 6 pages

Multiscale Analysis of the Interfacial Mechanical Behavior for Composite of Carbon Nanotube and α -Alumina, Tingting Yan and Gaofeng Wei
Volume 2014, Article ID 237097, 7 pages

New Two-Dimensional Polynomial Failure Criteria for Composite Materials, Shi Yang Zhao and Pu Xue
Volume 2014, Article ID 503483, 7 pages

Prediction of Effects of Geogrid Reinforced Granular Fill on the Behaviour of Static Liquefaction, A. Hemalatha, N. Mahendran, and G. Ganesh Prabhu
Volume 2014, Article ID 210843, 11 pages

Rock-Arch Instability Characteristics of the Sandstone Plate under Different Loading Conditions, Shuren Wang, Paul Hagan, Baowen Hu, Kanchana Gamage, Cheng Yan, and Dianfu Xu
Volume 2014, Article ID 950870, 9 pages

Research on Deterioration Mechanism of Concrete Materials in an Actual Structure, Shiping Zhang, Xiang Dong, Houxian Zhang, and Min Deng
Volume 2014, Article ID 306459, 6 pages



Application of Optimum Compaction Energy in the Development of Bricks Made with Construction Trash Soils, T. Lopez-Lara, C. L. Gonzalez-Vega, J. B. Hernandez-Zaragoza, E. Rojas-Gonzalez, D. Carreón-Freyre, R. Salgado-Delgado, E. Garcia-Hernandez, and M. Cerca
Volume 2014, Article ID 835620, 5 pages

Evaluation of Relationship between Water Absorption and Durability of Concrete Materials, S. P. Zhang and L. Zong
Volume 2014, Article ID 650373, 8 pages

Waste Tire Particles and Gamma Radiation as Modifiers of the Mechanical Properties of Concrete, Eduardo Sadot Herrera-Sosa, Gonzalo Martínez-Barrera, Carlos Barrera-Díaz, and Epifanio Cruz-Zaragoza
Volume 2014, Article ID 327856, 7 pages

Editorial

Novel Technologies and Applications for Construction Materials

**Gonzalo Martínez-Barrera,¹ Osman Gencel,²
João Marciano Laredo dos Reis,³ and Juan José del Coz Díaz⁴**

¹ *Laboratorio de Investigación y Desarrollo de Materiales Avanzados (LIDMA), Facultad de Química, Universidad Autónoma del Estado de México, Km. 12 de la Carretera Toluca-Atlaconulco, 50200 San Cayetano, MEX, Mexico*

² *Civil Engineering Department, Faculty of Engineering, Bartin University, 74100 Bartin, Turkey*

³ *Theoretical and Applied Mechanics Laboratory (LMTA), Universidade Federal Fluminense, 24220 Rio de Janeiro, Brazil*

⁴ *Departamento de Construcción, Universidad de Oviedo, 33204 Gijón, Spain*

Correspondence should be addressed to Gonzalo Martínez-Barrera; gonzomartinez02@yahoo.com.mx

Received 14 September 2014; Accepted 14 September 2014; Published 18 December 2014

Copyright © 2014 Gonzalo Martínez-Barrera et al. This is an open access article distributed under the Creative Commons Attribution License, which permits unrestricted use, distribution, and reproduction in any medium, provided the original work is properly cited.

In this volume, we discuss the recent progress in construction technologies and materials. The perspectives are to obtain new construction materials with improved properties at low cost by using easy and novel technologies and chemically sustainable for the environment. Different investigations are mentioned including those concretes strengthened with fiber reinforced polymers (FRP), either carbon or glass fibers, whose results show strength improvement and reduction of the cracks. Those called Engineered Cementitious Composites (ECC) reinforced with polypropylene (PP) are also discussed whose main purpose is to resolve earthquake consequences, as we know tremendous amount of seismic energy is released and structure is subjected to reverse loads. Such PP-ECCs materials can enhance strength and energy dissipation capacity. Moreover, The Ultra-Ductile Engineered Cementitious Composites (ECC) are applied as overlay in the repair of deteriorated concrete structures, significant improvements in load carrying capacity, and ductility over conventional concrete overlay are found. Also postfire behaviors of ECCs exposed at high temperature were discussed following different cooling regimes (quenching in water and cooling in air); the quenching in water has shown better mechanical properties than the cooling in air. Severe environmental conditions plus the relatively inferior frost resistance cause the deterioration of concrete and in consequence less durability. Nevertheless, usage of air entraining admixture can improve frost resistance and impermeability.

Also special concretes have been used widely in construction industry including infrastructure with special applications such as restoration and strengthening of existing structures against earthquake. Evaluation of the liquefaction potential of a liquefaction-prone area is important for geotechnical earthquake engineering, both for assessment for site selection and for planning and new constructions. By measuring different parameters as Standard Penetration Test (SPT) and the Shear Wave Velocity Test (VS) it is possible to obtain the liquefaction potential index (LPI). Studies on the effects of granular fill and geogrid reinforced granular fill on the behavior of the static liquefaction potential of the subsoil in the coastal area are reported. The experimental results revealed that the introduction of granular fill significantly increases the bearing capacity and effectively controls the settlement behavior of the footing.

The actual tendencies and global developments of novel materials include the use of recycled materials in construction. In polymer reinforced concrete the Young modulus of the cement matrix and polymers is responsible for the detrimental properties of the concrete, including compressive and tensile strength, as well as stiffness. For solving such problems a novel methodology is proposed by using waste tire particles and ionizing radiation, which have proven to be good tools for improvement of physical and chemical properties of concrete. Another investigation is related to the use of construction trash soils in the elaboration of resistant

masonry bricks of homogeneous and controlled density, as we know the expansive soils represent a problem for light buildings over them because of volumetric instability.

Different methods have been applied to relate applied forces and the subsequent modifications; for example, residual crack extension resistance curves are associated with cohesive force distribution on fictitious crack zone of complete fracture process. It was found that the residual fracture toughness increases with increasing crack length. Moreover, two new dimensional polynomial failure criteria have been proposed to predict the damage process of composite structures under loading. Four distinct failure modes including fiber tensile failure, fiber compressive failure, matrix tensile failure, and matrix compressive failure are considered. This can reduce the artificialness of choosing the criteria for the damage simulation of the failure modes. Moreover, multiscale methods for studying of the mechanical behavior of the interfaces are discussed.

Gonzalo Martínez-Barrera

Osman Gencel

João Marciano Laredo dos Reis

Juan José del Coz Díaz

Research Article

Strengthening Reinforced Concrete Beams with CFRP and GFRP

Mehmet Mustafa Önal

Vocational School, Ahi Evran University, 40100 Kırşehir, Turkey

Correspondence should be addressed to Mehmet Mustafa Önal; mmonal@ahievran.edu.tr

Received 18 November 2013; Revised 14 June 2014; Accepted 14 June 2014; Published 13 July 2014

Academic Editor: Osman Gencil

Copyright © 2014 Mehmet Mustafa Önal. This is an open access article distributed under the Creative Commons Attribution License, which permits unrestricted use, distribution, and reproduction in any medium, provided the original work is properly cited.

Concrete beams were strengthened by wrapping the shear edges of the beams twice at 45° in opposite directions by either carbon fiber reinforced polymer (CFRP) or glass fiber reinforced polymer (GFRP). The study included 3 CFRP wrapped beams, 3 GFRP wrapped beams, and 3 control beams, all of which were 150 × 250 × 2200 mm and manufactured with C20 concrete and S420a structural steel at the Gazi University Technical Education Faculty labs, Turkey. Samples in molds were cured by watering in the open air for 21 days. Four-point bending tests were made on the beam test specimens and the data were collected. Data were evaluated in terms of load displacement, bearing strength, ductility, and energy consumption. In the CFRP and GFRP reinforced beams, compared to controls, 38% and 42%, respectively, strength increase was observed. In all beams, failure-flexural stress occurred in the center as expected. Most cracking was observed in the flexural region 4. A comparison of CFRP and GFRP materials reveals that GFRP enforced parts absorb more energy. Both materials yielded successful results. Thicker epoxy application in both CFRP and GFRP beams was considered to be effective in preventing break-ups.

1. Introduction

Because of the increasing population of cities, there is a very high demand for apartments. Moreover, due to the ongoing trend toward moving to the city, there is a sharp increase in city populations and therefore new residential areas are needed to meet the high demand. Along with the population boom, the need for more public buildings, such as social facilities and schools, has arisen. Therefore, in order to use the national resources optimally, ways to repair and strengthen damaged buildings need to be explored.

The term “repairing” involves alterations in a functionally or visually damaged building to make it like new. “Strengthening” involves alterations in a building to increase its load-carrying capacity, rigidity, ductility, and stability. This study focuses on strengthening. Stirrup not placed according to the spacing values given in the construction plan, insufficient longitudinal main reinforcements, insufficiently anchored reinforcements, casual placement of reinforcements, collapse of non-load-bearing walls and chimneys, and using low quality concrete are some of the reasons resulting in the need for strengthening [1].

There is a need for such a strengthening method that, during the strengthening process, residents of the building do not need to empty the building; neighboring buildings are not affected by strengthening, and strengthening is completed in a short period of time. Moreover, by this particular strengthening method, the building is expected to be stronger and well-qualified in terms of earthquake resistance regulations. In addition, this particular method must be consistent with the current aesthetic condition and also it must be affordable.

Norris et al. strengthened concrete beams in tensile regions with FRP and analytically and experimentally studied the results. They found that CFRPs applied vertically to cracks increased the endurance and rigidity. They reported that, because of tension accumulation, brittle fractures were observed [2].

Kachlakev and McCurry applied 2 different reinforcement methods in dislocation regions of beams: textile application to the shear region entirely and partially. They suggested a cost-effective strengthening method with this study [3].

Yang and Nanni strengthened full-scale beams with FRP plates against bending and shear. Through 4-point

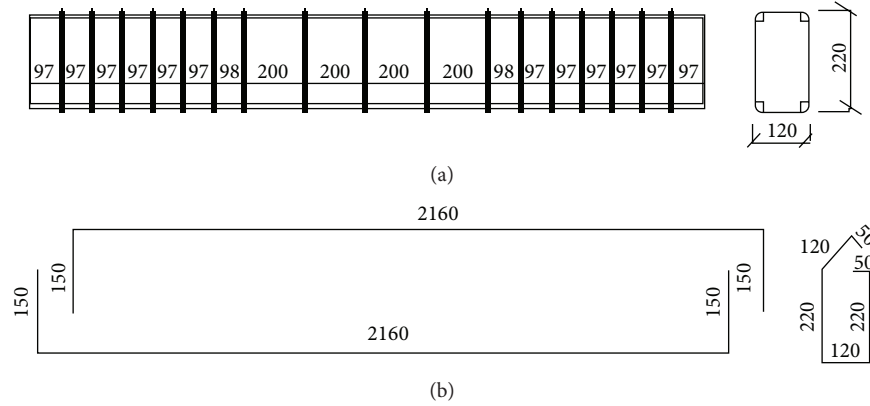


FIGURE 1: Reinforcement details of the experimental beams [12].

bending experiments, load reflection and tension values were determined. In all samples, a 150% increase in strength was observed [4].

Alkan investigated the process of corner rounding in FRP strengthening. In circular beams, FRP capacity reached 67%. The author highlighted the remarkable effect of corner rounding [5].

Perera et al. applied the same strengthening method to $60 \times 120 \times 500$ mm beam samples. The CFRP reinforced samples were exposed to the 3-point bending test. CFRP was wrapped as a single layer around the beams within the entire tensile region and half of the sides. Results showed that the reinforced beams carried 80% more load [6].

Maalej and Leong studied the bonding behavior of CFRP and concrete blocks and discussed it in terms of analytical results. Adherence surfaces of various samples were exposed to test and the damaged samples were examined with the finite elements model. In general, they reported a good correlation between computational solutions and experimental results [7].

2. Materials and Methods

2.1. Materials. Nine $150 \times 250 \times 2200$ mm samples were prepared with C20 and S240 materials. Deformed $\varnothing 8$ and $\varnothing 12$ bars were used. In both $1/3$ shear regions, 50% more reinforcement was used. Table 1 shows the strengthening plan and Figure 1 depicts the reinforcement details.

2.1.1. Mechanical Properties of the Mold Materials Used in the Study. Poplar wood (30 mm) was used as the mold material in the study. Nine $150 \times 250 \times 2200$ mm molds were constructed and prepared with form oil ready to use.

2.1.2. Mechanical Properties of the Concrete Used in the Study. C20 concrete used in the study was obtained from a ready-mixed concrete plant. The properties of the C20 concrete: cement type: CEM I 32.5, slump value = 10 cm, maximum aggregate size = 16 mm, water/cement ratio = 0.58, water weight = 228 kg, and cement weight = 393 kg. Concretes placed in molds were compressed using a vibrator obtained

TABLE 1: Strengthening plan [12].

The number of concrete beams used in the experiments and their dimensions (mm)	Comment
3 units $150 \times 250 \times 2200$	3 control beams (group 1)
3 units $150 \times 250 \times 2200$	3 concrete beams were strengthened with CFRP in the shear region (group 2) (both shear regions ($1/3$) were wrapped at 45° in both directions)
3 units $150 \times 250 \times 2200$	3 concrete beams were strengthened with GFRP in the shear region (group 2) (both shear regions ($1/3$) were wrapped at 45° in both directions)

from the construction laboratory. Samples in molds were cured by watering in the open air for 21 days. Sample concrete cylinders were tested 29 days after the production date and load and stress values are presented in Table 2.

2.1.3. Mechanical Properties of the Epoxy Mixture Used in the Study. Sikadur 330 (1.31 kg/L) with A and B components, which is stiff like dough, was used. A and B components were stirred individually in different containers for 3 min first and then A was poured onto B and they were mixed together. The mixture was applied on the surface with a plasterer's trowel and a flat scraper. The amount of adhesive was kept at 2 kg/m^2 . For attaching the second coat on CFRPs, epoxy was applied 1 day later. In order to avoid external effects, closing procedure was performed 1 day later. Temperature and the amount of adhesive used were carefully monitored during epoxy applications [8].

2.1.4. Mechanical Properties of the CFRP Used in the Study. CFRP, which is made of carbon fiber, was uniaxial Sika Wrap with 230 g/m^2 density, 0.13 mm thickness, and received as 0.60×50 m rolls [8].

TABLE 2: Detailed results of the sample concrete cylinders.

C20 samples	Cylinder diameter (mm)	Axial load (KN)	Section (mm ²)	Axial compressive stress (KN/mm ²)
1	150	64	17663	0.0038
2	150	63	17663	0.0039
3	150	62	17663	0.0036

TABLE 3: Mechanical properties of the sample beams.

Number	Sample	Type	Quantity	Surface (mm ²)	Reinforcement ratio	f_{ck} (N/mm ²)	f_{yk} (N/mm ²)	f_{su} (N/mm ²)
1	K101	S420a	2ø12	37500	0.00602	0.0036	44.93	68
2	K102	S420a	2ø12	37500	0.00602	0.0036	44.93	68
3	K103	S420a	2ø12	37500	0.00602	0.0036	44.93	68
4	KG201	S420a	2ø12	37500	0.00602	0.0036	44.93	68
5	KG202	S420a	2ø12	37500	0.00602	0.0036	44.93	68
6	KG203	S420a	2ø12	37500	0.00602	0.0036	44.93	68
7	KG301	S420a	2ø12	37500	0.00602	0.0036	44.93	68
8	KG302	S420a	2ø12	37500	0.00602	0.0036	44.93	68
9	KG303	S420a	2ø12	37500	0.00602	0.0036	44.93	68

f_{ck} : concrete cylinder compressive strength, f_{yk} : steel yield strength, and f_{su} : steel tensile strength.

2.1.5. Mechanical Properties of GFRP Used in the Study. GFRP, which is made of glass fiber, was uniaxial Sika Wrap 430 G with 430 g/m² density and received as 0.60 × 50 m rolls. Compressive strength of GFRP was 3300–4500 mpa and elongation at break was 0.048 [8].

2.1.6. Reinforcement Mechanical Properties and Symbols of the Sample Concrete Beams. Mechanical properties of the sample concrete beams manufactured for strengthening purposes are presented in Table 3.

2.2. Methods. A total of 9 beams (150 × 250 × 2200 mm) were manufactured with C20 concrete and S420a structural steel. Then, the beams were strengthened with either CFRP (3 beams) or GFRP (3 beams) by wrapping them twice at the shear zone at 45° opposing directions. Another set of 3 beams was used as controls. Entire tensile stress zone of the shear region was strengthened by wrapping. A total of 6 displacement transducers were set up to determine the cracks in 6 different zones: 2 spots on each side of the beams symmetrically and 2 spots in the tensile and pressure zones. In the sample beams, which were subjected to loading on 4 different points, the effective span was taken as 2000 mm. Loading and displacement values were also determined.

2.2.1. Types of Strengthening Materials and Methods. Types of strengthening materials and methods are presented in Table 4.

2.2.2. Preparation of the Beams. Sample beams were transferred into the laboratory 30 days after manufacturing. Three control samples were set aside and the remaining 6 beams were processed for surface preparation before strengthening. Sides and the bottom of the beams were ground to remove the uneven parts caused by the mould. Dust was removed

TABLE 4: Strengthening of the sample beams.

Number	Samples	Types of strengthening material and method
1	K101	Control
2	K102	Control
3	K103	Control
4	KC201	CFRP 45° double-wrapped in opposite directions
5	KC202	CFRP 45° double-wrapped opposite directions
6	KC203	CFRP 45° double-wrapped opposite directions
7	KG301	GFRP 45° double-wrapped opposite directions
8	KG302	GFRP 45° double-wrapped opposite directions
9	KG303	GFRP 45° double-wrapped opposite directions

by pressurized water. Preparation of experimental beams is shown in Figure 2.

2.2.3. Strengthening of the Beams by Affixing 45° CFRP or GFRP. The first 3 samples were set aside as controls and they were not strengthened. Tensile region of the beams (K101, K102, and K103; see Figure 3) were prepared for the experiment by removing all moving particles on the surface. One-third of each beam on both ends was determined as the strengthening area. Epoxy (2 kg/m²) was applied on the surface of the strengthening area. CFRP on 3 beams and GFRP on the other 3 beams were affixed at 45° without leaving any air pocket. In order to remove air pockets in between the textile and the beam, a rolling cylinder was used. One day later, the same amount of epoxy was applied to CFRP. One week later, assembly cubes for strain gauge were attached with epoxy on the spots where crack determination will be performed. Ten days after this process, loading experiments were performed. CFRP and GFRP application on concrete beams is shown in Figure 3.



FIGURE 2: Preparation of experimental beams.

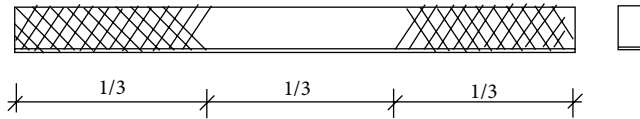


FIGURE 3: CFRP and GFRP application on concrete beams.

2.2.4. Experimental Setup. Experiments were carried with a loading device “Brand Model” at the Mechanics Laboratory of the Construction Education Department at Gazi University in Ankara. The device has 2 support points on a cart moving along a rail. The distance between these 2 supports was set to 2000 mm and one of which was fixed.

Four-point loading was applied on the top of the beams on 2 points. The distance between the loading zones was 660 mm. Metal plates with 10 mm thickness were obtained to be used on the zones where the loading was applied. A magnetized apparatus to which a linear variable differential transformer (LVDT) was attached was placed on top of the beams. Strain gauges were attached on each beam at the same 6 points. Data were recorded every 5 seconds with a data collection system through 8 channels: 6 crack, 1 displacement, and 1 loading data.

Loading was applied on 2 points on top of the beam and on 2 points where the support points are located at the bottom. One of the support points was fixed and the other was movable. Crack formation was observed using the data collected on 6 points on each beam. LVDT measuring displacement with 0.001 mm accuracy was placed in the middle of each beam. Recording was monitored on a data logger digital screen. Strain gauge device and LVDT are shown in Figure 4 and scheme of the loading mechanism is shown in Figure 5.

3. Results and Discussion

The data obtained in the present study are discussed in terms of load carrying capacity, load-displacement, tensile, and energy consumption capacity.



FIGURE 4: Strain gauge device and LVDT.

3.1. Load Carrying Capacity of the Concrete Beams. If loading is in low levels in a concrete beam prone to deflect, there may not exist any cracking in tensile regions. In that case, reinforcement and concrete carry the load on the tensile section altogether. However, because it would not be economical, except in pretension beams, to maintain all tensile sections in a quality preventing cracking, cracks occur in the tensile region of concrete materials [9].

Concrete between cracks may help the tensile a little bit. However, because this help is in a negligible amount, in a cracked section, all load carrying is assumed to be maintained by reinforcement. One thing that is for sure is that reinforcement cannot prevent cracking. The main function of reinforcement is to satisfy the tensile stress and keep cracks at minimum in size [10].

According to the Turkish Standards TS500 [11], in finding the concrete compressive strength in its compression zone, tensile stress distribution is converted to an equivalent rectangular by multiplying the f_{ck} value by 0.85. It is very useful to know the behavior of deflecting beams that are exposed to loading before calculating their load carrying capacity. The first cracks occurring in the tensile region are a result of the reach of the unit elongation of the outer tensile fiber to the upper tensile limit of the concrete. Crack moments of nonreinforced beams are assumed to be equal to their crushing moment [11].

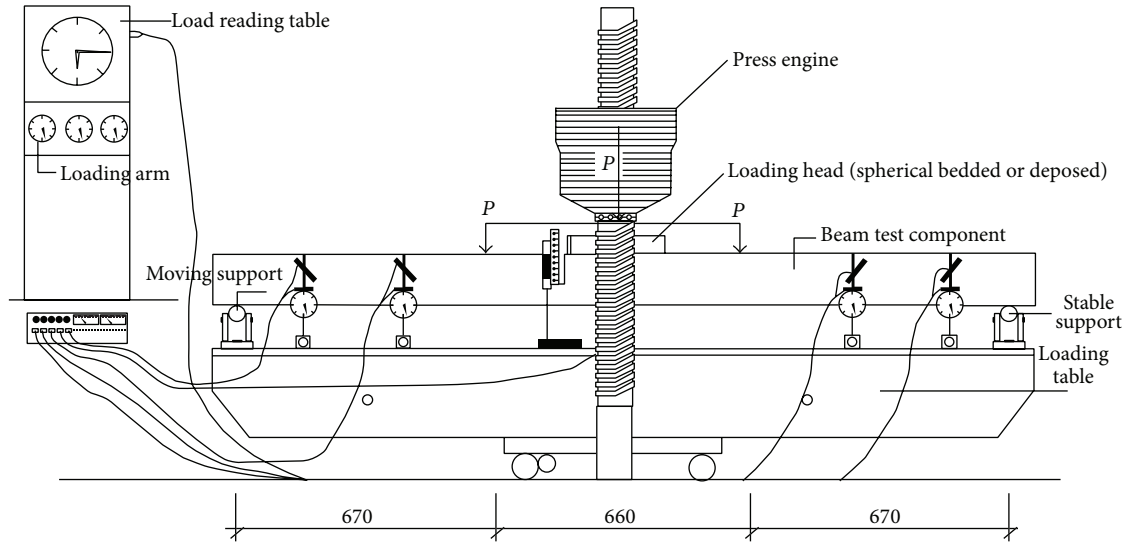


FIGURE 5: Scheme of the loading mechanism.

TABLE 5: Displacement values of each beam against the maximum load.

Sample beams	The maximum load (N)	Displacement (mm)
K101	99000	32
K102	92600	49
K103	95900	55
KC301	116400	26
KC302	119200	30
KC303	117500	12
KG301	122700	35
KG302	124600	28
KG303	121000	44

3.2. *Load-Displacement Charts.* Displacement values were recorded exactly at the center of the sample beams by LVDT at the same speed and by resetting the electronic meters each time. Displacement values of all sample beams against the maximum loading are presented in Table 5.

As a result of reinforcing, a reduction in displacement was observed. While there was a 35% increase in the strength of the beams with CFRP, there was 41% decrease in displacement. Furthermore, a 43% increase was observed in the strength of GFRP beams and 53.6% decrease in displacement.

Load-displacement chart of the sample beams diagrams K101, K102, and K103 is presented in Figure 6, load-displacement chart of the strengthened sample beams diagrams KC201, KC202, and KC203 is presented in Figure 7, load-displacement chart of the strengthened sample beams diagrams KG301, KG302, and KG303 is presented in Figure 8, respectively.

3.3. *Ductility Rates of the Beams.* Ductility rate was calculated by the load-displacement relationship. The deformation value at the point where the vertical line crosses the 85%

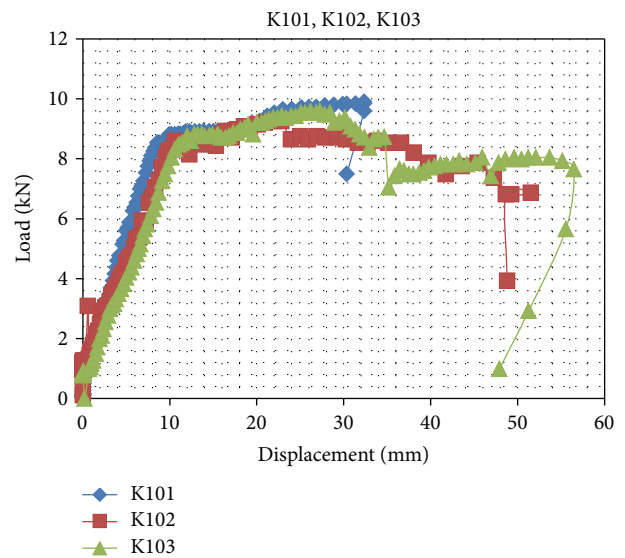


FIGURE 6: Load-displacement chart of the control sample beam.

of the monolithic beam strength of the load-displacement curve was determined. Ductility rate is defined as the value determined by dividing this deformation value by its creep deformation value. There are 2 types of ductility in reinforced concrete load bearing systems: curvature ductility and displacement ductility [10].

Although it is possible to use the moment ductility relationship to calculate ductility, load-displacement relationship was used instead.

3.4. *Energy Consumption in the Sample Beams.* In calculating the energy consumption of beams, load-displacement curves are used. The area under the curve yields the energy consumption [10].

TABLE 6: Shear cracks against the maximum load in sample beams.

Sample beams	Maximum load (N)	Strain gauge 2 (mm)	Strain gauge 5 (mm)
K101	99000	28	0.15
K102	92600	28	0.13
K103	95900	20	0.24
KC201	116400	0.57	0.16
KC202	119200	0.50	0.48
KC203	117500	0.59	0.80
KG301	122700	0.45	0.38
KG302	124600	0.30	0.25
KG303	121000	0.10	0.26

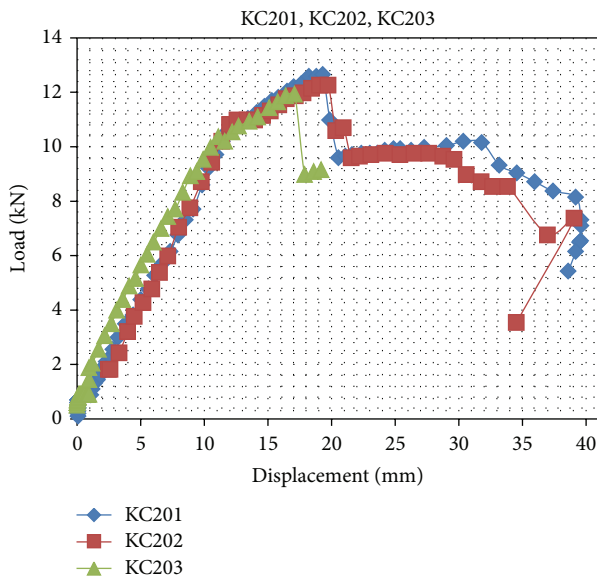


FIGURE 7: Load-displacement chart of the sample beam strengthened with CFRP.

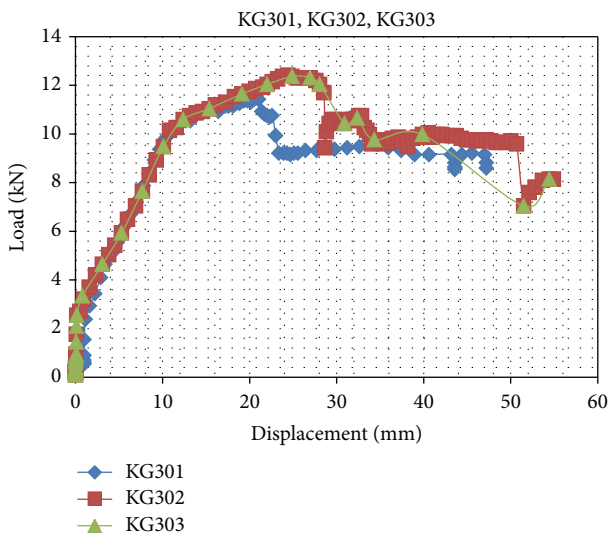


FIGURE 8: Load-displacement chart of the sample beam strengthened with GFRP.

TABLE 7: Flexural cracks against the maximum load in sample beams.

Sample beams	Maximum load (N)	Strain gauge 4 (mm)
K101	99000	62
K102	92600	68
K103	95900	74
KC201	116400	0.68
KC202	119200	0.71
KC203	117500	0.66
KG301	122700	0.14
KG302	124600	0.21
KG303	121000	0.22

Energy consumption rates of all beams were calculated using the area under the load-displacement curves. A certain amount of energy is spent as conversion to deformation. The amount of convertible energy is directly proportional with the length of the plastic region. As energy is the ability to do work, the amount of energy consumed has importance. In the load-displacement curve, energy consumption was found at the point where the maximum loading occurred.

3.5. Crack Loading Values. The data collected through 4 strain gauges placed on the shear region of the beams are presented in Table 6 and flexural cracks against the greatest load of beam samples presented in Table 7.

Shear cracks in the control beams were found as 28 mm in gauge 2 and 0.15 mm in 5. There was a 100% crack reduction in the CFRP sample in 2 while there was a 295% crack increase in 5. Cracks fell by 87% in the GFRP beams in gauge 2 and increased by 119% in 5. Also, by the help of reinforcement densification, shear region in region 2 was considerably strengthened. Shear effect was observed as more effective in region 5.

The changes in the tensile regions of the beams are as given above. The average change in the control beams against the maximum load was found as 70 mm. Cracks were reduced by 71% in the CFRP beams and 139% in GFRP beams. Improvements in this region are thought to improve the beam rigidity.

TABLE 8: Energy consumption capacity of the beams.

Sample beams	Max. Pu (kN)	Central failure (mm)	Energy consumption capacity (kNm)
K101	99000	45.44	942.216
K102	92600	41.13	985.482
K103	95900	50.24	1214.443
KC201	116400	35.28	1416.874
KC202	119200	29.54	1358.371
KC203	117500	31.50	1376.716
KG301	122700	37.63	1466.931
KG302	124600	29.40	1147.853
KG303	121000	33.74	1255.316

Pu: collapse load according to the steel yield load.

3.6. Energy Consumption Values. The amount of energy spent was calculated by locating the yield and failure moments. The curves obtained for all the beams and the areas under these curves are presented in Table 8. These values are considered in relation with the displacement and load values. Compared to the control beams, there was a 32% failure reduction in the CFRP beams while there was a 16.3% increase in energy consumption. Among the GFRP beams, 27% failure decrease and 22% energy consumption increase were observed.

4. Conclusions

Strength increasing of the beams strengthened with CFRP was 84% and the displacement reduction was found to be 39.5%. Strength increasing of the beams strengthened with GFRP was 45%, and the displacement reduction was found to be 53.6%.

In reinforced concrete beams strengthened with CFRP, there occurred a failure reduction by 29% as compared to control beams but energy consumption was increased 14.5%. In reinforced concrete beams specimens strengthened with GFRP, there occurred a failure reduction by 25% as compared to control beams specimens but energy consumption was increased 18%.

With increasing loading, the strengthened beams collapsed as shear fracture. In the samples, strength increased to some degree, but no increase was observed in terms of ductility and energy consumption. An apparent increase was observed in the bending strength. In the CFRP and GFRP reinforced beams, compared to controls, 38% and 42%, respectively, strength increase was observed.

GFRP beams were observed to break apart, as layers, easier than the CFRP beams. In all beams, failure-flexural stress occurred in the center as expected.

Most cracking was observed in the flexural region 4. In the control beams, crack size was observed as 0.25 mm in the secondary shear regions. On the other hand, in the same region, the crack size was 0.54 mm in CFRP beams and 0.33 mm in GFRP beams.

Cracking values recorded at the center and bottom of beams, where the maximum flexural and tensile stress were observed, were 0.68 mm in the control beams, and 0.71 mm and 0.14 mm in the CFRP and GFRP beams, respectively.

Displacement value of the control beams was observed as 45 mm and 21 mm and 29 mm in the CFRP and GFRP beams, respectively.

A comparison of CFRP and GFRP materials reveals that GFRP enforced parts absorb more energy. Both materials yielded successful results. In the present applications, it was observed that corner rounding was successful and that double wrapping in 2 opposing directions is not more effective than single wrapping compared to the literature. Thicker epoxy application in both CFRP and GFRP beams was considered to be effective in preventing break-ups. Because this material is lightweight, noncorroding, flexible, and available in large sizes, it is superior. Moreover, in case of fatigue, because of its elastic behavior, it has low ductility. Therefore, it is useful in temporary reinforcement applications.

Conflict of Interests

The author declares that there is no conflict of interests regarding the publication of this paper.

References

- [1] M. M. Önal, *An experimental research of the damaged rectangular cross-section beams repair by the method of coating [Ph.D. thesis]*, Gazi University Institute of Science, Ankara, Turkey, 2002.
- [2] T. Norris, M. Lean, H. Saadetmenesh, and M. R. Ehsani, "Analytical and experimental studies on strengthening of reinforced concrete beams with carbon FRP," *Journal of Structural Engineering, Arizona*, p. 903, 1997.
- [3] D. Kachlakev and D. D. McCurry, "Behavior of full-scale reinforced concrete beams retrofitted for shear and flexural with FRP laminates," *Composites B: Engineering*, vol. 31, no. 6-7, pp. 445-452, 2000.
- [4] X. B. Yang and A. Nanni, "Concrete beams strengthened with misaligned CFRP laminates," in *Fibre-Reinforced Plastics for Reinforced Concrete Structures-FRPRCS-5*, vol. 1, pp. 79-85, University of Cambridge, 2001.
- [5] A. M. Alkan, *Structure strengthening and improving by using polymer matrix composite [M.S. thesis]*, Sakarya University, Institute of Science and Technology, Sakarya, Turkey, 2002.
- [6] R. Perera, A. Recuero, A. de Diego, and C. López, "Adherence analysis of fiber-reinforced polymer strengthened RC beams,"

- Computers and Structures*, vol. 82, no. 23–26, pp. 1865–1873, 2004.
- [7] M. Maalej and K. S. Leong, “Effect of beam size and FRP thickness on interfacial shear stress concentration and failure mode of FRP-strengthened beams,” *Composites Science and Technology*, vol. 65, no. 7-8, pp. 1148–1158, 2005.
- [8] Teknomed Engineering Ltd, *Quake Wrap Product Catalog*, Istanbul, Turkey, 2000.
- [9] U. Ersoy and G. Özcebe, *Basic Principles of Reinforced Concrete TS-500-2000 and Calculated in Accordance with Regulations of the Turkish Earthquake*, Bizim Office Publications, Ankara, Turkey, 2001.
- [10] E. Atımtay, *Regulations with Explanations and Examples on Reinforced Concrete Structures to Be Built in Disaster Areas*, Bizim Office Publications, Ankara, Turkey, 2000.
- [11] TS 500, “Calculations and construction rules of reinforced concrete structures,” Turkish Standards.
- [12] M. Önal, “Repair and strengthening of damaged beams in reinforced concrete structures,” Scientific Research Projects 38/2004-01, Department of Gazi University, 2006.

Research Article

The Mechanical Behavior of Fiber Reinforced PP ECC Beams under Reverse Cyclic Loading

Yaw ChiaHwan and Han JianBo

Shenyang Architectural University, Hunnan East Road 9, Shenyang 110168, China

Correspondence should be addressed to Yaw ChiaHwan; 826125581@qq.com

Received 1 January 2014; Accepted 19 May 2014; Published 2 July 2014

Academic Editor: João Marciano Laredo dos Reis

Copyright © 2014 Y. ChiaHwan and H. JianBo. This is an open access article distributed under the Creative Commons Attribution License, which permits unrestricted use, distribution, and reproduction in any medium, provided the original work is properly cited.

When a structure is hit by earthquake, tremendous amount of seismic energy is released and structure is subjected to reverse loads. The mechanical properties of FRP reinforced PP ECC beams and coupon RC beam under reverse cyclic load controlled by displacement are investigated. Curing ages, reinforcement ratio, and volume fraction of PP fiber are parameters under survey. It is shown that multiple saturated cracking occurred in PP ECC beam and no crushing appeared. The PP ECC can enhance strength and energy dissipation capacity which are important to evaluate the performance of structures subjected to reverse cyclic loading.

1. Introduction

During the last decade, significant efforts have been made to develop ECC which exhibits tough, strain-hardening behavior under tension in spite of low fiber volume fraction [1]. ECC is a kind of ultraductile fiber reinforced cement based composite which has metal-like features when loaded in tension. The uniaxial stress-strain curve shows a yield point followed by strain-hardening up to several percent of strain, resulting in a material ductility of at least two orders of magnitude higher than normal concrete or standard fiber reinforced concrete [2]. ECC provides crack width to below $100\ \mu\text{m}$ even when deformed to several percent of tensile strain.

An increasingly large database of mechanical (including tension, compression, shear, fatigue, and creep) and physical properties (including shrinkage and freeze-thaw durability) of ECC is now being established around the world [3, 4], yet further research is needed for this novel composite. Anna [5] reported in Forbes self-healing phenomenon of PVA (Polyvinyl Alcohol) ECC and commented it as a novel composite which can bring revolution to civil engineering. Although Fisher and Li [6] have analyzed the failure mode of small scale connections and frames of PVA ECC, the tremendous cost has limited its application. The cost of PVA ECC is around 5 times that of ECC using PP (Polypropylene)

fibers. Therefore it is necessary to utilize cheap Polypropylene fibers to produce ECC with extraordinary properties. Until now, research work on PP ECC was only reported by Yang and Li [7] in the world. In this study Polypropylene fibers with surface improved by copolymer technology are utilized to produce PP ECC. The chemical bond of interface is enhanced in the microscale. The mechanical properties of PP ECC members such as toughness, ductility, dissipated energy, and impact resistance are improved. Figure 1 shows the four point bending test of plain PP ECC. By substituting traditional concrete with PP ECC, both FRP reinforcement and ECC are deforming compatibly in the inelastic deformation regime. The defects of low dissipated energy of concrete structures can be avoided. In this paper, five FRP reinforced PP ECC beams and one coupon concrete beam under reverse cyclic loading are investigated. The effect of parameters, that is, volume fraction of PP fiber, curing age of specimen, and FRP reinforcement ratio on cracking pattern, dissipated energy and stiffness degradation is analyzed.

2. Material Composition and Properties

The PP ECC contains PP (Polypropylene) fibers, cement, fly-ash, fine aggregates (maximum grain size $0.25\ \text{mm}$), and water. Viscosity modification agent (VMA) and high-range superplasticizer (SP) are used to enhance the fresh properties

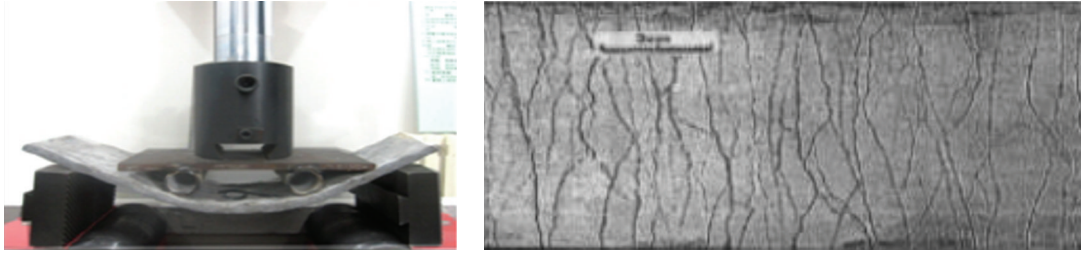
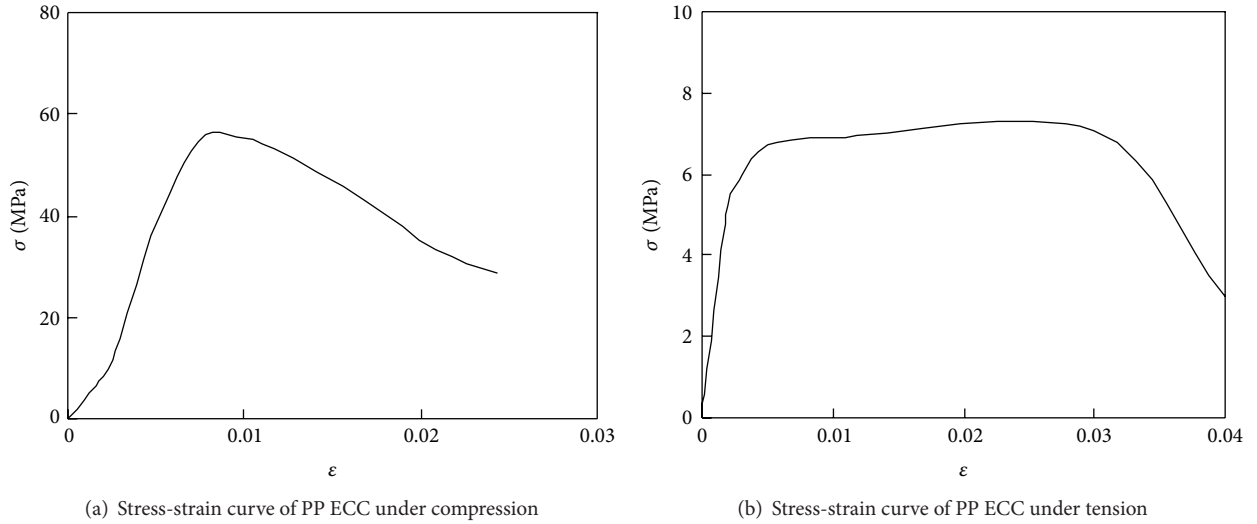


FIGURE 1: Four point bending test of plain PP ECC and multiple saturated cracking.



(a) Stress-strain curve of PP ECC under compression

(b) Stress-strain curve of PP ECC under tension

FIGURE 2: Stress-strain curves of PP ECC.

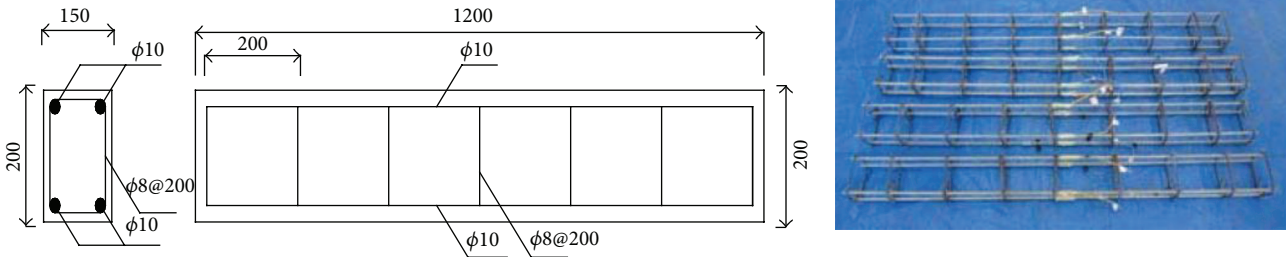


FIGURE 3: Dimensions and reinforcement details of specimens.

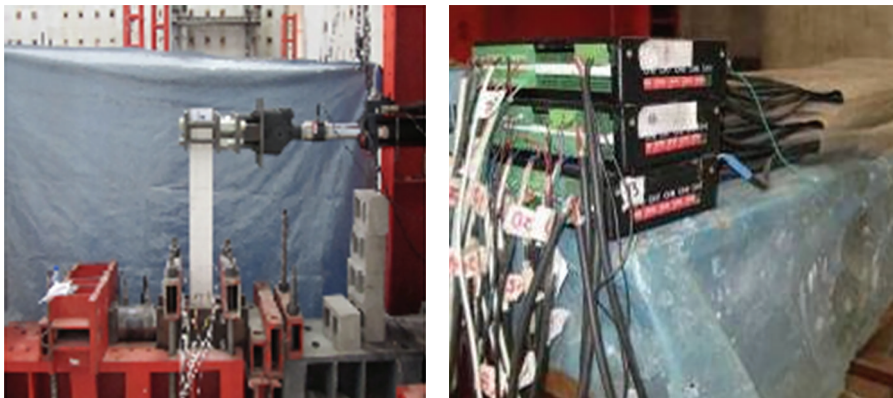


FIGURE 4: Setup of test and data acquisition board.

TABLE 1: Parameters of specimen.

Specimen number	Volume fraction of fiber (%)	Bar diameter φ (mm)	Reinforcement ratio ρ (%)	f_{cu} (MPa)	Curing age (days)
B1	1.5	8	0.76	56	60
B2	1.5	10	1.20	56	60
B3	2.0	10	1.20	40	60
B4	1.5	10	1.20	56	30
B5	1.5	12	1.72	56	60
B6	0	10	1.20	40	30

TABLE 2: Property of FRP bars.

Model	Density (g/cm ³)	Section area (cm ²)	Yield strength (MPa)	Tensile modulus (GPa)	Debonding strength (MPa)
FRP-8	3.16	0.56	707.5	64.0	>15 MPa
FRP-10	3.6	0.91	1027.5	89.0	>12 Mpa
FRP-12	3.21	1.31	836.6	65.3	>10 MPa

of the mixture. Concrete uses coarse aggregates (maximum grain size 10 mm), cement, water, and high-range SP.

When producing PP ECC, the sand and cement are mixed dryly first approximately for 30–60 seconds until the mixture becomes homogeneous. Then water, fly ash, SP, and VMA are added orderly. SP and VMA are used only when the mixer cannot mix further. At the end the fibers are added but the mixture can be mixed for only 30 s, otherwise it will be very clumpy. Stress-strain curves of PP ECC from this composition under uniaxial tension and compression were demonstrated in Figure 2.

In this paper, a selection of five PP ECC and 1 concrete beams involving FRP bars as reinforcing material is presented. FRP reinforcing bars with diameters of 8, 10, and 12 mm are arranged symmetrically in the beams of cross section of 150 × 200 mm as longitudinal reinforcement. The parameters under survey and specimen number are listed in Table 1. The parameters include volume fraction of PP fiber (1.5%–2.0%), curing age of specimen (30 and 60 days), and FRP reinforcement ratio.

FRP bars of 8, 10, and 12 mm diameter, respectively, with characteristic yield strengths of 707.5 MPa, 1027.5 MPa, and 836.6 MPa were used as conventional reinforcement satisfying the requirement of design code for minimum reinforcement. The property of FRP bars is shown in Table 2. Flexural failure of the beam was ensured by providing necessary shear reinforcement (stirrup of 6 mm diameter with 200 mm space). The geometry of the test specimen and reinforcement details are shown in Figure 3.

3. Test Specimen

The behavior of FRP reinforced PP ECC beams was experimentally investigated and compared to FRP reinforced concrete beam. All the flexural members were of cross section of 150 × 200 mm and a clear span of 1.2 m. A clear protection cover of 25 mm was provided in all specimens

In this study, reinforced PP ECC beams with different fiber volume fractions, bar diameters, and curing ages are

named as B1 to B5. A total of 5 PP ECC beams and 1 concrete beam were cast with ECC mix proportions given in Table 3. The coupon specimen of reinforced concrete beam is named as B6.

4. Experimental Setup and Testing Procedure

Cyclic tests were performed using MTS Hydroplus Machine with maximum capacity of 100 kN in static loading and 80 kN in dynamic loading. Schematic diagram of the experimental setup is shown in Figure 4. This loading configuration was chosen to promote a flexural deformation mode in all specimens. In this way, the effect of PP ECC properties on the expected plastic hinge region can be learned.

Lateral loading was applied through a MTS actuator according to a displacement-controlled reverse cyclic loading sequence. The loading rate was kept at 0.2 mm/second for imposed deflection. For each cycle, the imposed deflection increased by 2 mm or 4 mm before or after it reached 24 mm, respectively. The experiment stopped once the applied load dropped to 85% of the ultimate load.

In PP ECC specimen B1 with transverse reinforcement (Figure 5), flexural cracking formed during the initial loading cycles and extended up to 720 mm specimen height at 28 mm drift. The debonding between FRP bars and ECC started to occur. The approximate crack spacing was 40 mm and maximum crack width was below 0.1 mm. Then the number of flexural cracks increased significantly with crack formation up to 950 mm specimen height. At this loading stage, neither localization nor bond splitting of flexural cracks was observed. The average crack spacing reduced to 20 mm with a maximum crack opening of 0.2 mm at the cantilever base. However, few minor shear cracks formed in the midsection of the cantilever. At 32 mm drift, the number of flexural cracks stabilized and cracking localized at the cantilever base; shear failure was not observed. Additional cracks extended to 1080 mm height at a 45 degree angle and interconnected cracks which already existed. Beyond 48 mm drift, a tendency

TABLE 3: Mix proportions of ECC.

Cement	Silica sand	Fly ash	Water	Superplasticizer	Fiber volume fraction (%)	VMA
1.0	0.8	1.2	0.66	0.013%	2.0	0.03%

TABLE 4: Degeneration factor of load bearing capacity.

Degradation	Displacement							
	24 mm	28 mm	32 mm	36 mm	40 mm	44 mm	48 mm	52 mm
Specimen								
B1	0.91	0.91	0.96	0.93	0.9	0.87	0.89	0.91
B2	0.9	0.91	0.92	0.8	0.96	0.9	0.78	0.8
B3	0.9	0.92	0.88	0.82	0.85	0.91	0.9	0.9
B4	0.93	0.92	0.91	0.95	0.92	0.92	0.9	0.9
B5	0.92	0.93	0.93	0.92	0.9	0.91	0.92	0.93

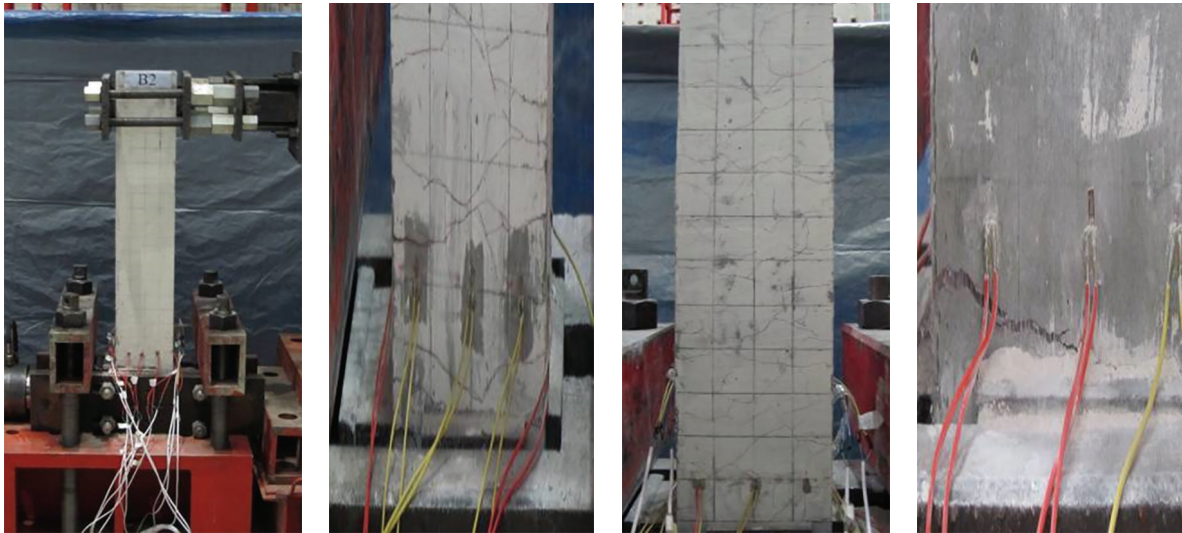


FIGURE 5: Failure modes of PP ECC specimen.



FIGURE 6: Failure modes of concrete specimen.

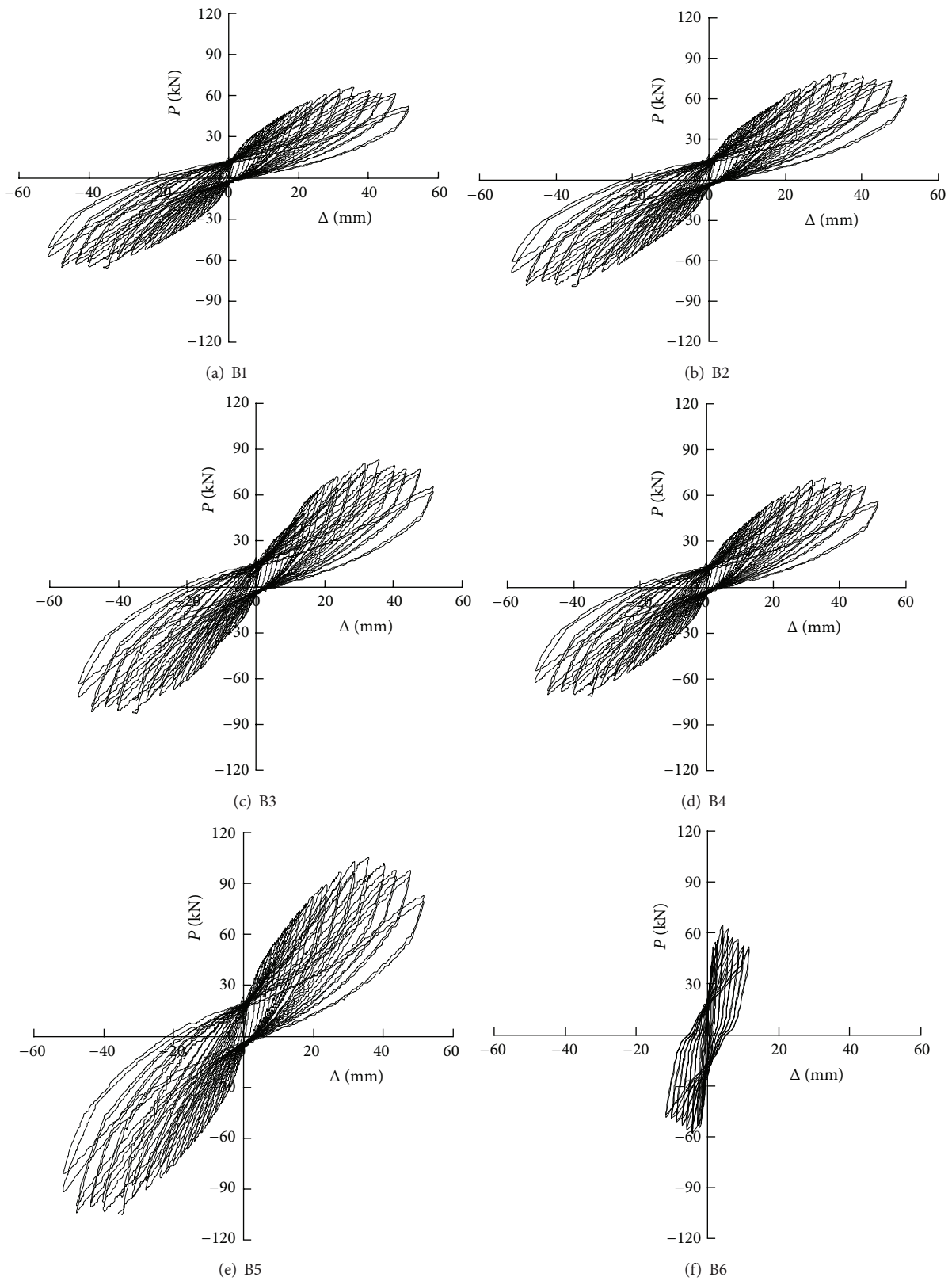


FIGURE 7: $P - \Delta$ hysteresis curve of FRP reinforced PP ECC and concrete specimen.

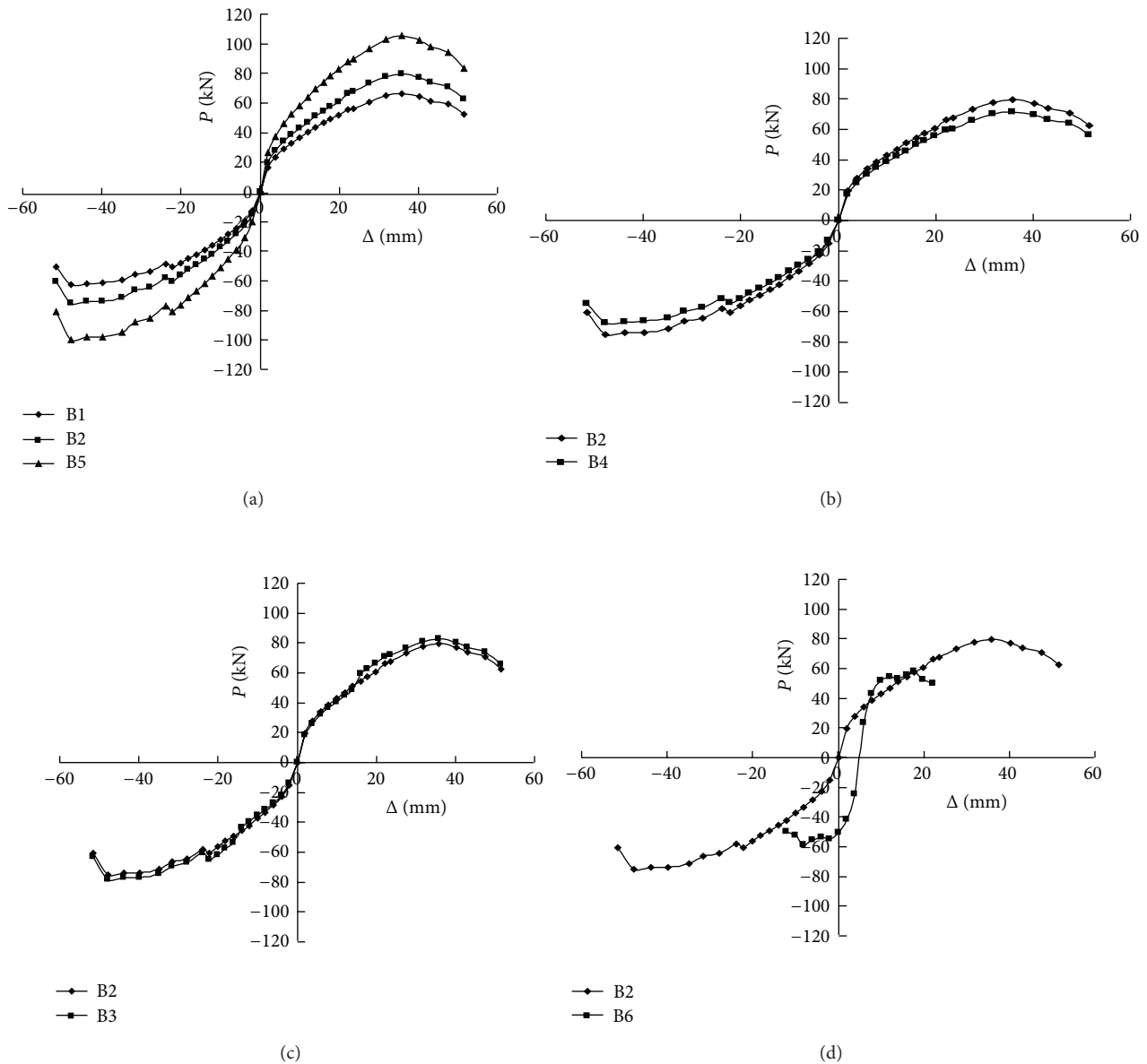


FIGURE 8: Influences of different parameters on $P - \Delta$ hysteresis curve.

of rotational sliding and grinding between the foundation and cantilever section along with interconnected flexural crack plane occurred, while only minor crushing of ECC observed.

The deformation behavior of Specimen B2–B5 was very similar to that of specimen B1. A concentration of flexural cracking was observed at the cantilever base and no obvious crushing of ECC occurred. All the crack width remained below 0.3 mm. However, the distribution of flexural cracking was more uniform with a larger average spacing and less significant shear crack formation. As the load surpassed the bearing capacity of the specimen, the width of the crack increased until a horizontal main crack appeared in the tension face near the cantilever base. Simultaneously, sound of the PP fibers being pulled out and ruptured from the matrix

can be clearly heard. Upon unloading, all the crack width returned to the state of initial loading cycles.

In beam B6 of reinforced concrete (Figure 6), no multiple cracking was observed and flexural cracking initiated at the cantilever base in the first loading cycle. Individual cracks propagated from the tension side and formed connecting crack paths upon reverse load. At deflection of 2 mm, only flexural cracking was observed at an approximate spacing of 100 mm. The maximum crack width of 1 mm was found on the tension face near the base of the specimen.

As the load increased, the number of flexural cracks slightly increased. Also the cracks extended to 840 mm height of the specimen with a maximum crack opening of 2 mm at the cantilever base. Additional cracks initiat-

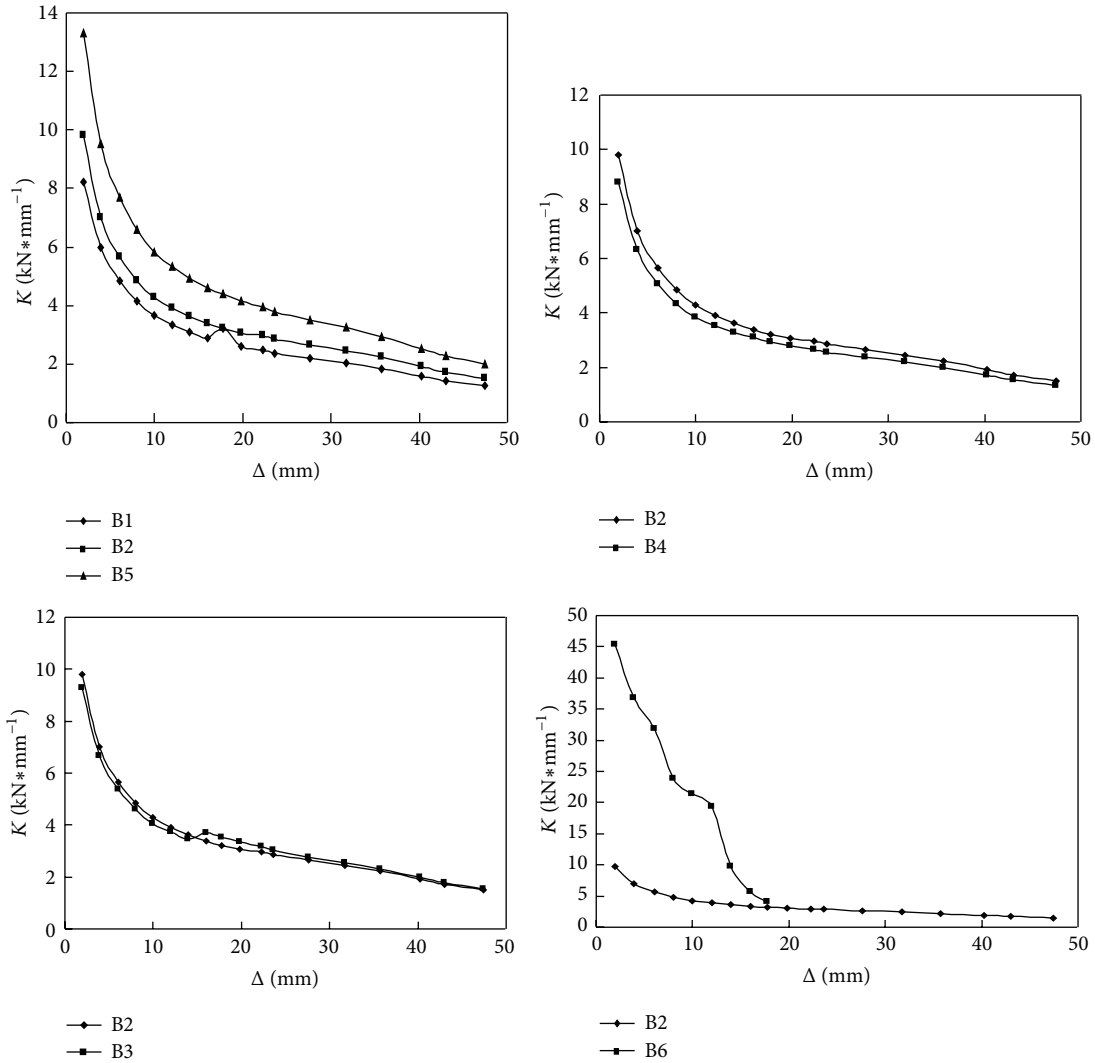


FIGURE 9: Influences of parameters on stiffness.

ing at the intersection of existing flexural cracks or longitudinal reinforcement became apparent at deflection of 4 mm. Then the cracks propagated along the FRP reinforcement under the influence of compressive stress in the reverse half-cycle. Due to further crushing of concrete in the initial half-cycle at deflection of 10 mm, the longitudinal FRP reinforcement experienced excessive compressive strain and ruptured by tension in the reverse half-cycle (Figure 6).

Spalling of concrete cover is a common problem with structural element subjected to reverse cyclic loading, because each element comes alternatively in compression and tension. In this experiment, the spalling of PP ECC cover did not occur. However the spalling of concrete cover was severe. It is due to the fact that before fibers break or slip from the matrix, they always hold the cementitious matrix tight by bridging the cracks. Reduction in the spalling of concrete by the use of PP fibers in structural member subjected to reverse cyclic loading can lead to less maintenance and rehabilitation cost after earthquake.

5. Hysteretic Response

Structures are expected to enter elastoplastic range under dynamic loading or strong earthquake, so hysteresis curve is useful for analysis of seismic elastoplastic response. Hysteresis loops ($P - \Delta$) are load-displacement relationships of structures under cyclic loading. Figure 7 shows the lateral force (P) versus top displacement (Δ) relationship for beams B1 to B6. For all specimens, maximum load during each cycle of imposed deflection was recorded.

The hysteretic curve is linear at the initial loading cycle for PP ECC beams B1–B5. At 60%–70% load bearing capacity, the hysteretic curves behaved nonlinearly as the specimens entered elastoplastic stage. When the drift Δ equals 30 mm, the hysteretic loop changed from spindle to reversed S shape. After that the loops began to flatten out, showing that less force was required to maintain the same displacement in the beam. Throughout the whole test, the loops became fatter and fatter as the load increased. The enlarged hysteretic loops

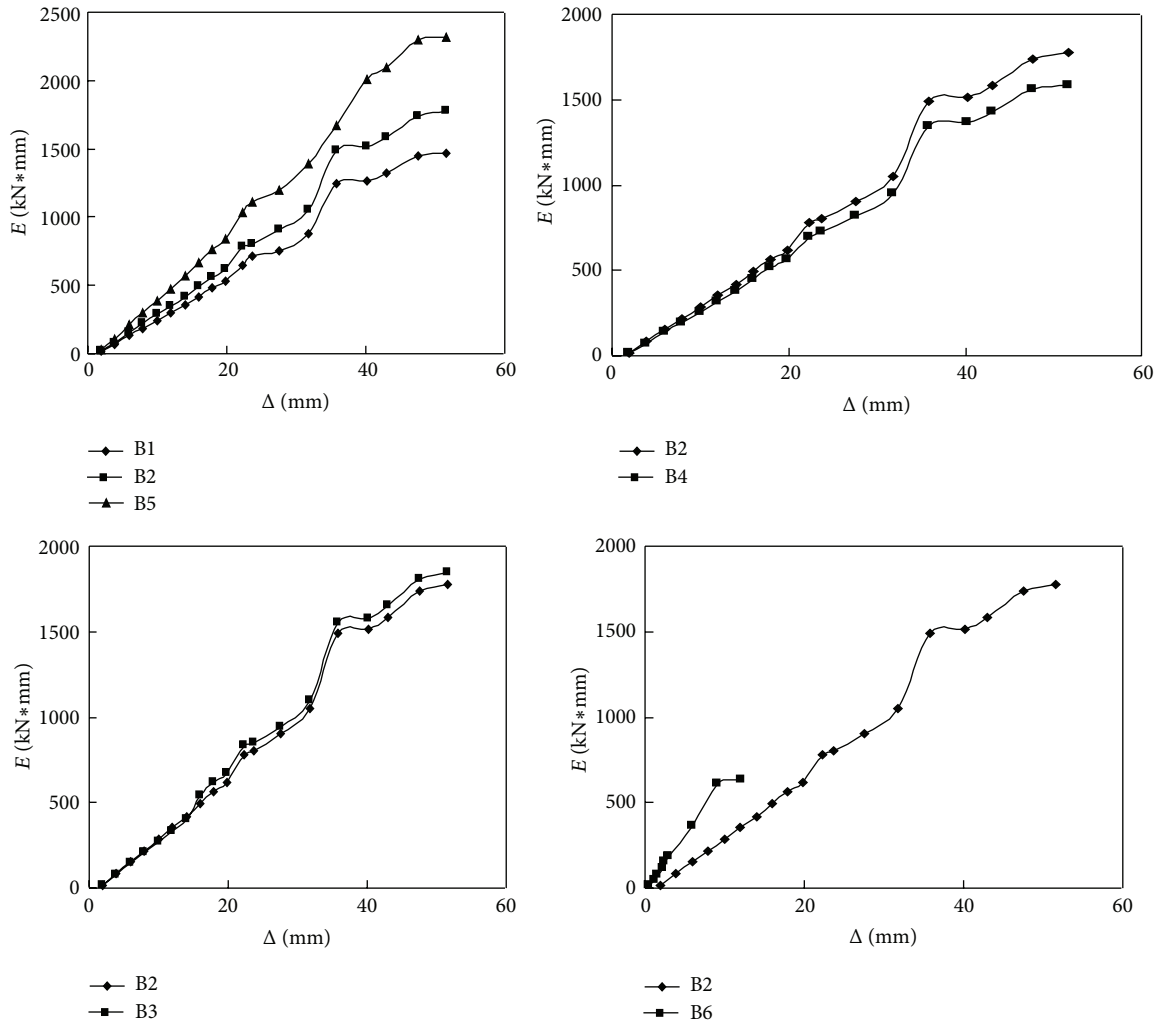


FIGURE 10: Influences of parameters on dissipated energy.

indicated an increase in energy dissipation. For reinforced concrete beam B6, no obvious pinching phenomenon can be observed in the hysteretic loop. As the top displacement Δ reached 10 mm, almost all the concrete protection cover near the base are crushed.

6. Skeleton Curve

The influence of reinforcement ratio, curing age, and volume fraction of PP fiber on skeleton curve is shown in Figure 8. It is found in Figure 8(a) that the load bearing capacity of PP ECC beams increased with higher reinforcement ratio. In Figure 8(b), it is shown that the load bearing capacity of beam B2 is higher than B3; however the ductility is obviously lower. Therefore it can be stated that the longer curing age of PP ECC, the higher load bearing capacity and lower ductility. It is observed in Figure 8(c) that there is no much difference for the skeleton curves of specimens B2 and B4. So the different volume fraction of fibers 1.5% and 2% does not have much effect on the ductility and load bearing capacity of reinforced

PP ECC beam. However, the shapes of skeleton curves of specimens B2 and B6 are different. The top displacement of PP ECC beam B2 especially is almost 3 times that of concrete beam B6. Therefore, it is obvious that the ductility of PP ECC is far better than concrete.

7. Degradation of Load Bearing Capacity and Stiffness

The factor of load bearing capacity degradation is defined as $\lambda = P_{2\max}/P_{1\max}$, namely, the ratio of peak load value at 2nd cycle to that of 1st cycle at the same drift level. The factor of load bearing capacity degradation of each hysteresis curve is shown in Table 4. The difference for λ of the five PP ECC specimens is not obvious, with 8% reduction at most. So the parameters including volume fraction of PP fiber (1.5%–2.0%), curing age of specimen (30 and 60 days), and FRP reinforcement ratio do not have much effect on λ . This is mainly due to the fact that no coarse aggregates are utilized in

PP ECC and more fibers are pulled out and ruptured during the 2nd loading cycle.

Stiffness of the beam under reverse cyclic load decreases as the load cycle number increases. Factor of stiffness degradation can be defined as $K = \sum P_i / \sum \Delta_i$, namely, the ratio of the sum of peak load value to the sum of top displacement during every adjacent two cycles of the same drift. The relationship of top displacement Δ and factor of stiffness degradation K is shown in Figure 9.

It is obvious that lower reinforcement ratio corresponds to lower stiffness of the beams. The degradation of PP ECC and concrete beams started at 10 mm and 18 mm drift, respectively. However the volume fraction of PP fiber does not make much difference to the stiffness degradation. Before yielding, the stiffness degradation of the PP ECC beam is almost the same at curing ages of 30 and 60 days. After yielding, the stiffness degradation of PP ECC beams with 30 days curing age is more obvious than that of 60 days. It is calculated that the original stiffness of concrete beam is around 5 times that of PP ECC beams. However the degradation of concrete is more serious at later stage.

8. Cumulative Dissipated Energy

Energy dissipation in a loading cycle is the area that hysteresis loop encloses in the corresponding load-deflection curve. The cumulative dissipated energy E is then determined by adding the energy dissipated in consecutive loops throughout the test (Figure 10). Overall speaking, the value of dissipated energy is greater for specimens with FRP bars of bigger diameter. The value of dissipated energy for specimens with different volume fractions of fiber (1.5% and 2%) does not have much difference. The value of dissipated energy for specimen of longer curing age (60 days) is greater than that of shorter curing age (30 days). The dissipated energy for concrete beam is more than that of PP ECC specimen before the drift Δ reached 10 mm. The drifts Δ of beams B2 and B6 at load bearing capacity are 35.8 mm and 4.3 mm, respectively. The total dissipated energy of PP ECC beam is around 3.2 times of coupon beam.

9. Conclusions

Through visual observations, it was found that reduction of flexural crack width in PP ECC beams occurred. Moreover, No spalling or crushing of ECC cover was observed. The top displacement Δ of PP ECC beams upon yielding is around 3 times that of concrete beam. The bigger the diameter of FRP bars, the bigger the load bearing capacity and the energy dissipation capacity of PP ECC beam. The difference of volume fraction of fiber does not have much effect on the ductility, stiffness degradation of reinforced PP ECC beam. However, the longer the curing age (60 days) of PP ECC, the higher the load bearing capacity and the lower the ductility. The curing age has limited effect on the stiffness degradation and dissipated energy. The dissipated energy of PP ECC beam is 2.9 times that of coupon concrete beam. Moreover, less damage is observed in PP ECC since fibers always try to hold the cementitious matrix by crack bridging.

During an earthquake, the structures are always required to withstand seismic forces without significant reduction in the strength and serviceability limit state. After the earthquake, rehabilitation and maintenance cost should be as low as possible. It is obvious that FRP reinforced PP ECC can improve load bearing capacity and energy dissipation capacity of the beams. Therefore, PP ECC is promising for future structures to behave more effectively against seismic action.

Conflict of Interests

The authors declare that there is no conflict of interests regarding the publication of this paper.

References

- [1] S. Wang, *Micromechanics based matrix design for engineered cementitious composites [Ph.D. thesis]*, University of Michigan, Ann Arbor, Mich, USA, 2005.
- [2] M. Maalej, S. T. Quek, and J. Zhang, "Behavior of hybrid-fiber engineered cementitious composites subjected to dynamic tensile loading and projectile impact," *Journal of Materials in Civil Engineering*, vol. 17, no. 2, pp. 143–152, 2005.
- [3] E. H. Yang, *Designing added functions in engineered cementitious composites [Ph.D. thesis]*, University of Michigan, Ann Arbor, Mich, USA, 2008.
- [4] E. H. Yang, S. Wang, Y. Yang, and V. C. Li, "Fiber-bridging constitutive law of engineered cementitious composites," *Journal of Advanced Concrete Technology*, vol. 6, no. 1, pp. 181–193, 2008.
- [5] V. B. Anna, "Self-healing concrete," *Forbes*, vol. 2, pp. 46–47, 2009.
- [6] G. Fischer and V. C. Li, "Effect of matrix ductility on deformation behavior of steel Reinforced ECC flexural members under reversed cyclic loading conditions," *ACI Structural Journal*, vol. 99, no. 6, pp. 781–790, 2002.
- [7] E. H. Yang and V. C. Li, "Strain-hardening fiber cement optimization and component tailoring by means of a micromechanical model," *Construction and Building Materials*, vol. 24, no. 2, pp. 130–139, 2010.

Research Article

Investigation of Soil Liquefaction Potential around Efteni Lake in Duzce Turkey: Using Empirical Relationships between Shear Wave Velocity and SPT Blow Count (N)

Ali Ateş,¹ İnan Keskin,² Ermedin Totiç,³ and Burak Yeşil⁴

¹ Geotechnical Division, Department of Civil Engineering, Duzce University, 81620 Duzce, Turkey

² Geotechnical Division, Department of Civil Engineering, Karabuk University, 78050 Karabuk, Turkey

³ Geotechnical Division, Department of Civil Engineering, Bartın University, 74100 Bartın, Turkey

⁴ Duzce Technical Science Vocational School Construction Division, Duzce University, 81620 Duzce, Turkey

Correspondence should be addressed to Ali Ateş; alimates@duzce.edu.tr

Received 7 January 2014; Accepted 19 May 2014; Published 1 July 2014

Academic Editor: Gonzalo Martínez-Barrera

Copyright © 2014 Ali Ateş et al. This is an open access article distributed under the Creative Commons Attribution License, which permits unrestricted use, distribution, and reproduction in any medium, provided the original work is properly cited.

Evaluation of the liquefaction potential of a liquefaction-prone area is important for geotechnical earthquake engineering, both for assessment for site selection and for planning and new constructions. The liquefaction potential index for the city of Duzce in northwestern Turkey using the empirical relationships between the Standard Penetration Test (SPT) and the Shear Wave Velocity Test (V_S) was investigated in this study. After, V_S values based on SPT blow counts (N) were obtained from the alluvial soils in the city of Duzce. The liquefaction potential indexes of the soils were determined using the empirical relationships between the Standard Penetration Test (SPT) and the Shear Wave Velocity Test (V_S) calculating for a probable earthquake of $M_W = 7.2$. In the result of the study, the liquefaction potential index (LPI) values were interpreted and compared evaluating the SPT N blow count values obtained from the study area. Based on the empirical relationships assumed for the soils, it was observed that there was not a perfect agreement between the results of the two methods. The liquefaction potential index values using the SPT N blow counts were found to be lower than those of the V_S method.

1. Introduction

The liquefaction resistance of soils can be evaluated using laboratory tests such as the cyclic simple shear and cyclic triaxial and cyclic torsional shear tests. Additionally, field methods such as the Standard Penetration Test (SPT), Cone Penetration Test (CPT), and Shear Wave Velocity Test (V_S) can be employed. The occurrence of liquefaction in soils is often evaluated using the simplified procedure originally developed and proposed by Seed and Idriss [1] based on the SPT blow counts correlated with the cyclic stress ratio (CSR), a parameter representing the seismic loading on the soil. This procedure has undergone several revisions and updates [2–4]. In addition to these, procedures have been developed based on the Cone Penetration Test (CPT), Becker Penetration Test (BPT), and small-strain Shear Wave Velocity (V_S) measurements. Youd et al. [2] provided and enhanced

a recent review of the Seed and Idriss simplified procedure and the in situ test methods commonly used to evaluate the liquefaction resistance of soils.

The use of V_S to determine the liquefaction resistance is influenced by factors such as confining stress, plasticity, and relative density [5–7]. In situ V_S can be measured by several seismic tests, including cross hole, down hole, seismic cone penetrometer (SCPT), suspension logger, and spectral analysis of the surface waves (SASW) [8].

During the past two decades, several procedures have been proposed to estimate liquefaction resistance based on V_S [8]. These procedures were developed from laboratory studies [8–15], analytical studies [16, 17], penetration V_S equations [18, 19], and in situ V_S measurements at earthquake sites [20–22]. Some of these procedures follow the general approach of the Seed-Idriss simplified procedure, in which the V_S is corrected with the cyclic stress ratio. This paper presents

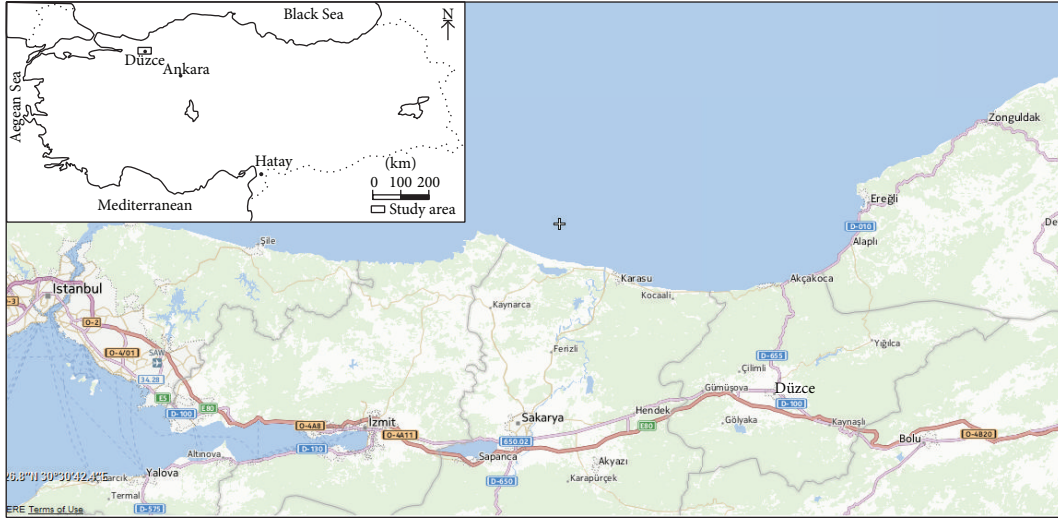


FIGURE 1: The study area (Duzce Province).



FIGURE 2: View of the Duzce fault [24].

the results of the comparison between the V_S and SPT methods of soil liquefaction potential evaluation carried out in Duzce Province in Turkey. Furthermore, the liquefaction potential indexes (LPI) for both aforementioned methods were calculated using the procedure of Iwasaki et al. [23].

2. Study Area

Duzce Province is located in northwestern Turkey (Figure 1). It is under the effect of the North Anatolian Fault Zone (NAFZ) and is about 30 km distant from the Black Sea. The provincial capital of Duzce is situated on an alluvial soil site.

2.1. Geomorphological and Geological Setting. The study area is situated in an active seismic earthquake zone [24]. Duzce

has been affected by the active faults. The 1957 Bolu ($M = 7$) and 1967 Adapazarı ($M = 7.1$) earthquakes occurred on the Bolu-Abant Dokurcun segments of the NAFZ. The active and probable active faults of Duzce, Hendek, and Çilimli are in close proximity to the study area [25] (Figure 2).

During the ($M = 7.4$) earthquake of 1999, the 30 km eastern segment of the 130 km fault rupture occurred on the western part of the Duzce Fault reaching to Efteni Lake [25]. Duzce plain is an active subsidence and deposition area controlled by lateral strike slip faults surrounded by pre-Quaternary-aged rocks. The oldest is the Yığılca Unit of Eocene-aged caycuma. Formations include volcanic sandstone, rottenstone, andesitic and basaltic lavas and volcanic breccia [26]. Quaternary-aged fan, deltaic, and marsh type

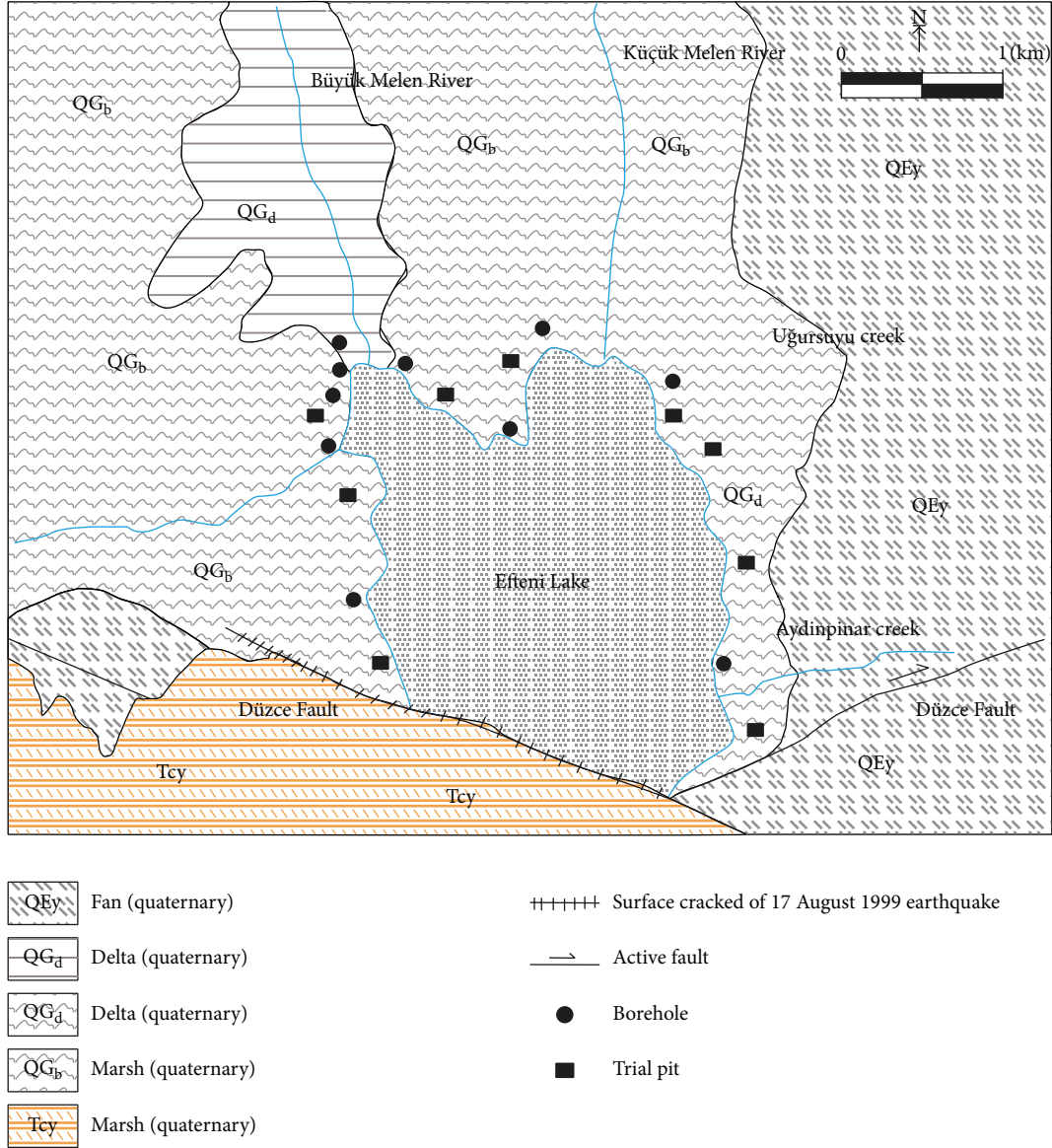


FIGURE 3: Geological map of the study area and some borehole locations [26].

deposits cover this unit, which consists of gravel, sand, silt, and clay material (Figure 3).

Due to the elevation of the surrounding rocks and as a result of the basin drainage, deposition occurred mostly in the Duzce area and its surroundings (Figure 4). Little Melen (Kucuk Melen) River discharges into the lake and continues flowing towards the only discharge from the lake, the Big Melen (Buyuk Melen) River. In addition, Aksu, Uğursuyu and Aydınpınar Creeks deposit alluvial fans and join in the lake basin. The surrounding rocks are extremely weathered by eroding, allowing the increase in sedimentation. The thickness of the sedimentation is about 260–300 m. The deposition areas have displaced laterally and the horizontal stratigraphy has been altered [25] (Figure 4).

2.2. *Seismotectonics of the Study Area.* Duzce plain is a pull apart type basin that is controlled by the lateral strike slip fault



FIGURE 4: View of the deposits in the Duzce area.

system in the NAFZ [28] (Figure 5). Paleo- and neotectonic period active faults exist at the north and south of the plain. There are several faults which are parallel and oblique to these major faults. During the 12 November 1999's earthquake, the surface rupture ranged through Golyaka on the south towards Kaynaşlı on the east, ending in the Asarsu Valley and

TABLE 1: Magnitude and damage records of earthquakes around the study area [24].

Locations	Date	Epicenter	M_w	Total damage on structures	Death	Injury
Murefte	09.08.1912	40.60–27.20	7.3	5.540	216	466
Hendek	20.06.1943	40.85–30.51	6.6	No	336	No
Gerede	01.02.1944	41.41–32.69	7.2	20.865	3.959	No
Duzce	10.02.1944	41.00–32.30	5.4	900	No	No
Mudurnu	05.04.1944	40.84–31.12	5.6	900	30	No
Yenice	18.03.1953	39.99–27.36	7.4	9.670	265	336
Abant	26.05.1957	40.60–31.20	7.1	4.201	52	100
Çınarcık	18.09.1963	40.77–29.12	6.3	230	1	26
Adapazarı	22.07.1967	40.60–30.89	7.2	5.569	89	235
Gelibolu	27.03.1975	40.45–26.12	6.4	980	7	No
Golcuk	13.09.1999	40.80–30.03	5.7	No	No	Unknown
Duzce	12.11.1999	40.79–31.21	7.2	15.389	845	4.948
Bolu	17.11.1999	40.83–31.51	5.0	No	No	No
Bolu	22.03.2000	40.94–31.58	5.4	No	No	No
Yigilca	26.08.2001	40.93–31.53	5.1	No	No	No

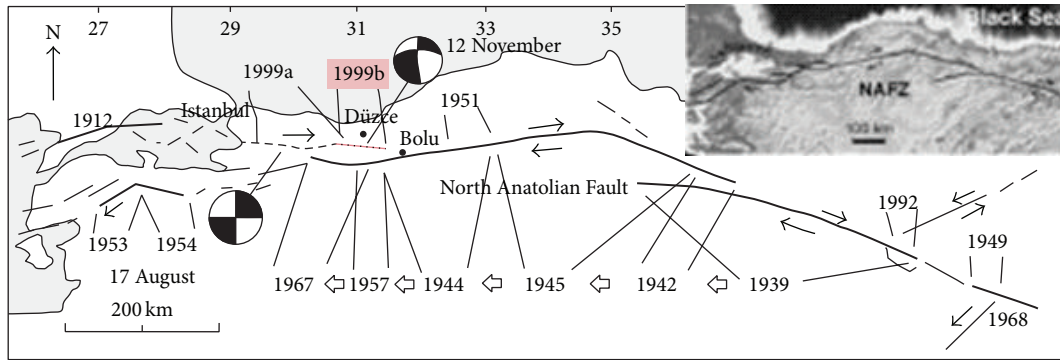


FIGURE 5: Epicenters of the earthquakes and historical earthquakes in the region [25].

the Bolu Tunnel. The city of Duzce is situated in the middle of the plain on a pressure ridge type hill, probably tectonically controlled. Major earthquake records are given in Table 1. Historical earthquakes have been recorded on the Abant-Bayramoren segment in the south. There were 12 earthquakes between 1967 and 1890. The great earthquake of 17 August, 1668 ($M_S = 8$), caused a disaster in Anatolia [29], with aftershocks continuing for 6 months [30]. The Bolu-Gerede earthquake ($M_w = 7.3$) on January 2, 1944, was a major one, recorded after the implementation of instruments for scientific measurement of magnitude. It was noted that 2,381 people died and 50,000 houses were damaged [31]. Although the 17 August, 1999, Marmara and 12 November, 1999, Duzce earthquakes occurred on the western segment of the North Anatolian Fault, the measured average value of the horizontal ground acceleration was 0.54 g in Duzce [32].

3. Materials and Methods

3.1. Field Investigations. Geotechnical bore holes were drilled at 40 locations. The depths of the boreholes ranged from 10 to 30 m, which measured to a total of 296 m. These boreholes were utilized to determine the consistency of fine-grained soils and the stiffness of the coarse soils, to

obtain undisturbed and disturbed samples and to measure the groundwater level. A Standard Penetration Test (SPT) [33] was carried out during the drillings and SPT N blow counts were obtained in the boreholes. In situ unit weight and moisture content values were obtained from the trial pits. Then, representative soil samples were obtained in order to determine the geomechanical properties of the soils. The 296 m-thick alluvium was very heterogeneous and included confined and unconfined aquifers. The groundwater level was mostly at the surface and ranged between 1.5 and 3.9 m.

In this study, the shear wave velocity (V_S) measurements were based on Andrus et al. [27] process for assessing liquefaction potential; V_S values were calculated using empirical equations between shear wave velocity and SPT blow count (N) for all types as follows [34]. The V_S values based on SPT blow count (N) were given below (Table 2):

$$V_S = 61 \cdot N^{0.5}, \quad (1)$$

$$V_S = 97 \cdot N^{0.314}, \quad (2)$$

$$V_S = 76 \cdot N^{0.33}, \quad (3)$$

$$V_S = 121 \cdot N^{0.27}, \quad (4)$$

$$V_S = 22 \cdot N^{0.85}. \quad (5)$$

TABLE 2: Field data of Duzce Province.

Boreholes number	SPT- <i>N</i> Depth (m)	SPT- <i>N</i>	Water Level	Shear Wave Velocity				
				Equation (1) ($61 \cdot N^{0.5}$)	Equation (2) ($97 \cdot N^{0.314}$)	Equation (3) ($76 \cdot N^{0.33}$)	Equation (4) ($121 \cdot N^{0.27}$)	Equation (5) ($22 \cdot N^{0.85}$)
BH1	3	32	3.5	345.06	287.99	238.5	308.45	418.7
BH1	9	32	3.5	435.06	287.99	238.5	308.45	418.7
BH2	3	25	3	305	265.5	219.9	288.6	339.4
BH2	6	15	3	236.3	227.02	185.75	251.4	219.9
BH2	15	45	3	409.2	320.5	266.9	338.2	559.3
BH3	4.5	32	4.00	345.06	227.02	185.75	251.4	219.9
BH3	6.00	32	4.00	345.06	227.02	185.75	251.4	219.9
BH3	7.5	28	4.00	322.8	276.17	228.4	297.52	373.7
BH3	12	31	4.00	339.7	285.14	236.02	305.9	407.5
BH4	3.00	31	2.5	339.7	285.14	236.02	305.9	407.5
BH4	6.00	13	2.5	219.95	217.01	177.2	241.9	194.7
BH4	7.5	16	2.5	244	231.7	189.8	255.8	232.3
BH4	9.00	13	2.5	219.94	217.1	177.2	242	194.6
BH4	17.00	13	2.5	219.94	217.1	177.2	242	194.6
BH5	No	No	No	No	No	No	No	No
BH6	3.00	28	2.5	322.8	276.2	228.24	297.52	373.7
BH6	4.5	23	2.5	292.54	260	213.9	282.2	316.2
BH6	7.5	21	2.5	279.6	252.3	207.56	275.3	292.7
BH6	12.00	32	2.5	345.06	252.3	207.56	275.3	292.7
BH7	No	No	No	No	No	No	No	No
BH8	9.00	11	4.0	202.3	206	167.7	231.2	168.9
BH8	10.50	26	4.0	311.1	269.9	222.7	292	350.9
BH8	13.500	28	4.0	322.8	276.2	228.24	297.52	373.7
BH9	9.00	28	4.00	322.8	276.2	228.24	297.52	373.7
BH9	16.5	81	4.00	549	385.6	324.1	396.4	922
BH10	No	No	No	No	No	No	No	No
BH11	7.5	14	3.5	228.3	222.2	182	246.7	207.4
BH11	10.5	40	3.5	386	308.9	256.7	327.6	506.1
BH12	4.5	32	3.25	345.1	252.3	207.56	275.3	292.7
BH12	6.0	36	3.25	366	298.9	248	318.5	463
BH12	10.5	42	3.25	395.4	313.7	260.9	331.9	527.8
BH13	No	No	No	No	No	No	No	No
BH14	3.0	15	3.5	236.3	227.02	185.8	251.4	219.9
BH14	4.5	37	3.5	372	302	250.1	320.8	473.6
BH14	6	26	3.5	132.6	269.9	222.8	291.7	350.9
BH14	7.5	30	3.5	334.5	282.3	233.5	303.2	396.7
BH15	No	No	No	No	No	No	No	No
BH16	4.5	22	2.5	286.2	256.1	210.8	278.8	304.5
BH17	3.0	13	3.5	219.94	217.1	177.2	242	194.6
BH17	4.5	10	3.5	192.9	199.9	162.5	225.4	155.8
BH17	6.0	21	3.5	279.6	252.3	207.56	275.3	292.7
BH17	7.0	26	3.5	311.1	269.9	222.7	292	350.9
BH18	15	34	4.5	355.7	293.6	243.4	313.6	440.1
BH19	3.0	13	3	219.94	217.1	177.2	242	194.6
BH19	4.5	18	3	258.9	240.1	197.3	264.1	256.7

TABLE 2: Continued.

Boreholes number	SPT-N Depth (m)	SPT-N	Water Level	Shear Wave Velocity				
				Equation (1) ($61 \cdot N^{0.5}$)	Equation (2) ($97 \cdot N^{0.314}$)	Equation (3) ($76 \cdot N^{0.33}$)	Equation (4) ($121 \cdot N^{0.27}$)	Equation (5) ($22 \cdot N^{0.85}$)
BH19	7.5	25	3	305	266.6	219.9	288.6	339.4
BH19	13.5	27	3	317	273	255.6	294.9	362.4
BH20	No	No	No	No	No	No	No	No
BH21	No	No	No	No	No	No	No	No
BH22	No	No	No	No	No	No	No	No
BH23	4.5	29	2.0	328.5	279.3	230.8	300.35	385.1
BH23	9.0	8	2.0	172.6	186.4	8.96	212.2	128.9
BH23	10.5	10	2.0	192.9	199.9	162.5	225.4	155.8
BH23	13.5	9	2.0	183	194	157	219	142.5
BH23	15.0	12	2.0	211.4	211.7	172.6	236.7	181.9
BH24	7.5	14	3.5	228.3	222.2	182	246.7	207.4
BH24	10.5	40	3.5	385.8	308.9	256.8	327.6	506.1
BH25	3.0	44	4.5	404.7	318.3	264.9	336.2	548.8
BH25	4.5	14	4.5	228.3	222.2	182	246.7	207.4
BH25	7.5	9	4.5	183	194	157	219	142.5
BH25	10.5	19	4.5	265.9	244.6	200.9	267.9	268.9
BH25	12.0	22	4.5	286.2	256.1	210.8	278.8	304.5
BH26	6.0	13	2.0	219.94	217.1	177.2	242	194.6
BH26	9.0	32	2.0	345.1	252.3	207.56	275.3	292.7
BH27	NO	No	No	No	No	No	No	No
BH28	No	No	No	No	No	No	No	No
BH29	7.5	27	3.5	317	273	255.6	294.9	362.4
BH29	10.5	23	3.5	292.54	260	213.9	282.2	316.2
BH29	12.0	50	3.5	431.2	331.2	276.4	347.95	612
BH30	No	No	No	No	No	No	No	No
BH31	No	No	No	No	No	No	No	No
BH32	4.5	7.0	3.0	161.3	178.8	144.5	204.7	115.1
BH32	6.0	32	3.0	345.1	252.3	207.56	275.3	292.7
BH32	9.0	40	3.0	385.8	308.9	256.8	327.6	506.1
BH32	12	54	3.0	448.3	339.5	283.5	355.3	653.1
BH33	No	No	No	No	No	No	No	No
BH34	3.0	20	3.0	272.9	248.5	204.3	271.7	280.74
BH34	4.5	21	3.0	279.6	252.3	207.56	275.3	292.7
BH35	3.0	9	2.5	183	194	157	219	142.5
BH35	4.5	8	2.5	172.6	186.4	150.9	212.2	128.9
BH35	7.5	10	2.5	192.9	199.9	162.5	225.4	155.8
BH35	12	12	2.5	211.4	211.7	172.6	236.7	181.9
BH36	3	16	3.5	244	232	189.8	255.8	232.3
BH36	4.5	16	3.5	244	232	189.8	255.8	232.3
BH37	No	No	No	No	No	No	No	No
BH38	No	No	No	No	No	No	No	No
BH39	No	No	No	No	No	No	No	No
BH40	3	20	2.25	272.9	248.5	204.3	271.7	280.74
BH40	4.5	49	2.25	427	329.3	274.5	346.1	602
BH40	9	16	2.25	244	232	189.8	255.8	232.3

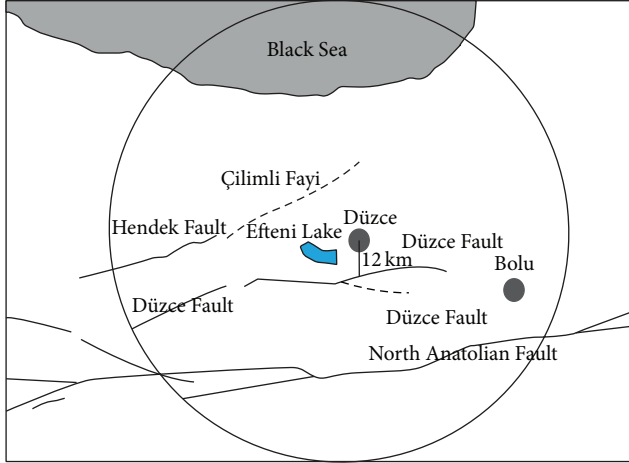


FIGURE 6: Identification of seismic sources within 100 km radius of the study area.

3.2. Calculation of Seismic Hazard Design Parameters. The Duzce Fault Zone is situated 13 km south of the study area, the North Anatolian Fault Zone is located 73 km south of the study area, and the Hendek Fault is found 29 km north-west of the study field (Figure 6). The fault zone with the highest possible acceleration in the study site is the North Anatolian Fault Zone. A circle with a radius of 100 km was drawn around the study area in order to identify the seismic design parameters. Within this circle, active seismic sources thought to affect the study field were vertically connected to calculate the shortest routes to the study field in km (Figure 6). These investigations and measurements showed that there were three main fault zones inside the circle. Then, the horizontal flying distances to the study field were calculated as 13 km for the Duzce Fault, 29 km for the Hendek Fault, and 73 km for the North Anatolian Fault [35].

The map of Turkey's active faults published by the Mineral Research and Exploration Institute indicates the total length of the Duzce, Hendek, and North Anatolian Faults as 85 km, 60 km, and 200 km, respectively [35]. The Duzce Fault, which is the shortest distance to the study area and has the potential to produce an earthquake, was taken into consideration in the main objective of the study when estimating the next earthquake expected to occur.

According to Mark [39], it is assumed that 1/3 of this fault zone could be ruptured. Therefore, the moment size of the probable seismic design was calculated by using the equation of Wells and Coppersmith [40], as seen below (6):

$$M = 4.86 + 1.32 \log L, \quad (6)$$

where M is *moment magnitude* and L is *fault length (km)*.

According to this approach, moment magnitude was calculated to be 7.2 in the case of a rupture of 1/3 of the fault length.

Horizontal earthquake acceleration (peak ground acceleration, PGA) was calculated by using the attenuation

relationship (7) developed for faults based on the earthquakes in Turkey [41]:

$$\text{PGA} = 2.18 e^{0.0218(33.3M_w - \text{Re} + 7.8427S_A + 18.9282S_B)}, \quad (7)$$

where $S_A = 0$ and $S_B = 1$ values are used for soft soils, Re is the shortest horizontal flying length to the respective fault zone from the settlement, and M_w is the magnitude of the earthquake. The peak horizontal earthquake acceleration that can be created by the seismic design was found to be 0.28 g.

4. Assessment of Liquefaction Potential

Prediction of the liquefaction potential of soils is based on cyclic laboratory testing on soil samples and use of in-situ tests and empirical methods. However, the use of laboratory testing is complicated due to difficulties associated with sample disturbance during both sampling and reconsolidation. Thus, empirical approaches based on the in-situ penetration test results have gained popularity in engineering practice as well as in engineering codes [42].

In this study, after obtaining the in situ test results, the evaluation of the liquefaction procedure was begun. The evaluation procedures based on the Standard Penetration Test (SPT) [43] and measurement of shear wave velocity (V_s) [27] require the measurement of three parameters: (1) the level of cyclic loading on the soil caused by the earthquake, expressed as an acyclic stress ratio (CSR); (2) the stiffness of the soil, expressed as overburden stress (corrected SPT blow count) due to shear wave velocity; and (3) the resistance of the soil to liquefaction, expressed as a cyclic resistance ratio (CRR). Guidelines for calculating each parameter are presented below [44].

4.1. Cyclic Stress Ratio (CSR). The cyclic stress ratio (CSR) characterizes the seismic demand induced by a given earthquake, and it can be determined from peak ground surface acceleration that depends upon site-specific ground motions [45]. The expression for the CSR induced by earthquake ground motions formulated by Idriss and Boulanger [46] is as follows:

$$\text{CSR} = 0.65 \frac{a_{\max}}{g} \frac{\sigma_V}{\sigma'_V} r_d \frac{1}{\text{MSF}} \frac{1}{K\sigma}, \quad (8)$$

where 0.65 is a weighing factor to calculate the equivalent uniform stress cycles required to generate the same pore water pressure during an earthquake; the a_{\max} is the peak horizontal ground acceleration; g is the acceleration of gravity; σ_V and σ'_V are total vertical overburden stress and effective vertical overburden stress, respectively, at a given depth below the ground surface; r_d is the depth-dependent stress reduction factor; MSF is the magnitude scaling factor; and $K\sigma$ is the overburden correction factor.

The stress reduction factor (r_d) accounts for the dynamic response of the soil column and represents the variation of shear stress amplitude with depth. Idriss and Boulanger [46]

formulated the following expressions to calculate the stress reduction factor (r_d) (9)–(11):

$$r_d = \exp [\alpha (z) + \beta (z) M_w], \quad (9)$$

$$\alpha (z) = -1.012 - 1.126 \sin \left(\frac{z}{11.73} + 5.133 \right), \quad (10)$$

$$\beta (z) = 0.106 + 0.118 \sin \left(\frac{z}{11.28} + 5.142 \right), \quad (11)$$

where z is the depth (m) and M_w is the moment magnitude. The arguments inside the sine terms in (10) and (11) are in radians. The above expression for r_d is valid up to a depth of $z \leq 34$ m, and the depths of the boreholes considered in the present analysis were less than 34 m.

The values of CSR that pertain to the equivalent uniform shear stress induced by an earthquake of magnitude, $M_w = 7.5$, were adjusted to an equivalent CSR for an earthquake of magnitude $M_w = 7.5$ through the introduction of the magnitude scaling factor (MSF), which accounts for the duration effect of ground motions. The MSF for $M_w < 7.5$ is expressed as follows (12):

$$\text{MSF} = 6.9 \exp \left(-\frac{M_w}{4} \right) - 0.058 \leq 1.8. \quad (12)$$

Since the liquefaction resistance increases with increasing confining stress, the overburden correction factor ($K\sigma$) was applied such that the values of CSR were adjusted to an equivalent overburden pressure σ'_V of 1 atmosphere equations (13)–(14):

$$K\sigma = 1 - C\sigma \left(\frac{\ln}{\sigma'_V} \right) \leq 1.0, \quad (13)$$

where

$$C\sigma = \frac{1}{18.9 - 2.5507 \sqrt{(N_1)_{60}}} \leq 0.3 \quad (14)$$

P_a is the atmospheric pressure (= 100 kPa).

4.2. Corrected SPT Blowcount and Shear Wave Velocity. In this study, the measured SPT N values (N) were corrected for overburden stress, energy ratio, diameter of boreholes, length of sampling rod, and the type of sampler by introducing a series of correction factors. N_{60} is the corrected N_m value for a 60% energy ratio with an assumption that 60% of the energy was transferred from the falling hammer to the SPT sampler. The corrected $(N_1)_{60}$ values were calculated as follows (15):

$$(N_1)_{60} = N_m C_N C_E C_B C_R C_S, \quad (15)$$

where C_N is a factor to normalize N_m to a common reference effective overburden stress; C_E is the correction for the hammer energy ratio (E_R); C_B is the correction factor for borehole diameter; C_R is the correction factor for rod length; and C_S is the correction for samplers with or without liners. The value of C_N was calculated as per (15) and was limited to a maximum value of 1.7. C_S , C_B , and C_E were assumed to be 1.1,

TABLE 3: The rod length correction with respect to the depth.

Depth d	Correction for rod length C_R
$d < 3$ m	0.75
$d = 3$ –4 m	0.8
$d = 4$ –6 m	0.85
$d = 6$ –10 m	0.95
$d = 10$ –30 m	1.0 m

1.0, and 0.6, respectively. Rod length correction with respect to the depth (C_R) at each borehole location was corrected as shown in Table 3, as suggested by Youd and Idriss [47].

The overburden correction (C_N) factor to normalize $(N_1)_{60}$ to a common reference effective overburden stress is as follows (16)–(17):

$$C_N = \left(\frac{P_a}{\sigma'_V} \right)^\alpha \leq 1.7, \quad (16)$$

where

$$\alpha = 0.784 - 0.0768 \sqrt{(N_1)_{60}}. \quad (17)$$

It can be observed from (16) and (17) that $(N_1)_{60}$ and C_N are interdependent. A series of iterations were carried out to determine $(N_1)_{60}$ and C_N until the difference between successive iteration values was less than 0.001.

In addition, shear wave velocities had to be corrected. In the procedure of liquefaction potential evaluation proposed by Andrus et al. [27], shear wave velocity was corrected to overburden stress and (18) was suggested:

$$V_{S1} = V_{S1} \left(\frac{P_a}{\sigma'_V} \right)^{0.25} \left(\frac{0.5}{K'_O} \right)^{0.125}, \quad (18)$$

where V_S is the shear wave velocity (m/s); V_{S1} is the stress-corrected shear wave velocity (m/s); P_a is the atmosphere pressure equal to 100 kPa; σ'_V shows the the effective overburden stress; and K'_O is the coefficient of effective earth pressure (in this study assumed equal to 0.5) [44].

4.3. Evaluation of the Cyclic Resistance Ratio (CRR). Determination of the cyclic resistance ratio (CRR) requires fines content (FC) of the soil to correct updated SPT blow count $(N_1)_{60}$ to an equivalent clean sand standard penetration resistance value $(N_1)_{60cs}$. Idriss and Boulanger [46] determined the CRR value for cohesionless soil with any fines content using the following expression (19)–(21):

$$\text{CRR} = \exp \left\{ \frac{(N_1)_{60cs}}{14.1} + \left(\frac{(N_1)_{60cs}}{126} \right)^2 - \left(\frac{(N_1)_{60cs}}{23.6} \right)^3 + \left(\frac{(N_1)_{60cs}}{25.4} \right)^3 - \frac{2.8}{1} \right\}, \quad (19)$$

$$(N_1)_{60cs} = (N_1)_{60} + \Delta(N_1)_{60}, \quad (20)$$

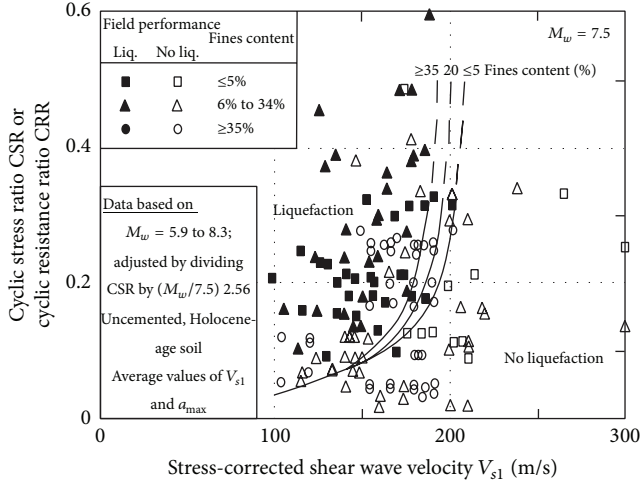


FIGURE 7: Recommended curves for evaluating CRR from shear wave velocity V_S for clean, uncemented soils with liquefaction data from compiled case histories [27].

where $\Delta(N_1)_{60}$ is the correction for fines content in percent (FC) present in the soil and is expressed as

$$\Delta(N_1)_{60} = \exp \left(1.63 + \frac{9.7}{FC + 0.1} - \left(\frac{15.7}{FC + 0.1} \right)^2 \right). \quad (21)$$

Separately, as regarding the use of V_S as an index of liquefaction resistance, it has been illustrated by several authors. The most popular CRR- V_S correlation (Figure 7) was proposed by Andrus and Stokoe [22] for uncemented Holocene-age soils, based on a database including 26 earthquakes and more than 70 test sites. The CRR is obtained as a function of an overburden-stress corrected shear wave velocity $V_{S1} = V_S(P_a/\sigma'_{V0})^{0.25}$, where V_S = measured shear wave velocity, P_a = atmospheric pressure ($\approx 100 \text{ kPa}$), and σ'_{V0} = initial effective vertical stress (same units as P_a). Andrus et al. [27] introduced age correction factors to extend the original correlation of Andrus and Stokoe [22] to soils older than Holocene. Their CRR- V_{S1} relationship (curves in Figure 7, for various fines contents) is approximated by:

$$\text{CRR} = \left[0.022 \left(\frac{K_{a1} V_{S1}}{100} \right)^2 + 2.8 \left(\frac{1}{V_{S1}^* - K_{a1} V_{S1}} - \frac{1}{V_{S1}^*} \right) \right] \times K_{a2}, \quad (22)$$

where V_{S1}^* = the limiting upper value of V_{S1} for liquefaction occurrence ($V_{S1}^* = 200 \text{ m/s}$ for the curve for fines content $\geq 35\%$); $V_{S1}^* = 215 \text{ m/s}$ for the curve for fines content $\leq 5\%$; V_{S1}^* varies linearly from 200 to 215 m/s for fines content between 35 and 5%; K_{a1} = factor to correct for high V_{S1} values caused by aging; and K_{a2} = Factor to correct for influence of age on CRR. Magnitude scaling factors should be used to scale (22) (for magnitude $M_w = 7.5$ earthquakes) to different magnitudes. Both K_{a1} and K_{a2} are 1 for uncemented soils of Holocene age. For older soils, suggested K_{a1} values (mostly in

TABLE 4: The level of liquefaction severity.

LPI	Iwasaki et al. [23]	Luna and Frost [37]	MERM [38]
LPI = 0	Very low	Little to none	None
$0 < \text{LPI} < 5$	Low	Minor	Low
$5 < \text{LPI} < 15$	High	Moderate	Medium
$15 < \text{LPI}$	Very high	Major	High

the range 0.6 to 0.8) are derived from SPT- V_{S1} relationships (e.g. Ohta and Goto [48], Rollins et al. [49], or site specific). Lower-bound values of K_{a2} (1.1 to 1.5) are based on the study by Arango et al. [50]. However, Andrus et al. [27] noted the associated high uncertainty and the need for additional work to quantify the influence of age on CRR, as well as on V_S .

4.3.1. *Determination of the Factor of Safety.* The factor of safety against liquefaction (FS) is commonly used to quantify liquefaction potential. The factor of safety against liquefaction (FS) can be defined as follows:

$$\text{FS} = \frac{(\text{CRR})_{M_w=7.5}}{(\text{CSR})_{M_w=7.5, \sigma'_v}} \text{MSF}. \quad (23)$$

Both CSR and CRR vary with depth and, therefore, the liquefaction potential is evaluated at corresponding depths within the soil profile.

4.3.2. *Determination of the Liquefaction Potential Index.* The liquefaction potential index (LPI) is a single-valued parameter to evaluate regional liquefaction potential. The LPI at a site is computed by integrating the factors of safety (FS) along the soil column up to a depth of 20 m. A weighting function is added to give more weight to the layers closer to the ground surface. The liquefaction potential index (LPI) proposed by Iwasaki et al. [36, 51] is expressed as follows (24). The criteria of the level of liquefaction severity indexes were given below (Table 4):

$$\text{LPI} = \int_0^{20} F(z) W(z) dz, \quad (24)$$

where z is the depth of the midpoint of the soil layer (0 to 20 m) and dz is the differential increment of depth. The weighting factor, $W(z)$, and the severity factor, $F(z)$, are calculated as per the following expressions (25):

$$\begin{aligned} F(z) &= 1 - \text{FS} \quad \text{for } \text{FS} < 1.0, \\ F(z) &= 0 \quad \text{for } \text{FS} \geq 1.0, \\ W(z) &= 10 - 0.5z \quad \text{for } z < 20 \text{ m}, \\ W(z) &= 0 \quad \text{for } z > 20 \text{ m}. \end{aligned} \quad (25)$$

For the soil profiles with depths of less than 20 m. The LPI was calculated using the following expression [37] (26)-(27):

$$\text{LPI} = \sum_{i=1}^n W_i F_i H_i \quad (26)$$

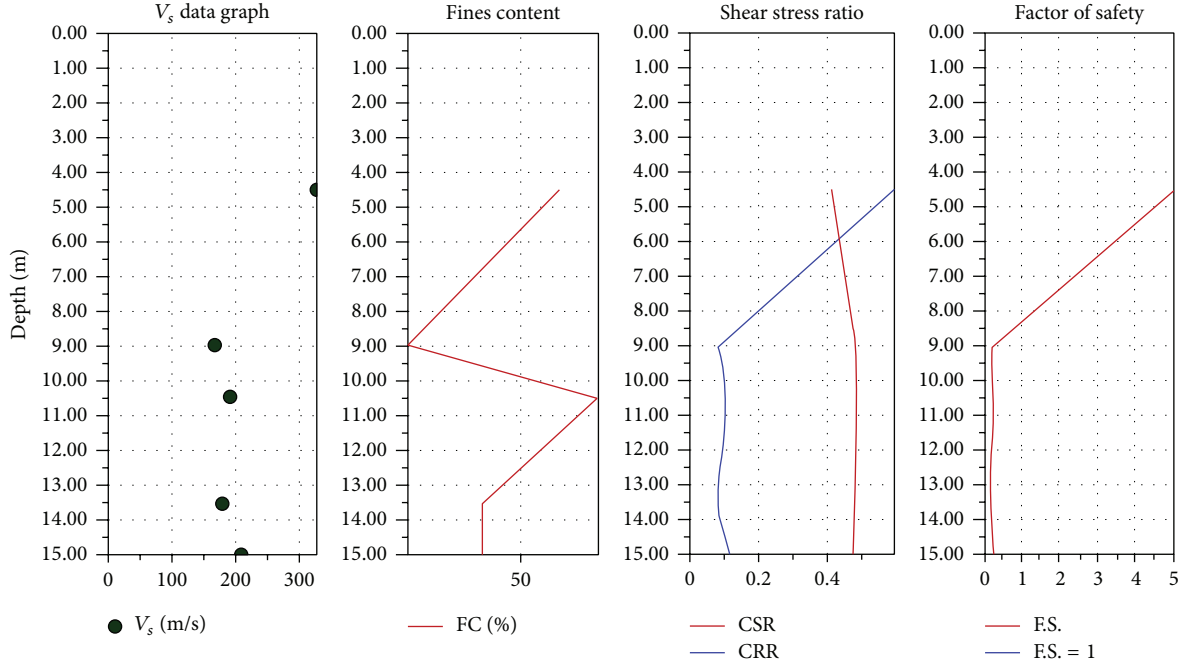


FIGURE 8: Borehole 23 was chosen to check and compare for liquefaction potential as a sample according to shear wave velocity values.

with

$$\begin{aligned}
 F_i &= 1 - FS_i \quad \text{for } FS_i < 1.0, \\
 F_i &= 0 \quad \text{for } FS_i \geq 1.0,
 \end{aligned}
 \tag{27}$$

where H_i is the thickness of the discretized soil layers; n is the number of layers; F_i is liquefaction severity for i th layer; FS_i is the factor of safety for i th layer; W_i is the the weighting factor ($= 10 - 0.5Z_i$); and Z_i is the depth of i th layer (m).

5. Assessment of the Liquefaction Potential Index

The city of Duzce has been reconstructed since the 12 November earthquake of 1999. The general form of construction had typically been a 4-5-storey reinforced-concrete frame and masonry structure. After the 12 November Duzce earthquake experience, regulations were changed to limit construction to 2-3-storey buildings. The city is located over deep alluvial deposits. The main soils deposited at this site are comprised of alluvial sand and silt. The boreholes in Duzce were drilled around the Efteni Lake at a depth of 200 m and did not reach bedrock. The shallow soils at approximately 10 m are recent deposits laid down by the Aksu and Melen Rivers that flooded the area.

Turkey is located in the active tectonic region of the Alp Himalayan Earthquake Zone, so this area is an active region seismologically. There are several active tectonic sections in Turkey, such as the North Anatolian Fault Zone, the East Anatolian Fault Zone, the West Anatolian Grabens, the Ecemiş Fault Zone, and the Tuzgolu Fault Zone [52]. Duzce Province is located near the Duzce Fault segment of the North Anatolian Fault Zone which is active in the Western Black Sea

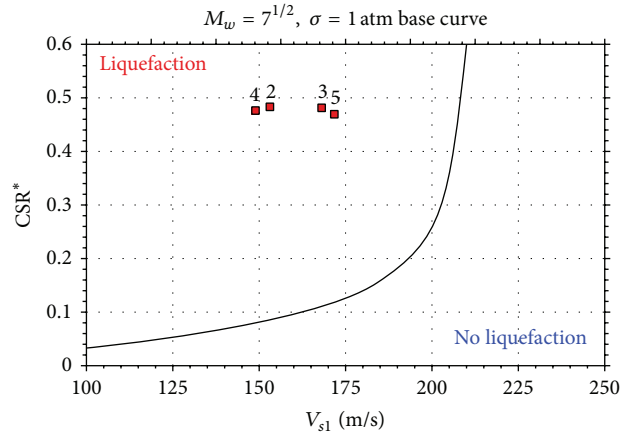


FIGURE 9: Borehole 23 was chosen to check and compare for liquefaction potential as a sample for shear wave velocity.

Region. Furthermore, this area consists of granular alluvial deposits which are loose to the surface. The groundwater is between 2.5 and 4m below the surface and changes seasonally. For the analysis of the liquefaction potential index of Duzce Province, a total of 40 geotechnical boreholes were drilled by the General Directorate of Mineral Research and Exploration. The field data of the works were assessed for the liquefaction potential index for Duzce Province. The SPT samples were implemented at depth intervals of 1.5 m from the first to the last of the boreholes, and the disturbed samples were used to describe the grain size distribution and Atterberg limits of the soils. The boundaries of the soil layers, SPT-N values, fines content, and the liquid limit for all layers

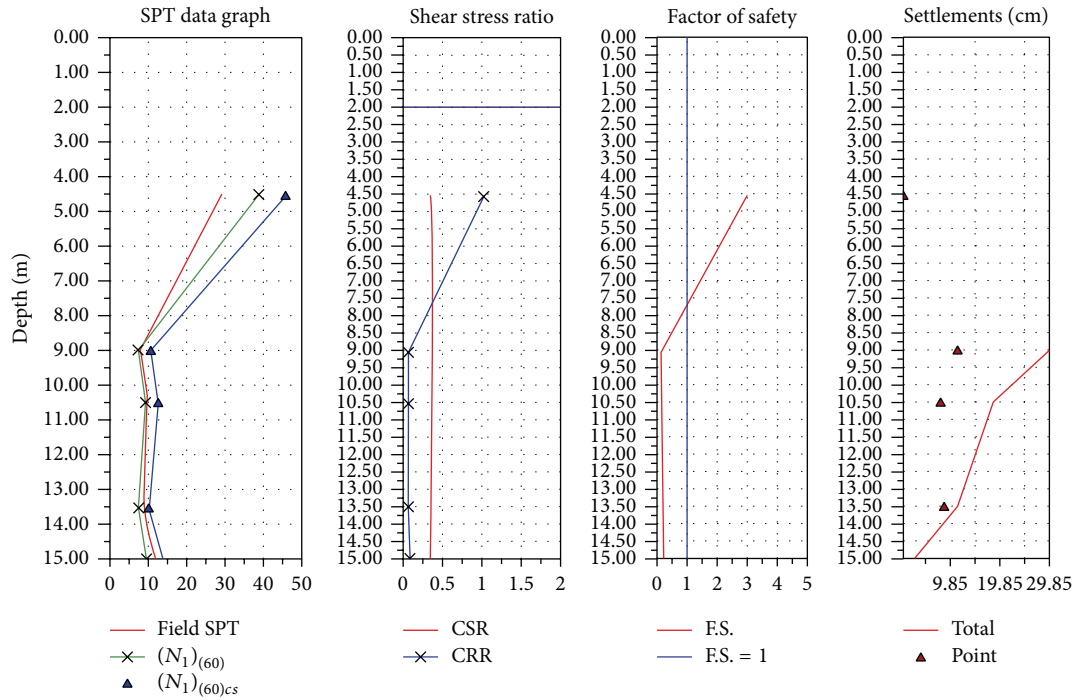


FIGURE 10: Borehole 23 was chosen to check and compare for liquefaction potential as a sample according to the SPT- N values.

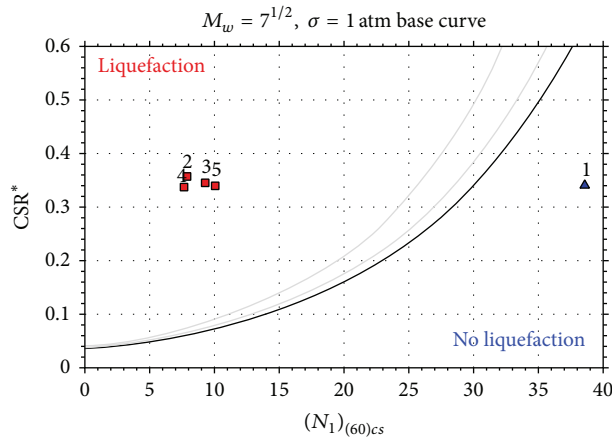


FIGURE 11: Borehole 23 was chosen to check and compare for liquefaction potential as scattering liquefaction points of sample for SPT- N values.

throughout the boreholes were employed as input parameters to determine the liquefaction potential index.

In addition, the magnitude of the earthquake and the maximum horizontal acceleration of those parameters to be created due to local faults were used here for evaluating the liquefaction potential index. The Duzce Fault Zone of the North Anatolian Fault Zone and surrounding zones were generated and showed an average of 7.2 moment magnitudes. For this reason, the magnitude of the projected earthquake was found by using 7.2 for the calculations. In this context, the typical computation of factors of safety against liquefaction for earthquakes ($M_w = 7.2$) yielded by the Duzce Fault Zone was carried out at the chosen borehole using (2) through (20). The LPI at this particular site was calculated from the FS

values based on the expression by Luna and Frost [37]. The LPI values were computed at the study site for magnitudes of $M_w = 7.2$.

Great effort was taken in the analysis of the other input parameter for determining the liquefaction potential, the maximum ground acceleration (a_{max}). However, some researchers have offered empirical equations for the maximum ground acceleration [41, 53, 54]. In particular, the comprehensive study of Ulusay et al. [41] should be mentioned as it relates to the iso-acceleration map of Turkey. In this study, the a_{max} values were calculated as approximately 502 gal for the Duzce Fault Zone segment. The liquefaction potential index indices for 40 boreholes were calculated and are given in Table 5 and Figures 8, 9, 10, and 11. In addition,

TABLE 5: Liquefaction potential index results.

Boreholes number	The level of liquefaction severity (LPI)				
	Equation (1)	Equation (2)	Equation (3)	Equation (4)	Equation (5)
BH1	0	0	0	0	0
BH2	0	0	14.14	19.79	0
BH3	0	0	35.63	0	0
BH4	30.32	13.35	39.17	0	28.97
BH5	Not performed	0	Not performed	Not performed	Not performed
BH6	0	0	23.09	0	0
BH7	Not performed	Not performed	Not performed	Not performed	Not performed
BH8	46.83	33.46	26.34	5.82	40.87
BH9	0	0	0	0	0
BH10	Not performed	Not performed	Not performed	Not performed	Not performed
BH11	5.43	0	0.8	0	24.39
BH12	0	0	0	0	0
BH13	Not performed	Not performed	Not performed	Not performed	Not performed
BH14	0	9.14	0	0	0
BH15	Not performed	Not performed	Not performed	Not performed	Not performed
BH16	0	0	0	0	0
BH17	10.5	5.37	0	0	8.90
BH18	0	0	0	0	0
BH19	0	0	24.17	0	0
BH20	Not performed	Not performed	Not performed	Not performed	Not performed
BH21	Not performed	Not performed	Not performed	Not performed	Not performed
BH22	Not performed	Not performed	Not performed	Not performed	Not performed
BH23	23.86	36.96	35.26	42.53	40.84
BH24	1.5	0	19.89	35.34	26.39
BH25	17.85	14.52	14.68	8.48	19.94
BH26	5.68	0	41.81	0	22.44
BH27	Not performed	Not performed	Not performed	Not performed	Not performed
BH28	Not performed	Not performed	Not performed	Not performed	Not performed
BH29	0	8	9.51	0	0
BH30	Not performed	Not performed	Not performed	Not performed	Not performed
BH31	Not performed	Not performed	Not performed	Not performed	Not performed
BH32	33.05	22.94	32.74	0	30.74
BH33	Not performed	Not performed	Not performed	Not performed	Not performed
BH34	0	0	0	0	0
BH35	66.53	31.64	56.95	2.84	59.78
BH36	0	0	9.67	0	0
BH37	Not performed	Not performed	Not performed	Not performed	Not performed
BH38	Not performed	Not performed	Not performed	Not performed	Not performed
BH39	Not performed	Not performed	Not performed	Not performed	Not performed
BH40	0	0	18.88	0	0

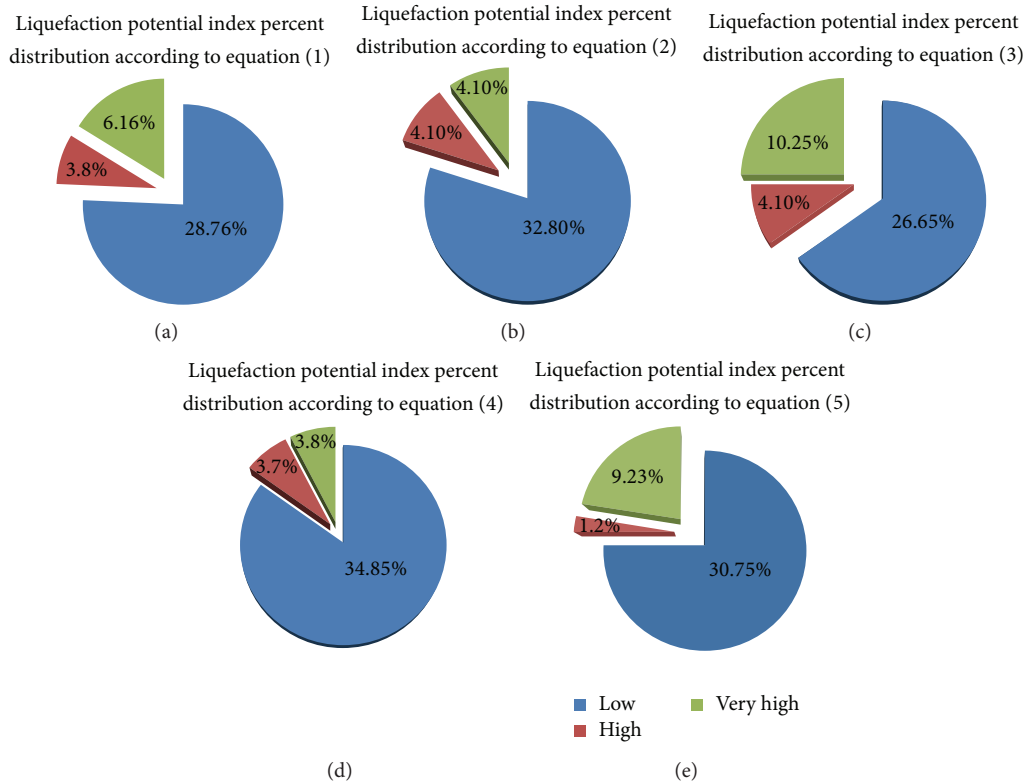


FIGURE 12: Pie charts showing the areas of the potential zones.

the distributions of liquefaction potential indexes are presented in Figure 12 as a pie chart.

6. Results and Conclusions

The evaluation of the liquefaction potential of a liquefaction-prone area is of vital importance in geotechnical earthquake engineering, both for assessment for site selection and for planning and construction. This study investigated two field methods used to evaluate the liquefaction potential of soils, the Standard Penetration Test (SPT) and the Shear Wave Velocity Test (V_s), based on the empirical relationships between them. Attempts were made to evaluate the factors of safety against liquefaction (FS) and corresponding liquefaction potential indices (LPI) for a local fault zone in order to produce the seismic movement for the province using SPT- N -based semiempirical procedures.

The concept of the liquefaction potential index was used in this study for liquefaction susceptibility, as proposed by Iwasaki et al. [36]. The distribution of the LPI was generated in order to predict the occurrence of damaging liquefaction for an earthquake to be yielded by the local fault zone in Duzce Province in the Western Black Sea Region of Turkey. This study area is under the effect of the North Anatolian Fault Zone through its segment, the Duzce Fault Zone, which was evaluated for producing the liquefaction potential indices by calculating for a probable earthquake of $M_w = 7.2$.

The comparison of the safety factors and liquefaction potential indexes reveal that the severity of liquefaction

occurrences in the study area based on the V_s methods (Equation (1) = 43.86, equation (2) = 40.84, equation (3) = 42.53, equation (4) = 36.96, equation (5) = 43.86) are bigger than the one based on the SPT method (35,36). Moreover, it can be observed that the relationships between the SPT method and the shear wave velocity are not suitable. Because the relationships used in the present study are dependent on soil type, fines content, type of tests, and their accuracy, it might be more valid to perform both methods for the same place and then compare the results in order to evaluate the liquefaction potential.

Finally, a very high susceptibility category of liquefaction was observed for the potential earthquake of $M_w = 7.2$; however, 3.8–10.2% of the study area is in the highly susceptible liquefaction class in five distribution charts according to (1)–(5). The percentage that is moderately susceptible takes up the least area from the other class: 1.2–4.1% for all locations in the distribution charts. The low susceptibility areas are 28.76–65%, respectively.

In conclusion, the areas developed on reclaimed land having large, thick deposits of soft soil and shallow groundwater levels were observed to be more prone to liquefaction. This paper reveals that some of the areas are more highly prone to liquefaction due to the greater thickness of the soft soil deposits and groundwater table at shallow depths. It can be observed from the distribution of the LPI that a high degree of liquefaction would occur at several sites in the Province of Duzce during a seismic event. These LPI distributions will

help the structural designers and city planners to check the vulnerability of the area against liquefaction.

Conflict of Interests

The authors declare that there is no conflict of interests regarding the publication of this paper.

Acknowledgments

The authors would like to express their gratitude to the Duzce Provincial Governorate and the General Directorate of Mineral Research and Exploration for information and the logs of geotechnical boreholes.

References

- [1] H. B. Seed and I. M. Idriss, "Simplified procedure for evaluating soil liquefaction potential," *Journal of the Soil Mechanics and Foundations Division*, vol. 97, no. 9, pp. 1249–1273, 1971.
- [2] T. L. Youd, I. M. Idriss, R. D. Andrus et al., "Liquefaction resistance of soils: summary report from the 1996 NCEER and 1998 NCEER/NSF workshops on evaluation of liquefaction resistance of soils," *Journal of Geotechnical and Geoenvironmental Engineering*, vol. 127, no. 10, pp. 817–833, 2001.
- [3] H. B. Seed, I. M. Idriss, and I. Arango, "Evaluation of liquefaction potential using field performance data," *Journal of Geotechnical Engineering*, vol. 109, no. 3, pp. 458–482, 1983.
- [4] H. B. Seed, K. Tokimatsu, L. F. Harder, and R. M. Chung, "The influence of SPT procedures in soil liquefaction resistance evaluation," *Journal of Geotechnical Engineering*, vol. 111, no. 12, pp. 1425–1445, 1985.
- [5] B. O. Hardin and V. P. Drnevich, "Shear modulus and damping in soils: design equation and curves," *Journal of Soil Mechanics and Foundation*, vol. 98, no. 7, pp. 667–692, 1972.
- [6] S. Kramer, *Geotechnical Earthquake Engineering*, Prentice Hall, Upper Saddle River, NJ, USA, 1996.
- [7] K. Ishihara, *Soil Behaviour in Earthquake Geotechnics*, Oxford Engineering Science Series, Oxford University Press, Oxford, UK, 1996.
- [8] A. F. Rauch, M. Duffy, and K. H. Stokoe II, "Laboratory correlation of liquefaction resistance with shear wave velocity," in *Proceedings of the Sessions of Computer Simulation of Earthquake Effects (Geo-Denver '00)*, vol. 110, pp. 66–80, Denver, Colo, USA, August 2000.
- [9] Y.-T. Huang, A.-B. Huang, Y.-C. Kuo, and M.-D. Tsai, "A laboratory study on the undrained strength of a silty sand from Central Western Taiwan," *Soil Dynamics and Earthquake Engineering*, vol. 24, no. 9-10, pp. 733–743, 2004.
- [10] C. Yunmin, K. Han, and C. Ren-Peng, "Correlation of shear wave velocity with liquefaction resistance based on laboratory tests," *Soil Dynamics and Earthquake Engineering*, vol. 25, no. 6, pp. 461–469, 2005.
- [11] Y.-G. Zhou, Y.-M. Chen, and B. Huang, "Experimental study of seismic cyclic loading effects on small strain shear modulus of saturated sands," *Journal of Zhejiang University: Science*, vol. 6, no. 3, pp. 229–236, 2005.
- [12] N. Liu, J. K. Mitchell, and M. Hon, "Influence of nonplastic fines on shear wave velocity-based assessment of liquefaction," *Journal of Geotechnical and Geoenvironmental Engineering*, vol. 132, no. 8, pp. 1091–1097, 2006.
- [13] Y.-G. Zhou and Y.-M. Chen, "Laboratory investigation on assessing liquefaction resistance of sandy soils by shear wave velocity," *Journal of Geotechnical and Geoenvironmental Engineering*, vol. 133, no. 8, pp. 959–972, 2007.
- [14] C. D. P. Baxter, A. S. Bradshaw, R. A. Green, and J.-H. Wang, "Correlation between cyclic resistance and shear-wave velocity for providence silts," *Journal of Geotechnical and Geoenvironmental Engineering*, vol. 134, no. 1, pp. 37–46, 2008.
- [15] F. Askari, R. Dabiri, A. Shafiee, and M. K. Jafari, "Liquefaction resistance of sand-silt mixtures using laboratory-based shear wave velocity," *International Journal of Civil Engineering*, vol. 9, no. 2, pp. 135–144, 2011.
- [16] R. D. Andrus, *In-situ characterization of gravelly soils that liquefied in the 1983 Borah Peak earthquake [Ph.D. thesis]*, University Of Texas, Austin, Tex, USA, 1994.
- [17] R. Dabiri, F. Askari, A. Shafiee, and M. K. Jafari, "Shear wave velocity-based liquefaction resistance of sand-silt mixtures: deterministic versus probabilistic approach," *Iranian Journal of Science and Technology—Transaction of Civil Engineering*, vol. 35, no. 2, pp. 199–215, 2011.
- [18] A. L. Lodge, *Shear wave velocity measurements for subsurface characterization [Ph.D. thesis]*, University of California, Berkeley, Calif, USA, 1996.
- [19] K. Kayabali, "Soil liquefaction evaluation using shear wave velocity," *Engineering Geology*, vol. 44, no. 1–4, pp. 121–127, 1996.
- [20] R. D. Andrus and K. H. Stokoe, "Liquefaction resistance based on shear wave velocity," in *Proceedings of the NCEER Workshop on Evaluation of Liquefaction Resistance of Soils*, T. L. Youd and I. M. Idriss, Eds., Technical Report NCEER-97-0022, pp. 89–128, National Center for Earthquake Engineering Research, Buffalo, NY, USA, Salt lake City, Utah, USA, January 1997 1996.
- [21] C. H. Juang, C. J. Chen, W. H. Tang, and D. V. Rosowsky, "CPT-based liquefaction analysis, part I: determination of limit state function," *Geotechnique*, vol. 50, no. 5, pp. 583–592, 2000.
- [22] R. D. Andrus and K. H. Stokoe II, "Liquefaction resistance of soils from shear-wave velocity," *Journal of Geotechnical and Geoenvironmental Engineering*, vol. 126, no. 11, pp. 1015–1025, 2000.
- [23] T. Iwasaki, K. Tokida, F. Tatsuoka, S. Watanabe, S. Yasuda, and H. Sato, "Microzonation for soil liquefaction potential using simplified methods," in *Proceedings of the 3rd International Conference on Microzonation*, pp. 1319–1330, Seattle, Wash, USA, June-July 1982.
- [24] NEMC, B.U. Kandilli Observatory and Earthquake Research Institute, National Earthquake Monitoring Centre, 2014, <http://www.koeri.boun.edu.tr/sismo>.
- [25] Tubitak-AU-MTA, *Investigation of Alternative Settlement Area after 17 August 1999 Earthquake in Duzce District (Bolu)*, Ankara, Turkey, 1999.
- [26] O. Emre, T. Y. Duman, and A. Doğan, *The Preassessment Report and Map of Surface Rupture in 17 August 1999 Eastern Marmara Earthquake*, No. 22, General Directorate of Mineral Research and Exploration, Ankara, Turkey, 1999.
- [27] R. D. Andrus, P. Piratheepan, B. S. Ellis, J. Zhang, and C. H. Juang, "Comparing liquefaction evaluation methods using penetration V_S relationships," *Soil Dynamics and Earthquake Engineering*, vol. 24, no. 9-10, pp. 713–721, 2004.
- [28] E. Gokten, V. Ozaksoy, and R. Demirtas, "Some neotectonical properties of the North Anatolian fault zone between bayramoren-abant (Turkey)," in *Active Tectonic Research Group First Meeting Proceeding*, pp. 68–77, ITU Mining Faculty-Eurasia Earth Sciences Institute, 1998.

- [29] R. Demirtas, *Kuzey anadolu fay zonu'nun abant-gerede arasında kalan bölümünün neotektonik Özellikleri ve paleosis-misitesi [Ph.D. thesis]*, University of Ankara, Ankara, Turkey, 2000.
- [30] N. N. Ambraseys, "Engineering seismology," *Earthquake Engineering & Structural Dynamics*, vol. 17, no. 1, pp. 1-105, 1988.
- [31] C. Tasman, "The Report About The Gerede-Bolu Earthquake," DAD/At. 46, 1944 (Turkish).
- [32] T. Ugras, Z. Colakoglu, U. Ceken et al., "17 Agustos Izmit Korfezi Depremi Kuvvetli Yer Hareketi Kayıtlarının Değerlendirilmesi," 17 Ağustos Izmit Korfezi Deprem Raporu, Bayındırlık Ve Iskan Bakanlığı, Afet Isleri Genel Müdürlüğü, Deprem Araştırma Dairesi, Ankara, Pp 156-189, 2000, (Turkish).
- [33] American Society for Testingmaterials, "Standard test for penetration test and split-barrel sampling of soils (ASTM D1596)," in *Annual Book of ASTM Standards*, vol. 04. 09, Section 4, p. 1092, 1994.
- [34] M. K. Jafari, A. Shafiee, and A. Razmkhah, "Dynamic properties of fine grained soils in south of tehran," *Journal of Seismology and Earthquake Engineering*, vol. 4, no. 1, pp. 25-36, 2002.
- [35] F. Şaroğlu, O. Emre, and I. Kuşçu, *Türkiye Diri Fay Haritası*, MTA Genel Müdürlüğü, Ankara, Turkey, 1992.
- [36] T. Iwasaki, K. Tokida, F. Tatsuko, and S. Yasuda, "A practical method for assessing soil liquefaction potential based on case studies at various sites in Japan," in *Proceedings of the 2nd International Conference on Microzonation*, pp. 885-896, San Francisco, Calif, USA, November-December 1978.
- [37] R. Luna and J. D. Frost, "Spatial liquefaction analysis system," *Journal of Computing in Civil Engineering*, vol. 12, no. 1, pp. 48-56, 1998.
- [38] Microzonation for Earthquake Risk Mitigation (MERM), *Microzonation Manual*, World Institute for Disaster Risk Management, 2003.
- [39] R. K. Mark, "Application of linear statistical model of earthquake magnitude versus fault length in estimating maximum expectable earthquakes," *Geology*, vol. 5, no. 8, pp. 464-466, 1977.
- [40] D. L. Wells and K. J. Coppersmith, "New empirical relationships among magnitude, rupture length, rupture width, rupture area, and surface displacement," *Bulletin of the Seismological Society of America*, vol. 84, no. 4, pp. 974-1002, 1994.
- [41] R. Ulusay, E. Tuncay, H. Sonmez, and C. Gokceoglu, "An attenuation relationship based on Turkish strong motion data and iso-acceleration map of Turkey," *Engineering Geology*, vol. 74, no. 3-4, pp. 265-291, 2004.
- [42] A. Ansal and G. Tonuk, "Source and site effects for microzonation," in *Earthquake Geotechnical Engineering: 4th International Conference on Earthquake Geotechnical Engineering-Invited Lectures*, K. Pitilakis, Ed., Geotechnical Geological and Earthquake Engineering, Chapter 4, pp. 73-92, Geotechnical Geological and Earthquake Engineering, 2007.
- [43] H. B. Seed, K. Tokimatsu, L. F. Harder, and R. M. Chung, "The influence of SPT procedures in soil liquefaction resistance evaluations," *Journal of Geotechnical Engineering*, vol. 111, no. 12, pp. 1425-1445, 1985.
- [44] M. K. Noutash, R. Dabiri, and M. H. Bonab, "The evaluation of soil liquefaction potential using shear wave velocity based on empirical relationships," *International Journal of Engineering*, vol. 6, no. 4, 2012.
- [45] J. Dixit, D. M. Dewaikar, and R. S. Jangid, "Assessment of liquefaction potential index for Mumbai city," *Natural Hazards and Earth System Science*, vol. 12, no. 9, pp. 2759-2768, 2012.
- [46] I. M. Idriss and R. W. Boulanger, "Semi-empirical procedures for evaluating liquefaction potential during earthquakes," *Soil Dynamics and Earthquake Engineering*, vol. 26, no. 2-4, pp. 115-130, 2006.
- [47] T. L. Youd and I. M. Idriss, "Liquefaction resistance of soils: summary report from the 1996 NCEER and 1998 NCEER/NSF workshops on evaluation of liquefaction resistance of soils," *Journal of Geotechnical and Geoenvironmental Engineering*, vol. 127, no. 4, pp. 297-313, 2001.
- [48] Y. Ohta and N. Goto, "Empirical shear wave velocity equations in terms of characteristic soil indexes," *Earthquake Engineering and Structural Dynamics*, vol. 6, no. 2, pp. 167-187, 1978.
- [49] K. M. Rollins, N. B. Diehl, and T. J. Weaver, "Implications of VS-BPT (N1)60 correlations for liquefaction assessment in gravels," in *Geotechnical Earthquake Engineering and Soil Dynamics III*, vol. 1 of *Geotechnical Special Publication No. 75*, pp. 506-517, ASCE, 1998.
- [50] I. Arango, M. R. Lewis, and C. Kramer, "Updated liquefaction potential analysis eliminates foundation retrofitting of two critical structures," *Soil Dynamics and Earthquake Engineering*, vol. 20, no. 1-4, pp. 17-25, 2000.
- [51] T. Iwasaki, K. Tokida, F. Tatsuoka, S. Watanabe, S. Yasuda, and H. Sato, "Microzonation for soil liquefaction potential using simplified methods," in *Proceedings of the 2nd International Conference on Microzonation*, pp. 1319-1330, Seattle, Wash, USA, 1982.
- [52] A. Yalcin, C. Gokceoglu, and H. Sönmez, "Liquefaction severity map for Aksaray city center (Central Anatolia, Turkey)," *Natural Hazards and Earth System Science*, vol. 8, no. 4, pp. 641-649, 2008.
- [53] W. B. Joyner and D. M. Boore, "Peak horizontal acceleration and velocity from strong-motion records from the 1997 imperial valley, California earthquake," *Bulletin of the Seismological Society of America*, vol. 71, no. 6, pp. 2011-2038, 1981.
- [54] O. Aydan, M. Sezai, and T. Yazar, "The seismic characteristics of Turkish earthquakes," in *Proceedings of the 11th International Conference on Earthquake Engineering*, pp. 1-8, Acapulco, Mexico, 1986.

Research Article

Crack Extension Resistance of Normal-Strength Concrete Subjected to Elevated Temperatures

Jing Chen and Zhoudao Lu

College of Civil Engineering, Tongji University, Shanghai 200092, China

Correspondence should be addressed to Zhoudao Lu; lzd@tongji.edu.cn

Received 5 March 2014; Revised 29 May 2014; Accepted 30 May 2014; Published 26 June 2014

Academic Editor: Juan José del Coz Díaz

Copyright © 2014 J. Chen and Z. Lu. This is an open access article distributed under the Creative Commons Attribution License, which permits unrestricted use, distribution, and reproduction in any medium, provided the original work is properly cited.

Determination of the residual crack extension resistance curves (K_R -curves) associated with cohesive force distribution on fictitious crack zone of complete fracture process is implemented in present research. The cohesive force distributes according to bilinear softening traction-separation law proposed by Petersson. Totally ten temperatures varying from 20°C to 600°C and the specimen size of 230 × 200 × 200 mm with initial-notch depth ratios 0.4 are considered. The load-crack mouth opening displacement curves (P -CMOD) of postfire specimens are obtained by wedge-splitting method from which the stress intensity factor curves (K -curves) are calculated. In each temperature, with the distribution of cohesive force along the fracture process zone, the residual fracture toughness K_R (Δa) increases with increasing crack length Δa , whereas the K_R -curves decrease with increasing temperatures T_m for the thermal damage induced. The stability analysis on crack propagation demonstrates that when the residual K_R -curve is higher than K -curve, the crack propagates steadily; otherwise, the crack propagates unsteadily.

1. Introduction

To describe the crack propagation in concrete structures, the crack extension resistance in terms of K_R has been measured and the related characteristics were investigated by Hilsdorf and Brameshuber in 1984 [1], Mai in 1984 [2], and Karihaloo and Shah in 1987 [3] as well as Xu and Reinhardt in 1999 [4] which was calculated using the conventional approach proposed by Irwin et al. in the early 1960s. Xu and Reinhardt in 1998 [5] proposed an analytical method to determine the crack extension resistance (K_R -curve) according to the cohesive force on the fictitious crack zone that is described directly by the softening traction-separation law. The basic principle of the approach is that the crack extension resistance is composed of two parts. One part is the inherent toughness K_{Ic}^{ini} , which resists the initial propagation of an initial crack under loading. This means that a crack does not propagate when the stress intensity factor at the initial crack tip is less than the inherent toughness K_{Ic}^{ini} . Another part is induced by the cohesive force distributed on the fictitious crack during crack propagation. Therefore, it is

a function of the cohesive force distribution $f(\sigma)$, the tensile strength f_t of the material, and the length of the propagating crack.

The main requirement for determining crack extension resistance curve based on cohesive force distribution during crack propagation is to know the load-crack mouth opening displacement (P -CMOD) curve a priori. Some characteristics of K_R -curve were investigated numerically on standard TPBT specimen for different concrete strength and specimen sizes [6]. It was observed that K_R -curve was dependent on compressive strength of concrete and had almost the same S-shape. It increased with increasing crack length and increasing strength of concrete. The obtained K_R -curves were almost independent of the specimen sizes. However, it was found that some difference could be noticed on the gained K_R -curve by using bilinear [7] and nonlinear [8] softening functions of concrete. The influence of specimen geometry (TPB and CT specimens) on the K_R -curves is considered by Kumar and Barai [9], and the influence of the specimen geometry on the K_R -curves was not observed for the specified specimen size and initial-crack length/depth ratio.

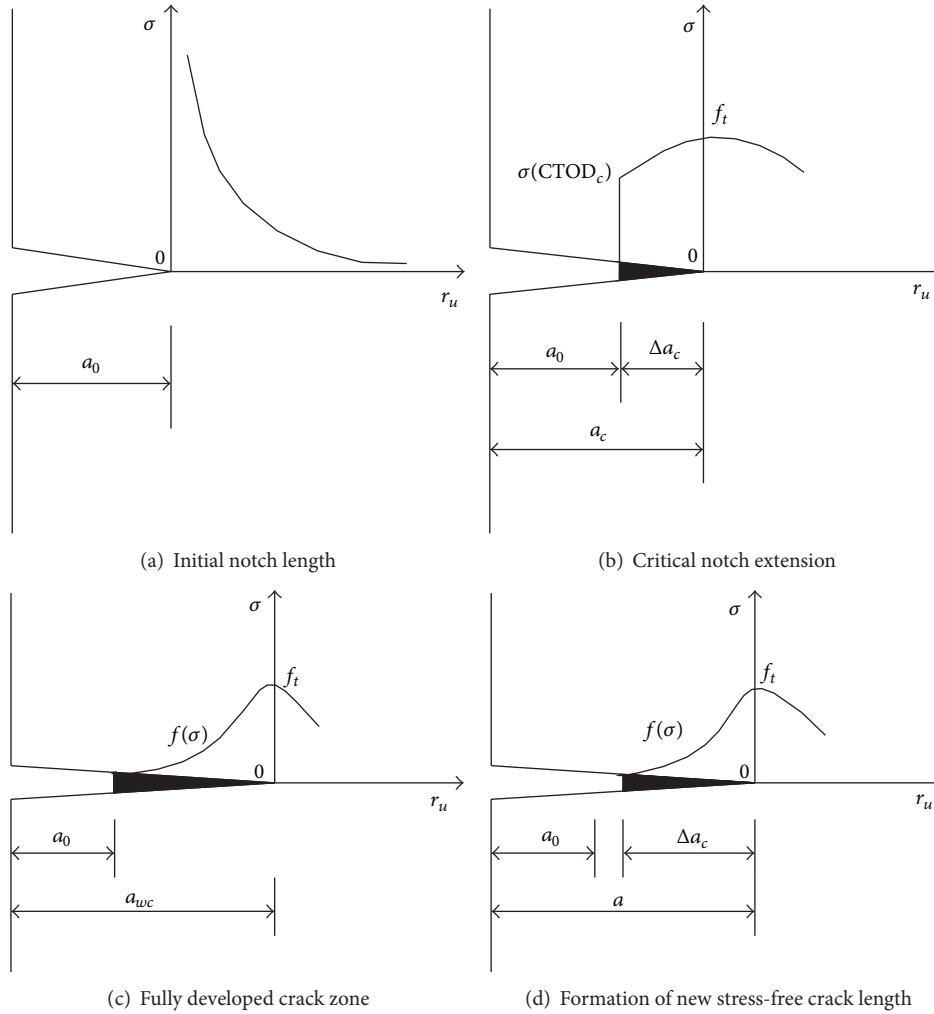


FIGURE 1: Four stages of crack propagation during the fracture process.

The influence of temperature on the fracture properties was considered by several researchers, mainly on the fracture energy and material brittleness [10–14], relative fewer discussions on the fracture toughness [15, 16], not mention the crack extension resistance of the complete fracture process. For the stability analyses of crack propagation, the comparison between K_R -curves and the corresponding stress intensity factor curves (K -curves) can be taken as a crack propagation criterion to judge the stability of the crack in the loaded structures. This criterion could also be used in the analysis of the stability of structures that suffered high temperature or fire in a real situation.

The main objective of this research is to determine the residual crack extension resistance (K_R -curve) of postfire concrete based on the cohesive force distributed on the fictitious crack zone, and the influence of temperatures on the K_R -curve is discussed. The wedge-splitting experiments of a total of ten temperatures varying from 20°C to 600°C and

the specimens size 230 × 200 × 200 mm with initial-notch depth ratios of 0.4 are implemented.

2. Determination of Residual K_R -Curve Based on Cohesive Stress Distribution

2.1. Background. According to K_R -curve criterion [5], the crack extension resistance of a cracked solid consists of the inherent toughness K_{IC}^{ini} and the cohesive toughness $K_c(\Delta a)$ which increases with the increasing amount of crack extension. The cohesive toughness depends upon cohesive stress distribution $f(\sigma)$ which is a function of crack opening displacement w and tensile strength of concrete f_t and the propagating crack length a . At the onset of unstable crack propagation, the stress intensity factor K at the tip of the propagating crack is expressed as

$$K = K_R(\Delta a), \quad (1)$$

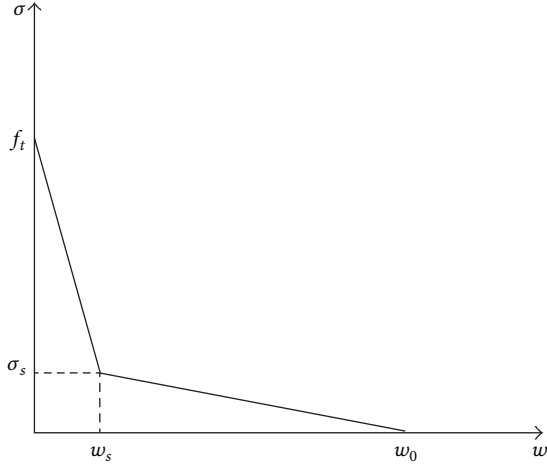


FIGURE 2: The bilinear softening traction-separation law.

where $K_R(\Delta a)$ is the crack extension resistance at crack extension length $\Delta a = a - a_0$. Also $K_R(\Delta a)$ is expressed in the following relation:

$$K_R(\Delta a) = K_{Ic}^{ini} + K_c(\Delta a), \quad (2)$$

$$K_c(\Delta a) = F_1(f_t, f(\sigma), \Delta a). \quad (3)$$

In order to develop the K_R -curve for complete fracture process considering the cohesive stress in fictitious fracture zone, the value of cohesive toughness K_c at every stage of loading is important to determine. During crack propagation, four different stages are considered with the help of three characteristic crack lengths (a_0 , a_c , and a_{wc}) as represented in Figure 1 in which r_u is the undamaged portion of the ligament, a_0 is initial crack length, a_c is crack length at critical condition of unstable crack propagation, and a_{wc} is the length of fully developed fictitious fracture zone after which the stress-free crack propagation will begin.

2.2. Softening Traction-Separation Law of Postfire Concrete.

The softening traction-separation law is a priori to determine the K_R -curve, at room temperature, and many expressions have been proposed based on direct tensile test [8, 17–20]. Based on numerical studies, simplified bilinear expressions for the softening traction-separation law (Figure 2) were suggested by Petersson in 1981 [17], Hilsdorf and Brameshuber in 1991 [19], and Phillips and Zhang in 1993. The area under the softening curve was defined as the fracture energy G_F by Hillerborg et al. in 1976 [21]. Therefore, one can get the following equation:

$$G_F = \frac{1}{2}(f_t w_s + \sigma_s w_0). \quad (4)$$

As a consequence, a general form of the simplified bilinear expression of the softening traction-separation law is given as follows:

$$\sigma = \begin{cases} \frac{f_t - (f_t - \sigma_s)w}{w_0} & 0 \leq w \leq w_s, \\ \frac{\sigma_s(w_0 - w)}{(w_0 - w_s)} & w_s \leq w \leq w_0, \\ 0 & w \geq w_0. \end{cases} \quad (5)$$

Different values of the break point (σ_s , w_s) and the crack width w_0 at stress-free point were used for the expression proposed by different researchers. In present work, the bilinear softening function of concrete proposed by Petersson is used for postfire specimens as follows:

$$\begin{aligned} \sigma_s &= \frac{f_t}{3}, \\ w_s &= \frac{0.8G_F}{f_t}, \\ w_0 &= \frac{3.6G_F}{f_t}. \end{aligned} \quad (6)$$

2.3. Analytical Method. The standard Green function [22] for the edge cracks with finite width of plate subjected to a pair of normal forces is used to evaluate the value of cohesive toughness. The general expression for the crack extension resistance for complete fracture associated with cohesive stress distribution in the fictitious fracture zone for Mode I fracture is given as follows:

$$K_R(\Delta a) = K_{Ic}^{ini} + \int_{a_0}^a \frac{2\sigma(x)F(x/a, a/h)}{\sqrt{\pi a}} dx, \quad (7)$$

where

$$\begin{aligned} F\left(\frac{x}{a}, \frac{a}{h}\right) &= \frac{3.52(1-x/a)}{(1-a/h)^{3/2}} - \frac{4.35-5.28x/a}{(1-a/h)} \\ &+ \left\{ \frac{1.30-0.30(x/a)^{3/2}}{\sqrt{1-(x/a)^2}} + 0.83 - 1.76\frac{x}{a} \right\} \\ &\times \left\{ 1 - \left(1 - \frac{x}{a}\right)\frac{a}{h} \right\}. \end{aligned} \quad (8)$$

Equation (7) is employed according to the conditions of four stages of crack propagation as mentioned below.

2.3.1. Case 1: When $a = a_0$. There is no advancement in the initial notch length at this stage of loading and the body remains in elastic condition, subjected to small load (up to P_{ini}) without any slow crack growth. Hence, cohesive stress $\sigma(x) = 0$; the crack growth resistance remains equal to initiation toughness of the material. From (7), it is expressed as

$$K_R = K_{Ic}^{ini}. \quad (9)$$

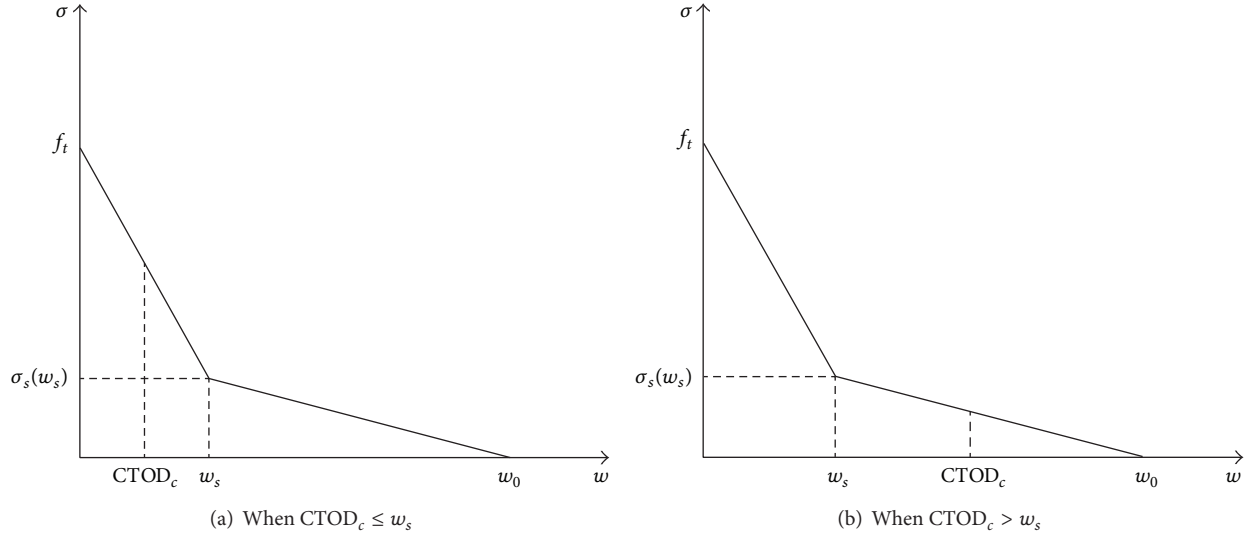
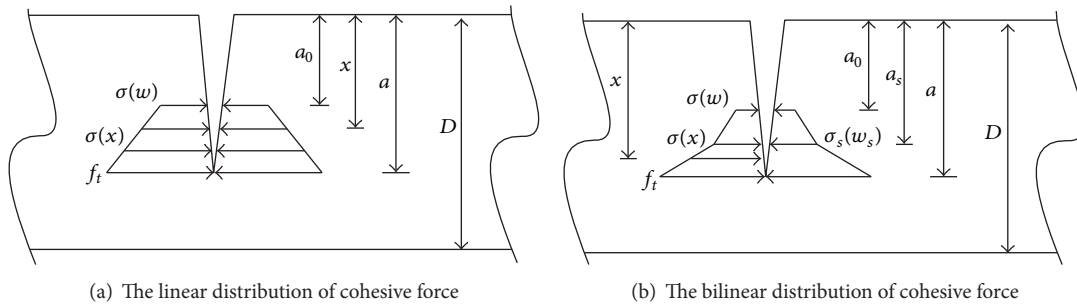
FIGURE 3: Two different situations for $CTOD_c$ and w_s .

FIGURE 4: The cohesive distribution of crack propagation stage II.

2.3.2. *Case 2: When $a_0 \leq a \leq a_c$.* The stable slow crack growth will take place until the effective crack extension a_c corresponding to the maximum load P_u is achieved. The cohesive force will start acting across the fictitious fracture zone resulting in the increase of crack extension resistance.

(a) For specimens subjected to temperatures less than 120°C , the critical $CTOD_c$ corresponding to maximum load P_u is less than w_s , as shown in Figure 3(a). The distribution of cohesive stress along the fictitious fracture zone is approximated to be linear, as shown in Figure 4(a). The variation of cohesive stress along the fictitious fracture zone for this loading condition, that is, $a_0 \leq a \leq a_c$ or $0 \leq CTOD \leq CTOD_c$, is written as

$$\sigma(x) = \frac{\sigma(w) + (f_t - \sigma(w))(x - a_0)}{(a - a_0)}, \quad (10)$$

where $\sigma(w)$ and w are the values of cohesive stress and crack opening displacement, being at the tip of initial notch,

respectively. The value of $\sigma(w)$ is determined by using bilinear softening function as follows:

$$\sigma(w) = \sigma_s(w_s) + \frac{w_s - w}{w_s} (f_t - \sigma_s(w_s)). \quad (11)$$

The crack extension resistance in this case is evaluated using (7) and (8).

(b) For specimens subjected to temperatures higher than 120°C , the critical $CTOD_c$ corresponding to maximum load P_u is wider than w_s , as shown in Figure 3(b). The distribution of cohesive stress along the fictitious fracture zone is approximated to be bilinear, as shown in Figure 4(b). The variation of cohesive stress along the fictitious fracture zone for this loading condition, also, $a_0 \leq a \leq a_c$ or $0 \leq CTOD \leq CTOD_c$, is written as

$$\begin{aligned} \sigma_1(x) &= \sigma(w) + (\sigma_s(w_s) - \sigma(w)) \frac{(x - a_0)}{(a_s - a_0)} \quad a_s \leq x \leq a_0, \\ \sigma_2(x) &= \sigma_s(w_s) + (f_t - \sigma_s(w_s)) \frac{(x - a_s)}{(a - a_s)} \quad a_s \leq x \leq a. \end{aligned} \quad (12)$$

The value of $\sigma(w)$ is determined by using bilinear softening function as follows:

$$\sigma(w) = \frac{w_0 - w}{w_0 - w_s} \sigma_s(w_s). \quad (13)$$

The limits of integration of (7) should be taken in two steps: $a_0 \leq x \leq a_s$ for cohesive stress $\sigma_1(x)$ and $a_s \leq x \leq a$ for cohesive stress $\sigma_2(x)$, respectively. The same Green's function $F(x/a, a/h)$ for a given effective crack extension will be determined using (8). The calculated formula is listed as follows:

$$K_R = K_{Ic}^{ini} + \int_{a_0}^{a_s} \frac{2\sigma_2(x) F(x/a, a/h)}{\sqrt{\pi a}} dx + \int_{a_s}^a \frac{2\sigma_3(x) F(x/a, a/h)}{\sqrt{\pi a}} dx. \quad (14)$$

The effective crack length at break point a_s (as shown in Figure 4(b)) is computed from the following nonlinear expression [23] by substituting COD(a_s), CMOD, a , and h :

$$\begin{aligned} \text{COD}(a_s) = \text{CMOD} & \left\{ \left(1 - \frac{a_s}{a} \right)^2 \right. \\ & + \left(1.018 - 1.149 \frac{a}{h} \right) \\ & \left. \times \left[\frac{a_s}{a} - \left(\frac{a_s}{a} \right)^2 \right] \right\}^{1/2}, \end{aligned} \quad (15)$$

where COD(a_s) is the crack opening displacement at a_s , a is the effective crack length (according to (18)), and h is the specimen height.

2.3.3. Case 3: When $a_c \leq a \leq a_{w0}$. During this stage of the applied load for all temperatures, corresponding CTOD and effective crack length have increased more than maximum load P_w , CTOD_{*c*}, and critical effective crack extension a_c , respectively. The cohesive stress distribution for this case will take a bilinear shape, as shown in Figure 4(b). It is the same situation as case 2 part (b), and the crack extension resistance K_R at this stage would be calculated according to (14). This case is shown in Figure 5.

2.3.4. Case 4: When $a \geq a_{w0}$. This situation of loading corresponds to the descending portion of P -CMOD curve. At the effective crack extension, a_{w0} , full shape of cohesive stress distribution is allowed to develop, and beyond further extension in crack during loading, a new stress-free crack in front of the initial notch tip will form. This case is shown

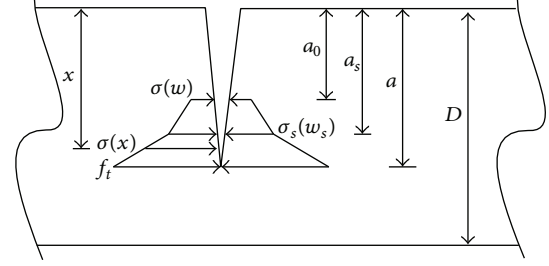


FIGURE 5: Crack propagation stage III.

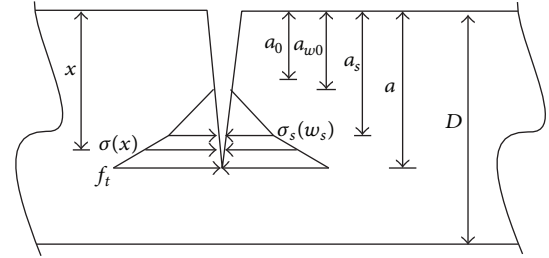


FIGURE 6: Crack propagation stage IV.

in Figure 6 and the stress distribution is expressed with the following relation:

$$\begin{aligned} \sigma_1(x) &= 0 \quad a_0 \leq x \leq a_{w0}, \\ \sigma_2(x) &= \sigma_s(w_s) \frac{(x - a_{w0})}{(a_s - a_{w0})} \quad a_s \leq x \leq a_{w0}, \\ \sigma_3(x) &= \sigma_s(w_s) + (f_t - \sigma_s(w_s)) \frac{(x - a_s)}{(a - a_s)} \quad a_s \leq x \leq a. \end{aligned} \quad (16)$$

Similar to (15), the effective crack length a_{w0} corresponding to zero stress of new fictitious fracture zone as shown in Figure 6 is computed from the following nonlinear expression:

$$\begin{aligned} \text{COD}(a_{w0}) = \text{CMOD} & \left\{ \left(1 - \frac{a_{w0}}{a} \right)^2 \right. \\ & + \left(1.018 - 1.149 \frac{a}{h} \right) \\ & \left. \times \left[\frac{a_{w0}}{a} - \left(\frac{a_{w0}}{a} \right)^2 \right] \right\}^{1/2}, \end{aligned}$$

$$\begin{aligned} \text{COD}(a_s) = \text{CMOD} & \left\{ \left(1 - \frac{a_s}{a}\right)^2 \right. \\ & + \left(1.018 - 1.149 \frac{a}{h}\right) \\ & \left. \times \left[\frac{a_s}{a} - \left(\frac{a_s}{a}\right)^2 \right] \right\}^{1/2}. \end{aligned} \quad (17)$$

The evaluation of crack extension resistance in this case is also done using (7) and (8).

2.4. Determination of Equivalent Crack Extension

2.4.1. Assumption. Linear asymptotic superposition assumption [5, 6] is considered to introduce the nonlinearity effect in P -CMOD curves during loading of concrete test specimens. This assumption enables us to introduce linear elastic fracture mechanics (LEFM) for calculating fracture parameters during every stage of loading in concrete structures. The hypotheses of the assumption are given as follows.

- (1) The nonlinear characteristic of the P -CMOD curve is caused by fictitious crack extension in front of a stress-free crack.
- (2) An effective crack consists of an equivalent-elastic stress-free crack and equivalent-elastic fictitious crack extension.

2.4.2. Equivalent Crack Extension for WS Specimen. The equivalent-elastic crack length for WS specimen is expressed as [24]

$$a = (h + h_0) \left\{ 1 - \left(\frac{13.18}{\text{CMODE}t/P + 9.16} \right)^{1/2} \right\} - h_0. \quad (18)$$

The empirical expression (18) is valid within 2% accuracy for $0.2 \leq \alpha \leq 0.8$. The residual Young's modulus E is calculated using the P -CMOD curve as

$$E = \frac{1}{t c_i} \left[13.18 \times \left(1 - \frac{a_0 + h_0}{h + h_0} \right)^2 - 9.16 \right], \quad (19)$$

where $c_i = \text{CMOD}/P$, the segment compliance; t is the specimens thickness; h is the specimens height; and h_0 is the thickness of clip gauge holder. The value of equivalent-elastic crack length a and residual E is listed in Table 1.

2.4.3. Calculation of Crack Opening Displacement. The crack opening displacement at position x along the fictitious crack line $\text{COD}(x)$ is computed from the known value of CMOD using the following expression [23]:

$$\begin{aligned} \text{COD}(x) = \text{CMOD} & \left\{ \left(1 - \frac{x}{a}\right)^2 \right. \\ & + \left(1.018 - 1.149 \frac{a}{h}\right) \left[\frac{x}{a} - \left(\frac{x}{a}\right)^2 \right] \right\}^{1/2}. \end{aligned} \quad (20)$$

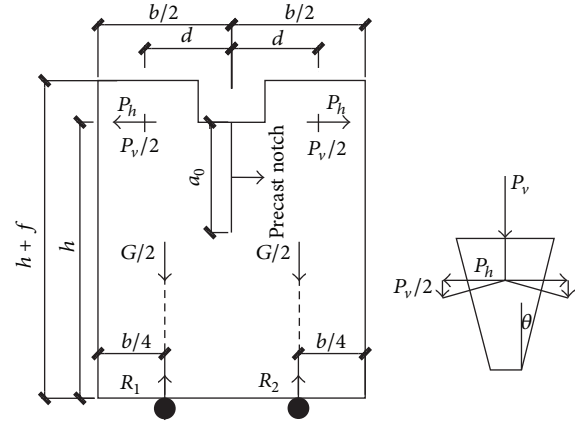


FIGURE 7: Geometry of specimens.

Also, the value of cohesive stress along the fictitious fracture zone corresponding to crack opening displacement at all stages of loading is evaluated using bilinear stress-displacement softening law as given in (3).

2.5. Calculation of Double-K Fracture Parameters. The parameters like initiation toughness K_{Ic}^{ini} and stress intensity factors (SIF) are required to be calculated to judge the stability of a propagating crack in a loaded structure using $K_R(\Delta a)$ curve analysis. The LEFM formula for the corresponding test specimen geometries is used for this purpose.

The SIF for WS test specimens is written as [24]

$$K(P, a) = \frac{P \times 10^{-3}}{t h^{1/2}} f(\alpha), \quad (21)$$

$$f(\alpha) = \frac{3.675 \times [1 - 0.12(\alpha - 0.45)]}{(1 - \alpha)^{3/2}}, \quad \alpha = \frac{a}{h}. \quad (22)$$

The empirical expression (21) is valid within 2% accuracy for $0.2 \leq \alpha \leq 0.8$.

3. Experimental Research

3.1. Experimental Program and Experimental Phenomena. To obtain the complete P -CMOD curves, the wedge-splitting tests were implemented. A total of 50 concrete specimens with the same dimensions $230 \times 200 \times 200$ mm were prepared, the geometry of the specimens is shown in Figure 7 ($b = 200$ mm, $d = 65$ mm, $h = 200$ mm, $f = 30$ mm, $a_0 = 80$ mm, and $\theta = 15^\circ$). The concrete mix ratios (by weight) were Cement : Sand : Coarse aggregate : Water = 1.00 : 3.44 : 4.39 : 0.80, with common Portland cement-mixed medium sand and 16 mm graded coarse aggregate. All the specimens had a precast notch of 80 mm height and 3 mm thickness, achieved by placing a piece of steel plate into the molds prior to casting. Each wedge splitting specimen was embedded with a thermal couple in the center of the specimens for temperature control.

Nine heating temperatures, ranging from 65°C to 600°C ($T_m = 65^\circ\text{C}, 120^\circ\text{C}, 200^\circ\text{C}, 300^\circ\text{C}, 350^\circ\text{C}, 400^\circ\text{C}, 450^\circ\text{C}$,

TABLE I: Experimental results of fracture parameters.

Specimen	Temperature	P_{ini} (kN)	CMOD _{ini} (mm)	P_u (kN)	CMOD _c (mm)	CTOD _c (mm)	E (GPa)	a_c (h)	K_{Ic}^{ini} (MPa·m ^{1/2})	K_{Ic}^{un} (MPa·m ^{1/2})	G_F (N/m)
WS1	20°C	6.19	0.068	8.33	0.174	0.065	15.30	0.53	0.505	1.061	234.15
WS2		6.28	0.047	9.81	0.120	0.039	20.51	0.48	0.523	1.070	483.66
WS3		7.26	0.063	10.40	0.210	0.079	20.66	0.57	0.610	1.497	438.22
WS4		7.02	0.086	7.92	0.152	0.060	18.88	0.56	0.357	1.091	219.39
WS5		5.65	0.060	9.39	0.237	0.096	15.45	0.54	0.503	1.213	321.05
Average		6.55	0.065	9.17	0.178	0.068	18.16	0.54	0.498	1.186	339.30
WS6	65°C	6.98	0.055	11.31	0.195	0.078	21.73	0.56	0.550	1.594	425.91
WS7		3.88	0.050	8.23	0.163	0.100	24.79	0.66	0.303	1.664	482.62
WS8		6.88	0.078	10.41	0.212	0.087	19.43	0.57	0.557	1.518	487.75
WS9		7.94	0.052	10.71	0.164	0.087	23.25	0.60	0.511	1.685	480.51
WS10		6.32	0.056	11.67	0.229	0.086	16.60	0.54	0.562	1.507	522.36
Average		6.42	0.058	10.47	0.193	0.088	21.16	0.59	0.480	1.594	479.83
WS11	120°C	5.03	0.064	8.37	0.191	0.056	10.65	0.47	0.518	0.900	396.52
WS13		4.69	0.093	8.25	0.224	0.084	11.87	0.53	0.417	1.058	517.82
WS12		4.71	0.070	7.53	0.357	0.152	9.48	0.60	0.419	1.202	654.73
WS14		2.79	0.030	7.53	0.198	0.083	15.42	0.58	0.249	1.107	345.46
WS15		—	—	—	—	—	—	—	—	—	—
Average		4.31	0.064	7.92	0.243	0.094	11.86	0.55	0.401	1.067	478.63
WS21	300°C	1.89	0.182	3.40	0.653	0.283	2.45	0.61	0.168	0.556	437.92
WS22		3.48	0.185	5.53	0.667	0.280	3.49	0.59	0.309	0.841	611.47
WS23		1.82	0.121	3.38	0.672	0.271	1.91	0.57	0.162	0.480	341.77
WS24		2.61	0.194	4.97	0.577	0.262	1.99	0.52	0.232	0.589	564.12
WS25		2.03	0.096	4.17	0.651	0.361	4.03	0.68	0.175	0.913	549.99
Average		2.37	0.156	4.29	0.644	0.291	2.78	0.59	0.209	0.676	501.05
WS36	450°C	1.52	0.126	3.37	1.009	0.544	1.41	0.62	0.135	0.582	611.53
WS37		—	—	—	—	—	—	—	—	—	—
WS38		1.52	0.163	3.26	1.419	0.660	1.46	0.62	0.135	0.527	482.45
WS39		1.12	0.296	3.07	1.348	0.617	1.34	0.64	0.100	0.563	663.10
WS40		0.99	0.105	2.94	1.394	0.666	1.58	0.68	0.088	0.659	678.79
Average		1.29	0.172	3.16	1.293	0.622	1.48	0.64	0.115	0.583	608.97
WS46	600°C	0.76	0.443	1.13	1.482	0.684	0.47	0.65	0.067	0.221	228.23
WS47		0.53	0.139	1.48	2.082	0.684	0.48	0.64	0.063	0.277	395.06
WS48		0.81	0.324	1.65	1.908	0.813	1.14	0.76	0.072	0.550	539.22
WS49		0.58	0.436	1.14	1.687	0.973	0.38	0.65	0.052	0.225	331.99
WS50		0.62	0.279	1.48	2.082	0.727	0.38	0.62	0.068	0.213	273.07
Average		0.62	0.324	1.38	1.848	0.799	0.57	0.67	0.064	0.297	353.51

500°C, and 600°C), were adopted with the ambient temperature as a reference. Because it was recognized that the fracture behavior measurements were generally associated with significant scatter, five repetitions were performed for each temperature. An electric furnace with net dimensions 300 × 300 × 900 mm was used for heating. When the designated T_m was reached, the furnace was shut down, and the specimens were naturally cooled for 7 days prior to the test.

A closed-loop servocontrolled hydraulic jack with a maximum capacity of 1000 kN was employed to conduct the wedge splitting test. Two clip-on extensometers were suited at the mouth and the tip of the crack to measure the crack mouth opening displacement (CMOD) and crack tip opening displacement (CTOD). To obtain the complete P -CMOD curves (as shown in Figure 8), the test rate was fixed at 0.4 mm/min, such that it took approximately 20 minutes to complete a single test of specimens subjected to less than 300°C and 30 minutes for beyond 300°C.

3.2. Experimental Results and Discussion. The recorded maximum load P_u , the recorded crack mouth opening displacement $CMOD_c$ at P_u , the calculated crack tip opening displacement $CTOD_c$ based on (20), the initial cracking load P_{ini} determined by graphical method, the calculated residual Young's modulus E based on (18), the double- K fracture parameters, that is, K_{Ic}^{ini} and K_{Ic}^{un} , and the residual fracture energy G_F are summarized in Table 1.

Figure 8 shows typical complete load-displacement curves for different heating temperatures up to 600°C. The figure shows that the ultimate load P_u decreases significantly with increasing temperatures T_m , whereas the crack mouth opening displacement (CMOD) increases with T_m . The initial slope of ascending branches decreases with heating temperatures and the curves become gradually shorter and more extended.

From Table 1, it is found that the initial load P_{ini} , ultimate load P_u , the residual Young's modulus E , and the double- K fracture parameters decrease with the increasing temperatures, whereas the $CMOD_{ini}$, $CMOD_c$, $CTOD_c$, and a_c/h increase with T_m . The G_F sustains a hold-increase-decrease tendency with T_m ; the detailed explanation could be found in our previous work [25].

4. Residual Crack Extension Resistance Curves (K_R -Curves) and Stability Criterion

4.1. Crack Extension Resistance at Various Temperatures. Since the K_R -curve is considered as a criterion for complete description of crack propagation in structure, it is regarded as the material properties of the complete fracture process. The procedure to calculate the crack extension resistance curves (K_R -curves) is programmed using the analytical expressions given in Section 3. The P -CMOD curves shown in Figure 8 are used. The K_R -curves at different temperatures with crack extension from 65°C to 600°C are plotted in Figures 9(a)~9(c).

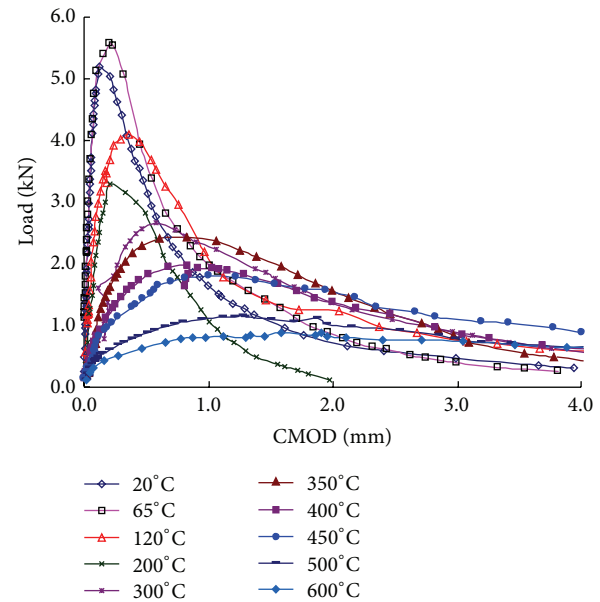


FIGURE 8: Load versus CMOD curves of specimens with temperatures.

When temperatures are less than 200°C, the K_R -curves have almost the same S-shape, which have a good coincidence with existed literature [5].

4.2. The Influence of Temperatures on Residual K_R -Curves. Figure 10 plots the K_R -curves of all temperatures; it is concluded that the K_R -curves decrease with increasing temperatures. Generally, temperatures under 120°C appear not to induce much thermal damage to concrete; the K_R -curves of 20°C, 65°C, and 120°C are close. Between 200°C and 600°C, higher temperatures cause more damage to the concrete, and the K_R -curves drop significantly. When temperature reaches 600°C, the K_R -curve almost increases linearly with a small margin.

4.3. The Stability Analysis of Crack Propagation. The K_R -curve presents the material properties of the complete fracture process. So, the K_R -curve can be taken as a criterion for describing the crack propagation in a structure or a structural component.

On the contrary, the stress intensity factor curve (K -curve) during the crack propagation in the structure or the structural component must be calculated already. At an arbitrary loading stage on a wedge-splitting specimen, the stress intensity factor at the tip of a propagating crack can be evaluated by inserting the load P and the length of the propagating crack a into formula (21). For the complete fracture process, the stress intensity factor at the tip of the propagating crack caused by the external load P can be plotted as a curve using formula (21).

Herein, the length of the propagating crack is taken as a horizontal axis, and the crack extension resistance $K_R(\Delta a)$, the stress intensity factor K , and the corresponding load P

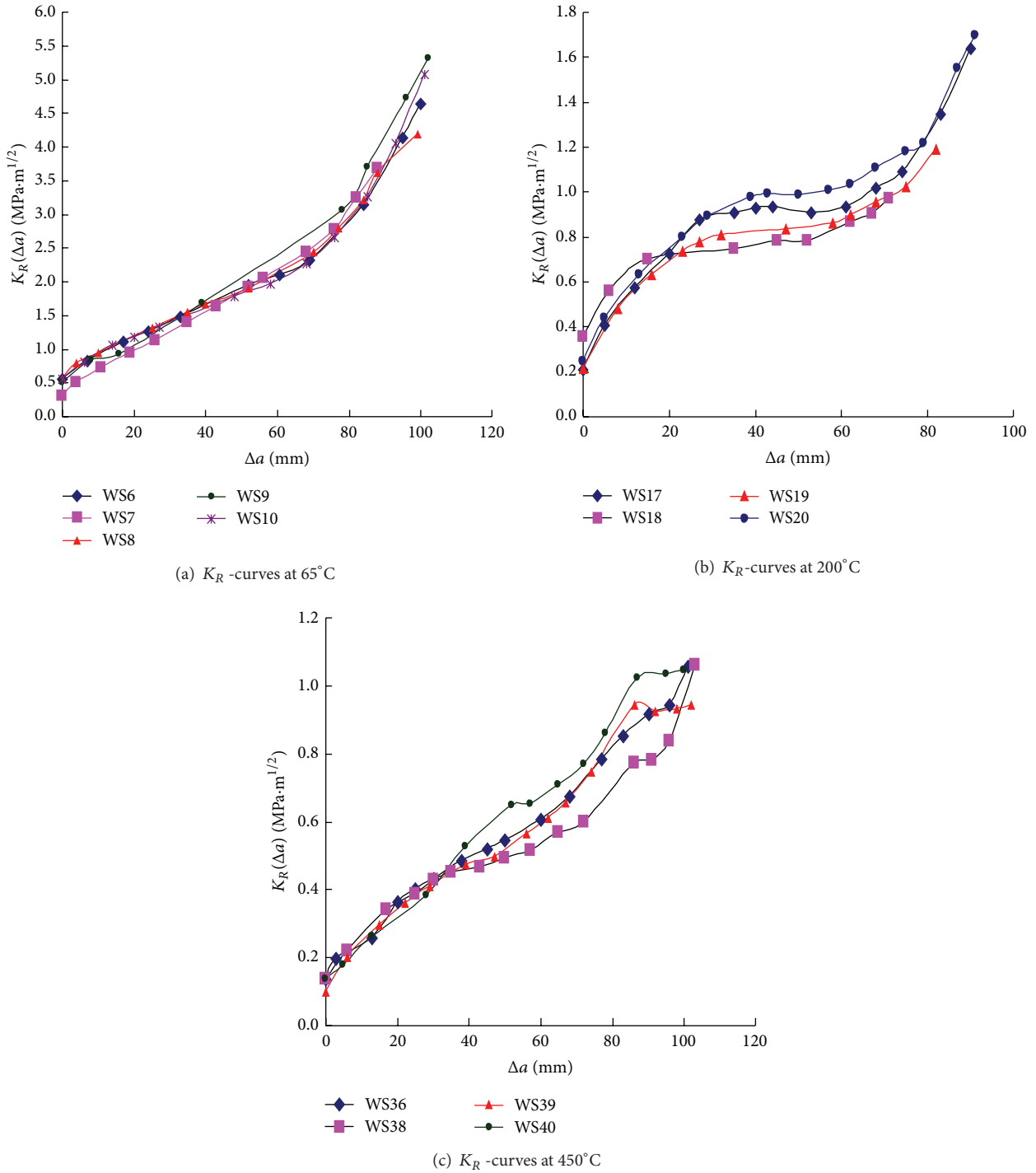


FIGURE 9: K_R -curves with crack extension length of various temperatures.

are plotted on the vertical axis in Figures 11(a)~11(d). From those figures, the stability analysis of the crack propagation during the complete fracture process could be carried out.

From the initial point B to the critically unstable point C during the crack propagation, the toughness of the material increases with increasing crack extension from the inherent toughness K_{Ic}^{ini} to the value of the crack extension resistance

at the critically unstable point which is denoted by $K_R(\Delta a_c)$. The difference between $K_R(\Delta a_c)$ and K_{Ic}^{ini} is caused by the cohesive force on the fictitious crack zone during the crack propagation.

A common character of Figures 11(a)~11(d) is that when the maximum load P_{max} is reached, the stress intensity factor curve (K -curve) coincides with the crack extension resistance

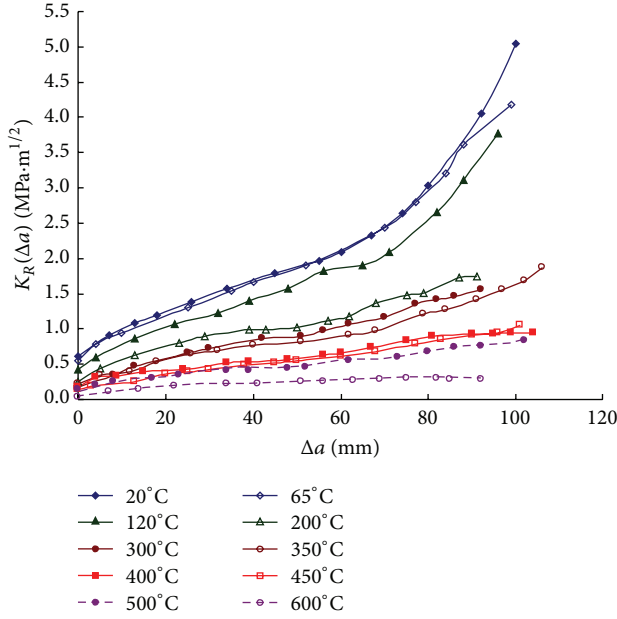


FIGURE 10: K_R -curves with crack extension length of all temperatures.

curve (K_R -curve) at the point at which the value of the vertical coordinate is equal to the value of the unstable fracture toughness K_{Ic}^{un} . All of them correspond to the related critical crack length a_c .

Furthermore, it can be seen that when the curve of the stress intensity factor is lower than the crack extension resistance curve, the crack propagates steadily which can be observed in the region between point *B* and point *C*. Otherwise, when the K -curve coincides with or is higher than the K_R -curve, the crack propagates unsteadily. The stability analysis can be expressed mathematically as given below:

$$K_{Ic}^{ini} < K(P, a) < K_{Ic}^{un} \quad \text{crack propagates steadily,} \quad (23)$$

$$K(P, a) > K_{Ic}^{un} \quad \text{crack propagates unsteadily.}$$

5. Conclusions

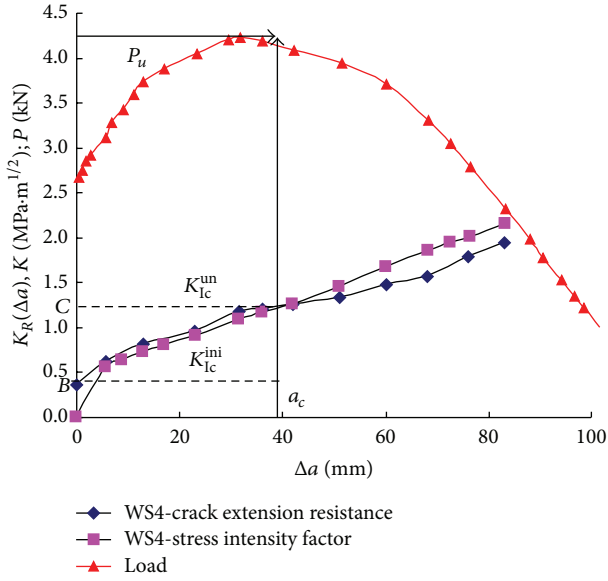
The residual crack extension resistance $K_R(\Delta a)$ associated with cohesive stress distribution in fictitious crack zone is evaluated for wedge-splitting specimens using analytical method. The analytical formulations of the residual $K_R(\Delta a)$ for the complete fracture process are presented which consist of two parts. One part is the initiation toughness of the material K_{Ic}^{ini} , and the other part is an overall value of stress intensity factor K_{Ic}^c caused by the cohesive stress along the fictitious crack zone that increases with the crack extension Δa . The distributions of the cohesive forces along the fictitious crack zone for varied loading stages are determined according to the softening traction-separation law of the concrete materials.

In the calculation of residual crack extension curves (K_R -curves) of wedge-splitting specimens subjected to different temperatures, it is found that in each temperature, the fracture toughness $K_R(\Delta a)$ increases with increasing crack length Δa , while the K_R -curves decrease with increasing temperatures. Generally, temperatures under 120°C appear not to induce much thermal damage to concrete; the K_R -curves of 20°C, 65°C, and 120°C are close. Between 200°C and 600°C, high temperatures cause more thermal damage to the concrete, and the K_R -curves drop significantly. When temperature reaches 600°C, the K_R -curve increases almost linearly with a small margin.

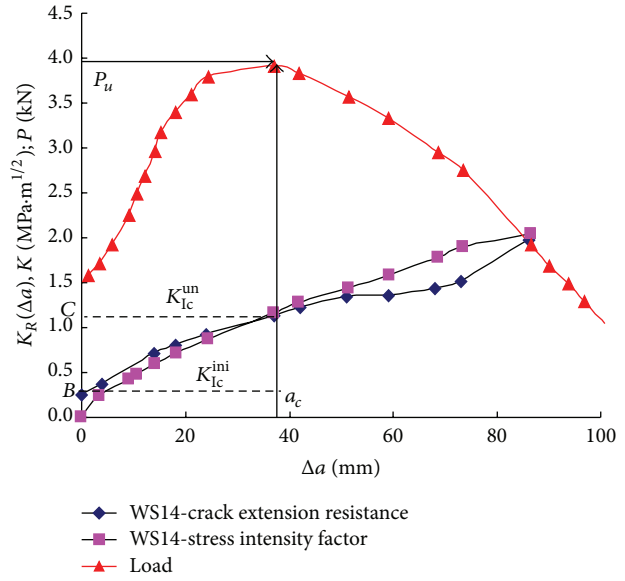
For the stability analyses of crack propagation, the comparison between K_R -curves and the corresponding stress intensity factor curves (K -curves) shows that K_R -curves can be taken as a crack propagation criterion to judge the stability of the crack in the loaded structures; that is, when the stress intensity factor $K(P, a)$ is smaller than the crack extension resistance $K_R(\Delta a)$, the crack propagates steadily. Contrarily, when $K(P, a)$ is larger than $K_R(\Delta a)$, the crack propagates unsteadily.

Nomenclature

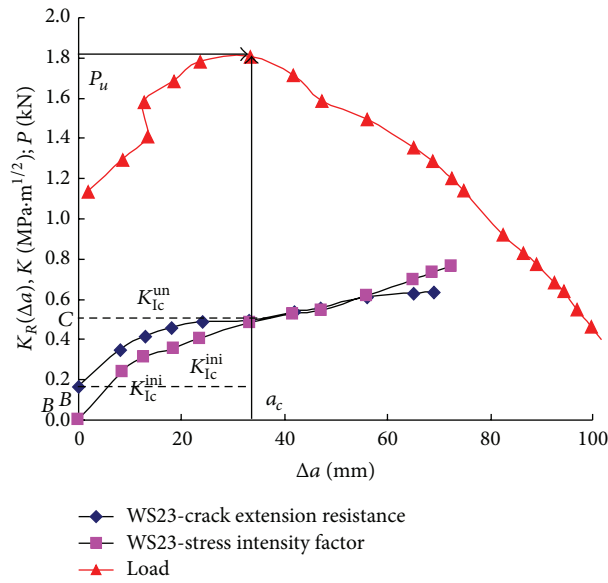
a :	Equivalent-elastic crack length
a_c :	Critical notch depth of the specimen
a_s :	Effective crack length corresponding to w_s
a_{w0} :	Effective crack length corresponding to zero stress of new fictitious fracture zone
CMOD:	Crack mouth opening displacement
CTOD:	Crack tip opening displacement
E :	Residual Young's modulus
G_F :	Fracture energy: N/m
h :	Height of wedge-splitting specimens
K_R :	Crack extension resistance
$K_c(\Delta a)$:	Cohesive toughness
$\sigma(w)$:	Cohesive stress at the tip of initial notch
$\sigma(x)$:	Cohesive stress at equivalent-elastic crack length x
P_u :	Maximum load
w_0 :	Crack width at stress-free point
w :	Crack opening displacement at the tip of initial notch
a_0 :	Initial notch depth of the specimen
Δa :	Crack extension length
a_{wc} :	Fully developed fictitious fracture zone length
CMOD _c :	Critical crack mouth opening displacement
CTOD _c :	Critical crack tip opening displacement
$f(\sigma)$:	Cohesive force distribution
f_t :	Tensile strength
h_0 :	Thickness of the clip gauge holder
K_{Ic}^{ini} :	Initial fracture toughness
K :	Stress intensity factor
$\sigma_s(w_s)$:	Cohesive stress at the break point of softening curve



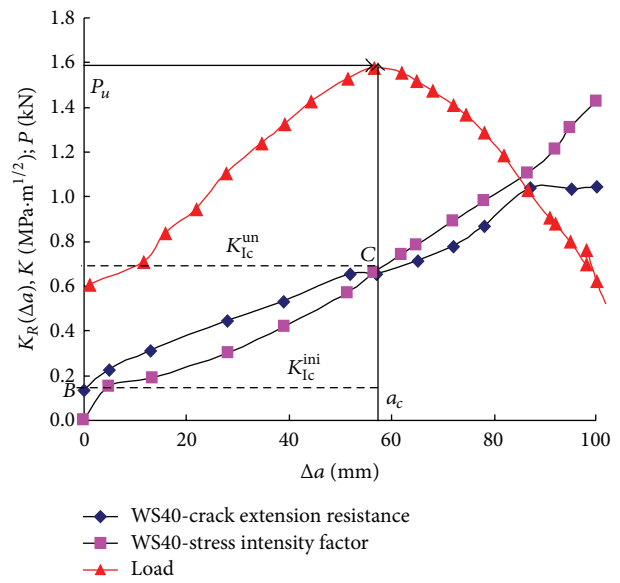
(a) Stability analysis of crack propagation at room temperature



(b) Stability analysis of crack propagation at 120°C



(c) Stability analysis of crack propagation at 300°C



(d) Stability analysis of crack propagation at 450°C

FIGURE 11: Stability analysis of crack propagation of various temperatures.

P_{ini} : The initial cracking load
 T_m : Heating temperatures
 w_s : Crack width at break point of softening curve.

Conflict of Interests

The authors declare that they have no conflict of interests regarding the publication of this paper.

Acknowledgments

The State Laboratory of Disaster Reduction in Civil Engineering (SLDRCE09-D-02) and the Young Scientist Project of Natural Science Foundation of China (NSFC: 51008235) have supported this research.

References

[1] H. K. Hilsdorf and W. Brameshuber, "Size effects in the experimental determination of fracture mechanics parameters," in

- Application of Fracture Mechanics to Cementitious Composites*, S. P. Shah, Ed., pp. 361–397, NATO-ARW, 1984.
- [2] Y. W. Mai, “Fracture measurements of cementitious composites,” in *Application of Fracture Mechanics to Cementitious Composites*, S. P. Shah, Ed., pp. 399–429, NATO-ARW, 1984.
- [3] B. L. Karihaloo and S. P. Shah, “Do plain and fiber-reinforced concretes have an R-curve behavior?” in *Fractures of Concrete and Rock*, S. P. Shah and S. E. Swartz, Eds., pp. 96–105, Springer, New York, NY, USA, 1987.
- [4] S. Xu and H. W. Reinhardt, “Determination of double-K criterion for crack propagation in quasi-brittle fracture, part I: experimental investigation of crack propagation,” *International Journal of Fracture*, vol. 98, no. 2, pp. 111–149, 1999.
- [5] S. Xu and H. W. Reinhardt, “Crack extension resistance and fracture properties of quasi-brittle softening materials like concrete based on the complete process of fracture,” *International Journal of Fracture*, vol. 92, no. 1, pp. 71–99, 1998.
- [6] S. Xu and H. W. Reinhardt, “Determination of double-K criterion for crack propagation in quasi-brittle fracture, part II: analytical evaluating and practical measuring methods for three-point bending notched beams,” *International Journal of Fracture*, vol. 98, no. 2, pp. 151–177, 1999.
- [7] Comité Euro-International du Béton (CEB), *CEB-FIP Model Code Bulletin D'Information*, EPF Lausanne, 1990.
- [8] H. W. Reinhardt, H. A. W. Cornelissen, and D. A. Hordijk, “Tensile tests and failure analysis of concrete,” *Journal of Structural Engineering*, vol. 112, no. 11, pp. 2462–2477, 1986.
- [9] S. Kumar and S. V. Barai, “Influence of specimen geometry and size-effect on the K_R -curve based on the cohesive stress in concrete,” *International Journal of Fracture*, vol. 152, no. 2, pp. 127–148, 2008.
- [10] Z. P. Bazand, P. Bazant, and P. C. Prat, “Effect of temperatures and humidity on fracture energy of concrete,” *ACI Materials Journal*, vol. 85, no. 4, pp. 262–271, 1988.
- [11] G. Baker, “The effect of exposure to elevated temperatures on the fracture energy of plain concrete,” *Materials and Structures*, vol. 29, no. 190, pp. 383–388, 1996.
- [12] B. Zhang, N. Bicanic, C. J. Pearce, and G. Balabanic, “Residual fracture properties of normal- and high-strength concrete subject to elevated temperatures,” *Magazine of Concrete Research*, vol. 52, no. 2, pp. 123–136, 2000.
- [13] C. V. Nielsen and N. Bićanić, “Residual fracture energy of high-performance and normal concrete subject to high temperatures,” *Materials and Structures*, vol. 36, no. 262, pp. 515–521, 2003.
- [14] B. Zhang and N. Bicanic, “Fracture energy of high-performance concrete at high temperatures up to 450°C: the effects of heating temperatures and testing conditions (hot and cold),” *Magazine of Concrete Research*, vol. 58, no. 5, pp. 277–288, 2006.
- [15] G. Prokopski, “Fracture toughness of concretes at high temperature,” *Journal of Materials Science*, vol. 30, no. 6, pp. 1609–1612, 1995.
- [16] H. Abdel-Fattah and S. A. Hamoush, “Variation of the fracture toughness of concrete with temperature,” *Construction and Building Materials*, vol. 11, no. 2, pp. 105–108, 1997.
- [17] P. E. Petersson, “Crack growth and development of fracture zones in plain concrete and similar materials,” Report TVBM-1006, Division of Building Materials, Lund Institute of Technology, Lund, Sweden, 1981.
- [18] V. S. Gopalaratnam and S. P. Shah, “Softening response of plain concrete in direct tension,” *Journal of the American Concrete Institute*, vol. 82, no. 3, pp. 310–323, 1985.
- [19] H. K. Hilsdorf and W. Brameshuber, “Code-type formulation of fracture mechanics concepts for concrete,” *International Journal of Fracture*, vol. 51, no. 1, pp. 61–72, 1991.
- [20] D. V. Phillips and Z. Zhang, “Direct tension tests on notched and un-notched plain concrete specimens,” *Magazine of Concrete Research*, vol. 45, no. 162, pp. 25–35, 1993.
- [21] A. Hillerborg, M. Modéer, and P.-E. Petersson, “Analysis of crack formation and crack growth in concrete by means of fracture mechanics and finite elements,” *Cement and Concrete Research*, vol. 6, no. 6, pp. 773–781, 1976.
- [22] H. Tada, P. C. Paris, and G. Irwin, *The Stress Analysis of Cracks Handbook*, Paris Productions Incorporated, St. Louis, Mo, USA, 1985.
- [23] Y. S. Jenq and S. P. Shah, “Two parameter fracture model for concrete,” *Journal of Engineering Mechanics*, vol. 111, no. 10, pp. 1227–1241, 1985.
- [24] S. Xu and H. W. Reinhardt, “Determination of double-K criterion for crack propagation in quasi-brittle fracture, Part III: compact tension specimens and wedge splitting specimens,” *International Journal of Fracture*, vol. 98, no. 2, pp. 179–193, 1999.
- [25] J. Yu, K. Yu, and Z. Lu, “Residual fracture properties of concrete subjected to elevated temperatures,” *Materials and Structures*, vol. 45, no. 8, pp. 1155–1165, 2012.

Research Article

Impact of High Temperature on the Compressive Strength of ECC

Xingyan Shang and Zhoudao Lu

College of Civil Engineering, Tongji University, Shanghai 200092, China

Correspondence should be addressed to Zhoudao Lu; lzd@tongji.edu.cn

Received 20 January 2014; Accepted 13 June 2014; Published 25 June 2014

Academic Editor: Osman Gencel

Copyright © 2014 X. Shang and Z. Lu. This is an open access article distributed under the Creative Commons Attribution License, which permits unrestricted use, distribution, and reproduction in any medium, provided the original work is properly cited.

The influence of different cooling regimes (quenching in water and cooling in air) on the residual mechanical properties of ECC (engineered cementitious composites) exposed to high temperature up to 800°C was discussed in this paper. The specimens quenching in water gained better mechanical properties than the ones cooling in air. The strengthening effect of quenching for specimens subjected to 800°C was more significant than for the ones subjected to 400°C. The microstructural characterization is examined before and after exposure to fire deterioration by using scanning electron microscopy. Results from the microtest well explained the mechanical properties variation of postfire specimens.

1. Introduction

Concrete is the most widely used construction material in the world. Although it was primarily designed for carrying compressive loads, concrete in real field conditions is also subjected to tensile stresses because of structural loading, shrinkage (if the shrinkage is restrained), chemical attack, and thermal deformations. The tensile strength of concrete is only approximately 10% of its compressive strength, and brittle concrete cracks when subjected to tensile stresses. In recent years, the effort to modify the brittle nature of ordinary concrete has resulted in modern concepts of ultrahigh performance fiber-reinforced cementitious composites (UHP-FRCC), which are characterized by tensile strain-hardening after first cracking. Depending on its composition, its tensile strain capacity can be up to several hundred times those of normal and fiber-reinforced concrete. ECC is a special type of UHP-FRCC designed based on micromechanical principles to strain-harden in tension. It offers high ductility under uniaxial tensile loading and improved durability due to an intrinsically tight crack width of less than 100 μm [1, 2]. During the last decade, the use of ECC has considerably grown up, and it was used in a variety of structures in various regions [3, 4].

Significant attention has been brought to the study of its rheological, mechanical, and durability related properties of ECC. With an increase in the application of ECC, the

risk of exposure to elevated temperatures increases as well. The behavior of ECC exposed to high temperature has to be evaluated in particular.

For normal cement based composite, high temperatures caused physical and chemical changes, resulting in its mechanical property deterioration, such as compressive strength and modulus of elasticity. Different cooling regimes, that is, cooling in air, quenching in water, or water spraying, also had a significant influence on the residual mechanical properties of postfire composite [5, 6]. Gencel [7] researched the effect of heating duration and cooling regimes on mechanical properties of high strength concrete containing different proportions of hematite. Researchers [8] studied the mechanical and physical properties of lightweight concrete after high temperature. The residual properties of ECC after exposure to high temperatures have also been studied by several researchers, mainly on the heating temperatures and mineral admixtures of fly ash and fiber influence [9, 10]. But there are still some aspects remaining to be studied. The main objective of this research is to gain a better understanding of the influence of cooling regimes on the postfire ECC specimens subjected to high temperature up to 800°C.

2. Experimental Studies

2.1. Materials, Mix Proportions, and Basic Mechanical Properties. The materials used in the production of ECC mixture

TABLE 1: Mixture properties of ECC.

	ECC
Cement (C) (kg/m ³)	650
Fly ash (FA) (kg/m ³)	325
Water (W) (kg/m ³)	375
PVA fiber (kg/m ³)	26
Sand (kg/m ³)	480
HRWR (kg/m ³)	12
HPMC (kg/m ³)	1.90
W/(C + FA)	0.38
FA/C	50%

were Type I Portland cement (C), Class F fly ash (FA), sand, water, polyvinyl alcohol (PVA) fibers, a polycarboxylic ether type high-range water-reducing admixture (HRWR), and hydroxypropyl methylcellulose (HPMC). The mix details are given in Table 1. Unlike typical fiber-reinforced cementitious composites, the component characteristics and proportions within the ECC are carefully determined with the use of micromechanical design tools to achieve the desired strain-hardening response [11, 12]. The PVA fibers with a diameter of 39 μm and a length of 8 mm are purposely manufactured with a tensile strength (1620 MPa), elastic modulus (42.8 GPa), and maximum elongation (6.0%) matching those needed for strain-hardening performance. Additionally, the surface of the PVA fibers is coated with a proprietary oiling agent 1.2% by mass to tailor the interfacial properties between fiber and matrix for strain-hardening performance [11].

To characterize the direct tensile behavior of the ECC mixtures, the dog-bone specimens were used. Direct tensile tests [13] were conducted under displacement control at a loading rate of 0.005 mm/s. The typical tensile stress-strain curves of the ECC mixtures at 28 days are shown in Figure 1. The ECC composites exhibited a strain capacity of 4.4% at 28 days, with an ultimate strength of about 5 MPa.

2.2. Test Specimen Preparation and Testing. Specimens were removed from the molds at 1 day and kept in a water tank until the age of 28 days. Five specimens were tested under compression immediately after conditioning; these control specimens will be referred to as those tested after exposure to normal curing condition (unheated).

Computer controlled furnace was used for the heating of specimens with constant heating rate of about 13.3°C/min to reach the prescribed 200, 400, 600, and 800°C temperature levels. The temperature was measured in the air at a position above the specimen inside the furnace. The temperature was maintained constant for an hour to achieve the thermal steady state condition after the target temperature was reached. It was expected that because of small size of specimens used in this study, the temperature in the center of the specimen reached the target temperature during the one-hour stabilization phase. The heating regime is shown in Figure 2. After heating, the samples were subjected to two cooling regimes as given in Table 2. After cooling, the specimens were sealed for 7 days before the compressive test. The compressive test [14] was performed under displacement control at a loading rate

TABLE 2: Two cooling regimes for different curing age ECC specimens.

Temperature	Cooling in room temperature	Quenching in water
200°C	✓	None
400°C	✓	✓
600°C	✓	None
800°C	✓	✓

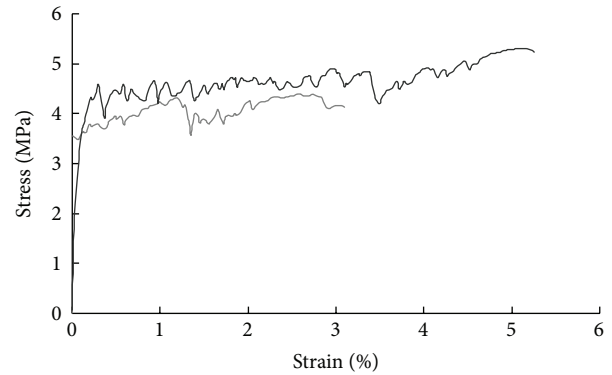


FIGURE 1: Typical tensile stress-strain response of ECC at 28 days.

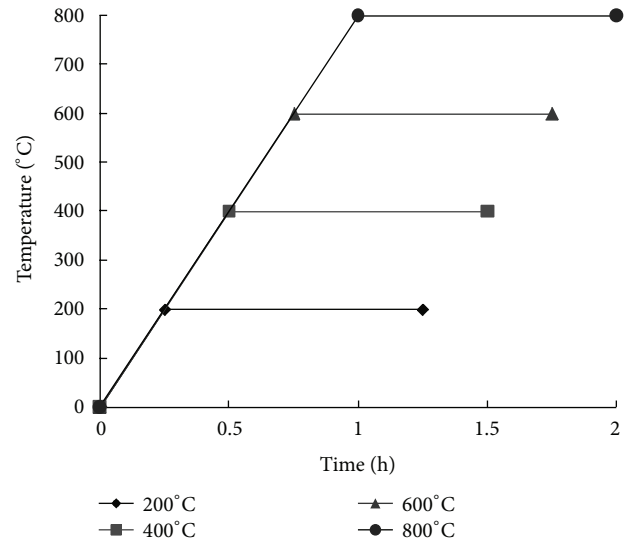


FIGURE 2: Heating regime for ECC specimens.

of 0.005 mm/s on a closed-loop controlled material testing system with 100 kN capacity. During the compressive tests, the load and the deflection values (obtained from a pair of LVDT's attached to the test set-up) were recorded on a computerized data acquisition system. Four samples were tested for each heating temperature and cooling regime.

The specimens are named as follows: temperature-cooling regime, for example, 400 A(W); here A means cooling in air and W means cooling in water for 5 minutes. The weight of each specimen was also measured before and after exposure to calculate the mass loss of fire-deteriorated specimens.

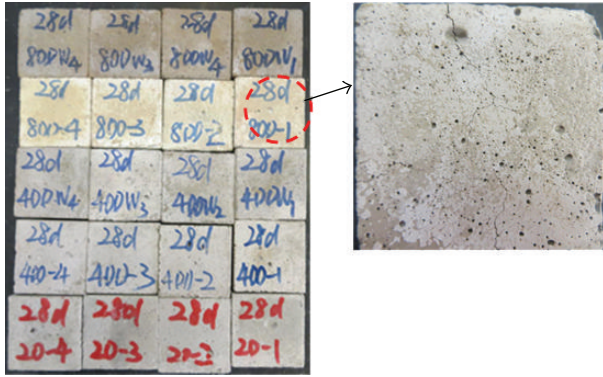


FIGURE 3: Color changes and surface cracks of postfire specimens.

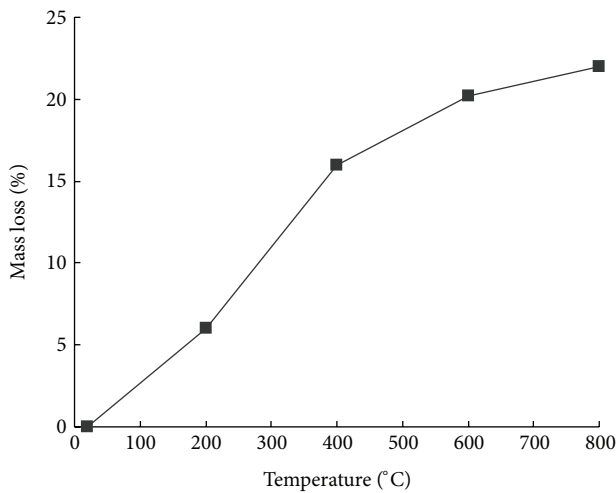


FIGURE 4: Mass loss of specimens of all curing ages with temperatures.

3. Experimental Results and Discussions

3.1. Surface and Internal Characteristics. It is observed that when the ECC specimens were exposed to high temperatures, some changes in color occurred. Figure 3 shows that the color of ECC specimens changed from gray at 20°C to light yellow at 800°C due to the loss of water and chemical decomposition. The specimens are small and we cannot write many words on them, so the specimens with “W” mean cooling in water and without “W” mean cooling in air. The color of the specimens subjected to 800°C and then quenching in water turned to dark gray which may be due to the further hydration of the composite.

Surface crack patterns of ECC specimens due to the high temperature exposure were almost the same up to 800°C. Cracks became apparent after 400°C, and hairline cracks were monitored above 400°C. Increasing the exposure temperature to 800°C increased the size of microcracking as consistent with pore structure variation of the specimens. However, quenching in the water may help to heal the surface crack due to the further hydration.

3.2. Mass Loss. The deterioration of specimens subjected to various elevated temperatures was also assessed by mass loss measurements. Figure 4 shows the relation between mass

loss $(M_0 - M_i)/M_0$ (in percentage) and temperature of heat-exposed ECC. M_i is the mass after a specific thermal heat exposure, and M_0 is initial mass, prior to heat exposure. As seen in Figure 4, the mass loss increased with the increasing temperature of thermal exposure, a result mainly associated with the liberation of free and physically bound water. At higher temperatures of 600 and 800°C, the weight change of ECC was caused by the dehydration of paste [15]. During a heat treatment up to 400°C, the weight of the melted fibers also had an influence on mass loss.

3.3. Microstructure Characterization by Using SEM Observations. The microstructure of specimens was investigated using scanning electron microscope (SEM) observation. The results of the microscopic investigations gave a good explanation of the change in macrobehavior of ECC in comparison to ECC matrix mixtures.

To study the behavior of fibers and matrix microstructure after various elevated temperatures, observations with an SEM were performed on samples taken from the core of post-fire ECC specimens that had been exposed to a temperature between 200 and 800°C for one hour. The specimens that had been quenched in the water for 5 minutes were also observed. Figure 5 shows the SEM micrographs of various postfire ECC specimens exposed to different heating temperature and cooling regimens. Figures 5(a) and 5(b) show the SEM micrographs of ECC specimens for 200 A and 400 A. The fiber did not melt when the specimens were subjected to 200°C. After exposure to 400°C, PVA fibers melt completely, creating additional interconnected pores and small channels in the matrix, and fibers alone constitute a connected net work. Therefore, the use of PVA fiber clearly affects porosity at high temperatures. After exposure to 400°C, the number and width of microcracks increase obviously compared to specimens subjected to 200°C from the SEM observation. From Figure 5(c), it can be seen that the hydration products did not decompose totally. For the specimens exposure to 800°C (Figure 5(d)), almost all hydration products appear as ill-crystallized or amorphous structures by losing the characteristic crystal structure. From Figures 5(e) and 5(f), we can see the typical crystal structure of specimens quenching in water and curing for 7 days. The produce of new crystal enhances the strength of specimens which would be discussed in the following section. Additionally, there are more new generated crystals in 800 W specimens than in 400 W specimens, which results in a more significant mechanical increase in 800 W specimens.

3.4. Residual Compressive Strength and Stress-Strain Curves. Figure 6 shows the influence of temperature on the compressive strength and stiffness of postfire ECC specimens. Relative strength, stiffness, and displacement were the ratios of the strength, stiffness, and displacement of specimens after high temperature to those of the control (unheated) specimens. Each point in Figure 6 was obtained from the average of at least four test specimens. The coefficient of variance (COV) values for the compressive strength values ranged from 2% to 9%. The narrow range of COV values is an indication of the consistent repeatability of the compressive strength test method even for fire-deteriorated specimens.

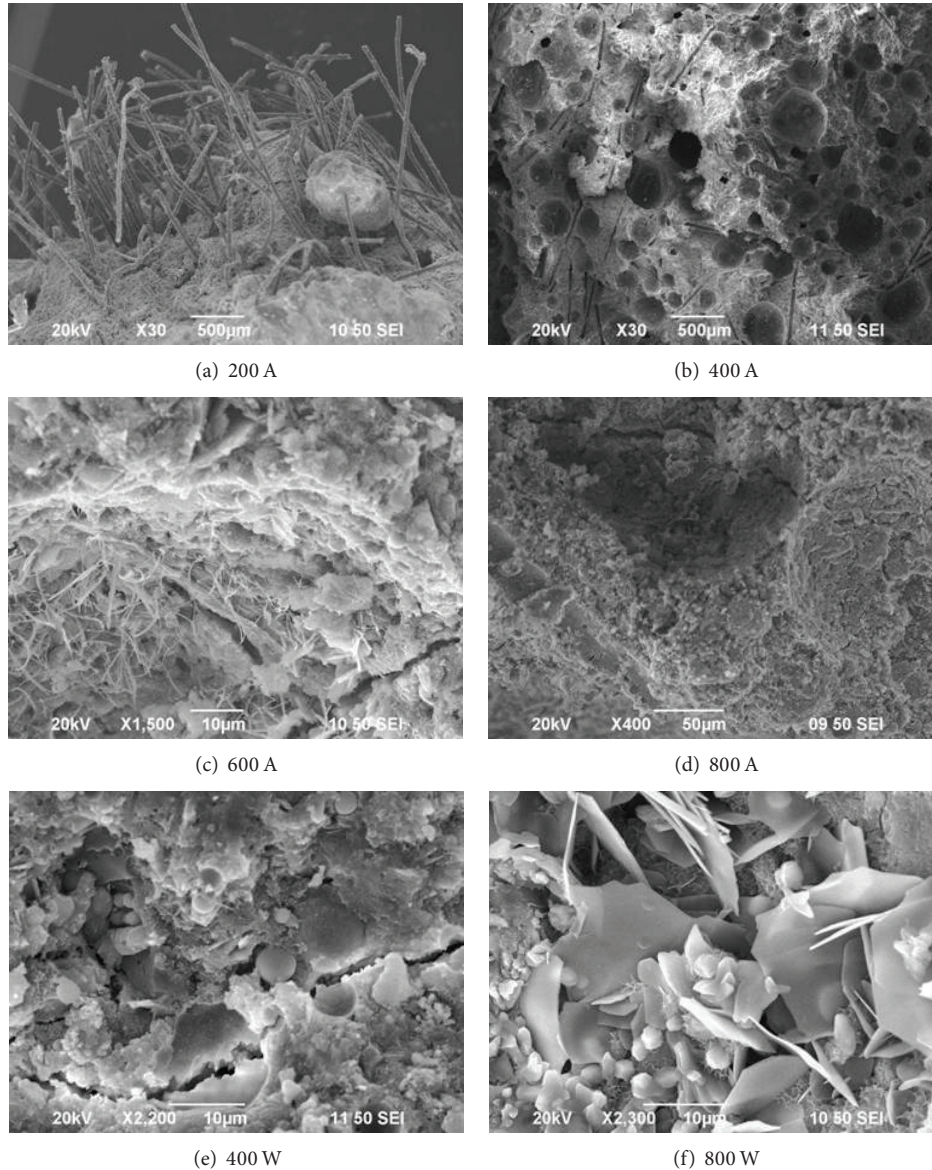


FIGURE 5: SEM micrograph of ECC specimens subjected to different heating temperatures and cooling regimes.

As seen in Figure 6 and as expected, exposure to high temperature influenced the residual compressive strength of ECC specimens substantially. However, percent variation in compressive strength can be classified in four distinct patterns of strength loss, 23–200°C, 200–400°C, 400–600°C, and 600–800°C. Temperature no more than 200°C seems to help the strength increase. Mean compressive strength of 28-day ECC specimens increases by 1% after exposure to 200°C. The influence of high temperature exposure on the residual compressive strength is not prominent up to 400°C with the mean compressive strength decreased by 32% after exposure to 400°C. This might be due to the less sensitivity of compressive strength to minor microcracks. Heating up to 400°C generated a relatively small amount of cracking, which did not cause any immediate loss of carrying capacity in compression because the slightly cracked concrete could work as a highly redundant structure [12]. Beyond 400°C,

however, compressive strength dropped drastically by 62% and 77% at 600°C and 800°C, respectively. According to the variation of the residual compressive strength, temperature of 600°C and above might be regarded as critical temperature range for the strength loss of ECC. The present test results are in line with the findings of previous studies [9, 10].

Residual compressive strength variations are consistent with the pore structure variations in previous studies [16, 17]. The total intruded porosity and percent of pore size between 50 nm and 500 nm increased slightly with the increase in temperature up to 400°C. The increase in porosity up to 400°C is most likely due to the small channels created in ECC by melting PVA fibers with the diameter of 39 μm. However, after exposure to 600°C, the main causes of deterioration in compressive strength might be attributed both to the physical transformation of the matrix and to chemical transformation of hydration products. When the temperature was raised

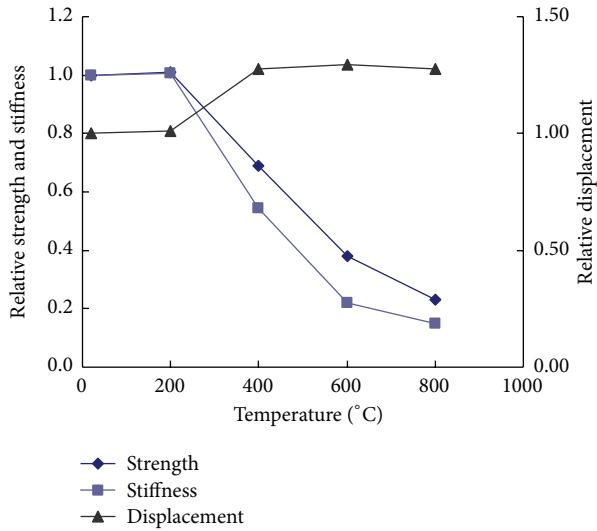


FIGURE 6: Compressive strength, stiffness, and displacement corresponding to peak load with temperatures.

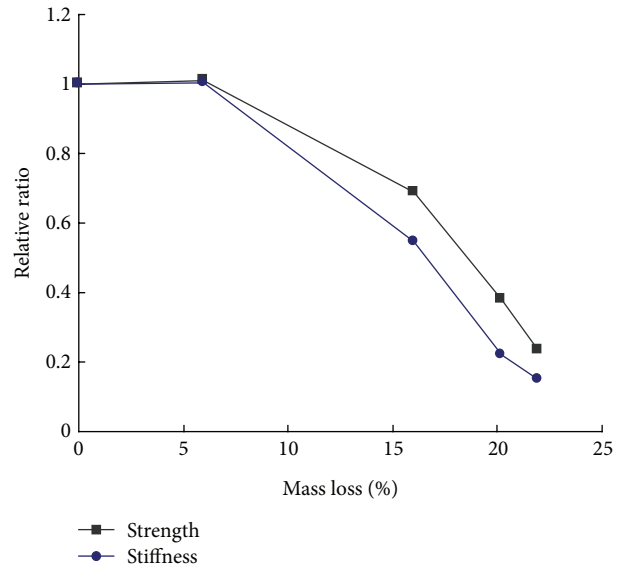


FIGURE 8: Relationship of strength and stiffness to mass loss.

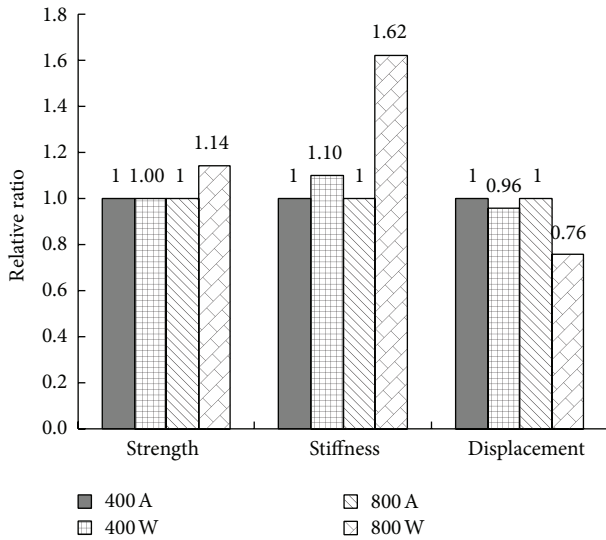


FIGURE 7: Influence of cooling regimes on compressive strength, stiffness, and displacement corresponding to peak load.

to 600°C, decomposition of the major hydrate, known as tobermorite (gel), was inevitable [18], causing severe increase in the microstructure of its matrix and the loss of binder property.

From Figure 6, it can be seen that the stiffness of postfire specimens shares a similar but more sensitive tendency [19, 20] with exposure temperatures, which also could be classified into four stages. The mean compressive stiffness of ECC specimens increased by 0.5% after exposure to 200°C, while it decreased by 46%, 78%, and 85% after exposure to 400, 600, and 800°C.

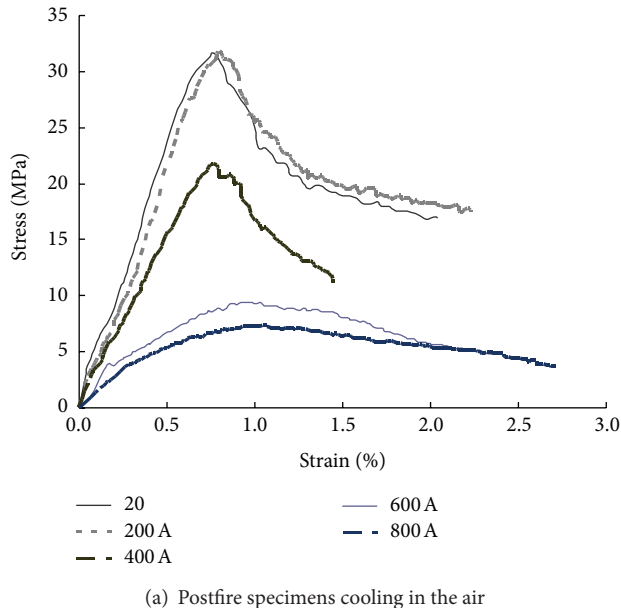
Figure 7 shows the influence of cooling regimes on the residual mechanical properties. Relative strength, stiffness, and displacement were the ratios of the strength, stiffness, and displacement of specimens cooling in water to those of the specimens cooling in air. For the specimens subjected

to heating temperature of 400°C, the compressive strength and stiffness of specimens quenching in water increased by 0.5% and 14% compared to the ones cooling in air, while, for 800°C, the compressive strength and stiffness of specimens quenching in water were 1.10 and 1.62 times to the ones cooling in air. As mentioned in Section 3.3, there are more new generated crystals in 800 W specimens than in 400 W specimens, which results in a more significant mechanical increase in 800 W specimens. The result again shows that the stiffness is more sensitive than strength to microcracks, which could also be seen from the result of Figure 8. The meaning of relative ratio is the same with that in Figure 6. Meanwhile, the displacement corresponding to the peak load of 400 W and 800 W decreased by 4% and 24% compared to the specimens cooling in air.

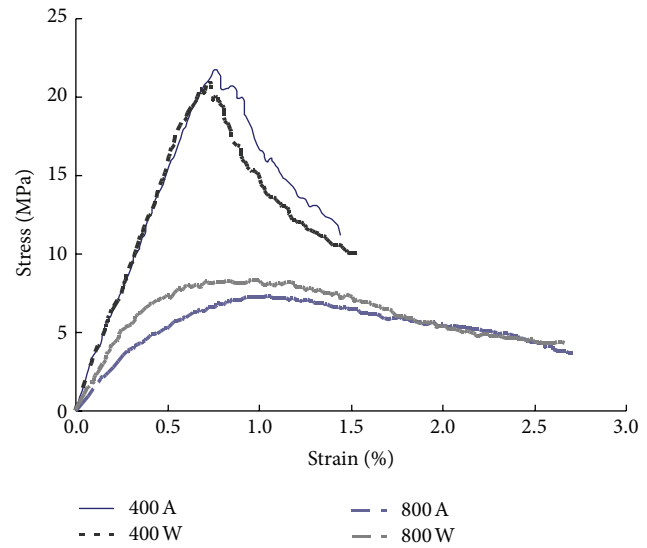
The stress-strain curves of ECC specimens at room temperature and elevated temperatures are compared in Figure 9. Ultimate stress decreased with the increasing temperature, particularly for temperatures exceeding 400°C, while the strain corresponding to the peak strength increased with temperature. The slope decreased with the increase in exposure temperature up to 800°C, indicating a reduction in the stiffness of the ECC. The reduction in ECC stiffness was relatively low up to 400°C; however, beyond 400°C, a dramatic reduction was monitored in the ECC stiffness. As expected, with the increase in exposure temperature, the postpeak stress of the ECC specimens dropped faster, resulting in a smaller postpeak area under the curve. This behavior becomes more evident when the exposure temperature level reaches 800°C: ECC specimens failed soon after reaching their peak strength. This means that increasing the exposed temperature level tends the ductile nature of ECC to brittle nature.

4. Conclusions

The influence of cooling regimes on the mechanical properties of ECC specimens subjected to elevated temperatures was



(a) Postfire specimens cooling in the air



(b) Stress-strain curve of specimens subjected to different cooling regimes

FIGURE 9: Stress-strain curves of ECC specimens for different curing ages.

investigated in this paper and the following conclusions can be drawn.

- (1) The color of ECC specimens changed from gray at 20°C to light yellow at 800°C; the specimens quenching in water turned to dark grey. Hairline cracks were monitored above 400°C and quenching in the water helps to heal the surface crack. The mass loss increased with the increasing temperature of thermal exposure.
- (2) The compressive strength can be classified into four distinct patterns of strength loss: 23–200°C, 200–400°C, 400–600°C, and 600–800°C. From 23 to 200°C, the compressive strength of specimens increases with temperature. The influence of high temperature exposure on the residual compressive strength is not prominent up to 400°C. Beyond 600°C, ECC specimens showed severe deterioration.
- (3) The cooling regime of quenching in water helped the strength and stiffness recovery. Ultimate stress decreases with the increasing temperature, while the strain corresponding to the peak strength increases with temperature. High temperature causes a reduction in the stiffness of ECC. Increasing the exposed temperature level tends the ductile nature of ECC to brittle nature.

Conflict of Interests

The authors declare that there is no conflict of interests regarding the publication of this paper.

Acknowledgment

The authors gratefully acknowledge the financial assistance of the National Science Foundation of China (51378397).

References

- [1] V. C. Li, "ECC—tailored composites through micromechanical modeling," in *Proceedings of the Fiber Reinforced Concrete: Present and the Future Conference*, N. Banthia, Ed., pp. 64–97, CSCE Press, 1998.
- [2] V. C. Li, "On engineered cementitious composites (ECC) A review of the material and its applications," *Journal of Advanced Concrete Technology*, vol. 1, no. 3, pp. 215–230, 2003.
- [3] M. Şahmaran and V. C. Li, "De-icing salt scaling resistance of mechanically loaded engineered cementitious composites," *Cement and Concrete Research*, vol. 37, no. 7, pp. 1035–1046, 2007.
- [4] M. Sahmaran, M. Li, and V. C. Li, "Transport properties of engineered cementitious composites under chloride exposure," *ACI Materials Journal*, vol. 104, no. 6, pp. 604–611, 2007.
- [5] X. Luo, W. Sun, and S. Y. N. Chan, "Effect of heating and cooling regimes on residual strength and microstructure of normal strength and high-performance concrete," *Cement and Concrete Research*, vol. 30, no. 3, pp. 379–383, 2000.
- [6] G. F. Peng, S. H. Bian, Z. Q. Guo, J. Zhao, X. Peng, and Y. Jiang, "Effect of thermal shock due to rapid cooling on residual mechanical properties of fiber concrete exposed to high temperatures," *Construction and Building Materials*, vol. 22, no. 5, pp. 948–955, 2008.
- [7] O. Gencel, "Effect of elevated temperatures on mechanical properties of high-strength concrete containing varying proportions of hematite," *Fire and Materials*, vol. 36, no. 3, pp. 217–230, 2012.
- [8] F. Koksall, O. Gencel, W. Brostow, and H. E. Hagg Lobland, "Effect of high temperature on mechanical and physical properties of lightweight cement based refractory including expanded

- vermiculite,” *Materials Research Innovations*, vol. 16, no. 1, pp. 7–13, 2012.
- [9] M. Sahmaran, M. Lachemi, and V. C. Li, “Assessing mechanical properties and microstructure of fire-damaged engineered cementitious composites,” *ACI Materials Journal*, vol. 107, no. 3, pp. 297–304, 2010.
- [10] M. Şahmaran, E. Özbay, H. E. Yücel, M. Lachemi, and V. C. Li, “Effect of fly ash and PVA fiber on microstructural damage and residual properties of engineered cementitious composites exposed to high temperatures,” *Journal of Materials in Civil Engineering*, vol. 23, no. 12, pp. 1735–1745, 2011.
- [11] V. C. Li, C. Wu, S. Wang, A. Ogawa, and T. Saito, “Interface tailoring for strain-hardening polyvinyl alcohol-engineered cementitious composite (PVA-ECC),” *ACI Materials Journal*, vol. 99, no. 5, pp. 463–472, 2002.
- [12] T. T. C. Hsu, F. O. Slate, G. M. Sturman, and G. Winter, “Microcracking of plain concrete and the shape of the stress-strain curve,” *ACI Mater*, vol. 60, no. 2, pp. 209–224, 1963.
- [13] Japan Society of Civil Engineers, *Recommendations for Design and Construction of High Performance Fiber Reinforced Cement Composite with Multiple Fine Cracks*, (Japanese).
- [14] ASTM C109/C109M-12, “Standard test method for compressive strength of hydraulic cement mortars (using 2-in. or [50-mm] cube specimens)”.
- [15] H. F. W. Taylor, *The Chemistry of Cements*, Academic Press, London, UK, 1964.
- [16] T. K. Erdem, “Specimen size effect on the residual properties of engineered cementitious composites subjected to high temperatures,” *Cement and Concrete Composites*, vol. 45, pp. 1–8, 2014.
- [17] Y. N. Chan, X. Luo, and W. Sun, “Compressive strength and pore structure of high-performance concrete after exposure to high temperature up to 800°C,” *Cement and Concrete Research*, vol. 30, no. 2, pp. 247–251, 2000.
- [18] G. A. Khoury, B. N. Grainger, and P. J. E. Sullivan, “Transient thermal strain of concrete: literature review, conditions within specimen and behavior of individual constituents,” *Magazine of Concrete Research*, vol. 37, no. 132, pp. 131–144, 1985.
- [19] Y. Xu, Y. L. Wong, C. S. Poon, and M. Anson, “Influence of PFA on cracking of concrete and cement paste after exposure to high temperatures,” *Cement and Concrete Research*, vol. 33, no. 12, pp. 2009–2016, 2003.
- [20] B. Wu, X. Su, H. Li, and J. Yuan, “Effect of high temperature on residual mechanical properties of confined and unconfined high-strength concrete,” *ACI Materials Journal*, vol. 99, no. 4, pp. 399–407, 2002.

Research Article

Application of Interfacial Propagation and Kinking Crack Concept to ECC/Concrete Overlay Repair System

Yaw ChiaHwan and Li Wei

Shenyang Architecture and Building University, Hunnan East Road No. 9, Shenyang 110168, China

Correspondence should be addressed to Yaw ChiaHwan; 826125581@qq.com

Received 1 January 2014; Revised 19 May 2014; Accepted 21 May 2014; Published 23 June 2014

Academic Editor: Juan José del Coz Díaz

Copyright © 2014 Y. ChiaHwan and L. Wei. This is an open access article distributed under the Creative Commons Attribution License, which permits unrestricted use, distribution, and reproduction in any medium, provided the original work is properly cited.

Research on the application of ultraductile engineered cementitious composite (ECC) as overlay in the repair of deteriorated concrete structures is performed in this paper. Also, interfacial crack kinking and trapping mechanism experimentally observed in ECC/concrete overlay repair system are described by comparison of toughness and energy release rate. The mechanism involves cycles of extension, kinking, and arrest of interfacial crack into the overlay. Experimental testing of overlay repair system reveals significant improvements in load carrying capacity and ductility over conventional concrete overlay. The commonly observed overlay system failure mode of delamination or spalling is eliminated when ECC is applied. These failure modes are suppressed when ECC is used as an ideal and durable candidate overlay repair material.

1. Introduction

A large number of existing concrete structures worldwide, including previously repaired ones, suffer from deterioration or distress under combined mechanical and environmental loading conditions. These structures are in urgent need of repair. Therefore, it is of research significance and challenge to develop effective and durable repairs, which can fundamentally solve the underlying concrete deterioration problems and protect the old concrete from aggressive environments on the long run.

Concrete repair failure results from a combination of physical, chemical, and mechanical processes. Generally, it is due to repair surface cracking or interface delamination between the overlay and the substrate which are causes of many repair durability problems. Bonded interface between two dissimilar materials is often separated by crack. At certain instance, crack kinks out of the interface and will advance in one of the two materials. It is pointed out in [1, 2] that questions, such as whether the crack lies on interface or advances along the interface or would kink out of the interface, are important in the design of the interface between overlay and substrate.

By utilization of analytical solutions and experiments, the present research investigates the performance of ECC as a repair material to improve durability of concrete structures. It is stated [3] that engineered cementitious composite (ECC) is a fiber reinforced cement based composite micromechanically tailored to exhibit metal-like tensile response with ultra-high tensile strain capacity of 3–5%, which is about 300 to 500 times the tensile strain capacity of normal concrete and FRC (Figure 1). The superiority of ECC has been brought about by the micromechanics approach and the development in fiber, matrix, interface, and composites processing technology. As demonstrated [4, 5], micromechanics relates macroscopic properties to the microstructure of a composite and forms the backbone of material design theory. Especially, it allows systematic microstructure tailoring of ECC as well as material optimization which can lead to extreme composite ductility.

It is reported by Forbes [6] self-healing phenomenon of PVA (polyvinyl alcohol) ECC which is commented as a novel composite to bring revolution to civil engineering. Although failure mode of small scale connections and frames of PVA ECC is analyzed [7], the tremendous cost has limited its application. The cost of PVA ECC is around 5 times that of ECC using PP (polypropylene) fibers. Therefore, it

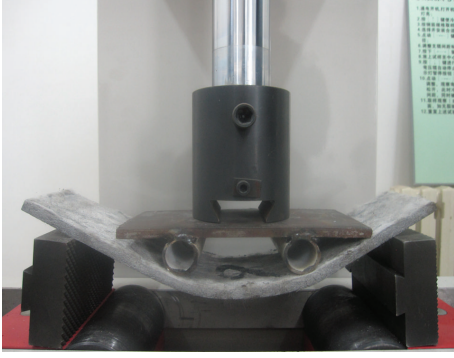


FIGURE 1: Four-point bending test of plain PP ECC.

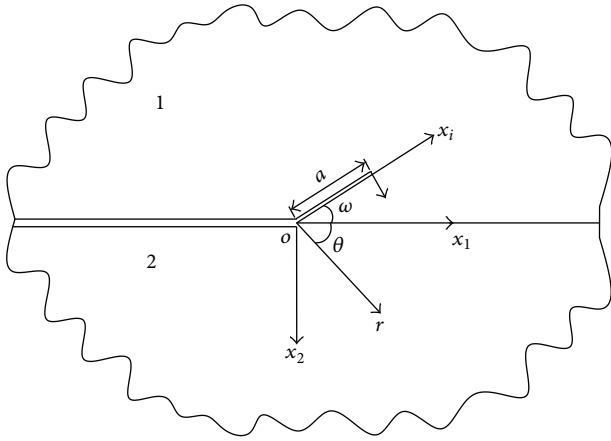


FIGURE 2: Geometry of a crack propagating along and kinking out of the interface.

is necessary to utilize cheap polypropylene fibers to produce ECC with extraordinary properties.

In this paper, findings from experimental and analytical studies carried out on layered repair systems under different surface preparations are reported. For either interpretation of trapping in interface or in the ECC, improvement in mechanical performance is unequivocally demonstrated to exist in the concrete/ECC bimaterial system. The durability of repaired concrete structure using ECC as a repair material is demonstrated in several practical road works.

1.1. Problem Formulation of Propagation and Kinking of Interfacial Crack. For the problem of crack propagating and kinking out of an interface (Figure 2), the two different semi-infinite isotropic elastic materials (overlay as 1 and substrate as 2) are bonded along the positive part of the x_1 -axis. The main crack lies on the interface and a straight crack segment of length a and inclination angle ω kinks into material 2.

In overlay repair applications, tensile stress is developed in the repair layer, and a combination of tensile and shear stresses is built up along the interface between the repair and the concrete substrate. Tensile stress at repair/substrate interface is the x_2 direction stress that opens the interface, which delaminates the interface in the x_2 direction. Shear stress at repair/substrate interface is the x_1 direction stress

that causes the repair layer to slide along the surface of the substrate, which delaminates the interface in x direction. These stresses can cause repair surface cracking and/or interface delamination. Crack width and delamination magnitude determine the transport properties through this repair system; therefore, they are closely related to repair durability.

The overlay material toughness and interface toughness are Γ_c and Γ_{ic} , respectively. Fracture along the interface is more likely to occur than damage of the overlay material if

$$\frac{\Gamma_c}{\Gamma_{ic}} > \frac{G_0}{G_i}, \quad (1)$$

where G_0 and G_i are energy release rates of kinking crack and interface crack, respectively. The stress intensity factors K_I and K_{II} for the kinked crack and K_1 and K_2 for the interfacial crack are dependent on the kinking angle ω and material moduli. The stress field prior to kinking ($a \rightarrow 0$) is the singularity field of an interface crack characterized by a complex stress intensity factor:

$$K = K_1 + iK_2. \quad (2)$$

1.2. Problem of Interfacial Crack Propagating along the Surface of Bimaterial. The near tip stress field for the specific problem of crack lying along dissimilar isotropic bimaterial interface is a linear combination of two types of fields. The first is coupled oscillatory field defined by K as shown in (2), while the second is nonoscillatory field scaled by a real mode stress intensity factor K_3 :

$$\sigma_{ij} = \frac{1}{\sqrt{2\pi r}} \left[\operatorname{Re}(Kr^{i\epsilon}) \sum_{ij}^1(\theta, \epsilon) + \operatorname{Im}(Kr^{i\epsilon}) \sum_{ij}^2(\theta, \epsilon) + K_3 \sum_{ij}^3(\theta) \right], \quad (3)$$

where r and θ are polar coordinates and indices i, j refer to coordinates x_1, x_2 , and x_3 , respectively.

$\sum_{ij}^{1,2,3}(\theta)$ are the angular functions corresponding to tensile stress, in-plane shear stress, and antiplane shear stress across the interface, respectively [8].

The parameter ϵ called the bielastic constant or the oscillatory index is given by

$$\epsilon = \frac{1}{2\pi} \ln \left(\frac{1-\beta}{1+\beta} \right). \quad (4)$$

The Dundurs parameters are defined, respectively, as

$$\alpha = \frac{\mu_2(\kappa_1 + 1) - \mu_1(\kappa_2 + 1)}{\mu_2(\kappa_1 + 1) + \mu_1(\kappa_2 + 1)}, \quad (5)$$

$$\beta = \frac{\mu_2(\kappa_1 - 1) - \mu_1(\kappa_2 - 1)}{\mu_2(\kappa_1 + 1) + \mu_1(\kappa_2 + 1)}.$$

Both α and β vanish when the materials are identical. μ_i and ν_i are shear modulus and Poisson's ratio, respectively; $\kappa_i = 3 - 4\nu_i$ for plane strain and $\kappa_i = (3 - \nu_i)/(1 + \nu_i)$ for plane stress.

TABLE 1: Property of concrete base and repair material.

Material	Elastic modulus E (Gpa)	Shear modulus μ (Gpa)	Poission's ratio	α	β	Γ_c [N/mm]
Concrete base	25.8	10.75	0.2	0	0	0.09
Concrete overlay	24.9	9.96	0.25	-0.006	0.019	0.09
PVA ECC	21.3	8.24	0.27	-0.012	0.013	1.587
PP ECC	18.0	6.82	0.32	-0.028	0.009	1.164

Subscripts 1 and 2 refer to materials 1 and 2, respectively. The complex stresses at distance r ahead of the crack tip take the following form:

$$\begin{aligned} (\sigma_{22} + i\sigma_{12})_{\theta=0} &= \frac{K_I r^{i\epsilon}}{\sqrt{2\pi r}}, \\ (\sigma_{23})_{\theta=0} &= \frac{K_3}{\sqrt{2\pi r}}. \end{aligned} \quad (6)$$

It is clear that $\Sigma_{ij}^{1,2,3}(\theta)$ correspond to modes 1, 2, and 3 of crack growth. When all three modes are present, the mode mixity is fully specified by two solid angles Ψ and ϕ in (K_1, K_2, K_3) space:

$$tg\Psi = \frac{K_2}{K_1}, \quad \cos\phi = \frac{K_3}{\sqrt{K_1^2 + K_2^2 + K_3^2}}, \quad (7)$$

where Ψ is called the phase angle of the complex stress intensity factor or the phase angle of the applied load. It is dependent on applied load, ratio of elastic moduli, and characteristic dimensions of the cracked body.

The complex stress intensity factor for the interfacial crack of the bimaterial is

$$K = K_1 + iK_2. \quad (8)$$

Therefore, it follows that the stress intensity factors are, respectively,

$$K_1 = \text{Re}(Kh^{i\epsilon}), \quad (9a)$$

$$K_2 = \text{Im}(Kh^{i\epsilon}). \quad (9b)$$

For the special case that $\beta = 0$ and $\epsilon = 0$, K_1 and K_2 measure the normal and shear component of the traction singularity acting on the interface.

The stress field on the straight line ($x'_1 > 0$, $x'_2 = 0$) ahead of the kinked crack tip is characterized by combination of the standard mode I and mode II stress intensity factors K_I and K_{II} :

$$\sigma_{2'2'} + i\sigma_{1'2'} = (K_I + iK_{II}) (2\pi r')^{-1/2}, \quad (10)$$

where $x'_1 x'_2$ is the coordinate system centered at the tip of the kinked crack.

The stress intensity factors of the kinked crack K_I and K_{II} have dimensions of stress (length)^{1/2}. The relationship

between them and the prescribed complex stress intensity factor K can be written as

$$K_I + iK_{II} = c(\omega) K a^{i\epsilon} + \bar{d}(\omega) \bar{K} a^{-i\epsilon}, \quad (11)$$

where $\bar{()}$ denotes complex conjugation. All information for crack kinking out of an interface can be derived from $c(\omega)$ and $d(\omega)$:

$$\begin{aligned} c(\omega) &= \frac{1}{2} \sqrt{\frac{1-\beta}{1+\alpha}} \left(e^{-i\omega/2} + e^{-3i\omega/2} \right), \\ d(\omega) &= \frac{1}{4} \sqrt{\frac{1-\beta}{1-\alpha}} \left(e^{-i\omega/2} - e^{-3i\omega/2} \right). \end{aligned} \quad (12)$$

Since the crack has been taken to kink upward, the loading combinations which result in an opening at both the interfacial and kinking crack tip generally require $K_I > 0$ and $\Psi \geq 0$.

The relationship between the energy release rate G_i of the interfacial crack and complex interface stress intensity factor $K = K_1 + iK_2$ is

$$G_i = \left(\frac{\kappa_1 + 1}{\mu_1} + \frac{\kappa_2 + 1}{\mu_2} \right) \frac{K\bar{K}}{16ch^2(\epsilon\pi)}. \quad (13)$$

The energy release rate G_0 of the kinked crack ($a > 0$) is given by

$$G_0 = \frac{\kappa_2 + 1}{8\mu_2} (K_I^2 + K_{II}^2). \quad (14)$$

Using (13), one obtains

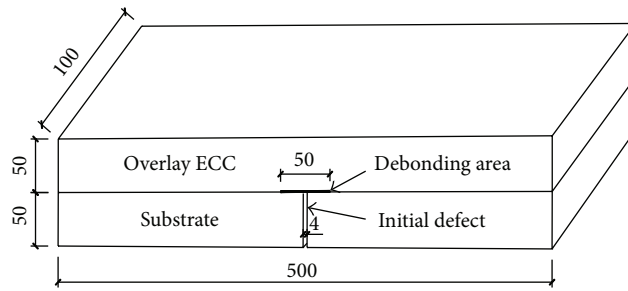
$$G_0 = \frac{\kappa_2 + 1}{8\mu_2} \left[|c|^2 + |d|^2 K\bar{K} + 2\text{Re}(cdK^2 a^{2i\epsilon}) \right]. \quad (15)$$

2. Trapping Mechanism Experiment Verification of the Overlay System

Besides the PVA and PP ECC/concrete bimaterial system, one additional concrete/concrete system was tested as coupon specimen. All involve base concrete as Material 2, while the overlay systems have concrete, PVA, or PP ECC as Material 1. The concrete (Material 2) was five weeks old when the other material (Material 1) was cast on it. The bimaterial system had two weeks curing before testing. The material compositions and Dundar's elastic mismatch parameters are tabulated in Table 1. The difference of elastic modulus between base

TABLE 2: The property of four interfaces with different preparation methods.

Specimen number	Repair material	Surface preparation	τ_{xy} (Mpa)	Γ_{ic} [N/mm]
1	Concrete	Coupon untouched	0.776	0.0772
2	PVA ECC	Coupon untouched	2.287	1.002
3	PP ECC	Sandblast and moisture	1.138	0.881
4	PP ECC	Sandblast and scrape	2.238	0.507



(a)



(b)

FIGURE 3: Test setup.

concrete (Material 1) and concrete for Material 2 is due to differences in their age of curing.

The specimen includes an initial defect of length 50 mm in the form of an interfacial crack between the base material and the repair Material 1 as well as a joint in the base material. The four-point bending setup is illustrated in Figure 3 and loading speed is 0.3 mm/min.

Different surface roughening strategies together with a coupon untouched surface were investigated and shown in Table 2. The necessity of having various surface preparation methods is to obtain different bond strengths which are suitable for various requirements of applications.

The different substrate surface roughening techniques exploited during tests are as follows.

- (1) Coupon surface is created by the substrate surface as cast against the mould. In fact, it is a mechanically untouched surface for reference purposes.
- (2) Sandblast and moisture surface is a roughening of the substrate surface with sandblasting until the coarse aggregate is exposed to about one millimeter clearance. Later, water is put on the surface to make it moist.
- (3) Sandblast and scrape surface is a roughening of the substrate surface with sandblasting and then a sharp edged scraping plate is used to scrape the thin, weaker outer layer of the substrate surface and expose the tougher inner material to increase roughness on a micro level. Both the chemical adhesion and

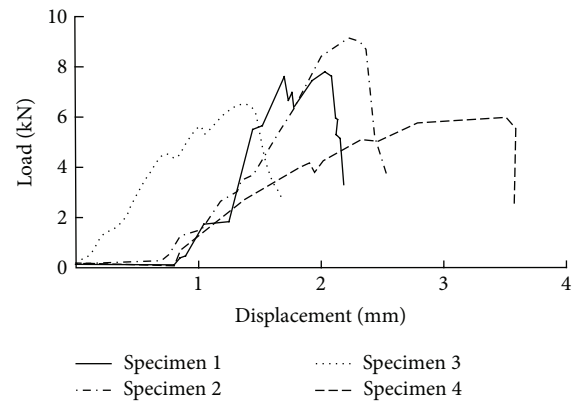


FIGURE 4: Load-deflection curve of four repair overlay specimen: (a) Specimen 1, (b) Specimen 2, (c) Specimen 3, and (d) Specimen 4.

mechanical interlocking between the two materials on a mesoscale are enhanced. The ratio of toughness Γ_c/Γ_{ic} can be measured while the overlay repair system is loaded.

2.1. Experimental Result and Analysis. The load-deflection curve of the four specimens is shown in Figure 4 to compare the effect of different repair material and surface preparation method on the ultimate bearing capacity of the overlay system. It is obvious that the ultimate bearing capacity of Specimen 1 is maximum and reached 9.1325 kN. The

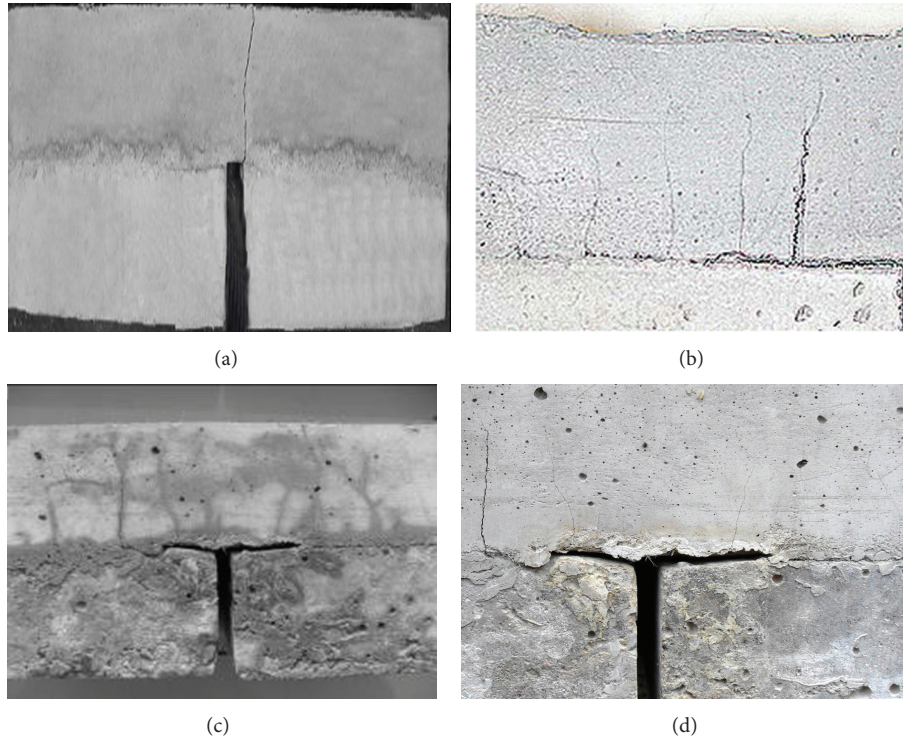


FIGURE 5: Damage pattern of concrete and ECC repair overlay system. (a) Concrete overlay system, (b) PVA ECC, (c) PP ECC sandblast and moisture, and (d) PP ECC sandblast and scrape.

ultimate bearing capacity of PVA ECC repair overlay system is 7.7935 kN. It is shown that the larger the elastic modulus of the repair system, the larger the ultimate bearing capacity. Although the elastic modulus and shear modulus of PP ECC are smaller, the deflection of PP ECC reached 3.3824 mm and 1.3556 mm, respectively.

As expected, the concrete/ECC bimaterial system shows the distinctive trapping mechanism under this experimental condition. The failure process with trapping mechanism shows tremendous differences compared with those of the control specimens (Figure 5). In Figure 5(a), the concrete/concrete overlay system damaged without obvious deflection and only one macrocrack with large width occurred.

The brittle feature is demonstrated by large crack opening displacement of the kinking crack. The concrete/ECC system shows macroscopic strain-hardening response. The concept of interface crack trapping mechanism is introduced, and its existence is confirmed in experimental investigations. In the concrete/ECC system, the initial interface crack propagated along the interface by about 5 mm, followed by kinking out from the interface. Subsequently, the kinked crack appeared trapped inside the ECC and the mother crack (interface crack) propagated along the interface again (about 27 mm). Then, the interface crack kinked and was trapped again. After several times of cracking and kinking, the final failure occurred due to the large opening of a flexural crack in the middle of the specimen. In the PVA ECC overlay system (Figure 5(b)), the angle of kinking crack is around 90° . In

the PP ECC overlay system with sandblast and moisture surface (Figure 5(c)), many kinking microcracks emerged around the interface crack and the phase angle is at the range of 45° – 90° . While the kinking crack number is less for the PP ECC overlay system with sandblast and scrape surface (Figure 5(d)), it is obvious that the overlay system did not absorb much energy during the damaged process. It can be stated that PP ECC with super toughness and ductility can make the overlay system possess more load bearing capacity and durability than common concrete repair overlay. This dramatic improvement in terms of strength, deflection, energy absorption capacity, and ultimate failure mode is not feasible without the trapping mechanism.

2.2. Analysis of Trapping Mechanism. While the phase angle Ψ is small, the value of Γ_c is also not big. Under this status, the interfacial crack does not kink easily and vice versa. For the experiment performed in this paper, the value of Ψ for the different specimen is 54.2, 28.9, 32.7, and 43.8. In Figure 6, the relationship between G_0/G_i and kinking angle for the specimen is illustrated.

3. Conclusions

By utilization of analytical solutions and experiments, the present research investigates the performance of ECC as a repair material to improve durability of concrete structures. The condition of whether the crack is going to propagate into

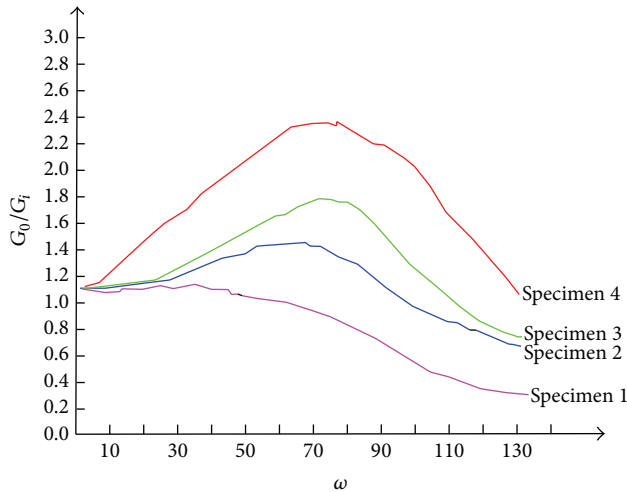


FIGURE 6: Relationship between G_0/G_i and kinking angle ω .

the substrate or into the upper overlay material is defined. Values of the energy release rate, the stress intensity factor, and mode mixity parameter are determined in terms of dimensionless factor-kinking angle ω , which is a function of geometry and materials elastic properties. The results for the kinked crack can be used to assess whether an interface crack will propagate in the interface or whether it will kink out of the interface. Findings from experimental and analytical studies carried out on layered repair systems under different surface preparations are reported. For interpretation of trapping either in interface or in the ECC, improvement in mechanical performance is unequivocally demonstrated to exist in the concrete/ECC bimaterial system.

Conflict of Interests

The authors declare that there is no conflict of interests regarding the publication of this paper.

References

- [1] H. Stander, *Interfacial Bond Properties for ECC Overlay System [M.S. thesis]*, University of Stellenbosch, 2007.
- [2] T. Nishioka, Z.-D. Zhou, and J.-H. Yu, "Analysis of in-plane transonically propagating interface crack with a finite contact zone," *International Journal of Fracture*, vol. 142, no. 3-4, pp. 241-254, 2006.
- [3] J. H. Yu, *Properties and Applications of Engineered Cementitious Composites*, China Construction Publication House, Beijing, China, 2010.
- [4] E. H. Yang, *Designing added functions in engineered cementitious composites [Ph.D. thesis]*, University of Michigan, 2008.
- [5] T. Kamada and V. C. Li, "Effects of surface preparation on the fracture behavior of ECC/concrete repair system," *Cement and Concrete Composites*, vol. 22, no. 6, pp. 423-431, 2000.
- [6] A. V. Broek, "Self-healing concrete," *Forbes*, vol. 184, no. 8, pp. 46-48, 2009.
- [7] G. Fischer and V. C. Li, "Effect of matrix ductility on deformation behavior of steel Reinforced ECC flexural members under

reversed cyclic loading conditions," *ACI Structural Journal*, vol. 99, no. 6, pp. 781-790, 2002.

- [8] Z. Suo and J. W. Hutchinson, "Interface crack between two elastic layers," *International Journal of Fracture*, vol. 43, no. 1, pp. 1-18, 1990.

Research Article

Multiscale Analysis of the Interfacial Mechanical Behavior for Composite of Carbon Nanotube and α -Alumina

Tingting Yan and Gaofeng Wei

School of Mechanical and Automotive Engineering, Qilu University of Technology, Jinan 250353, China

Correspondence should be addressed to Gaofeng Wei; weigaofeng@126.com

Received 4 December 2013; Accepted 10 April 2014; Published 16 June 2014

Academic Editor: Gonzalo Martínez-Barrera

Copyright © 2014 T. Yan and G. Wei. This is an open access article distributed under the Creative Commons Attribution License, which permits unrestricted use, distribution, and reproduction in any medium, provided the original work is properly cited.

Based on multiscale methods the mechanical behavior for the interface of carbon nanotube and α -alumina is analyzed. The stress transfer between nanotube and alumina is provided by van der Waals interaction. Using cohesive law the relationship between normal stress (shear stress) and displacement is studied, as well as the stress intensity. The stress distribution of the interface is obtained by improved COX model. The strain rate of nanotube-composite is presented when the interfacial slip occurs through the van der Waals interaction.

1. Introduction

The main goal of computational materials science is the rapid and accurate prediction of properties of new materials before their development and production. In order to develop new materials and composites with designed new properties, it is essential that these properties can be predicted before preparation, processing, and characterization.

In recent years, a new field in the improvement of ceramic brittle has been opened up by using short fiber as the reinforcement, and there are more and more experiments and theoretical research publishing the toughening effect by using carbon nanotube (CNTs) as the ceramic reinforcement [1–4]. However, carbon nanotubes do not bond well to ceramic, and their interactions are due to van der Waals force, which is much weaker than covalent bonds. This leads to sliding of CNTs in the ceramic-matrix when subjected to loading.

Nanocomposites possess a large amount of interfaces due to the small size of reinforcements. The interface behavior can significantly affect the mechanical properties of nanocomposites. Chowdhury and Okabe [5] studied the mechanical behavior of the interface of CNTs and polymer by using molecular dynamics method that there are chemical cross-links in it. Chen et al. [6] analyzed the failure mode and designed optimal toughness of carbon nanotube-reinforced composites when there is chemical bond in the interface.

Liu et al. [7] used the pull-out model which, based on both van der Waals and electrostatic interaction, numerically studied the interfacial mechanical behavior of CNTs and alumina, but this method is limited to temporal and spatial scales and can only be used to solve the fraction of the interfacial mechanical behavior.

Both Jiang et al. [8, 9] and Lu et al. [10, 11] established the nonlinear cohesive law for the CNT/polymer interfaces directly from the Lennard-Jones potential for van der Waals interactions. Chen et al. [12] used COX model to analyse the interfacial characteristics of CNTs reinforced aluminum oxide nanocomposites. Xiao and Zhang [13] analyzed the stress transfer efficiency of a single-walled carbon nanotube in epoxy matrix and manifested that a smaller tube diameter has a more effective reinforcement and there exists an optimal tube length at which reinforcement is maximized, and there is a greater stress transfer efficiency compared with solid fiber.

In this paper, a micromechanics model is provided to predict the interfacial behavior of multiwall carbon nanotubes (MWCNTs) and the crystal lattice structure of α -alumina since MWCNTs are widely used as reinforcements in nanocomposites. The van der Waals interactions between a carbon atom and a α -AlO₂ unit are given, as well as between a pair of carbon atoms. The effect of MWCNT radius is neglected to establish a cohesive law between multilayer paralleled graphenes and α -alumina based on van der Waals

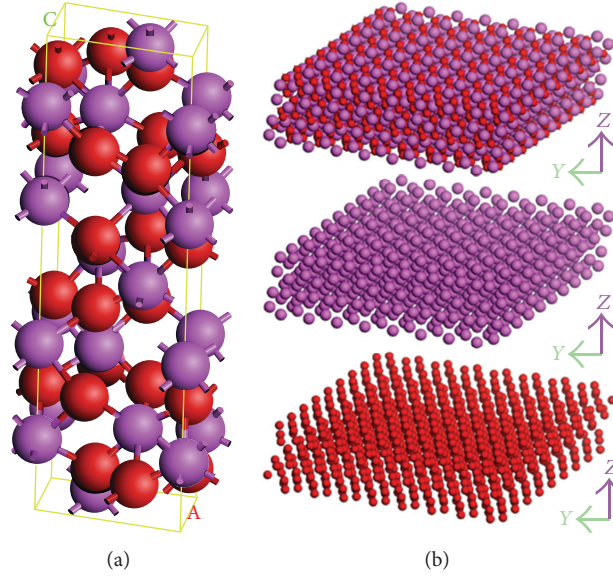


FIGURE 1: Crystal structure of α -alumina. (a) The crystal structure cell, $a = 0.4759$ nm, $b = 0.4759$ nm, and $c = 1.2991$ nm; (b) the crystal structure of α -alumina, the oxygen atom cluster and aluminum atom cluster.

interactions. The stress distribution and the stress intensity are obtained by improved COX model. From cohesive law and COX model, the strain rate of nanotube-composite is given when the interfacial slip begins to occur through van der Waals interaction.

2. The Stress Transfer Efficiency between SWCNTs and Matrix

As the reinforcement of hard brittle material, such as Alumina, the weak connected effect of the interface between CNTs and α -Alumina plays an important role. Generally, the interaction of atoms between CNTs and α -alumina is provided by long-range potential, such as Lenard-Jones potential, as follows:

$$V(r) = 4\epsilon \left(\frac{\sigma^{12}}{r^{12}} - \frac{\sigma^6}{r^6} \right), \quad (1)$$

where V is the potential energy when the distance of two atoms is r , $\sqrt[6]{2}\sigma$ is the equilibrium distance between the atoms, and ϵ is the bond energy at the equilibrium distance.

The crystal structure cell of α -alumina is shown in Figure 1(a); the values of ρ_{Al} and ρ_O are obtained; ϵ_{C-O} and ϵ_{C-Al} can be achieved from $\epsilon_{A-B} = \sqrt{\epsilon_A \epsilon_B}$, respectively. The crystal structure of α -alumina was divided into two parts, oxygen atom cluster and aluminum atom cluster, as shown in Figure 1(b), and then we can analyze the cohesive model, respectively.

Using the RVE as shown in Figure 2(a), the different cohesive model is established from both nonboundary interface, Figure 2(b), and boundary interface, Figure 2(c), respectively; the cohesive energy is representative via van der Waals force.

For nonboundary interface,

$$\begin{aligned} \Phi &= \int_{-\infty}^{-h} 2\pi\rho_C\rho_{Al_2O_3}\epsilon\sigma^2 \left(\frac{2\sigma^{10}}{5z^{10}} - \frac{\sigma^4}{z^4} \right) dz \\ &= 2\pi\rho_C\rho_{Al}\epsilon_{C-Al}\sigma_{C-Al}^3 \left(\frac{\sigma_{C-Al}^3}{3h^3} - \frac{2\sigma_{C-Al}^9}{45h^9} \right) \\ &\quad + 2\pi\rho_C\rho_O\epsilon_{C-O}\sigma_{C-O}^3 \left(\frac{\sigma_{C-O}^3}{3h^3} - \frac{2\sigma_{C-O}^9}{45h^9} \right). \end{aligned} \quad (2)$$

For boundary interface, the cohesive energy is obtained by a banding area of CNT.

Given L is the overlapping length.

Consider

$$\begin{aligned} \Phi_{\text{Line}} &= \int_{-\infty}^{-h} 2\pi\rho_C\rho_{Al}\epsilon_{C-Al}\sigma_{C-Al} \left(\frac{2\sigma_{C-Al}^{10}}{5z^{10}} - \frac{\sigma_{C-Al}^4}{z^4} \right) L \\ &\quad \times \left[1 + \left(\frac{h^4}{L^4} \right) \right] dz \\ &\quad + \int_{-\infty}^{-h} 2\pi\rho_C\rho_O\epsilon_{C-O}\sigma_{C-O} \left(\frac{2\sigma_{C-O}^{10}}{5z^{10}} - \frac{\sigma_{C-O}^4}{z^4} \right) L \\ &\quad \times \left[1 + \left(\frac{h^4}{L^4} \right) \right] dz. \end{aligned} \quad (3)$$

Ignoring the higher order indefinite small value of (3), (2) and (3) have the same result of equilibrium spacing h and can be given as

$$h = 0.429 (\sigma_{C-Al} + \sigma_{C-O}). \quad (4)$$

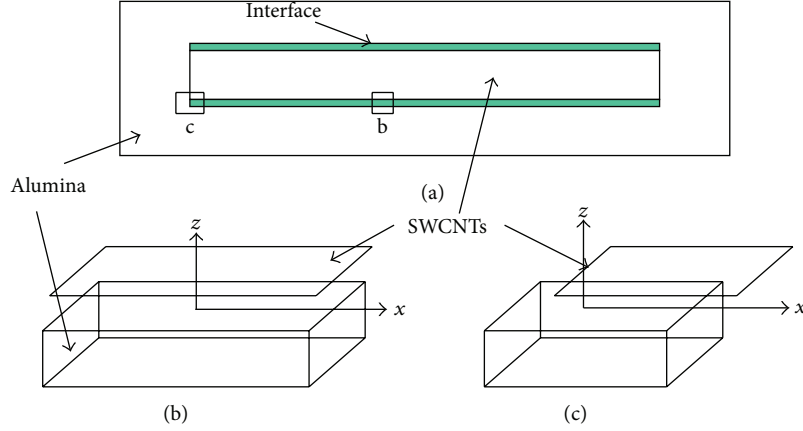


FIGURE 2: SWCNT-alumina composites. (a) Representative volume element, (b) nonboundary interface, and (c) boundary interface.

If a displacement (u, v) is given, (2) and (3) are changed as

$$\Phi = 2\pi\rho_C\rho_{Al}\varepsilon_{C-Al}\sigma_{C-Al}^3 \left(\frac{\sigma_{C-Al}^3}{3(h+v)^3} - \frac{2\sigma_{C-Al}^9}{45(h+v)^9} \right) + 2\pi\rho_C\rho_O\varepsilon_{C-O}\sigma_{C-O}^3 \left(\frac{\sigma_{C-O}^3}{3(h+v)^3} - \frac{2\sigma_{C-O}^9}{45(h+v)^9} \right), \quad (5)$$

$$\begin{aligned} \Phi_{\text{line}}(u, v) &= 2\pi\rho_C\rho_{Al}\varepsilon_{C-Al}\sigma_{C-Al}^3 \left(\frac{\sigma_{C-Al}^3}{3(h+v)^3} - \frac{2\sigma_{C-Al}^9}{45(h+v)^9} \right) (L-u) \\ &+ 2\pi\rho_C\rho_O\varepsilon_{C-O}\sigma_{C-O}^3 \left(\frac{\sigma_{C-O}^3}{3(h+v)^3} - \frac{2\sigma_{C-O}^9}{45(h+v)^9} \right) (L-u). \end{aligned} \quad (6)$$

The partial derivatives of (u, v) are easily deduced from (5) and (6), respectively. The normal stress of nonboundary and boundary interface is given as

$$\begin{aligned} \sigma_{\text{cohesive}} &= 2\pi\rho_C\rho_{Al}\varepsilon_{C-Al}\sigma_{C-Al}^2 \left(\frac{2\sigma_{C-Al}^{10}}{5(h+v)^{10}} - \frac{\sigma_{C-Al}^4}{(h+v)^4} \right) \\ &+ 2\pi\rho_C\rho_O\varepsilon_{C-O}\sigma_{C-O}^2 \left(\frac{2\sigma_{C-O}^{10}}{5(h+v)^{10}} - \frac{\sigma_{C-O}^4}{(h+v)^4} \right). \end{aligned} \quad (7)$$

The shear stress of nonboundary interface is 0. For boundary interface, the shear force of bonding area is given as

$$\begin{aligned} F_{\text{tangent}} &= \frac{\partial\Phi_{\text{line}}(u, v)}{\partial u} \\ &= 2\pi\rho_C\rho_{Al}\varepsilon_{C-Al}\sigma_{C-Al}^3 \left(\frac{2\sigma_{C-Al}^9}{45(h+v)^9} - \frac{\sigma_{C-Al}^3}{3(h+v)^3} \right) \\ &+ 2\pi\rho_C\rho_O\varepsilon_{C-O}\sigma_{C-O}^3 \left(\frac{2\sigma_{C-O}^9}{45(h+v)^9} - \frac{\sigma_{C-O}^3}{3(h+v)^3} \right). \end{aligned} \quad (8)$$

So the average shear stress of boundary interface is given as

$$\begin{aligned} \tau_{\text{cohesive}} &= \frac{F_{\text{tangent}}}{L-u} = 2\pi\rho_C\rho_{Al}\varepsilon_{C-Al}\sigma_{C-Al}^2 \\ &\times \left(\frac{2\sigma_{C-Al}^9}{45(h+v)^9} - \frac{\sigma_{C-Al}^3}{3(h+v)^3} \right) \frac{\sigma_{C-Al}}{L-u} \\ &+ 2\pi\rho_C\rho_O\varepsilon_{C-O}\sigma_{C-O}^2 \\ &\times \left(\frac{2\sigma_{C-O}^9}{45(h+v)^9} - \frac{\sigma_{C-O}^3}{3(h+v)^3} \right) \frac{\sigma_{C-O}}{L-u}, \end{aligned} \quad (9)$$

where $\rho_C = 4/3\sqrt{3}l_C^2$ and $l_C = 0.142$ nm. $\rho_{Al} = 6.969/\text{nm}^3$ and $\rho_O = 6.195/\text{nm}^3$ are the volume density of aluminum and oxygen atoms number of alumina, respectively [14]. $\sigma_{C-Al} = 0.4028$ nm, $\sigma_{C-O} = 0.392$ nm [15], $\varepsilon_{C-Al} = 0.0038$ eV, and $\varepsilon_{C-O} = 0.0058$ eV [16].

The cohesive stress of the interface of CNTs and alumina is achieved by substituting the above parameters into (7) and (9), respectively. For short fiber reinforcement, there is only one free edge produced on each CNT's end, and the material can be supposed as an infinite along the x -axis. So the practical value of shear stress is only 1/2 of the result of (9).

From Figures 3 and 4, we can find that the normal stress intensity of CNTs and alumina material is about 240 MPa, the average shear force of bounding area is about 27.5 MPa·nm, and the cohesive shear force is concentrated in CNTs' ends. The normal and shear stress intensity of the interface that is provided by van der Waals force can be achieved through the above analysis.

3. Stress Distribution of CNTs and Alumina with Shear-Lag Model

A RVE is taken from nanocomposites. Considering a perfect interfacial bonding, the COX model is changed by a hollow of

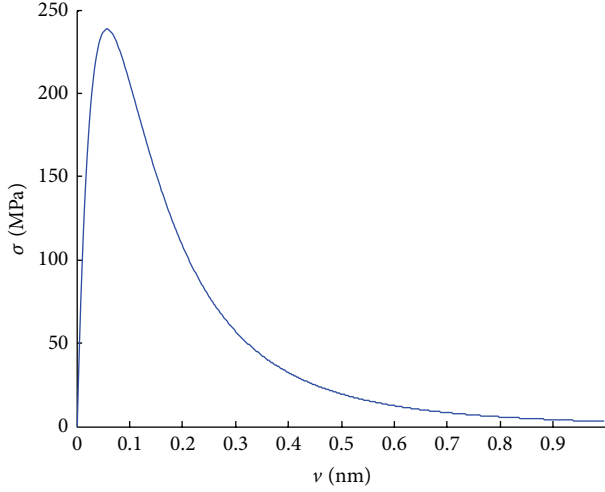


FIGURE 3: The relationship of normal stress and displacement based on van der Waals force.

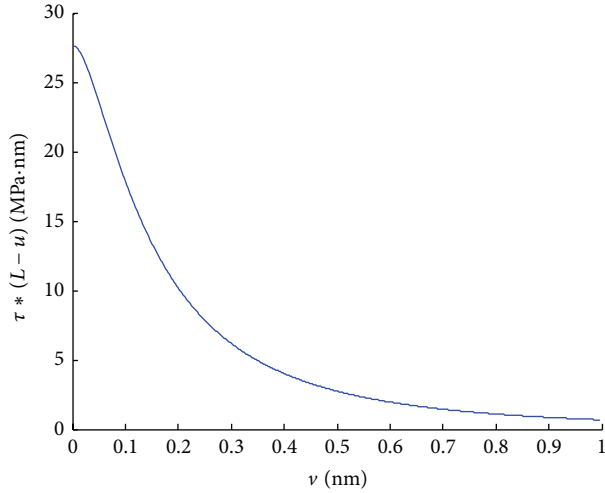


FIGURE 4: The relationship of shear stress and displacement based on van der Waals force.

SWCNTs, as shown in Figure 5. The stress of CNTs along tube length is σ_t and the shear stress of interface is τ as follows:

$$\sigma_t = E_t e \left[1 - \frac{\cosh \beta (L/2 - x)}{\cosh \beta (L/2)} \right], \quad (10)$$

$$\tau = \frac{E_t e A_t \beta}{2\pi r_2} \times \frac{\sinh \beta (L/2 - x)}{\cosh \beta (L/2)}, \quad (11)$$

$$\beta = \sqrt{\left(\frac{G_m}{E_t} \right) \left(\frac{2\pi}{A_t \ln(R/r_2)} \right)}, \quad (12)$$

where e is the strain along CNT's length, L is the length of CNT, G_m is the shear modulus of matrix material, E_t is Young's modulus of CNT, R is the radius of RVE, $A_t = \pi(r_2^2 - r_1^2)$ is the cross-sectional area, and the value is 2.8413 nm^2 with the parameters of $d = 3 \text{ nm}$, $r_1 = 1.16 \text{ nm}$,

and $r_2 = 1.5 \text{ nm}$. The above formulae will reduce to the original COX model when the value of r_1 is zero.

In the following calculations, we take $E_t = 1.0 \text{ TPa}$, $G_m = 143.44 \text{ GPa}$, and $e = 0.0686\%$, which is the ultimate strain of alumina material [17], and $R/r_2 = 7.236$ from $R/r_2 = (\pi/4V_f)^{1/2}$, where $V_f = 1.5\%$ is the volume content of CNTs in composites. $t = r_2 - r_1$ is the thickness of CNTs, where $t = 0.34 \text{ nm}$.

Figure 6 shows the tensile stress distributions in various tube lengths. There is a maximum value when the length is longer than 30 nm , and the value exists in the middle of CNTs. The shear stress of the interface between CNTs and alumina is concentrated in the end of CNTs. In the condition of the strain rate of material achieved to ultimate strain, the shear stress of CNTs beard is about 0.06 GPa . The shear stress distribution of the end is not effected by the length of CNTs (shown in Figure 7).

In order to compare to the maximum value that van der Waals force can afford, we make an integral of shear stress to the bonding area along the tube length as follows:

$$F_{\text{line}} = \int_0^{L/2} \tau dx. \quad (13)$$

And then

$$F_{\text{line}} = 28.69 \text{ MPa} \cdot \text{nm} > 27.5 \text{ MPa} \cdot \text{nm}. \quad (14)$$

Equation (14) shows that shear stress in perfect interfacial bonding is more beyond than that afforded by van der Waals force, and slipping has occurred. So the ultimate stress afforded by van der Waals force is defined as the static stress limit.

Substituting the result $F_{\text{line}} = 27.5 \text{ MPa} \cdot \text{nm}$ into (13), we can obtain a simulated result from (11) and (13); the strain limit of nanocomposites is taken out as follows:

$$e_1 = 0.0091\%. \quad (15)$$

The tensile stress of CNTs and shear stress of interface are shown in Figures 8 and 9 when the strain rate is smaller than 0.0091% .

Figure 10 shows the relationship between volume content of CNTs and tensile stress. Figure 10(a) shows that the tensile stress is decreasing with the increasing of radius of CNTs when the volume content is constant. Figure 10(b) shows that the maximum tensile stresses value can be achieved when the length of CNTs is longer than the effective length.

4. Conclusions

Based on multiscale method, the interfacial mechanical behavior of CNTs-alumina composites is analyzed. The interfacial stress is discussed by using cohesive law, which was reformed by using the crystal lattice of SWCNTs and α -alumina. Based on van der Waals force, the maximum normal and shear stress are achieved, respectively. The tensile and shear stress distribution is achieved by using improved COX model. Giving a perfect interfacial bonding and long enough tube, there is a maximum value (0.68 GPa) of tensile stress

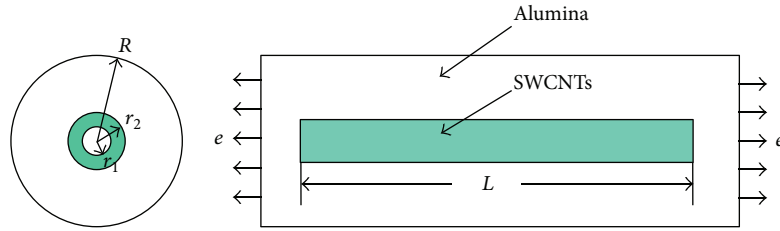


FIGURE 5: The RVE of SWCNTs reinforcement alumina composites.

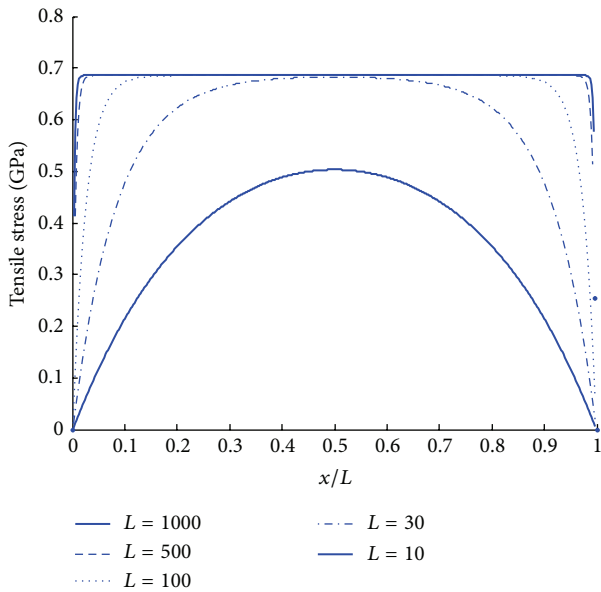


FIGURE 6: Tensile stress distributions at various tube lengths ($d = 3$ nm, $t = 0.34$ nm).

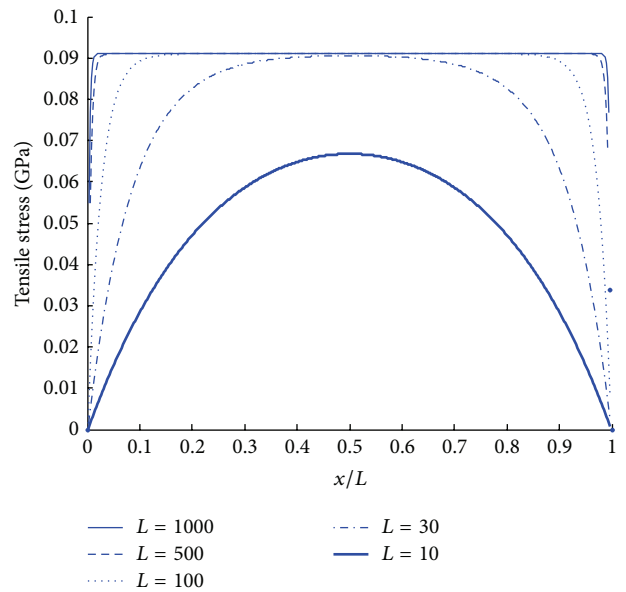


FIGURE 8: Tensile stress distributions at various tube lengths provided by van der Waals force ($d = 3$ nm, $t = 0.34$ nm).

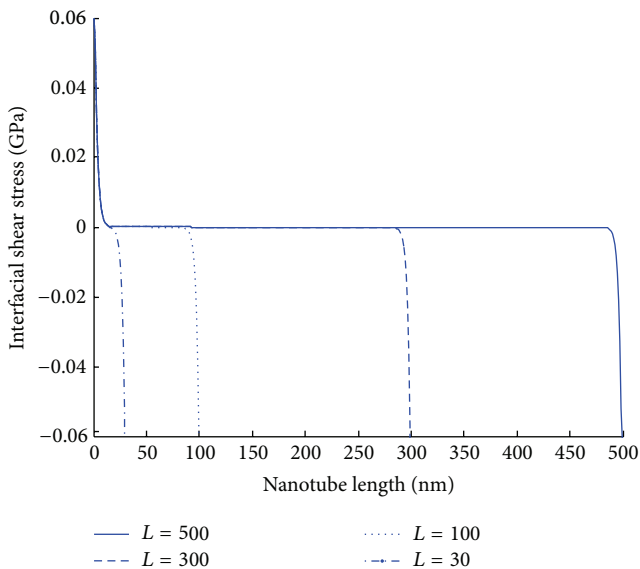


FIGURE 7: Shear stress distribution at SWNT/alumina interface along the tube length ($d = 3$ nm, $t = 0.34$ nm).

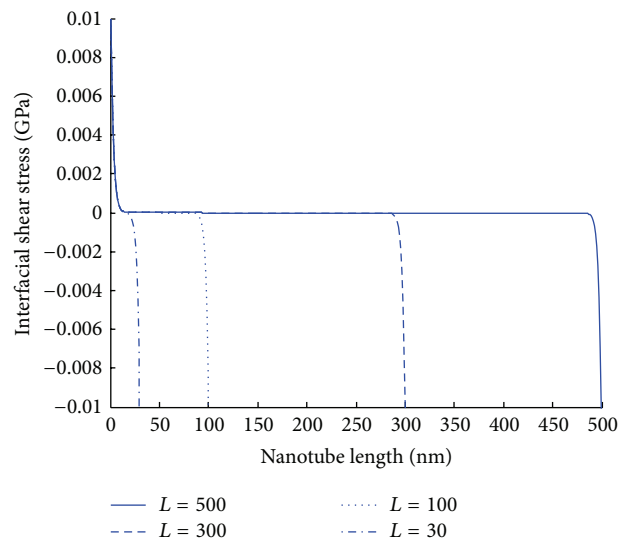


FIGURE 9: Shear stress at the SWNT/alumina interface along the tube length provided by van der Waals force ($d = 3$ nm, $t = 0.34$ nm).

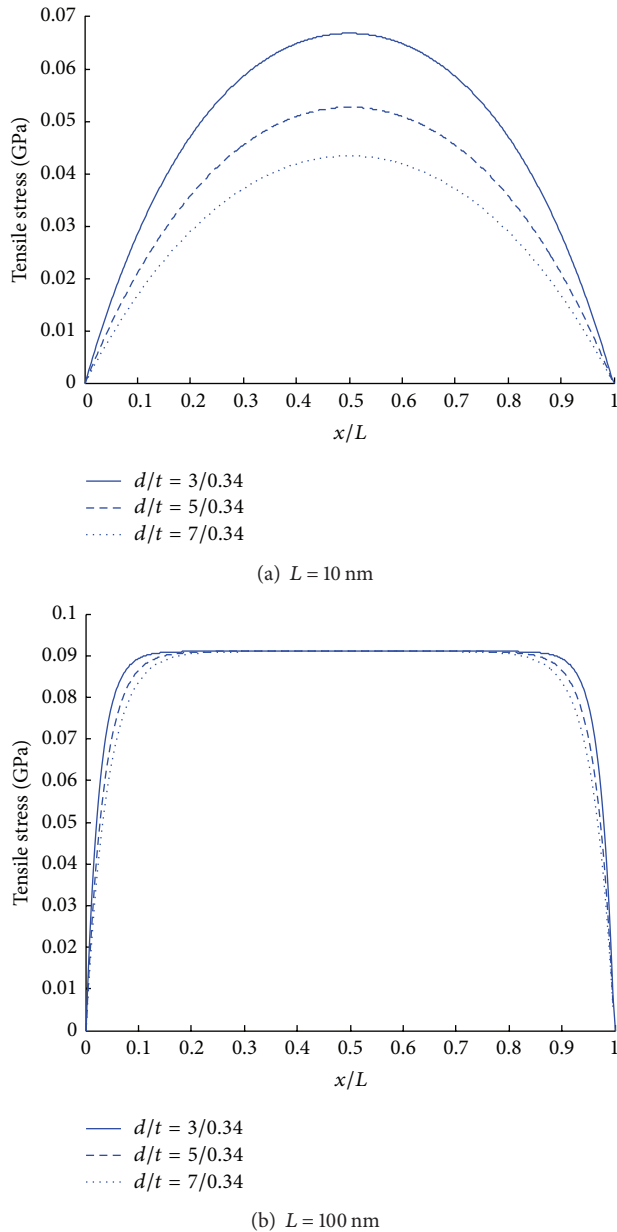


FIGURE 10: Effects of tube diameter d on the tensile stress, (a) $L = 10$ nm and (b) $L = 100$ nm.

under the biggest strain (0.686%) that the matrix can afford. The maximum value of shear stress exists in the end of CNTs. The integral of shear stress to the bonding area along the tube length is made and compared with the shear stress provided by van der Waals force. The result shows that the ultimate stress afforded by van der Waals interaction is achieved when the strain rate is 0.0091%, and the interfacial slip begins to occur. The simple analysis is used as a basis of regulating suitable interaction to adapting to different situations.

Conflict of Interests

The authors declare that there is no conflict of interests regarding the publication of this paper.

Acknowledgments

The work is supported by the National Natural Science Foundation of China through Grant I1271234 and the Science Program of Shandong Provincial Education Department through Grant J13LJ51.

References

- [1] I. Ahmad, H. Cao, H. Chen, H. Zhao, A. Kennedy, and Y. Q. Zhu, "Carbon nanotube toughened aluminium oxide nanocomposite," *Journal of the European Ceramic Society*, vol. 30, no. 4, pp. 865–873, 2010.
- [2] J. Sun, L. Gao, and W. Li, "Colloidal processing of carbon nanotube/alumina composites," *Chemistry of Materials*, vol. 14, no. 12, pp. 5169–5172, 2002.
- [3] M. Estili, A. Kawasaki, H. Sakamoto, Y. Mekuchi, M. Kuno, and T. Tsukada, "The homogeneous dispersion of surfactantless, slightly disordered, crystalline, multiwalled carbon nanotubes in α -alumina ceramics for structural reinforcement," *Acta Materialia*, vol. 56, no. 15, pp. 4070–4079, 2008.
- [4] C. N. He, F. Tian, and S. J. Liu, "A carbon nanotube/alumina network structure for fabricating alumina matrix composites," *Journal of Alloys and Compounds*, vol. 478, no. 1-2, pp. 816–819, 2009.
- [5] S. C. Chowdhury and T. Okabe, "Computer simulation of carbon nanotube pull-out from polymer by the molecular dynamics method," *Composites A: Applied Science and Manufacturing*, vol. 38, no. 3, pp. 747–754, 2007.
- [6] Y. L. Chen, B. Liu, X. Q. He, Y. Huang, and K. C. Hwang, "Failure analysis and the optimal toughness design of carbon nanotube-reinforced composites," *Composites Science and Technology*, vol. 70, no. 9, pp. 1360–1367, 2010.
- [7] S. Liu, N. Hu, G. Yamamoto et al., "Investigation on CNTs/alumina interface properties using molecular mechanics simulations," *Carbon*, vol. 49, pp. 3698–3704, 2011.
- [8] L. Y. Jiang, Y. Huang, H. Jiang et al., "A cohesive law for carbon nanotube/polymer interfaces based on the van der Waals force," *Journal of the Mechanics and Physics of Solids*, vol. 54, no. 11, pp. 2436–2452, 2006.
- [9] L. Y. Jiang, "Macroscopic behavior of carbon nanotube (CNT)-reinforced composite accounting for interface cohesive force," *Journal of Adhesion*, vol. 86, no. 3, pp. 273–289, 2010.
- [10] W. B. Lu, J. Wu, L. Y. Jiang, Y. Huang, K. C. Hwang, and B. Liu, "A cohesive law for multi-wall carbon nanotubes," *Philosophical Magazine*, vol. 87, no. 14-15, pp. 2221–2232, 2007.
- [11] W. B. Lu, J. Wu, J. Song, K. C. Hwang, L. Y. Jiang, and Y. Huang, "A cohesive law for interfaces between multi-wall carbon nanotubes and polymers due to the van der Waals interactions," *Science Direct*, vol. 197, pp. 3261–3267, 2008.
- [12] Y. Chen, K. Balani, and A. Agarwal, "Analytical model to evaluate interface characteristics of carbon nanotube reinforced aluminum oxide nanocomposites," *Applied Physics Letters*, vol. 92, no. 1, Article ID 011916, 2008.
- [13] K. Q. Xiao and L. C. Zhang, "The stress transfer efficiency of a single-walled carbon nanotube in epoxy matrix," *Journal of Materials Science*, vol. 39, pp. 4481–4486, 2004.
- [14] S. J. V. Frankland and V. M. Harik, "Analysis of carbon nanotube pull-out from a polymer matrix," *Surface Science*, vol. 525, no. 1-3, pp. L103–L108, 2003.

- [15] D. P. Li, J. M. Xie, H. Sun, S. Q. Wang, and Q. S. Du, "Quantum chemical study of molecular potential energies in methane hydrate structure-unit cell," *Journal of Tianjin Normal University*, vol. 25, no. 4, pp. 1-8, 2005.
- [16] W. D. Cornell, P. Cieplak, C. I. Bayly et al., "A second generation force field for the simulation of proteins, nucleic acids, and organic molecules," *Journal of the American Chemical Society*, vol. 117, no. 19, pp. 5179-5197, 1995.
- [17] Y. S. Yin, J. D. Jing et al., *Alumina Ceramics and Composites*, Chemical Industry Press, Peking, China, 2001.

Research Article

New Two-Dimensional Polynomial Failure Criteria for Composite Materials

Shi Yang Zhao and Pu Xue

School of Aeronautics, Northwestern Polytechnical University, Xi'an 710072, China

Correspondence should be addressed to Shi Yang Zhao; haiyangrongyang@sina.com

Received 6 March 2014; Revised 27 April 2014; Accepted 28 April 2014; Published 28 May 2014

Academic Editor: Gonzalo Martínez-Barrera

Copyright © 2014 S. Y. Zhao and P. Xue. This is an open access article distributed under the Creative Commons Attribution License, which permits unrestricted use, distribution, and reproduction in any medium, provided the original work is properly cited.

The in-plane damage behavior and material properties of the composite material are very complex. At present, a large number of two-dimensional failure criteria, such as Chang-Chang criteria, have been proposed to predict the damage process of composite structures under loading. However, there is still no good criterion to realize it with both enough accuracy and computational performance. All these criteria cannot be adjusted by experimental data. Therefore, any special properties of composite material cannot be considered by these criteria. Here, in order to solve the problem that the criteria cannot be adjusted by experiment, new two-dimensional polynomial failure criteria with four internal parameters for composite laminates are proposed in the paper, which include four distinct failure modes: fiber tensile failure, fiber compressive failure, matrix tensile failure, and matrix compressive failure. In general, the four internal parameters should be determined by experiments. One example that identifies parameters of the new failure criteria is given. Using the new criteria can reduce the artificialness of choosing the criteria for the damage simulation of the failure modes in composite laminates.

1. Introduction

Fiber-reinforced polymer (FRP) composites are widely applied in aerospace, marine, and many other industries due to their lightweight, high stiffness, strength, and damping properties [1]. In order to get strong and reliable structures, it is very important to study the mechanical behavior of FRP. In the studies, the finite element method is proved to be effective and successful which can predict the behavior of composite structures under various loading conditions. From the literatures, many researches can be found on the behavior of composites, such as buckling loads, modal characteristics, damage, and failure. Zhang and Yang [2] gave comprehensive reviews and some of the future research on composite laminated plates. Orifici et al. [3] also gave a critical review to assess the state of the art in material constitutive modeling and composite failure theories. They summarized the various theories and approaches within the context of the dissipated energy framework. The dissipated energy function, with units of energy per unit volume, could

be determined from experimental testing and was postulated to be a property of the material. Based on the continuum damage mechanics (CDM), Liu and Zheng [4] reviewed the damage constitutive modeling, the failure criteria, and the finite element implementation in the progressive failure analysis which predicted the stiffness degradation and failure strengths of composite laminates. Specially, the methodologies to solve the numerical convergence problems due to the loss of element stiffness in the finite element analysis were discussed.

The failure behavior and damage analysis of the composite laminated structures by the finite element method are paid the most attention by researchers. Michopoulos's work [5] shows that there is a relationship among many criteria. Hinton et al. [6–11] listed 19 theories of failure criteria proposed for composite laminates and gave a comparison of their predictive capabilities. They showed similarities and differences between the predictions of the 19 theories by comparing the initial and final failure envelopes and representative stress-strain curves. They also explained the

differences between the predictions. They did not intend to prove which theory is the best but just clarified their differences between their predictions.

Despite a large number of published papers on the damage and failure behavior of the composite laminates under various loadings, a very effective criterion to predict the failure behavior of composites has not achieved yet. Several widely used phenomenological failure criteria, such as the maximum stress, Hoffman, Tsai-Wu, and Tsai-Hill failure criteria [8, 11–14], are proposed to describe the whole ply failure of composite material structures. Other popular phenomenological failure criteria, such as Hashin criteria, Hou criteria, Chang-Chang criteria, Linde criteria, LaRC04 criteria, and Maimí criteria [15–21], can describe the damage process of composite structures in detail, such as fiber breakage, fiber buckling, matrix cracking, therefore, matrix compression. All these criteria cannot be adjusted by experiments. Therefore, any special properties of composite material cannot be considered by these criteria. By studying the problems of dynamic bending failure of composite laminated beams, Santiuste et al. [22] suggested that Hashin criteria may be suitable for ductile composite material, and Hou criteria may be suitable for brittle material in unidirectional laminated beams. Therefore, for different material and different structures, just one failure criterion which cannot be adjusted by experiments could not satisfy various requirements.

When we use some known criteria in our study directly, it has used a supposition that material properties used in your own engineering are the same as that in the study which proposed the known criteria. In fact, the failure criteria should be decided by experiments. If one criterion is decided by experiments, the criterion can consider special properties of any material used in engineering. And also, you can use the new failure criteria in numerical simulation to get better numerical results. Here we try to propose new two-dimensional polynomial failure criteria, which can be adjusted by experiments.

New two-dimensional polynomial failure criteria with four internal parameters for composite laminates are proposed in the paper. Four distinct failure modes including fiber tensile failure, fiber compressive failure, matrix tensile failure, and matrix compressive failure are considered in the extended criteria. Meanwhile, when some special values are given to the four internal parameters, the extended criteria will become some classical failure criteria such as Chang-Chang criteria, Hashin criteria, and Hou criteria in two dimensional case. Finally, the features of the failure criteria are discussed in detail. And one example that chooses proper values for the parameters in the criteria is given.

2. New Two-Dimensional Failure Criteria

The damage of composite laminates under loading includes intraply failure and interply failure [23]. Intraply failure modes are fiber kinking, fiber fracture, matrix cracking, and matrix-fiber debonding. Interply failure modes are interface cracks between plies.

New two-dimensional polynomial failure criteria for composite laminates are with four internal parameters. And each failure mode has a parameter. Therefore, four failure modes all can be adjusted by experiments. And almost special properties of each failure mode can be considered. New two-dimensional polynomial failure criteria are obtained by comparing common and characteristic parts of the present failure criteria, such as Chang-Chang criteria, Hou Criteria, Hashin criteria, and Linde criteria.

2.1. Definition of Variables. The related variables include stress components, σ_1 , σ_2 , σ_{12} ; the tensile damage variable of fiber, d_{ft} ; the compressive damage variable of fiber, d_{fc} ; the tensile damage variable of matrix, d_{mt} ; the compressive damage variable of matrix, d_{mc} ; some material properties: longitudinal failure stress strength, X_T , X_C ; transverse failure stress strength, Y_T , Y_C ; in-plane shear failure stress strength, S_{12} ; the subscripts “T” and “C” refer to tension and compression.

2.2. Fiber Tensile Failure. Under tension loading, fiber is the main portion to carry load. In composites with high fiber volume fraction and those whose failure strain of the matrix is higher than that of the reinforcing fiber, such as carbon-epoxy composites, longitudinal failures start by isolated fiber fractures in weak zones [20]. The localized fractures increase the normal and interfacial shear stresses in adjoining fiber, and the local stress concentration promotes matrix cracking and fiber and matrix debonding [24].

Fiber failure criteria in tension are the most simple damage form for composite laminates. After the accumulation of fracture energy, individual fiber will fail until that the whole ply failure happens. And the whole laminates will carry any loads. In general, the maximum stress strength or strain strength is used to predict fiber failure.

A new fiber failure criterion in tensile is

$$d_{ft} = k_1 * \left(\frac{\sigma_1}{X_T} \right)^2 + (1 - k_1) * \frac{\sigma_1}{X_T} + \beta_1 \frac{\sigma_{12}^2 / 2G_{12} + 3/4\alpha\sigma_{12}^4}{S_{12}^2 / 2G_{12} + 3/4\alpha S_{12}^4} \geq 1, \quad \sigma_1 \geq 0, \quad (1)$$

where k_1 is a parameter of the criteria of fiber failure; β_1 is used to consider the interaction form involving in-plane shear, which can take two values: 0 or 1; α is a parameter for the shear nonlinear effect, which can take two values: 0 or 1.

2.3. Fiber Compressive Failure. Under fiber compression loads, laminate failure modes are complex and depend on the material properties. The modes may be microbuckling, kinking, and fiber failure [25, 26]. The structures may be in the state of collapse.

The criteria for fiber compressive failure are almost the same as the fiber tensile failure, although the failure phenomenon of fiber compressive failure is more complex than the fiber tensile failure.

A new fiber failure criterion in compression is

$$d_{fc} = k_2 * \left(\frac{\sigma_1}{X_c} \right)^2 + \gamma * (k_2 - 1) * \frac{\sigma_1}{X_c} + \beta_2 * \left(\frac{\sigma_{12}}{S} \right)^2 \geq 1, \quad \sigma_1 \leq 0, \quad (2)$$

where k_2 is a parameter; β_2 is used to consider the interaction form involving in-plane shear, which can take two values: 0 or 1; γ is a parameter which can take two values: 1 and 0.

2.4. Failure Criteria for Matrix. Under transverse loading, the behavior of the material is more complex than the fiber failure. A nonlinear stress-strain response will be observed if the laminate is loaded in the transverse direction or in the shear direction. The famous Chang-Chang failure criteria considered the nonlinear shear effects and introduced a coefficient to characterize the nonlinearity. The nonlinear constitutive relation proposed by Richard and Blacklock [27] introduced an exponential degradation form. In general, the fracture plane is perpendicular to the mid-plane of the ply under transverse tensile load. But the angle of the fracture plane will change if transverse stress increases under the compressive load. Generally, for carbon-epoxy and glass-epoxy composites loaded in pure transverse compression, the fracture plane is at an angle of $53^\circ \pm 3^\circ$ with respect to the thickness direction [20, 28]. The LaRC04 criteria consider the alterative influence of the angle. However, the computational efficiency decreases if the fracture angle changes frequently, so Maimí et al. assumed that the fracture angle can only take one of the two discrete values: 0° or 53° [20].

Here, two-dimensional matrix failure criteria for composite materials are expressed by a quadratic polynomial. They will also not include the variable of the mutative fractural angle.

2.4.1. Matrix Tensile Failure. The criteria for matrix tensile failure involve an interaction between the tensile normal and in-plane shear stresses.

A new matrix failure criterion in tension is

$$d_{mt} = k_3 \left(\frac{\sigma_2}{Y_T} \right)^2 + (1 - k_3) \frac{\sigma_2}{Y_T} + \frac{\sigma_{12}^2/2G_{12} + 3/4\alpha\sigma_{12}^4}{S_{12}^2/2G_{12} + 3/4\alpha S_{12}^4}, \quad (3)$$

$$\sigma_2 \geq 0,$$

where k_3 is a parameter; α is used to consider the nonlinear interaction form involving in-plane shear.

2.4.2. Matrix Compressive Failure. The criteria for matrix tensile failure are complex in Hashin criteria, Hou criteria, and Chang-Chang criteria. The coefficients of quadratic polynomials are different. Therefore, it is advisable to define the matrix failure criterion in compression with parameters. Parameters should be chosen by experiments.

A new matrix failure criterion in tension is as follows:

$$d_{mc} = k_4 \left(\frac{\sigma_2}{Y_c} \right)^2 + (k_4 - 1) \frac{\sigma_2}{Y_c} + \frac{\sigma_{12}^2/2G_{12} + 3/4\alpha\sigma_{12}^4}{S_{12}^2/2G_{12} + 3/4\alpha S_{12}^4}, \quad (4)$$

$$\sigma_2 \leq 0,$$

where k_4 is a parameter; α is used to consider the nonlinear interaction form involving in-plane shear.

So far, the two-dimensional failure criteria for composite materials are given.

3. Features of the New Criteria

3.1. Unified Expression of Fiber and Matrix Failure Criteria. The new failure criteria for primary damage failure behavior are given above. In fact, the new criteria can be rewritten as a tensor form as follows:

$$d_{il} = k_i * \left(\frac{\sigma_i}{X_{il}} \right)^2 + \gamma_i * (1 - k) * \left| \frac{\sigma_i}{X_{il}} \right| + \beta_i * \left(\frac{\sigma_{12}^2/2G_{12} + 3/4\alpha_i\sigma_{12}^4}{S_{12}^2/2G_{12} + 3/4\alpha_i S_{12}^4} \right)^2 \geq 1, \quad (5)$$

where k_i is a parameter; β_i is used to consider the interaction form involving in-plane shear; γ_i is a parameter which can take two values: 1 and 0; \parallel is the sign of the absolute value; i is used to denote the damage category: fiber or matrix; l is for the stress direction: tensile or compression.

3.2. Some Special Forms of the New Criteria. In fact, Chang-Chang criteria, Hou criteria, and so forth are proposed from some special materials, such as carbon/epoxy and graphite epoxy. Therefore, the validity of parameters in these criteria is very limited. All these known criteria are just good at simulating some special material. If more accurate numerical results are needed, the failure criteria of every material should consider their own material properties and be given one set of special values of parameters. And all these parameters are from experiments. When some special values got by experiments are given to four parameters of the new criteria, it will get good numerical results. Meanwhile, when some special values are given to the four internal parameters, the new criteria will become these classical failure criteria such as Chang-Chang criteria, Linde criteria, Hashin criteria, and Hou criteria in two dimensional case.

When $k_1 = 1$, $\beta_1 = 1$, $\alpha = 0$; $k_2 = 1$, $\beta_2 = 0$, $\gamma = 0$; $k_3 = 1$; $k_4 = (Y_c/2/S_{23})^2$, the new criteria will become Hashin criteria in two-dimensional case as follows:

$$d_{ft} = \left(\frac{\sigma_1}{X_T} \right)^2 + \left(\frac{\sigma_{12}}{S} \right)^2 \geq 1, \quad \sigma_1 \geq 0,$$

$$d_{fc} = \left(\frac{\sigma_1}{X_c} \right)^2 \geq 1, \quad \sigma_1 \leq 0,$$

$$\begin{aligned}
d_{mt} &= \left(\frac{\sigma_{22}}{Y_T} \right)^2 + \left(\frac{\sigma_{12}}{S_{12}} \right)^2, \quad \sigma_{22} \geq 0, \\
d_{mc} &= \left(\frac{Y_c}{2S_{23}} \right)^2 \left(\frac{\sigma_{22}}{Y_c} \right)^2 + \left[\left(\frac{Y_c}{2S_{23}} \right)^2 - 1 \right] \frac{\sigma_{22}}{Y_c} \\
&\quad + \left(\frac{\sigma_{12}}{S_{12}} \right)^2 \geq 1, \quad \sigma_{22} < 0.
\end{aligned} \tag{6}$$

When $k_1 = 1, \beta_1 = 1, \alpha = 0; k_2 = 1, \beta_2 = 1, \gamma = 0; k_3 = 1; k_4 = (Y_c/2/S_{12})^2$, the new criteria will become Hou criteria in two dimensional case as follows:

$$\begin{aligned}
d_{ft} &= 1 * \left(\frac{\sigma_1}{X_T} \right)^2 + (1 - 1) * \sigma_1 + \left(\frac{\sigma_{12}}{S} \right)^2 \geq 1, \quad \sigma_1 \geq 0, \\
d_{fc} &= \left(\frac{\sigma_1}{X_T} \right)^2 + \left(\frac{\sigma_{12}}{S} \right)^2 \geq 1, \quad \sigma_1 \leq 0, \\
d_{mt} &= \left(\frac{\sigma_{22}}{Y_T} \right)^2 + \left(\frac{\sigma_{12}}{S_{12}} \right)^2 + \left(\frac{\sigma_{23}}{S_{23}} \right)^2, \quad \sigma_{22} \geq 0, \\
d_{mc} &= \frac{1}{Y_c} \left[\left(\frac{Y_c}{2S_{12}} \right)^2 - 1 \right] \sigma_{22} + \frac{\sigma_{22}^2}{4S_{12}^2} \\
&\quad + \left(\frac{\sigma_{12}}{S_{12}} \right)^2 \geq 1, \quad \sigma_{22} < 0.
\end{aligned} \tag{7}$$

When $k_1 = X_T/X_c, \beta_1 = 0, \alpha = 0; k_2 = X_c/X_T, \beta_2 = 0, \gamma = 1; k_3 = Y_T/Y_c; k_4 = Y_c/Y_T$, the new criteria will become Linde criteria in two dimensional case as follows:

$$\begin{aligned}
d_f &= \left(\frac{1}{X_T} - \frac{1}{X_c} \right) \sigma_1 + \frac{1}{X_T X_c} \sigma_1^2, \\
d_m &= \left(\frac{1}{Y_T} - \frac{1}{Y_c} \right) \sigma_2 + \frac{1}{Y_T Y_c} \sigma_2^2 + \left(\frac{\sigma_{12}}{S_{12}} \right)^2.
\end{aligned} \tag{8}$$

When $k_1 = 1, \beta_1 = 1, \alpha = 1; k_2 = 1, \beta_2 = 0, \gamma = 0; k_3 = 1; k_4 = 1$, the new criteria will become Chang-Chang criteria as follows:

$$\begin{aligned}
d_{ft} &= \left(\frac{\sigma_1}{X_T} \right)^2 + \frac{\sigma_{12}^2/2G_{12} + 3/4\alpha\sigma_{12}^4}{S_{12}^2/2G_{12} + 3/4\alpha S_{12}^4} \geq 1, \quad \sigma_1 \geq 0, \\
d_{fc} &= \left(\frac{\sigma_1}{X_c} \right)^2 \geq 1, \quad \sigma_1 \leq 0, \\
d_{mt} &= \left(\frac{\sigma_{22}}{Y_T} \right)^2 + \frac{\sigma_{12}^2/2G_{12} + 3/4\alpha\sigma_{12}^4}{S_{12}^2/2G_{12} + 3/4\alpha S_{12}^4}, \quad \sigma_{22} \geq 0, \\
d_{mc} &= \left(\frac{\sigma_{22}}{Y_c} \right)^2 + \frac{\sigma_{12}^2/2G_{12} + 3/4\alpha\sigma_{12}^4}{S_{12}^2/2G_{12} + 3/4\alpha S_{12}^4}, \quad \sigma_{22} \leq 0.
\end{aligned} \tag{9}$$

TABLE 1: Failure strengths of T300/914C.

X_T /Mpa	X_C /Mpa	Y_T /Mpa	Y_C /Mpa	S_{12} /Mpa
1500	900	27	200	80

TABLE 2: Failure strengths of E-glass/Ly556/HT907/DY063 epoxy.

X_T /Mpa	X_C /Mpa	Y_T /Mpa	Y_C /Mpa	S_{12} /Mpa	G_I /J/m ²
1500	900	27	200	80	165

When $k_3 = G_{Ic}/G_{IIc}, \alpha = 0$, (3) will be one part of the failure criteria LaR04, shown in (10). G_{Ic}, G_{IIc} are the fracture toughness of Mode I and Mode II, respectively,

$$d_{mt} = \frac{G_{Ic}}{G_{IIc}} \left(\frac{\sigma_2}{Y_T} \right)^2 + \left(1 - \frac{G_{Ic}}{G_{IIc}} \right) \frac{\sigma_2}{Y_t} + \left(\frac{\sigma_{12}}{S_{12}} \right)^2, \quad \sigma_2 \geq 0. \tag{10}$$

From (5)–(9), we find that the new criteria with four parameters have enough capability to match the failure criteria which are used widely in the damage analysis of composite materials.

The parameters of the new failure criterion can be defined by experimental data to get better numerical results.

4. Identifying Parameters of the New Failure Criteria

The process of identifying parameters of the new failure criteria by experiments is shown here.

Biaxial tests of E-glass and carbon fiber reinforced composite laminates were performed by Soden et al. [29]. In biaxial tests, just σ_1, σ_2 , and σ_{12} can be obtained. Therefore, just parameters k_1, k_2, k_3 , and k_4 can be identified by experimental data. The other parameters $\beta_1, \beta_2, \alpha, \gamma$ in the new criteria are not the main items. In fact, γ is used to consider the influence of linear item, σ_1 , to the fiber tensile damage; β_1 is used to consider the influence of shear stress, σ_{12} , to the fiber tensile damage; β_2 is used to consider the influence of shear stress, σ_{12} , to the fiber compressive damage; α is used to consider the influence of nonlinear factor of material. The corresponding real values of the parameters of $\beta_1, \beta_2, \alpha, \gamma$ in Chang-Chang criteria, Linde criteria, Hashin criteria, and Hou criteria in two dimensional case are almost the same. Therefore, based on the four failure criteria above, the parameters, $\beta_1 = 1, \beta_2 = 1, \alpha = 0, \gamma = 1$, are assumed. In order to reduce the complexity of identifying parameters, k_1, k_2, k_3, k_4 , we just choose the corresponding coefficients of those parameters from Hashin, Hou, Linde, and Chang-Chang criteria, such as $k_1 = 1, X_T/X_C; k_2 = 1, (X_c/X_T)^2$ and $X_c/X_T; k_3 = 1, Y_T/Y_c$ and $G_{Ic}/G_{IIc}; k_4 = (Y_c/2S_{12})^2, 1$ or Y_c/Y_T .

4.1. Experiments. E-glass and carbon fiber reinforced composite laminates were used in biaxial tests [29]. Their material properties are listed in Tables 1 and 2, respectively.

Biaxial failure for unidirectional T300/914C carbon/epoxy lamina is expressed under combined longitudinal and

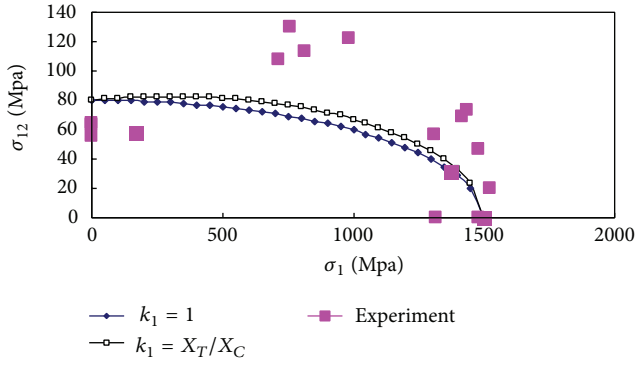


FIGURE 1: Fiber tensile failure envelope.

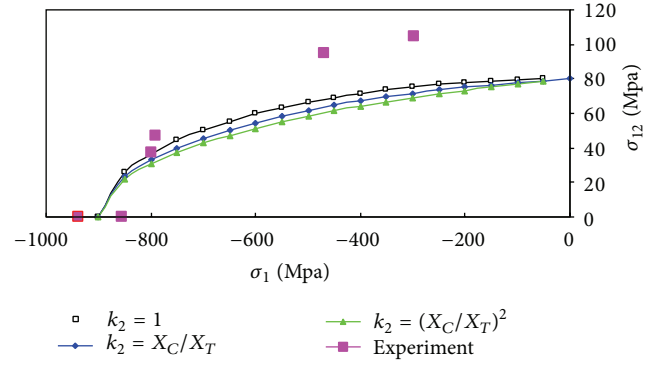


FIGURE 2: Fiber compressive failure envelope.

shear loading (σ_1 versus σ_{12}). The specimens were in the form of axially wound tubes made from prepreg T300/BSL914C carbon/epoxy. The tubes were tested under combined axial tension or compression and torsion. All the tubes were end reinforced and grips were used to transmit the torque to the tubes [29].

Biaxial failure for unidirectional E-glass/Ly556/HT907/DY063 epoxy lamina is expressed under combined transverse and shear loading (σ_2 versus σ_{12}). The tubes with filament wound by circumferentially wound were 60 mm in internal diameter and 2 mm in thickness and were constructed from 62% by volume Vetrotex 21*K43 E-glass fiber (Gevetex) rovings and a Ciba-Geigy epoxy resin system Ly556/HT907/DY063 mixed in weight proportions of 100:85:4. The tubes were cured at 100°C for 2 h and postcured at 150°C for 2 h [29].

4.2. Determination of Parameters. The parameters, $\beta_1 = 1$, $\beta_2 = 1$, $\alpha = 0$, $\gamma = 1$, are assumed, which are based on Chang-Chang criteria, Linde criteria, Hashin criteria, and Hou criteria in two dimensional case. And (1)–(4) of the new criteria should be rewritten as follows.

4.2.1. For Fiber Tensile Failure. Consider

$$d_{ft} = k_1 * \left(\frac{\sigma_1}{X_T} \right)^2 + (1 - k_1) * \frac{\sigma_1}{X_T} + \left(\frac{\sigma_{12}}{S_{12}} \right) \geq 1, \quad \sigma_1 \geq 0, \quad (11)$$

where k_1 is a parameter which can take two values: 1 and X_T/X_C . The curves of (11) are shown in Figure 1. The curve of $k_1 = 1$ and the curve of $k_1 = X_T/X_C$ are both lying between the experimental data, which are both effective. However, the curve of $k_1 = X_T/X_C$ is close to a large number of experimental data above in Figure 1. Therefore, the curve of $k_1 = X_T/X_C$ is used for failure analysis of T300/914C carbon/epoxy lamina.

4.2.2. For Fiber Compressive Failure. Consider

$$d_{fc} = k_2 * \left(\frac{\sigma_1}{X_C} \right)^2 + (k_2 - 1) * \frac{\sigma_1}{X_C} + \left(\frac{\sigma_{12}}{S_{12}} \right) \geq 1, \quad \sigma_1 \leq 0, \quad (12)$$

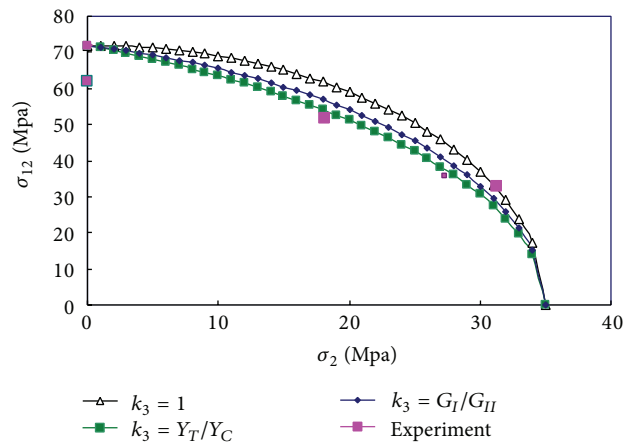


FIGURE 3: Matrix tensile failure envelope.

where k_2 is a parameter which can take three values: 1, $(X_C/X_T)^2$, and X_C/X_T . The curves of (12) are shown in Figure 2. The curve of $k_2 = 1$ is outmost among all curves in Figure 2, and the experimental data is almost out of the envelope of all curves. The difference of the curve of $k_2 = 1$ with the data is minimal. Therefore, the value $k_2 = 1$ should be used for failure analysis of T300/914C carbon/epoxy lamina.

4.2.3. For Matrix Tensile Failure. Consider

$$d_{mt} = k_3 * \left(\frac{\sigma_{22}}{Y_T} \right)^2 + (1 - k_3) * \sigma_{22} + \left(\frac{\sigma_{12}}{S_{12}} \right)^2, \quad \sigma_{22} \geq 0, \quad (13)$$

where k_3 is a parameter which can take three values: 1, Y_T/Y_C , and G_{Ic}/G_{IIc} . The curves of (13) are shown in Figure 3. The number of the experimental data is just five. The curve of $k_3 = Y_T/Y_C$ is nethermost. Three data are just in the curve of $k_3 = Y_T/Y_C$, and the difference of the curve $k_3 = Y_T/Y_C$ is minimal. Therefore, the value $k_3 = Y_T/Y_C$ should be used for failure analysis of E-glass/Ly556/HT907/DY063 epoxy lamina.

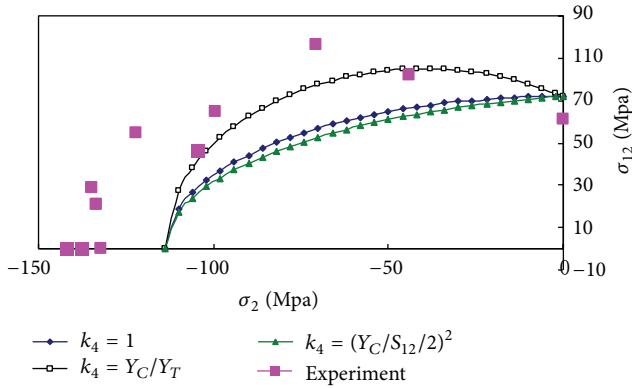


FIGURE 4: Matrix compressive failure envelope.

4.2.4. For Matrix Compressive Failure. Consider

$$d_{mc} = k_4 \left(\frac{\sigma_{22}}{Y_c} \right)^2 + (k_4 - 1) \frac{\sigma_{22}}{Y_c} + \left(\frac{\sigma_{12}}{S_{12}} \right)^2 \geq 1, \quad \sigma_{22} < 0, \quad (14)$$

where k_4 is a parameter which can take three values: $(Y_c/2S_{12})^2$, 1, or Y_c/Y_T . The curves of (14) are shown in Figure 4. Because of the difference between the strength obtained through experiments and that used in material property, three curves are all not perfect. From Figure 4, the curve of $k_4 = Y_c/Y_T$ is close to experimental data. Therefore, the value of $k_4 = Y_c/Y_T$ should be used in failure analysis of E-glass/Ly556/HT907/DY063 epoxy lamina.

From the discussion above, it is found that it is not enough for the damage criterion that has only one set of the parameters. The failure criteria should be adjusted by experimental data for the materials to meet higher accurate requirement.

5. Conclusions

In this work, new two-dimensional failure criteria with four parameters for composite materials are given. The new criteria include fiber failure criteria in tension and compression and matrix failure criteria in tension and compression.

The new criteria can be adjusted with four parameters to consider different material properties in engineering. In general, when we use some known criteria in our study, it has to assume that our material properties are the same as that in the study which proposed the known criteria. Those problems above can be solved by the new criteria proposed in this paper. Meanwhile, when some special values are given to the four internal parameters, the new criteria have the same expression as some classical failure criteria, such as Chang-Chang criteria, Hashin criteria, Linde criteria, and Hou criteria in two dimensional case, which are used frequently in the research of damage process for the composite structures.

In general, the four internal parameters should be chosen by experiments. One example that chooses proper values for the parameters is given, which also validates that there is no one and only set of value for the parameters in any criterion.

Conflict of Interests

The authors declare that there is no conflict of interests regarding the publication of this paper.

Acknowledgment

This work is financially supported by the National Natural Science Foundation of China under Grant 11072202.

References

- [1] S. Agrawal, Kalyan Kumar Singh, and P. K. Sarkar, "Impact damage on fibre-reinforced polymer matrix composite—a review," *Journal of Composite Materials*, vol. 48, no. 3, pp. 317–332, 2014.
- [2] Y. X. Zhang and C. H. Yang, "Recent developments in finite element analysis for laminated composite plates," *Composite Structures*, vol. 88, no. 1, pp. 147–157, 2009.
- [3] A. C. Orifici, I. Herszberg, and R. S. Thomson, "Review of methodologies for composite material modelling incorporating failure," *Composite Structures*, vol. 86, no. 1–3, pp. 194–210, 2008.
- [4] P. F. Liu and J. Y. Zheng, "Recent developments on damage modeling and finite element analysis for composite laminates: a review," *Materials and Design*, vol. 31, no. 8, pp. 3825–3834, 2010.
- [5] J. G. Michopoulos, "On the reducibility of failure theories for composite materials," *Composite Structures*, vol. 86, no. 1–3, pp. 165–176, 2008.
- [6] M. J. Hinton and P. D. Soden, "Failure criteria for composite laminates," *Composites Science and Technology*, vol. 58, no. 7, pp. 1001–1010, 1998.
- [7] P. D. Soden, M. J. Hinton, and A. S. Kaddour, "Lamina properties and lay-up configurations and loading conditions of a range fiber reinforced composite laminates," *Composites Science and Technology*, vol. 58, pp. 1137–1150, 1998.
- [8] P. D. Soden, M. J. Hinton, and A. S. Kaddour, "A comparison of the predictive capabilities of current failure theories for composite laminates," *Composites Science and Technology*, vol. 58, no. 7, pp. 1225–1254, 1998.
- [9] M. J. Hinton, P. D. Soden, and A. S. Kaddour, "Evaluation of failure prediction in composite laminates: background to Part B of the exercise," *Composites Science and Technology*, vol. 62, pp. 1481–1488, 2002.
- [10] M. J. Hinton, A. S. Kaddour, and P. D. Soden, "A further assessment of the predictive capabilities of current failure theories for composite laminates: comparison with experimental evidence," *Composites Science and Technology*, vol. 64, no. 3–4, pp. 549–588, 2004.
- [11] A. S. Kaddour, M. J. Hinton, and P. D. Soden, "A comparison of the predictive capabilities of current failure theories for composite laminates: additional contributions," *Composites Science and Technology*, vol. 64, no. 3–4, pp. 449–476, 2004.
- [12] O. Hoffman, "The brittle strength of orthotropic material," *Journal of Composite Materials*, vol. 9, no. 2, pp. 200–205, 1975.
- [13] R. Narayanaswami and H. M. Adelman, "Evaluation of the tensor polynomial and Hoffman strength theories for composite materials," *Journal of Composite Materials*, vol. 11, no. 4, pp. 366–377, 1977.
- [14] S. W. Tsai and E. M. Wu, "A general theory for anisotropic materials," *Journal of Composite Materials*, vol. 5, pp. 58–80, 1971.

- [15] Z. Haszin, "Failure criteria for unidirectional fiber composites," *Journal of Applied Mechanics, Transactions ASME*, vol. 47, no. 2, pp. 329–334, 1980.
- [16] J. P. Hou, N. Petrinic, C. Ruiz, and S. R. Hallett, "Prediction of impact damage in composite plates," *Composites Science and Technology*, vol. 60, no. 2, pp. 273–281, 2000.
- [17] F.-K. Chang and K.-Y. Chang, "A progressive damage model for laminated composites containing stress concentrations," *Journal of Composite Materials*, vol. 21, no. 9, pp. 834–855, 1987.
- [18] K.-Y. Chang, S. Liu, and F.-K. Chang, "Damage tolerance of laminated composites containing an open hole and subjected to tensile loadings," *Journal of Composite Materials*, vol. 25, no. 3, pp. 274–301, 1991.
- [19] P. Maimi, J. A. Mayugo, and P. P. Camanho, "A three-dimensional damage model for transversely isotropic composite laminates," *Journal of Composite Materials*, vol. 42, no. 25, pp. 2717–2745, 2008.
- [20] P. Maimi, P. P. Camanho, J. A. Mayugo, and C. G. Dávila, "A continuum damage model for composite laminates—part I—constitutive model," *Mechanics of Materials*, vol. 39, no. 10, pp. 897–908, 2007.
- [21] P. Linde, J. Pleitner, H. D. Boer, and C. Carmore, "Modelling and simulation of fiber metal laminates," in *Proceedings of the ABAQUS User's Conference*, pp. 421–439, Boston, Mass, USA, 2004.
- [22] C. Santiuste, S. Sánchez-Sáez, and E. Barbero, "A comparison of progressive failure of composite laminated beams," *Composite Structures*, vol. 92, pp. 2406–2414, 2010.
- [23] T. Anderson, *Fracture Mechanics—Fundamentals and Applications*, 2nd edition, 1995.
- [24] I. M. Daniel and O. Ishai, *Engineering Mechanics of Composite Materials*, Oxford University, 1994.
- [25] S. T. Pinho, *Modelling failure of laminated composites using physically based failure models [Ph.D. thesis]*, Imperial College, 2005.
- [26] M. I. Ribeiro, Volnei Tita, and D. Vandepitte, "A new damage model for composite laminates," *Composite Structures*, vol. 94, pp. 635–642, 2012.
- [27] R. M. Richard and J. R. Blacklock, "Finite element analysis of inelastic structures," *AIAA Journal*, vol. 7, pp. 432–438, 1969.
- [28] A. Puck and H. Schürmann, "Failure analysis of FRP laminates by means of physically based phenomenological models," *Composites Science and Technology*, vol. 62, no. 12-13, pp. 1633–1662, 2002.
- [29] P. D. Soden, M. J. Hinton, and A. S. Kaddour, "Biaxial test results for strength and deformation of a range of E-glass and carbon fibre reinforced composite laminates: failure exercise benchmark data," *Composites Science and Technology*, vol. 62, no. 12-13, pp. 1489–1514, 2002.

Research Article

Prediction of Effects of Geogrid Reinforced Granular Fill on the Behaviour of Static Liquefaction

A. Hemalatha,¹ N. Mahendran,² and G. Ganesh Prabhu³

¹ NPR College of Engineering and Technology, Dindigul, Tamil Nadu 624401, India

² PSNA College of Engineering and Technology, Dindigul, Tamil Nadu 624622, India

³ Department of Civil Engineering, Chungnam National University, Daejeon 305-764, Republic of Korea

Correspondence should be addressed to G. Ganesh Prabhu; gganeshlingesh@gmail.com

Received 3 March 2014; Revised 23 April 2014; Accepted 23 April 2014; Published 20 May 2014

Academic Editor: Gonzalo Martínez-Barrera

Copyright © 2014 A. Hemalatha et al. This is an open access article distributed under the Creative Commons Attribution License, which permits unrestricted use, distribution, and reproduction in any medium, provided the original work is properly cited.

The experimental investigation on the effects of granular fill and geogrid reinforced granular fill on the behaviour of the static liquefaction potential of the subsoil is reported in this study. A series of plate load test were carried out with different thickness of the granular fill, number of geogrid layers, and size/dimension of the footing. The test results were presented in terms of bearing capacity and subgrade modulus for the settlement of δ_{10} , δ_{15} , and δ_{20} . The experimental results revealed that the introduction of granular fill significantly increases the bearing capacity and effectively control the settlement behaviour of the footing. The introduction of geogrid in granular fill enhanced the Percentage of Control in Settlement and Bearing Capacity Ratio by a maximum of 328.54% and 203.41%, respectively. The introduction of geogrid in granular fill interrupts the failure zone of the granular fill and enhances the subgrade modulus of the footing by a maximum of 255.55%; in addition subgrade modulus of the footing was increased with an increase in the number of geogrid layers. Based on the test results it is suggested that the footing with large size has beneficial improvement on the reinforced granular fill.

1. Introduction

The liquefaction behaviour of soil during earthquakes has severely damaged the various buildings, roads, and other structures. Static liquefaction of loose and very loose saturated sands is a modern classical mechanics subject and the sudden increase in pore water pressure causes subsidence of foundations and damage to earth structures. Therefore, it is very important to consider the liquefaction potential of dams, embankments, slopes, foundation materials, and placed fills [1] in addition to the fact that a new stabilization method should be identified to efficiently combat this problem. The traditional improvement methods to prevent the liquefaction of granular soils are draining and densification techniques such as dynamic compaction, vibro techniques, stone columns, and compaction grouting [2]. Another technique to enhance the strength of the soil is using chemical admixtures like calcium carbonate powder, cement, lime, fly ash, and so forth [3, 4]. Even though these techniques have been shown to be successful in practice, densification and draining of deep

soil profiles are often ineffective [5] and they required heavy equipment. Recently reinforcing of soil using geocomposites has been emerged and the tension and lateral confinement provided by reinforcement significantly increase the strength properties of the soil and also the reinforced soil effectively sustains the applied loads [6]. The main advantages of mixing discontinuous fibers with a soil mass are the absence of potential planes of weakness that can develop parallel to oriented reinforcement [7]. However, compared with these, reinforcing of soil using geogrid is very simple and the primary advantages of the geogrid are providing lateral and vertical restraint to the soil mass and significantly reduce the settlement [8]. In the past few decades, the application of geogrids in soil reinforcing has been widely carried out and reported.

Alawaji [9] studied the effects of width and depth of the geogrid on the behaviour of collapse settlement, deformation modulus, and bearing capacity of collapsible soil. The increase in geogrid width and decrease in depth increase the efficiency of the geogrid system. The geogrid having a width

of four times the diameter of loaded areas and a depth of $0.1D$ is recommended as an efficient and economical reinforcement. Liu et al. [10] conducted a large scale, shear test to study the interface shear strength of different soils (sand, gravel, and laterite) against PET-yarn geogrids of various tensile strengths and the test results had shown that the soil/PET-yarn geotextile interface has significantly lower shear strength than soil strength. Phanikumar et al. [11] conducted a series of laboratory plate load tests on fine, medium, and coarse sand beds reinforced with different layers of circular geogrids of 120 mm diameter. Test results had shown that the increase in the number of geogrid layers and decrease in spacing between them improve the load-settlement response and Load Improvement Ratio (LIR) further. The large scale direct shear test on geogrid reinforced fresh and fouled ballast indicated that the geogrid considerably increases the shear strength and apparent angle of shearing resistance [12]. Field test using seven different footing diameters and different granular fill layer thicknesses was conducted by Ornek et al. [13]. The test results indicated that the use of granular fill layers over natural clay soil has a considerable effect on the bearing capacity characteristics. Demir et al. [14] carried out sixteen field tests to evaluate the effects of replacing natural clay soil with a stiffer granular fill layer and single-multiple layers of geogrid reinforcement. The test results had shown that use of granular fill and geogrid for reinforced soil footings (RSF) has considerable effects on the subgrade modulus and bearing capacity. Very recently Kolay et al. [15] investigated the improvement in the bearing capacity of silty clay soil with thin sand layer on top and placing geogrids at different depths. The test results revealed that the bearing capacity for the soil increases with the increase in number of geogrid layers.

The research carried out so far focused on increasing the shear strength capacity of the soil using geogrid and also none of these studies demonstrated the influence of geogrid sheets in improving liquefaction resistance of granular soil. In addition, studies that are related to large scale field test on bearing capacity of geogrid reinforced soil are very limited. The main objective of this study is to experimentally investigate the effects of granular fill and geogrid multiple layers in the behaviour of bearing capacity and static liquefaction resistance. Plate load tests were conducted using model footing to evaluate the granular fill and geogrid multiple layers in liquefaction resistance of soil in terms of bearing capacity and settlement behaviour. The experimental parameters were thickness of the granular fill ($0.30D$, $0.45D$, $0.60D$, $0.75D$, and $0.90D$), number of geogrid layers (one and two), and size/dimension of the footing ($0.5D$ and $0.75D$).

2. Experimental Program

2.1. Material Properties

2.1.1. Subsoil Characterization. The entire testing program was carried out in the coastal area located in Nagapattinam Taluk, Thanjavur District, Tamilnadu, India. Geotechnical site investigation both laboratory and in situ tests were

TABLE 1: Properties of geogrid.

1	Structure	Bidirectional
2	Aperture shape	Square
3	Mesh aperture size	10×10 mm
4	Raw material	Polypropylene
5	Colour	Black
6	Thickness of sheet	4 mm
7	Tensile strength	15 kN/m
8	Elongation at nominal strength	22.7%

conducted to explore the soil properties in the experimental test area [16]. In situ tests such as borehole drillings and test pit excavation were performed to identify the soil profile of the experimental test area and four types of subsoil were identified [17]. A layer of transported soil having a depth of 1 m was observed initially. After that a layer of silty clay marl was observed between the depths of 1 m and 5 m. Stiffened clay later was observed below the silty clay marl between the depths of 5 m and 9 m. After 9 m depth, the soil layer was changed from clay to hard strata. The excavation continued up to the depth of 12 m, a layer of limestone profile was observed at the depth of 12 m. The standard penetration test [18] was conducted during the drilling process and “ N ” value was varied in the range of $5N$ to $50N$ as shown in Figure 1. The specific gravity values of the soils were determined from the laboratory test [19] and the value varies in the range of 2.6 to 2.71 along the entire depths which is shown in Figure 2. Unconfined shear strength (c_u) of the soil samples was evaluated [20] through an unconfined compression test and the value varies between 60 and 75 kN/m^2 as shown in Figure 3.

2.1.2. Granular Fill Material. Silty gravel obtained from Karaikudi, Sivagangai District, Tamilnadu, India was used as a granular fill material in this study. The conventional laboratory tests were conducted to obtain the engineering properties of the granular fill [21]. The specific gravity value [19] of the granular fill was about 2.64. From the standard proctor compaction test [22] the optimum moisture content and maximum dry unit weight were obtained and the values were about 7% and 21.7 kN/m^3 , as shown in Figure 4. The direct shear test [23] was performed and the obtained internal friction angle and the cohesion of the granular fill were 43° and 15 kN/m^2 . In order to keep the homogeneity granular fill passing through 4.75 mm was used in both laboratory and field tests.

2.1.3. Geogrid. Netlon 121 CE was used as horizontal geogrid reinforcement in this study. It is a bidirectional polypropylene sheet having a thickness of 4 mm. The maximum tensile strength of the sheet was 15 kN/m^2 with a square aperture size of 100 mm^2 (10×10 mm). The typical geogrid sheet is shown in Figure 5. The physical and mechanical properties of the geogrid provided by the manufacturer are summarized in Table 1.

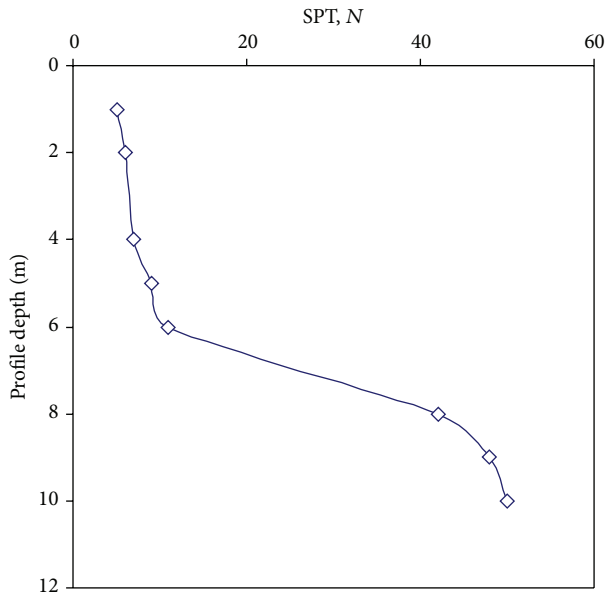


FIGURE 1: Typical SPT (N) values obtained from borehole drillings.

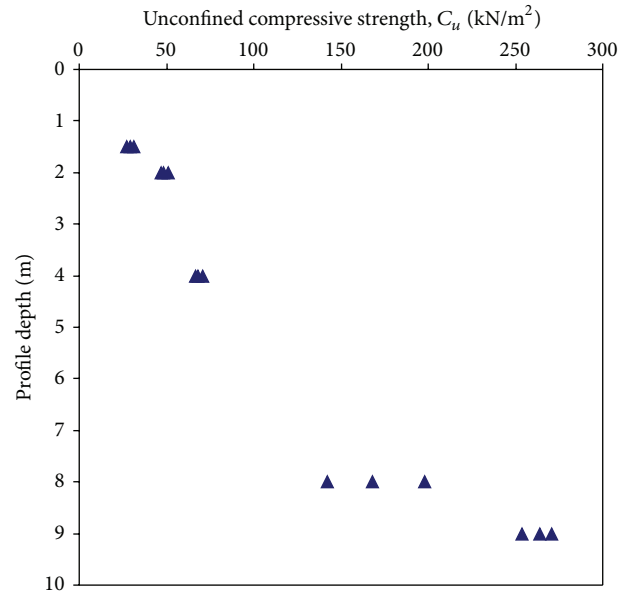


FIGURE 3: Unconfined shear strength distribution of subsoil.

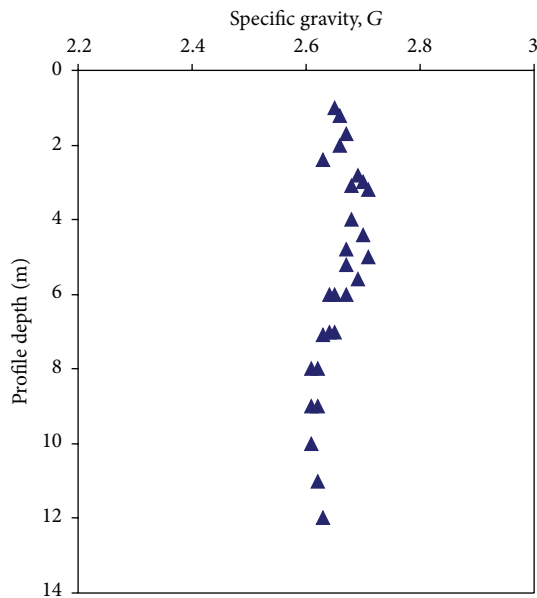


FIGURE 2: Specific gravity distribution of subsoil.

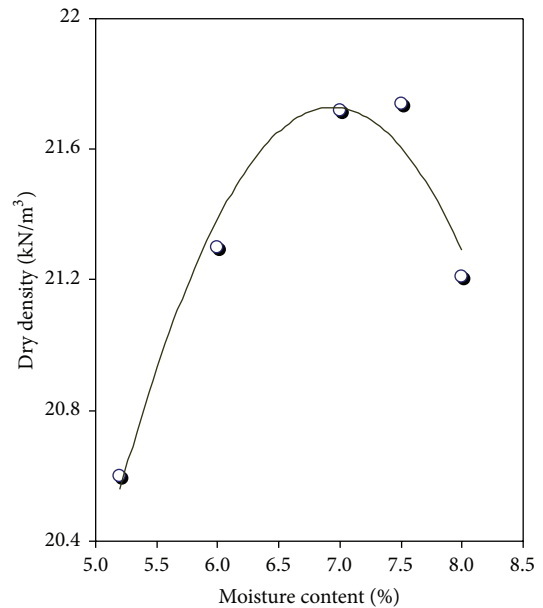


FIGURE 4: Standard proctor compaction test curve for granular fill.

2.2. *Experimental Setup and Procedures.* After the laboratory and in situ test, the reaction loading frame was installed at the site. After that the 1.6 m depth of soil was removed and the surface of the test area was leveled. For granular fill initially, the amount of granular fill and water required for each layer was calculated then the granular fill and the water was mixed well using a counter current mixer. After that the granular fill was placed layer by layer and the layer was compacted using an earth rammer to the predetermined height to achieve the desired density. The size of the foundation of 2.1×2.1 m was kept constantly in the entire test and the depth of the granular fill or thickness of granular fill (H) was varied according to

the footing diameter ($0.30D$, $0.50D$, $0.70D$, and $0.90D$). For each reinforced condition, the granular fill was prepared in the above same manner and the layer was compacted to the predetermined height. When the granular fill reached the preferred depth, a layer of geogrid was placed and then the compaction was continued until the granular fill reached its desired height. The footing was positioned on the ground, taking care to ensure that its centerline was exactly in line with the axis of the hydraulic jack and the loading frame. The downward load was applied to the footing or base plate by a hydraulic jack and the axial deformation of the footing was measured by using two linear voltage displacement



FIGURE 5: Netlon 121 CE, geogrid.

transducers (LVDT) which was kept at the top surface of the footing. The hydraulic jack and the two linear variable displacement transducers (LVDT) were connected to a data logger. The testing program was performed according to the ASTM D 1196-93 (ASTM, 1997) and the testing program was stopped; neither the applied vertical load was obviously reduced nor the settlement of the footing was considerable for the small increment in the applied load. The experimental setup is shown in Figure 6. The influence of granular fill with and without geogrid on the behaviour of bearing capacity and liquefaction was studied in this research. Three series of tests such as Series I, Series II, and Series III were performed. Series I consisted of various diameters (D) of the footing ($0.50M$ and $0.75M$) on the surface that is without granular fill and geogrid. Series II is very similar to Series I, except the footing was placed on the top of the granular fill with various thicknesses (H) according to the footing diameter ($0.30D$, $0.50D$, $0.75D$, and $0.90D$). Series III consisted of footing on the granular fill with geogrid reinforcement. The experimental parameters are number of geogrid layers (N) (one and two) and the distance between the bottom surface of the footing to the top of the geogrid layer (H_{FTG}) ($0.1D$ and $0.2D$). Throughout the test the distance between the two geogrid layers was kept constant as 200 mm (H_{GG}).

3. Description of Tests

To identify the tests easily, sixteen tests in three series were designated with names such as $RT-0.50M$ and $RT-0.75M$ (Series I); $0.50-G(0.30D)$, $0.50-G(0.50D)$, $0.50-G(0.75D)$, $0.50-G(0.90D)$, $0.75-G(0.30D)$, $0.75-G(0.50D)$, $0.75-G(0.75D)$, and $0.75-G(0.90D)$ (Series II); $0.50-N1-0.1D$, $0.50-N1-0.2D$, $0.50-N2-0.1D$, $0.75-N1-0.1D$, $0.75-N1-0.2D$, and $0.75-N2-0.1D$ (Series III). For example, in test $RT-0.50M$, first character “RT” indicates the reference test and the second character refers to the footing diameter. In test $0.75-G(0.30D)$, number “0.75” refers to the footing diameter and the following character “G(0.30D)” indicates the granular fill having a thickness of 0.30 of diameter of the footing. In test $0.50-N1-0.2D$, number “0.50” refers to the

footing diameter and next character indicates the number of geogrid layers (one and two) and the last “0.2D” indicates the depth of the geogrid layer from the bottom of the footing.

4. Results and Discussion

4.1. Series I: without Granular Fill and Geogrid. A total of two tests with the footing size of 0.50 m and 0.75 m ($RT-0.50D$ and $RT-0.75D$) were conducted in Series I without any soil improvement. It is the reference test which is used to compare the test results of Series II and Series III. The Load-settlement behaviour of the unimproved soil for both footing sizes is shown in Figure 7. In all reference tests, from the initial stage, the settlement of the footing is directly proportional to the applied pressure, and the load-settlement behaviour of the tests in Figure 8 is clear evidence for the local shear failure of the subsoil. In addition to that, in both tests the ultimate bearing capacity of the soil was not clearly identified. From the load-settlement plots, the subgrade modulus of the soil was calculated by (1) and the subgrade modulus were calculated for the settlement of δ_{10} , δ_{15} , and δ_{20} , since determining the bearing capacity and subgrade modulus would have been more appropriate for the case where allowable settlement controls performance. The results were shown and listed in Figure 9 and Table 2, respectively:

$$k = \frac{q}{\delta}, \quad (1)$$

where k is subgrade modulus, q is the bearing capacity, and δ is the footing settlement. Figure 8 clearly shows that the subgrade modulus of the soil increased when increasing the footing size and the subgrade modulus was decreased with the increase in footing settlement. The results were discussed in terms of settlement to diameter ratio (s/D). Figures 7 and 8 clearly show that the experimental results revealed that the bearing capacity of the soil was increased when increasing the size of the footing. This is a result of the fact that the increase in resistive pressure area exerted by the soil and the development of resistive pressure is directly proportional to the footing area. The bearing capacity value of both tests was obtained at the s/D ratio of 3% [13], and the bearing capacity value of the test $RT-0.50M$ was 216 kN/m^2 which is 47.5% less than the test $RT-0.75M$. In addition the s/D ratio of 2% and 4% was used throughout the test to discuss the enhancement in bearing capacity.

4.2. Series II: with Granular Fill and without Geogrid. The influence of granular fill and the increase in granular fill thickness on the behaviour of bearing capacity and the settlement of the footing were evaluated [24] in Series II. A series of tests with the footing diameter of $0.50M$ and $0.75M$ was conducted on the granular fill bed and the thickness of the granular fill was varied according to the footing diameter ($0.30D$, $0.50D$, $0.75D$, and $0.90D$). The applied load and the corresponding settlement for various thicknesses of granular fill in both cases are shown in Figures 9 and 10. From Figures 9 and 10, it can be seen that, for a small load range, the relation

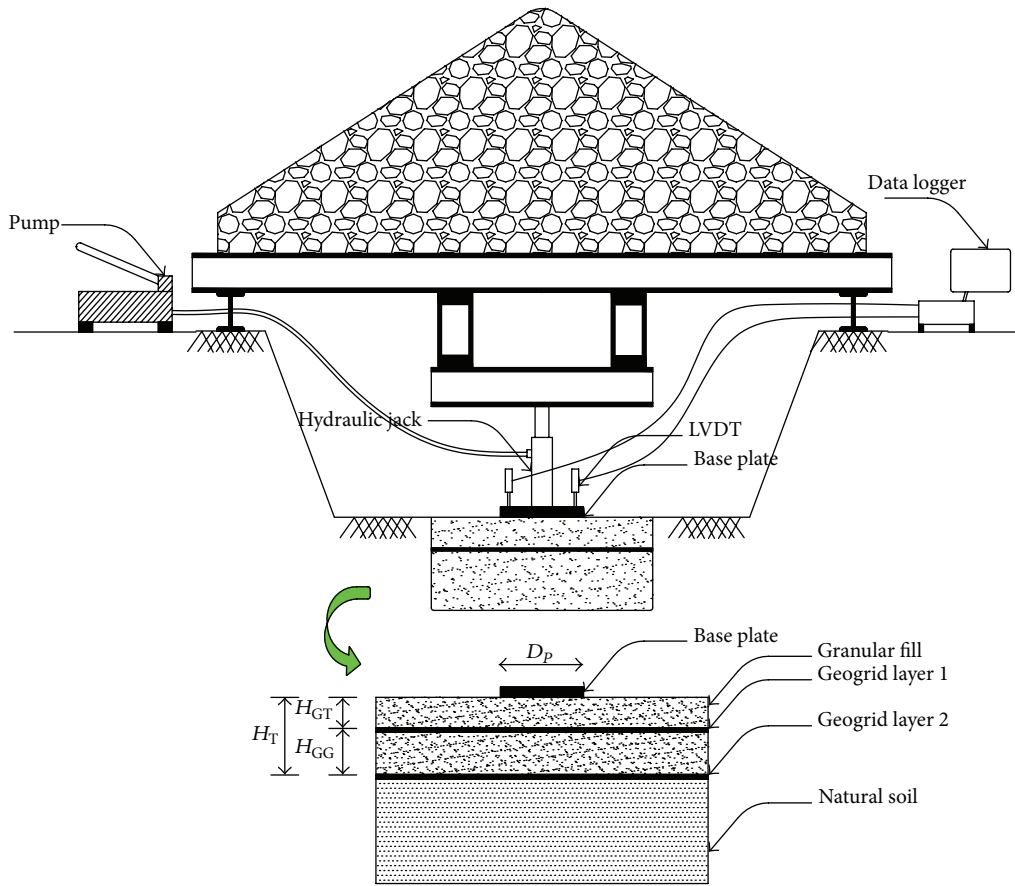


FIGURE 6: Experimental setup.

TABLE 2: Bearing capacity and subgrade modulus for Series I, II, and III.

Test series	Test names	Bearing capacity (kN/m ²)			Subgrade modulus (MN/m ³)		
		δ —10 mm (δ_{10})	δ —15 mm (δ_{15})	δ —20 mm (δ_{20})	δ —10 mm (δ_{10})	δ —15 mm (δ_{15})	δ —20 mm (δ_{20})
Series I	RT-0.50D	172	216	240	17.20	14.40	12.00
	RT-0.75	244	292	324	24.40	19.47	16.20
Series II	0.50-G(0.30D)	320	388	428	32.00	25.87	21.40
	0.50-G(0.50D)	368	442	488	36.80	29.47	24.40
	0.50-G(0.75D)	448	518	556	44.80	34.53	27.80
	0.50-G(0.90D)	488	556	588	48.80	37.07	29.40
	0.75-G(0.30D)	340	416	456	34.00	27.73	22.80
	0.75-G(0.50D)	410	484	518	41.00	32.27	25.90
	0.75-G(0.75D)	474	536	570	47.40	35.73	28.50
	0.75-G(0.90D)	542	618	658	54.20	41.20	32.90
Series III	0.50-N1-0.1D	686	768	818	68.60	51.20	40.90
	0.50-N1-0.2D	578	656	698	57.80	43.73	34.90
	0.50-N2-0.1D	760	828	836	76.00	55.20	41.80
	0.75-N1-0.1D	716	796	842	71.60	53.07	42.10
	0.75-N1-0.2D	595	678	728	59.50	45.20	36.40
	0.75-N2-0.1D	784	850	890	78.40	56.67	44.50

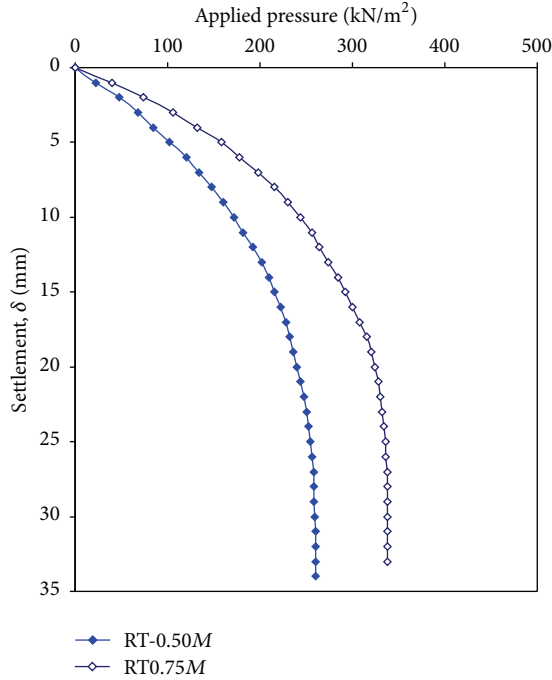


FIGURE 7: Load-settlement curve for reference tests, comparison.

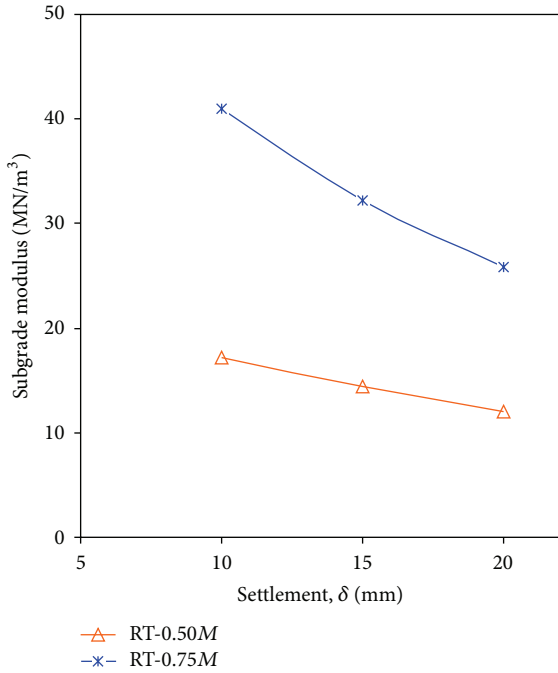


FIGURE 8: Subgrade modulus for reference tests, comparison.

between the applied load and settlement exhibited the linear behaviour, loading further the load-settlement behaviour has become nonlinear and in addition the peak load was not clearly identified. The failure mode observed in all test of Series II was a local shear failure. The experimental results revealed that the introduction of granular fill significantly increases the bearing capacity and effectively control the

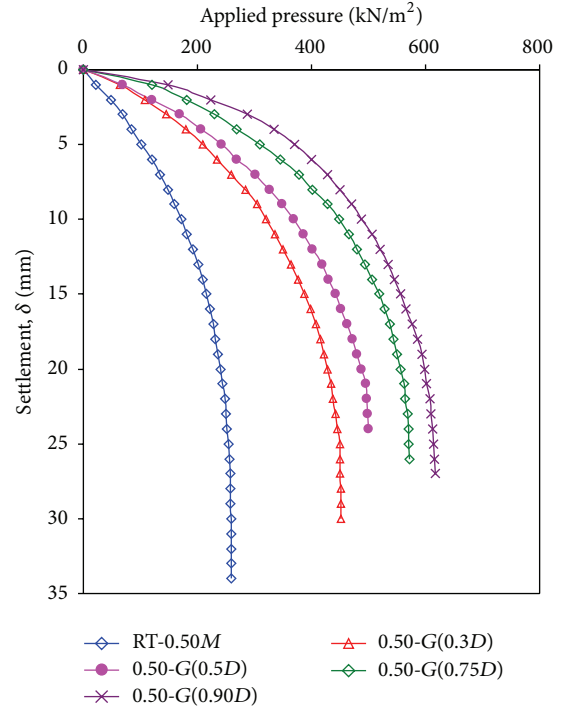


FIGURE 9: Load-settlement curve for Series II ($D = 0.50M$), comparison.

static liquefaction of the subsoil and in addition the load-settlement behaviour becomes very stiffer with the increase in the H/D ratio, namely, increase in granular fill thickness. The placing of granular fill decreases the pore water pressure developed because of a decrease in interstitial pressure distribution. The performance improvements of bearing capacity due to the granular fill are expressed in terms of Bearing Capacity Ratio (BCR) [14] and the following equation was used for evaluating the BCR:

$$BCR = \frac{q_G}{q_0}, \tag{2}$$

where q_G is the bearing capacity of the soil reinforced with granular fill and q_0 is the bearing capacity of the unreinforced or reference soil. The BCR ratio was obtained for the s/D ratio of 3%. The relation between BCR and H/D ratio is shown in Figure 11. From Figure 12, it can be observed that the bearing capacity and the BCR value of the footing have increased with the increase in granular fill thickness in all cases. However, the BCR has decreased when increasing the footing diameter. Figure 11 clearly shows that the correlation between the granular fill thickness and BCR was too strong for all footing diameters ($R^2 = 0.985$). Figures 9, 10, and 11 clearly show that the bearing capacity of the footing was significantly increased for the granular fill having the thickness of $H/D = 0.75$; however, a close observation of Figures 9, 10, and 11 exhibits that the enhancement of bearing capacity is not significant beyond the H/D value of 0.75. From the results, the granular fill having a thickness of $H/D = 0.75$ was selected as the most advantageous fill height and the same

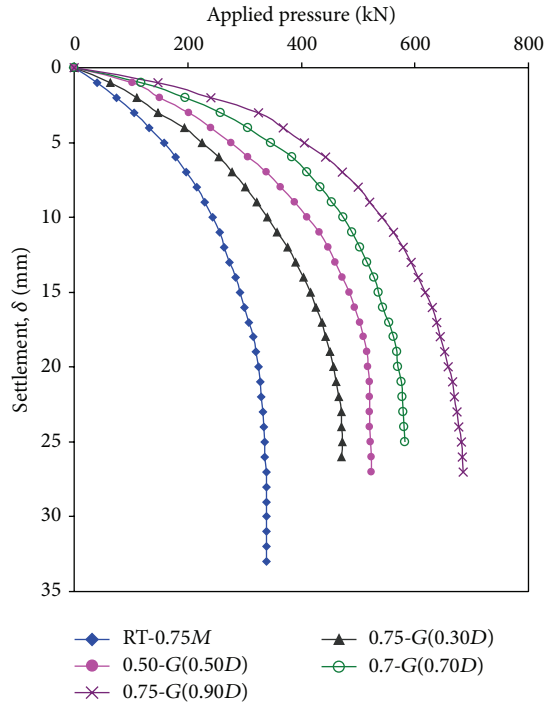


FIGURE 10: Load-settlement curve for Series II ($D = 0.75M$), comparison.

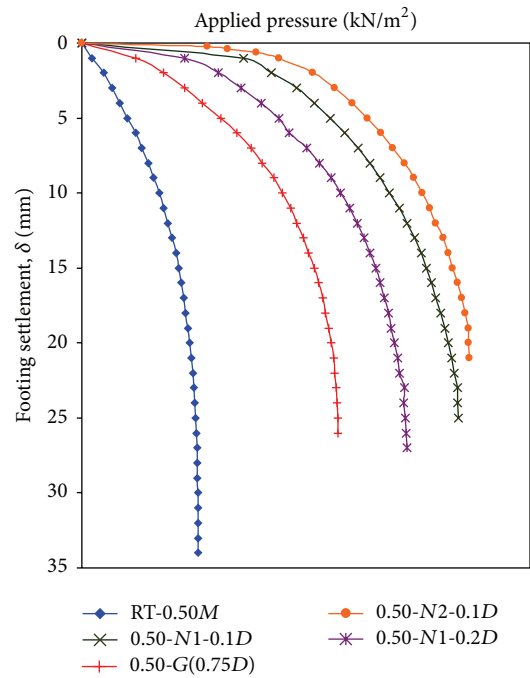


FIGURE 12: Load-settlement curve for Series III ($D = 0.50M$), comparison.

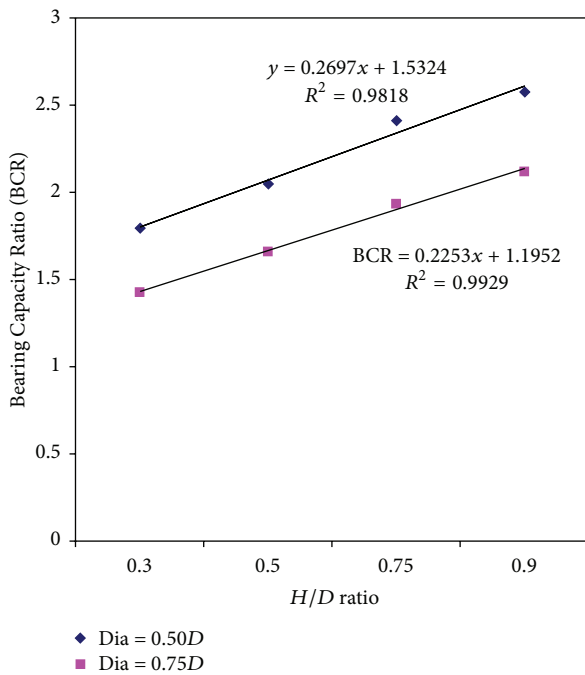


FIGURE 11: Bearing Capacity Ratio (BCR) for Series I, comparison.

thickness was introduced in Series III. Compared to the RT-0.50M, test 0.50-G(0.75D) increased its load bearing capacity by 30.21%, in similar manner test 0.75-G(0.75D) increased its bearing capacity by 32.68% than that of RT-0.75M.

4.3. Series III: Geogrid Reinforced Granular Fill. The main objective of this research is to effectively evaluate the influence of geogrid reinforced granular fill on the behaviour of bearing capacity, subgrade modulus, and BCR. From the test results obtained from Series II, the thickness of granular fill was maintained as $H = 0.75D$ throughout the test. Figures 12 and 13 show the load-settlement behaviour of different footing with different geogrid layers. As expected the introduction of single geogrid layers at the distance of $0.1D$ from the bottom surface of the footing in both footing cases comparatively improves the liquefaction behaviour of the soil, load-settlement behaviour, and the bearing capacity which is shown in Figures 12 and 13. This is a result of the fact that the introduction of geogrid interrupts the failure zone of the granular fill and the stress sharing area has been increased at a geogrid depth due to the wider dispersion of stress affected by horizontal geogrid reinforcement [11]. As a result, the stress in the granular fill considerably reduced, resulting in a smaller amount of settlement. Another possible reason is that the tensile stress in geogrid is produced by the applied load fully defied by the geogrid resulting in improved load-settlement behaviour of the system. The results in Figures 12 and 13 show that, when lifting up the depth of geogrid from $0.1D$ to $0.2D$ (test 0.50-N1-0.2D), the test results have not shown any considerable improvement in the load-settlement behaviour and in addition the bearing capacity was moderately low when compared to the test 0.50-N1-0.1D. From the observation, it can be understood that the geogrid very near to footing will provide considerable improvement in the load-settlement behaviour and bearing capacity and the introduction of geogrid at profound depths

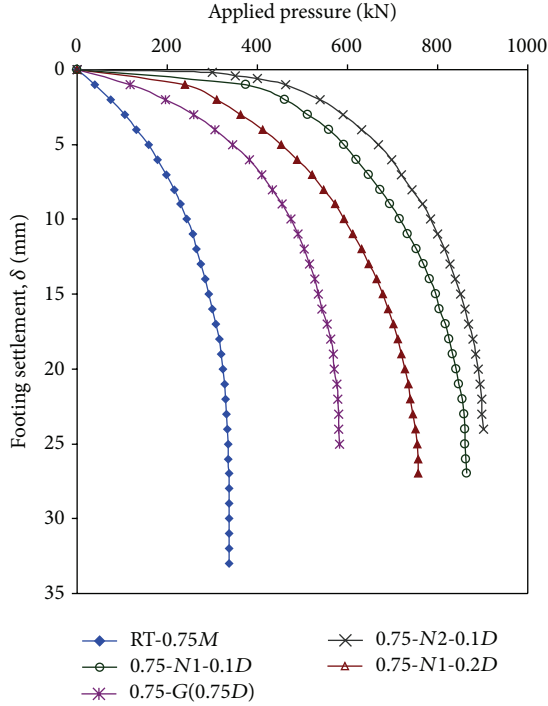


FIGURE 13: Load-settlement curve for Series III ($D = 0.75M$), comparison.

is not advisable. The decrease in performance may be due to the depth of reinforcement considerably deep, and resulting work efficiency of the geogrid has decreased. The above similar finding was observed in footing with the diameter of $0.75D$. The introduction of another geogrid layer with the H_{GG} of 200 mm (0.50-N2-0.1D) in the granular fill, showing further improvement in the load-settlement behaviour and the beneficial effect, is much greater than that of a granular fill with single layer in both footing cases ($0.50M$ and $0.75M$). This is a result of the fact that during loading the interlocking between the geogrid and granular fill has greatly improved and the geogrid reinforced granular fill started to behave like a geogrid composite plate. This composite plate action significantly resists the applied pressure and slows down the soil failure and also significantly restrains the load-settlement behaviour. The influence of the geogrid reinforced granular fill on the behaviour settlement compared to the unreinforced footing evaluated through the parameter called Percentage of Control in Settlement (PCS). The PCS were calculated at the settlement of δ_{15} or for the s/D ratio of 3% using the following equation:

$$PCS = \frac{\delta_{15} - \delta_R}{\delta_R} \times 100, \quad (3)$$

where δ_{15} is the settlement of the unreinforced footing and δ_R is the settlement of the reinforced footing at the footing pressure of unreinforced one having a settlement value of δ_{15} . Figures 14 and 15 show the comparison of PCS factors with respect to the footing with granular fill (0.50-G(0.75D) and 0.75-G(0.75D)). Compared to 0.50-G(0.75D),

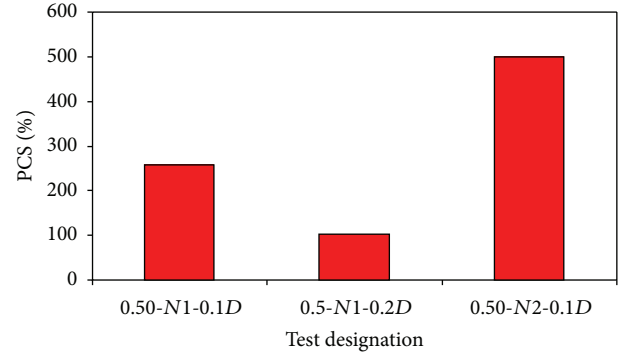


FIGURE 14: Percentage of Control in Settlement (PCS) for Series III ($D = 0.50M$).

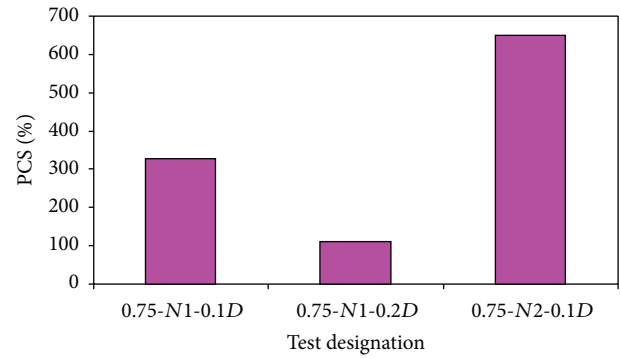


FIGURE 15: Percentage of Control in Settlement (PCS) for Series III ($D = 0.75M$).

the test 0.50-N1-0.1D and 0.50-N1-0.2D increased its PCS by 257.14% and 101.25%, respectively, as shown in Figure 14. Compared to 0.70-G(0.75D), tests 0.75-N1-0.1D and 0.75-N1-0.2D improved their PCS by 328.54% and 111.54%, respectively, which is shown in Figure 15. Compared to the single layer of geogrid, the PCS of granular fill reinforced with two layers of geogrid was outperformed and the tests 0.50-N2-0.1D and 0.75-N2-0.1D enhanced their PCS by 67.15% and 81.74%, respectively, when compared to the tests 0.50-N1-0.1D and 0.75-N1-0.1D, respectively.

The Bearing Capacity Ratio (BCR) for each test was calculated from (1) for the settlement of δ_{10} , δ_{15} , and δ_{20} . From Figure 16, it can be understood that the BCR increases with the increase in the number of geogrid layers. However, Figure 16 clearly shows that the BCR value of the reinforced granular fill has decreased with increase in settlement in all cases. This may be attributed to the composite layer of geogrid not able to affect the dispersion of stress at large settlement and not able to defy the tensile stress induced by the applied pressure. The tests 0.50-N1-0.1D and 0.50-N1-0.2D increased their BCR by 203.41% and 157.26%, respectively, when compared to 0.50-G(0.75D); their BCR values were 3.55 and 3.07, respectively, at the s/D ratio of 3%. Also tests 0.75-N1-0.1D and 0.75-N1-0.2D improved their BCR by 115.87% and 87.15% than that of 0.75-G(0.75D) and the BCR values were 2.89 and 2.32 which is shown in Figure 17.

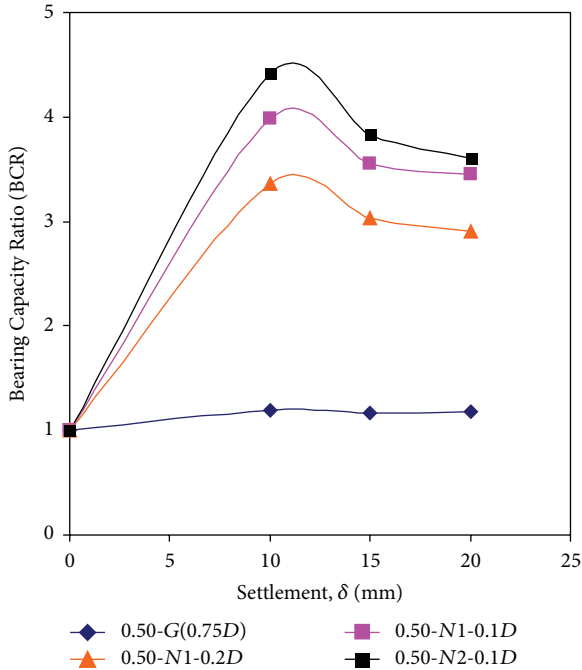


FIGURE 16: Bearing Capacity Ratio (BCR) for Series III ($D = 0.50M$), comparison.

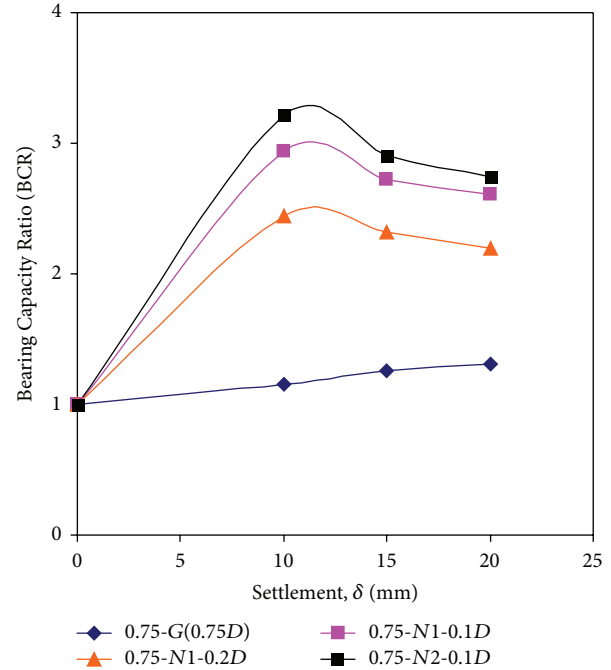


FIGURE 17: Bearing Capacity Ratio (BCR) for Series III ($D = 0.75M$), comparison.

The comparison of subgrade modulus obtained from series III at the settlement of δ_{10} , δ_{15} , and δ_{20} is shown in Figures 18 and 19 and presented in Table 2. Figures 18 and 19 mean that the subgrade modulus of the footing decreased with the increase in settlement and in addition the introduction of geogrid in granular fill enhances the subgrade modulus and reduces the footing settlement. At the s/D ratio of 3% the subgrade modulus of the tests 0.50-N1-0.1D, 0.50-N1-0.2D, 0.75-N1-0.1D, and 0.75-N1-0.2D was 51.21 MN/m^3 , 43.73 MN/m^3 , 53.67 MN/m^3 , and 45.21 MN/m^3 , respectively, which is 255.55%, 203.68%, 176.507%, and 132.97%, respectively, higher than that of an unreinforced footing (RT-0.50D and RT-0.75D). On the whole geogrid reinforced granular fill resulted in improved load-settlement behaviour, load bearing capacity, and decrease in internal pore water pressure resulting in liquefaction control and in addition provided a more economic advantage. Based on the test results it is suggested that the footing with large size has beneficial improvement on the reinforced granular fill.

5. Conclusion

A series of field tests were carried out to understand the influence of granular fill and the geogrid reinforced granular fill on the behaviour of static liquefaction potential, bearing capacity, and load-settlement behaviour of the subsoil in the coastal area located in Nagapattinam Taluk, Thanjavur District, Tamilnadu. Based on the test results the following conclusion can be made.

- (i) In all reference tests, the failure mode of the subsoil was a local shear failure and in addition the ultimate

bearing capacity of the subsoil was not clearly identified.

- (ii) The introduction of granular fill significantly increases the bearing capacity and effectively controls the static liquefaction of the subsoil
- (iii) Compared to the reference test, the introduction of granular fill, with the depth of $0.3D$, $0.50D$, and $0.75D$, increased its load bearing capacity of the footing by 6.84%, 16.2054%, and 30.21%, respectively, and the bearing capacity values were 388 kN/m^2 , 442 kN/m^2 , and 518 kN/m^2 , respectively.
- (iv) The introduction of geogrid very near to footing will provide considerable improvement in the load-settlement behaviour and bearing capacity and the introduction of geogrid at profound depths is not advisable.
- (v) Compared to 0.50-G(0.75D), the tests 0.50-N1-0.1D and 0.50-N1-0.2D increased their PCS by 257.14% and 101.25%, respectively.
- (vi) The subgrade modulus of the footing decreased with the increase in settlement and in addition the introduction of geogrid in granular fill enhances the subgrade modulus and reduces the footing settlement.
- (vii) The geogrid reinforced granular fill resulted in improved load-settlement behaviour, load bearing capacity, and decrease in internal pore water pressure resulting in liquefaction control and in addition provided a more economic advantage. It is suggested that the footing with large size has beneficial improvement on the reinforced granular fill.

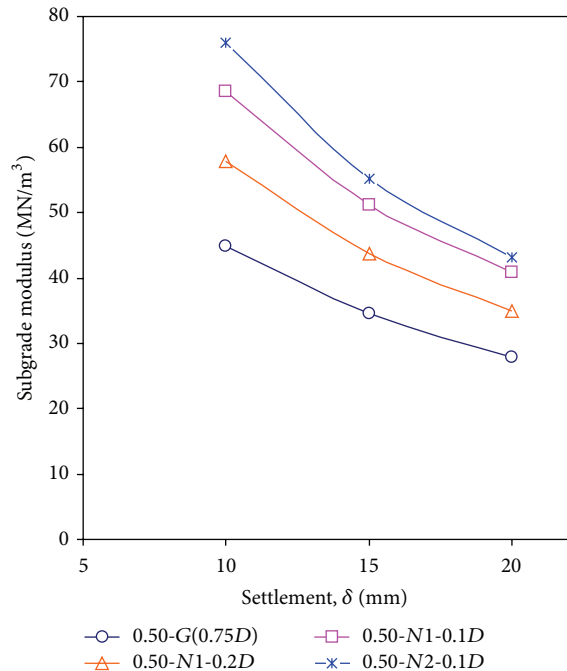


FIGURE 18: Subgrade modulus for Series III ($D = 0.50M$), comparison.

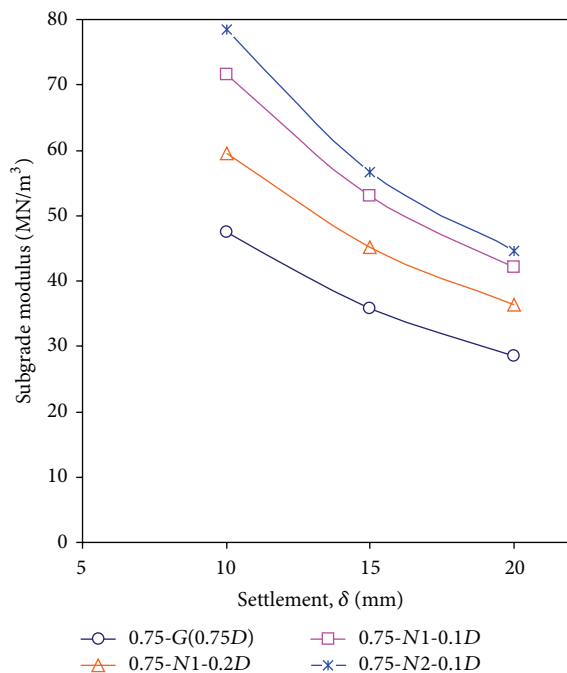


FIGURE 19: Subgrade modulus for Series III ($D = 0.75M$), comparison.

Conflict of Interests

The authors declare that there is no conflict of interests regarding the publication of this paper.

References

- [1] J. Liu, G. Wang, T. Kamai, F. Zhang, J. Yang, and B. Shi, "Static liquefaction behavior of saturated fiber-reinforced sand in undrained ring-shear tests," *Geotextiles and Geomembranes*, vol. 29, no. 5, pp. 462–471, 2011.
- [2] D. Forcellini and A. M. Tarantino, "Assessment of stone columns as a mitigation technique of liquefaction-induced effects during Italian earthquakes (May 2012)," *The Scientific World Journal*, vol. 2014, Article ID 216278, 8 pages, 2014.
- [3] K. Park, S. Jun, and D. Kim, "Effect of strength enhancement of soil treated with environment-friendly calcium carbonate powder," *The Scientific World Journal*, vol. 2014, Article ID 526491, 11 pages, 2014.
- [4] F. N. Okonta and O. O. Ojuri, "The stabilization of weathered dolerite aggregates with cement, lime, and lime fly ash for pavement construction," *Advances in Materials Science and Engineering*, vol. 2014, Article ID 574579, 11 pages, 2014.
- [5] E. Ibraim, A. Diambra, D. Muir Wood, and A. R. Russell, "Static liquefaction of fibre reinforced sand under monotonic loading," *Geotextiles and Geomembranes*, vol. 28, no. 4, pp. 374–385, 2010.
- [6] A. Anubhav and P. K. Basudhar, "Modeling of soil-woven geotextile interface behavior from direct shear test results," *Geotextiles and Geomembranes*, vol. 28, no. 4, pp. 403–408, 2010.
- [7] B. K. Maheshwari, H. P. Singh, and S. Saran, "Effects of reinforcement on liquefaction resistance of solani sand," *Journal of Geotechnical and Geoenvironmental Engineering*, vol. 138, no. 7, pp. 831–840, 2011.
- [8] G. Yang, B. Zhang, P. Lv, and Q. Zhou, "Behaviour of geogrid reinforced soil retaining wall with concrete-rigid facing," *Geotextiles and Geomembranes*, vol. 27, no. 5, pp. 350–356, 2009.
- [9] H. A. Alawaji, "Settlement and bearing capacity of geogrid-reinforced sand over collapsible soil," *Geotextiles and Geomembranes*, vol. 19, no. 2, pp. 75–88, 2001.
- [10] C.-N. Liu, Y.-H. Ho, and J.-W. Huang, "Large scale direct shear tests of soil/PET-yarn geogrid interfaces," *Geotextiles and Geomembranes*, vol. 27, no. 1, pp. 19–30, 2009.
- [11] B. R. Phanikumar, R. Prasad, and A. Singh, "Compressive load response of geogrid-reinforced fine, medium and coarse sands," *Geotextiles and Geomembranes*, vol. 27, no. 3, pp. 183–186, 2009.
- [12] B. Indraratna, N. T. Ngo, and C. Rujikiatkamjorn, "Behavior of geogrid-reinforced ballast under various levels of fouling," *Geotextiles and Geomembranes*, vol. 29, no. 3, pp. 313–322, 2011.
- [13] M. Ornek, M. Laman, A. Demir, and A. Yildiz, "Prediction of bearing capacity of circular footings on soft clay stabilized with granular soil," *Soils and Foundations*, vol. 52, no. 1, pp. 69–80, 2012.
- [14] A. Demir, M. Laman, A. Yildiz, and M. Ornek, "Large scale field tests on geogrid-reinforced granular fill underlain by clay soil," *Geotextiles and Geomembranes*, vol. 42, pp. 1–15, 2012.
- [15] P. K. Kolay, S. Kumar, and D. Tiwari, "Improvement of bearing capacity of shallow foundation on geogrid reinforced silty clay and sand," *Journal of Construction Engineering*, vol. 2013, Article ID 293809, 10 pages, 2013.
- [16] SP 36: Part 2: 1988 Compendium of Indian standards on soil engineering: Part 2 Field testing.
- [17] IS 1498: 1970 Classification and identification of soils for general engineering purposes.
- [18] IS 2131: 1981 Method for Standard Penetration Test for Soils.
- [19] IS 2720: Part 3: Sec 1: 1980 Methods of test for soils: Part 3 Determination of specific gravity Section 1 fine grained soils.

- [20] IS 2720: Part 10: 1991 Methods of test for soils: Part 10 Determination of unconfined compressive strength.
- [21] SP 36: Part 1: 1987 Compendium of Indian standards on soil engineering: Part 1 Laboratory testing of soils for civil engineering purposes.
- [22] IS 2720: Part 9: 1992 Methods of test for soils: Part 9 Determination of dry density-moisture content relation by constant weight of soil method.
- [23] IS 2720: Part 13: 1986 Methods of Test for Soils—Part 13: Direct Shear Test.
- [24] IS 13094: 1992 Guidelines for selection of ground improvement techniques for foundation in weak soils.

Research Article

Rock-Arch Instability Characteristics of the Sandstone Plate under Different Loading Conditions

Shuren Wang,^{1,2} Paul Hagan,³ Baowen Hu,⁴ Kanchana Gamage,³
Cheng Yan,³ and Dianfu Xu¹

¹ School of Civil Engineering and Mechanics, Yanshan University, Qinhuangdao 066004, China

² Opening Laboratory for Deep Mine Construction, Henan Polytechnic University, Jiaozuo 454003, China

³ School of Mining Engineering, University of New South Wales, Sydney, NSW 2052, Australia

⁴ Civil and Environmental Engineering Institute, University of Science and Technology, Beijing 100083, China

Correspondence should be addressed to Shuren Wang; wangshurenysu@163.com

Received 23 February 2014; Accepted 21 April 2014; Published 19 May 2014

Academic Editor: Juan José del Coz Díaz

Copyright © 2014 Shuren Wang et al. This is an open access article distributed under the Creative Commons Attribution License, which permits unrestricted use, distribution, and reproduction in any medium, provided the original work is properly cited.

Under the concentrated loading and the uniform loading, the tests on the brittle fracture and the hinged arching until the rock-arch instability of the sandstone plate were conducted using self-developed loading device, and the sensitivity of influent factors on the rock-arch failure was analyzed by numerical test based on the particle flow code (PFC). The results showed that sandstone plate instability presented four phases: small deformation elastic stage, brittle fracture arching stage, rock-arch bearing stage, and rock-arch instability stage. Under the uniform loading, the maximum vertical force of the rock-arch instability was much higher than that under the concentrated loading condition, but the maximum lateral force was almost the same. The number of acoustic emission (AE) and its positioning results of the sandstone plate showed that the extent of the plate damage under the uniform loading was higher than that under the concentrated loading condition. The friction coefficient effect, size effect, loading rate effect, and the initial horizontal force effect on the rock-arch instability were analyzed by the PFC^{3D} numerical experiment.

1. Introduction

Over the past years in China, there are numerous shallow mined-out areas left due to the disordered mining by the private coal mines. It is of important theoretical and practical value for the roof stability evaluation and disaster forecasting to research on the deformation rupture, instability mechanism, and failure mode of the rock roof in the mined-out areas.

The studies on the instability of the rock roof in the mining field have been the main topic all the time for home and abroad scholars. For example, according to elastic thin plate theory, Wang et al. analyzed the fracture instability characteristics of the roof under different mining distances in the mining work face [1]. Wang et al. analyzed the rheological failure characteristics of the roof in the mined-out areas through combining the thin plate and rheology theories [2–4]. Pan had conducted the analytical analysis

of the variation trend of the bending moment, the deflection, and the shear force of the hard roof in the mining field [5]. These researches mentioned above are inclined to adopted traditional analytic methods to probe into the roof stability. There are also new theories and methods used in recent years. Zhao et al. utilized the catastrophe theory to set up vertical deformation model of the overlapping roof in the mined-out areas and put forward the criteria for evaluating the roof stability [6]. Wang et al. analyzed the chaos and stochastic resonance phenomenon produced in the roof during the evolutionary process of the rock beam deformation [7]. Meanwhile, some numerical computation methods were applied in discussing the mechanical response of rock plate or beam. Wang et al. analyzed the blast-induced stress wave propagation and the spalling damage in a rock plate by using the finite-difference code [8]. Nomikos et al. researched the mechanical response of the multijointed roof beams using two-dimensional distinct element code

[9]. Bakun-Mazor et al. examined the arching mechanism of the blocky rock mass deformation after the underground tunnel was excavated using the discrete element method [10]. Cravero and Iabichino discussed the flexural failure of a gneiss slab from a quarry face by virtue of linear elastic fracture mechanics (LEFM), finite element method (FEM) [11], and so forth [12–14].

In summary, though many research achievements have been made, the results that the rock plate was supposed to be the thin plate or beam were lacking laboratory test to be verified. In addition, some numerical calculations were based on the continuum mechanics, which could not reflect the spatial heterogeneity and the anisotropic effect of the roof in the mining field. Only a few researchers utilized the discrete element methods to study the macromechanical response of the rock plate and did not further explore the microscopic damage of the rock plate. Therefore, a new loading device was developed to study the rock-arch instability characteristics of the plate, and particle flow code was used to further probe into the microscopic damage of the rock plate under the concentrated and the uniform loading, respectively.

2. Loading Experiment of Rock Plate

2.1. Sample of Rock Plate. The rock plate samples in the test were Hawkesbury sandstone, obtained from Gosford Quarry in Sydney, Australia. The quartz sandstones were formed in marine sedimentary basin of the Mid-Triassic and located on the top of the coal-bearing strata, which contained a small quantity of feldspars, siderite, and clay minerals. The surface of the specimen exhibited local red rather than usual white because of the content and distribution of the iron oxide. According to the definition of the thin plate and thick plate in elastic mechanics, the specimen size of the thick plate was designed to be 190 mm × 75 mm × 24 mm (length, width, and thickness) and that of the thin plate was designed to be 190 mm × 75 mm × 14 mm (length, width, and thickness). Each kind of rock plate was prepared for at least three plates.

2.2. Loading Equipment. The MTS-851 rock mechanics testing machine was selected as loading equipment, the load was controlled by vertical displacement, and loading rate was set 1×10^{-2} mm/s [15]. The vertical force and displacement occurring in the process of test were automatically recorded in real time by data acquisition system.

As shown in Figure 1, the concentrated and the uniform loading test sets were designed to mainly consist of three parts. The top was a point loading for the concentrated loading or an assembly of the steel balls for the uniform loading. The middle was loading framework which included four bolts with nuts connecting the steel plates on both sides, and the lateral pressure cell was placed between the deformable steel plate and the thick steel plate so as to monitor the horizontal force. The capacity of the lateral pressure cell LPX was 1000 kg. The bottom was a rectangle steel foundation, and the rotatable hinge supports were set on both sides of the loading framework to maintain connection with the steel plates.

2.3. Acoustic Equipment and Data Acquisition System. In order to monitor the cracks initiate and identify the failure location of the rock plate, and the USB AE nodes were used in the test. The USB AE node is a single channel acoustic emission (AE) digital signal processor with full AE hit and time based features. In the test there were four USB AE nodes being connected to a USB hub for multichannel operation (Figure 2). All these AE nodes were made in MISTRAS Group, Inc., USA.

3. Experiment Results and Analysis

3.1. Characteristic of Force-Displacement Curve. As shown in Figure 3, the vertical force-displacement curves appeared two peaks under both the concentrated loading and the uniform loading, and the second peak value is higher than the first one. The thin rock plate showed the similarity cases in the test with the thick plate; only the peak values of the vertical and the horizontal force were lower than that of the thick one. In general, the curves of the force-displacement could be classified as four mechanical response stages as follows (Figure 1(a)).

Stage One. The rock plate was in the small deformation elastic stage. With the vertical force slowly increasing, the vertical displacement grew gradually. On the contrary, the horizontal force showed the slight decrease, which was mainly caused by the slight horizontal shrink of the rock plate during the loading process.

Stage Two. The rock plate produced brittle rupture and formed the rock-arch structure. As the vertical displacement went to about 2.5 mm, the vertical force appeared with abrupt increase firstly and then dropped sharply in a small interval, which indicated the rock plate producing brittle rupture. Subsequently, the rock-arch structure was formed under the vertical and the horizontal reaction forces, and the horizontal force started to increase.

Stage Three. The rock-arch structure began to bear loads and produced deformation. With the vertical force increasing, the middle hinge point of the rock-arch structure moved down, and the two flanks of the rock-arch rotated around the hinge point, respectively. Such kinds of motion would stretch the rock-arch structure in the horizontal direction and squeeze the plate in two sides, and the horizontal force showed a significant growth.

Stage Four. The instability of the hinged rock-arch structure happened. With the vertical force continuously increasing, the middle hinged point of the rock-arch structure moved down constantly, and when the hinged point exceeded the horizontal line formed by the hinged point and two ends of the plate, the rock-arch structure went into instability thoroughly.

Under the uniform loading, the damage and fracture extent of the rock plate was more serious than that under the concentrated loading, especially at the two ends of the

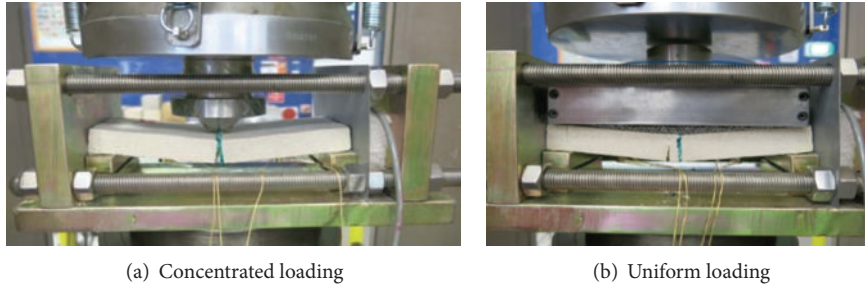


FIGURE 1: Loading experiment for rock plate.

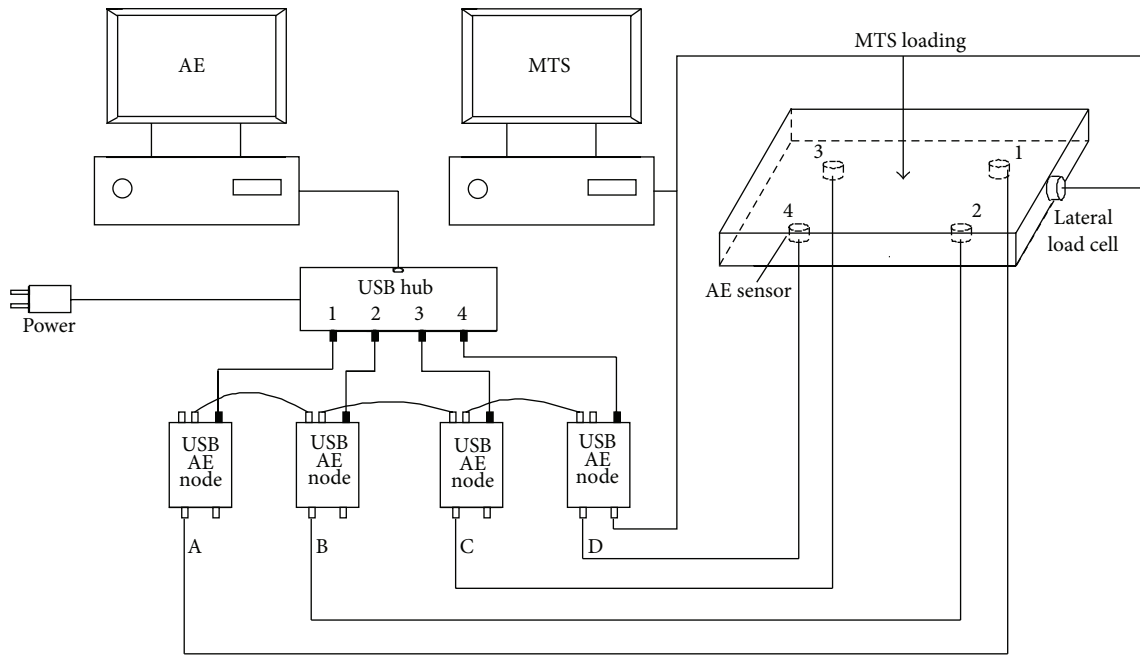


FIGURE 2: MTS connection with AE monitoring system diagram.

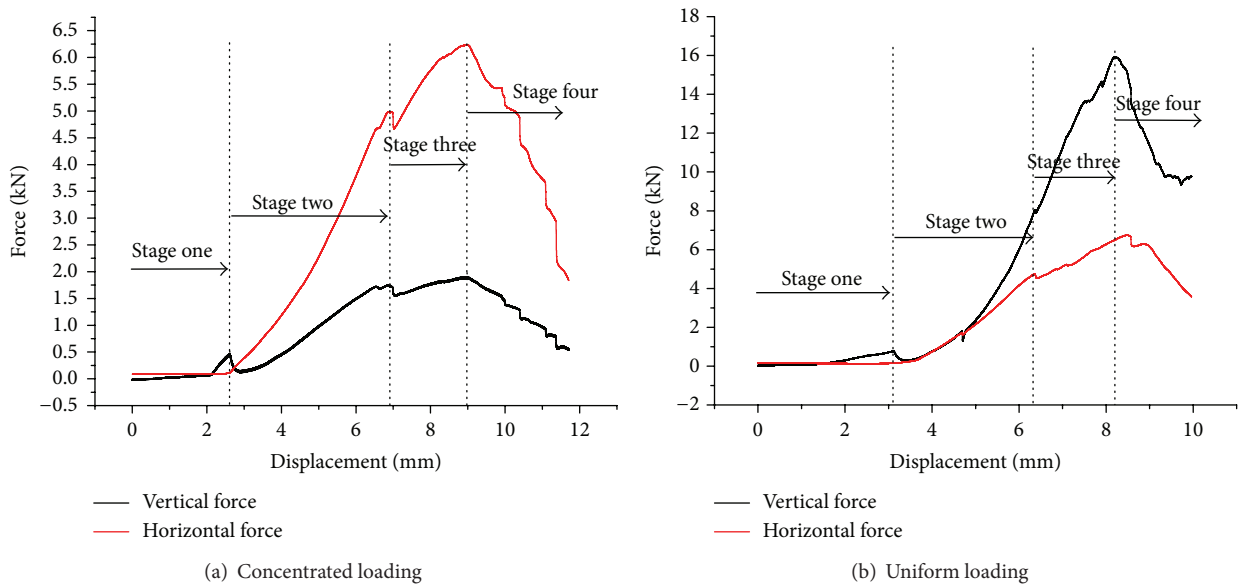


FIGURE 3: Force-displacement curves under different loading conditions.

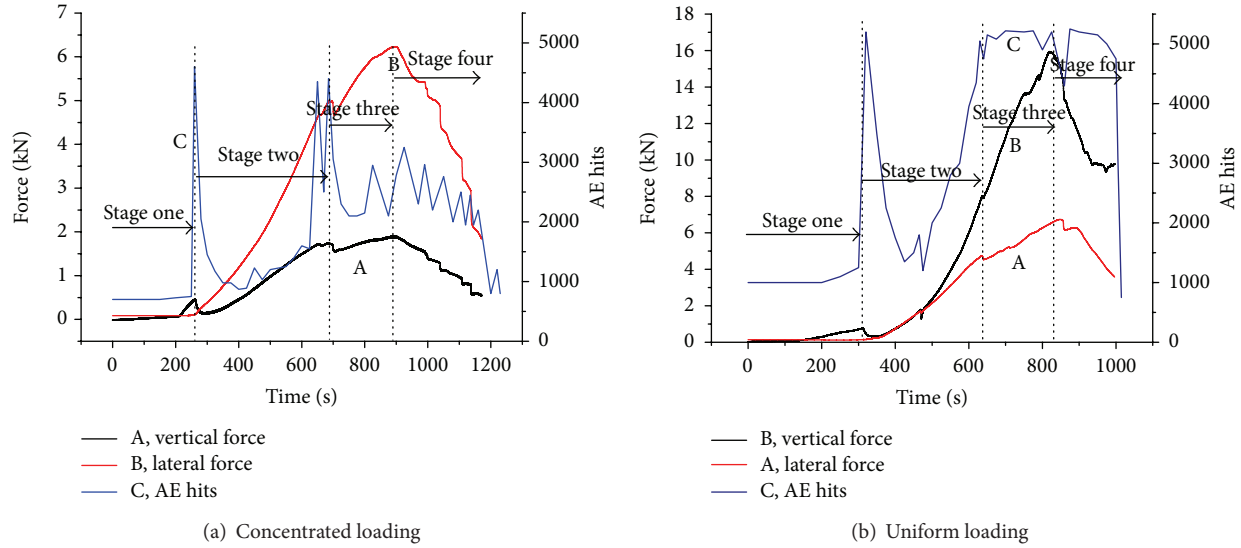


FIGURE 4: AE hits and force-displacement curves under different loading conditions.

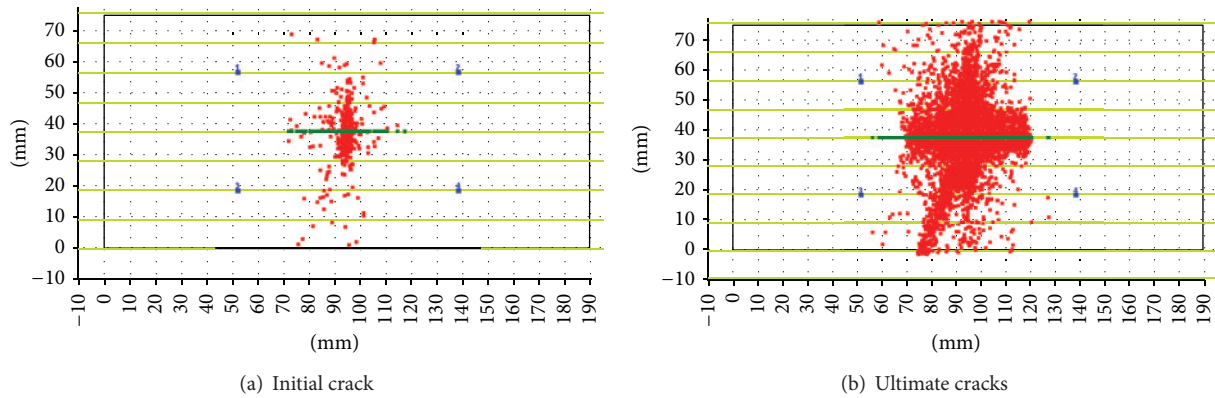


FIGURE 5: AE location of rock plate under concentrated loading.

rock plate (Figure 1(b)). As shown in Figure 3, the load-displacement curve showed similarity with the concentrated loading, and the peak value of the vertical force was greater than that under the concentrated loading, while the maximum value of the horizontal force showed basically the same (about 6.2 kN) with each other.

3.2. Acoustic Characteristic in the Process of the Rock Plate Failure. As shown in Figure 4, in the beginning of stage two, the AE hits under the uniform loading were greater than that under the concentrated loading, which were about 5000 and 4500, respectively. In stage three and stage four, the AE hits were also greater and more evenly distributed under the uniform loading compared with the concentrated loading, which were about 5000 and 3000, respectively.

As shown in AE location map (Figures 5 and 6), the results showed obvious differences in the initial crack position and the cracks distribution of the rock plate under different loading conditions. When the rock-arch structure went into instability, the differences in the damage extent and scope

between the two loading methods were shown. All in all, the results of AE hits and location showed that the over damage extent and scope of the rock plate caused by the uniform loading were more serious than that under the concentrated loading condition.

4. Numerical Simulations of the Loading Test of the Rock Plate

4.1. Parameters Calibration of the Rock Plate. The rock plate was treated as the porous and solid material that consisted of particles and cement bodies. The force-displacement curve was simulated under the concentrated loading using the PFC^{3D}.

Before the numerical simulation model being built, the microparameters needed to be adjusted repeatedly and finalized until the macromechanical parameters calculated were consistent with the physical macromechanical parameters [16].

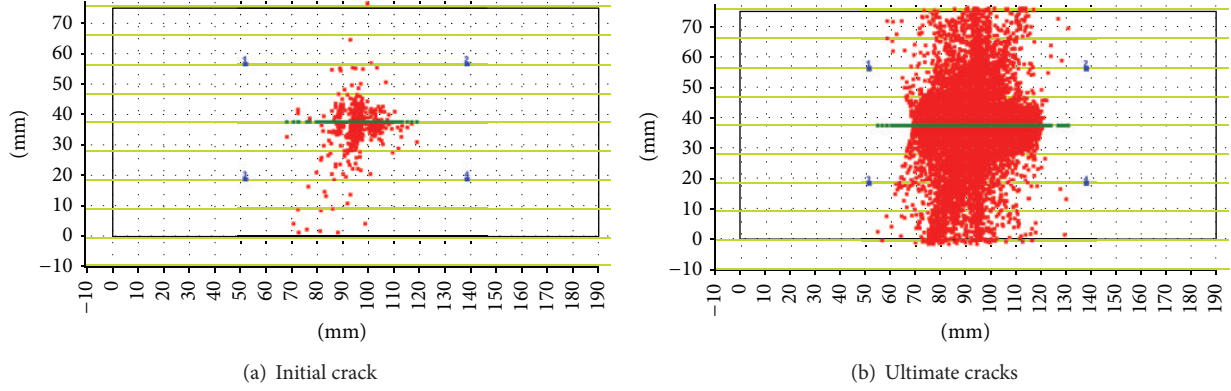


FIGURE 6: AE location of rock plate under uniform loading.

 TABLE 1: Microparameters of the model in PFC^{3D}.

$\rho/\text{kg/m}^3$	R_{\min}/m	R_{ratio}	μ	$\bar{\lambda}$	E_c/Pa	\bar{E}_c/Pa	k_n/k_s	\bar{k}_n/\bar{k}_s	$\bar{\sigma}_c/\text{Pa}$	$\bar{\tau}_c/\text{Pa}$
2650	$1.2e-3$	1.66	0.5	1.0	$2.7e9$	$2.8e9$	1.8	1.8	$16e6$	$16e6$

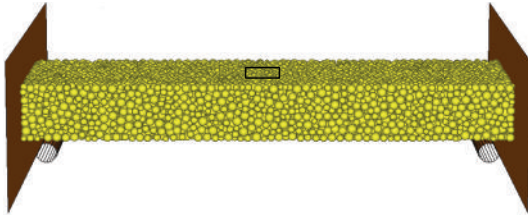


FIGURE 7: Computational model and its boundaries.

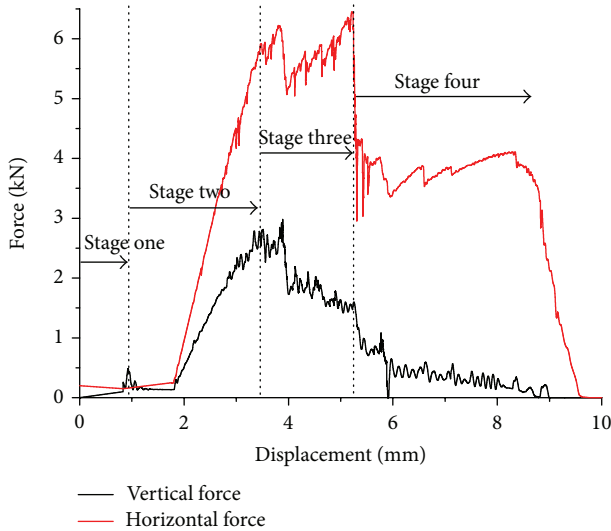


FIGURE 8: Force-displacement relationship curves.

The microparameters required to be adjusted were as follows: ρ is ball density, R_{\min} is minimum ball radius, R_{ratio} is ratio of the largest to the smallest radii, $\bar{\lambda}$ is parallel-bond radius multiplier, E_c is ball-ball contact modulus, \bar{E}_c is parallel-bond modulus, k_n/k_s is ball stiffness ratio, \bar{k}_n/\bar{k}_s is

parallel-bond stiffness ratio, μ is ball friction coefficient, $\bar{\sigma}_c$ is parallel-bond normal strength, and $\bar{\tau}_c$ is parallel-bond shear strength. The microparameters required to be adjusted were listed in Table 1.

4.2. Building the Computational Model. The thick plate of $190 \text{ mm} \times 75 \text{ mm} \times 24 \text{ mm}$ (length, width, and thickness) was taken as an example to show how to build the numerical calculation model.

Firstly, a parallelepiped specimen consisting of arbitrary particles confined by six frictionless walls was generated by the radius expansion method. Secondly, the radii of all particles were changed uniformly to achieve a specified isotropic stress so as to reduce the magnitude of locked-in stresses that would develop after the subsequent bond installation. In this paper the isotropic stress was set to 0.1 MPa. Thirdly, the floating particles that had less than three contacts were eliminated. Fourthly, the parallel bonds were installed throughout the assembly between all particles that were in near proximity to finalize the specimen. Lastly, the loading devices were installed on the rock plate as shown in Figure 7.

A square wall with sides of 10 mm was made on the top of the rock plate as the concentrated loading, and the loading rate was set to 0.01 m/s (the loading rate could be regarded as the quasistatic loading). The two cylinder walls were placed on the right and left at the bottom, respectively, as supporting base. The two walls located in both sides could install the initial horizontal force at the specified value. During the loading, the cracks generated in the rock plate were monitored in real time. The red cracks represented the tensile fracture, and the black ones represented the shear fracture.

4.3. Analysis of the Numerical Simulation Results. As shown in Figure 8, since the interaction forces among the particles

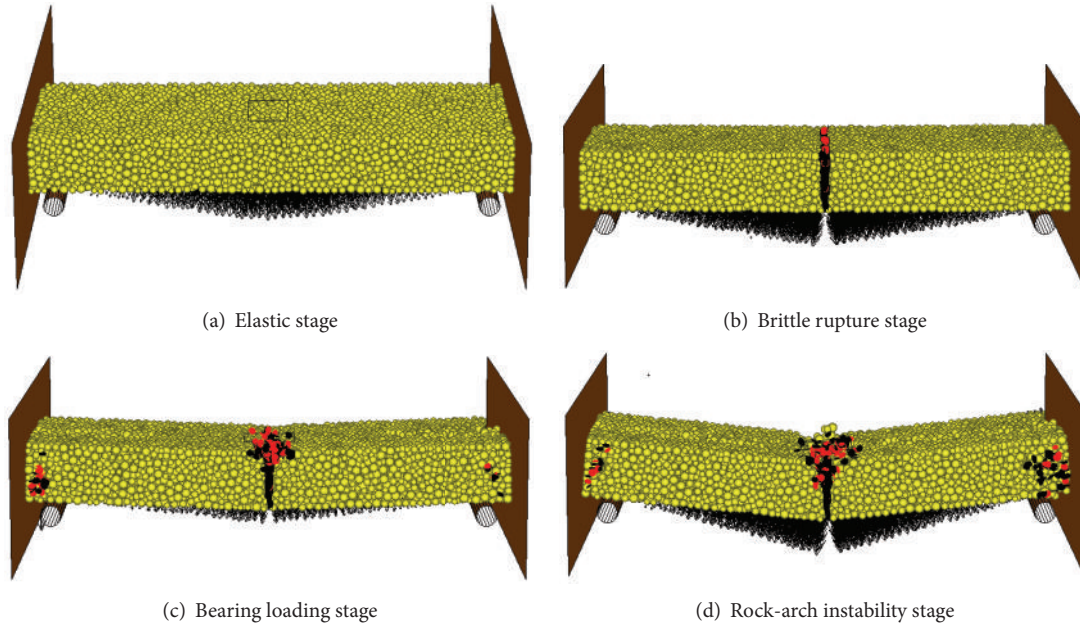


FIGURE 9: Rock-arch instability process under the concentrated loading.

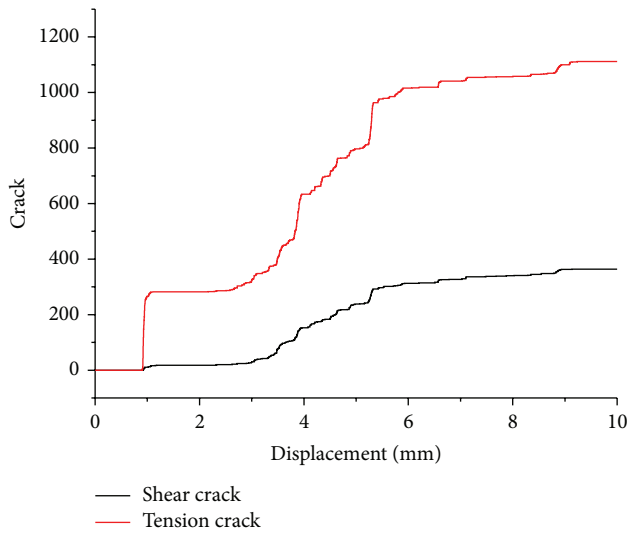


FIGURE 10: Crack-displacement curves.

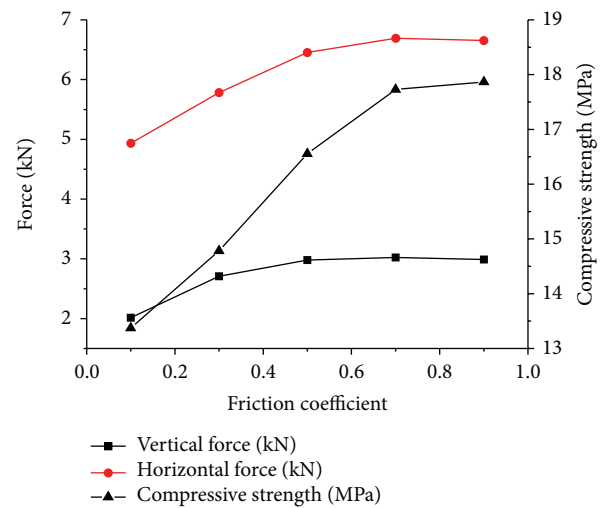


FIGURE 11: Force-friction coefficient curves.

were simplified in PFC^{3D}, there were some differences in the vertical force-horizontal force-displacement simulated curves compared with the physical experimental curves, but the variation trend of the curves was basically the same for two cases, so the physical experimental results confirmed the numerical credibility.

In the elastic deformation stage (Figure 9(a)), the displacement vector field described that a slight elastic deformation was produced in the rock plate and at the same time there was no crack generated in this stage. In the brittle rupture stage (Figure 9(b)), there were many tensile cracks produced in the rock plate, and these tensile cracks formed a tensile failure plane in the rock plate. In the rock-arch bearing load

stage (Figure 9(c)), there were the shearing and tension cracks emerging in the hinged plane and both ends of the rock plate. In the rock-arch instability stage (Figure 9(d)), the rock-arch structure had a large deformation, and parts of the particles in the hinged plane of both sides had escaped from the rock plate mainly due to the squeezing fracture.

As shown in Figure 10, the number of shear cracks obeyed the S-figure curve during the whole mechanical response process, which was also applicable to the tensile cracks only after the brittle rupture. When the vertical displacement reached around 1.0 mm, the number of the tensile cracks surged to 300. As the displacement varied in the interval 1.0–2.5 mm, the crack development kept almost unchanged. However, with the displacement continuously increasing, the number

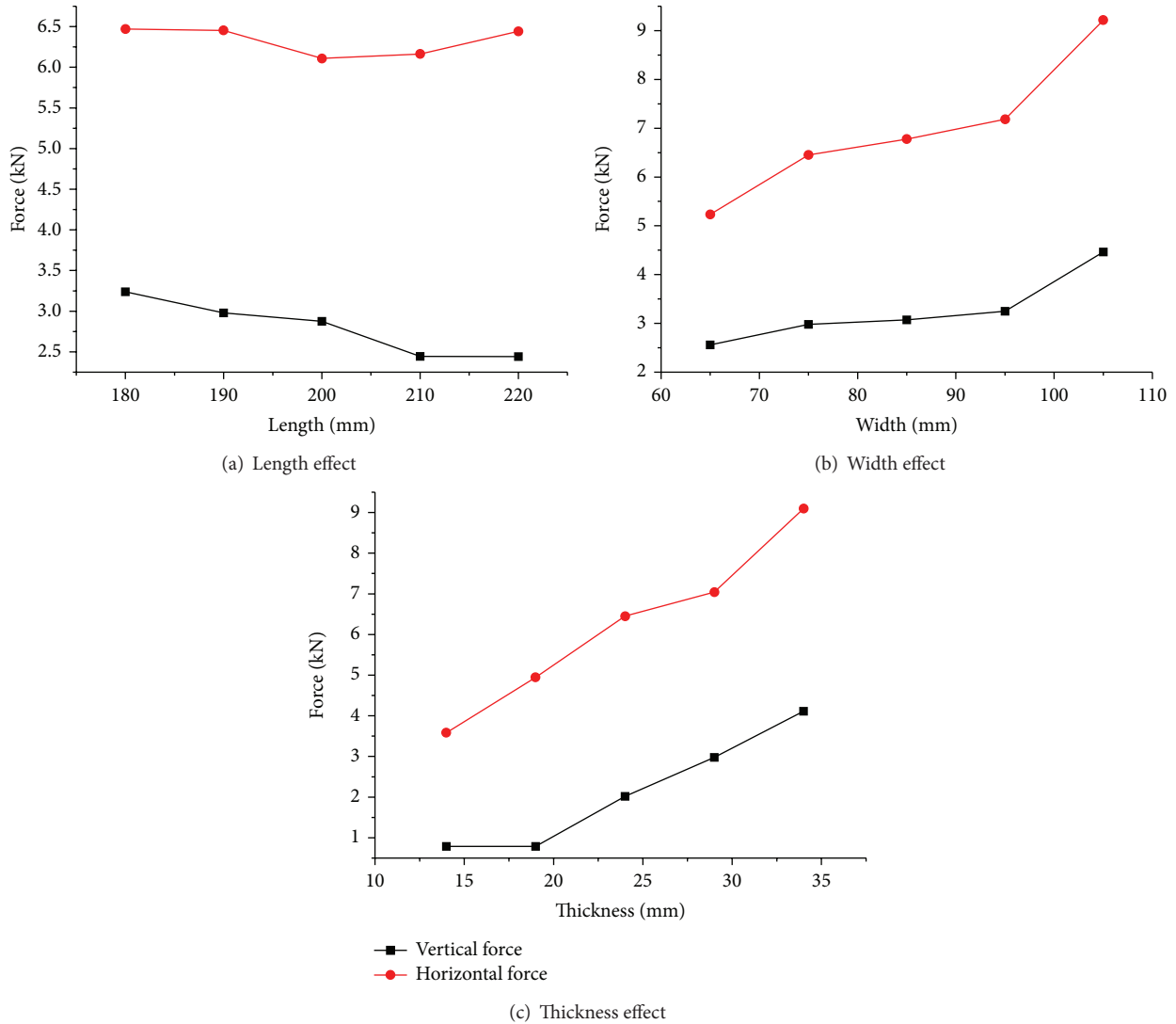


FIGURE 12: The forces variation with the rock plate geometry parameters.

of both shearing and tension cracks kept increasing, the hinged planes and both ends of the rock plate showed the mixture of shearing and tensile cracks. As rock-arch structure went into instability, the number of cracks still kept significant increase until the displacement reached 6 mm.

5. Sensitive Analysis of Influence Factors of the Rock-Arch Instability

5.1. Material Parameter Effect. As shown in Figure 11, with the friction coefficient of the particles increasing, the peak values of the vertical force and the horizontal force of the rock-arch structure also increased. This was mainly because the friction growth enhanced the peak strength of the rock material; namely, after breakage of the parallel bond, the strength of the rock material was often contributed by the contact friction of the particles.

5.2. Geometry Size Effect. As shown in Figure 12, the length, width, and thickness of the rock plate were changed, respectively, to reveal the size effect on the instability of the rock-arch structure. With the length of the rock plate increasing, the peak values of the vertical and the horizontal force were gradually decreased, and the whole variation interval was small. With the width and the thickness of the rock plate increasing, the peak values of the vertical and the horizontal force showed obvious growth. In short, the response of the rock-arch structure instability was more sensitive to the width and thickness compared with the length.

5.3. Loading Rate and Initial Horizontal Force Effect. As shown in Figure 13(a), when the loading rate exceeded 10 mm/s, with the loading rate increasing, the peak values of the vertical and the horizontal force showed the linear growth trend, and the amplitude of that variation was small.

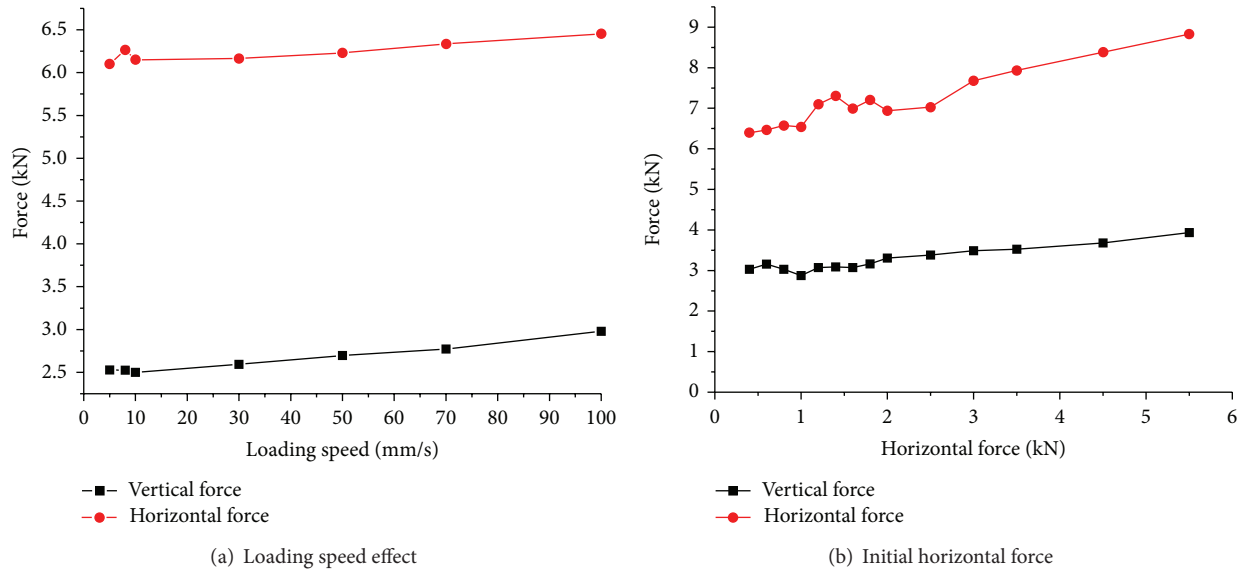


FIGURE 13: Forces versus the loading speed and the initial horizontal force.

When the loading rate was in the interval of 1.0 mm/s~10 mm/s, the peak values were almost unchanged; therefore, such loading rate could be regarded as the quasistatic loading.

As shown in Figure 13(b), when the initial horizontal force was less than 2.0 kN, with the initial horizontal force increasing, the vertical and the horizontal force of the rock plate showed the nonlinear fluctuating growth trend. When the initial horizontal force was larger than 2.0 kN, with the initial horizontal force increasing, the vertical and the horizontal force would show the linear growth trend.

6. Conclusions

Under the concentrated and the uniform loading, there were the elastic deformation, brittle rupture, rock-arch bearing load, and rock-arch instability four stages in the force-displacement curves. The peak value of the vertical force under uniform loading was greater than that under the concentrated loading. The number of AE hits and AE location showed that the damage extent and scope of the rock plate under the uniform loading were greater than that under the concentrated loading.

The simulation results showed that the tensile cracks of the rock plate were dominating during the concentrated loading. The numerical test results showed that the instability of the rock-arch structure was more sensitive to the width and thickness compared with the length. The loading rate could be regarded as the quasistatic loading when it was less than 10 mm/s. The vertical and the horizontal force would show the growth trend with the initial horizontal force increasing.

In order to obtain the more precise simulation results in calculation by using PFC^{3D} compared with the physical experimental results, the more precise description for the numerical model and the interaction forces among the particles should be improved.

Conflict of Interests

The authors declare that there is no conflict of interests regarding the publication of this paper.

Acknowledgments

This work was financially supported by the National Natural Science Foundation of China (51074140; 51310105020), the Natural Science Foundation of Hebei Province of China (E2014203012), and Program for Taihang Scholars; all these are gratefully acknowledged.

References

- [1] H. Wang, Z. Chen, Z. Du, and J. Li, "Application of elastic thin plate theory to change rule of roof in underground stope," *Chinese Journal of Rock Mechanics and Engineering*, vol. 25, no. 2, pp. 3769–3774, 2006.
- [2] J.-A. Wang, X.-C. Shang, H. Liu, and Z.-Y. Hou, "Study on fracture mechanism and catastrophic collapse of strong roof strata above the mined area," *Journal of the China Coal Society*, vol. 33, no. 8, pp. 849–855, 2008.
- [3] S. R. Wang and H. H. Jia, "Analysis of creep characteristics of shallow mined-out areas roof under low stress conditions," *Applied Mechanics and Materials*, vol. 105–107, pp. 832–836, 2012.
- [4] J.-A. Wang, X. C. Shang, and H. T. Ma, "Investigation of catastrophic ground collapse in Xingtai gypsum mines in China," *International Journal of Rock Mechanics and Mining Sciences*, vol. 45, no. 8, pp. 1480–1499, 2008.
- [5] Y. Pan, S. T. Gu, and Y. S. Qi, "Analytic solution of tight roof's bending moment, deflection and shear force under advanced super charger load and supporting resistance before first weighting," *Chinese Journal of Rock Mechanics and Engineering*, vol. 32, no. 8, pp. 1545–1553, 2013.

- [6] Y. Zhao, Q. Wu, W. Wang, W. Wan, and F. Zhao, "Strength reduction method to study stability of goaf overlapping roof based on catastrophe theory," *Chinese Journal of Rock Mechanics and Engineering*, vol. 29, no. 7, pp. 1424–1434, 2010.
- [7] S. R. Wang, H. Wang, and B. W. Hu, "Analysis of catastrophe evolution characteristics of the stratified rock roof in shallow mined-out areas," *Disaster Advances*, vol. 6, no. 1, pp. 59–64, 2013.
- [8] Z.-L. Wang, Y.-C. Li, and J. G. Wang, "Numerical analysis of blast-induced wave propagation and spalling damage in a rock plate," *International Journal of Rock Mechanics and Mining Sciences*, vol. 45, no. 4, pp. 600–608, 2008.
- [9] P. P. Nomikos, A. I. Sofianos, and C. E. Tsoutrelis, "Structural response of vertically multi-jointed roof rock beams," *International Journal of Rock Mechanics and Mining Sciences*, vol. 39, no. 1, pp. 79–94, 2002.
- [10] D. Bakun-Mazor, Y. H. Hatzor, and W. S. Dershowitz, "Modeling mechanical layering effects on stability of underground openings in jointed sedimentary rocks," *International Journal of Rock Mechanics and Mining Sciences*, vol. 46, no. 2, pp. 262–271, 2009.
- [11] M. Cravero and G. Iabichino, "Analysis of the flexural failure of an overhanging rock slab," *International Journal of Rock Mechanics and Mining Sciences*, vol. 41, supplement 1, pp. 605–610, 2004.
- [12] S. R. Wang and M. S. Chang, "Reliability analysis of lining stability for hydraulic tunnel under internal water pressure," *Disaster Advances*, vol. 5, no. 4, pp. 166–170, 2012.
- [13] J. F. Yin, S. R. Wang, Z. Q. Wang, J. M. Yu, and C. Cao, "Disturbance effects analysis of the coal pillar-roof system caused by a sudden instability coal pillar," *Disaster Advances*, vol. 6, no. 13, pp. 29–37, 2013.
- [14] J. H. Yang, S. R. Wang, C. L. Li, and Y. Li, "Disturbance deformation effect on the existing tunnel of asymmetric tunnels with small spacing," *Disaster Advances*, vol. 6, no. 13, pp. 269–277, 2013.
- [15] R. Ulusay and J. A. Hudson, *The Complete ISRM Suggested Methods for Rock Characterization, Testing and Monitoring: 1974–2006*, Kozan Ofset, Ankara, Turkey, 2007.
- [16] D. O. Potyondy and P. A. Cundall, "A bonded-particle model for rock," *International Journal of Rock Mechanics and Mining Sciences*, vol. 41, no. 8, pp. 1329–1364, 2004.

Research Article

Research on Deterioration Mechanism of Concrete Materials in an Actual Structure

Shiping Zhang,¹ Xiang Dong,¹ Houxian Zhang,¹ and Min Deng²

¹ Department of Architecture Civil Engineering, Nanjing Institute of Technology, No. 1 Hongjing Road, Nanjing 211167, China

² College of Materials Science and Engineering, Nanjing University of Technology, No. 5 Xin Mofan Road, Nanjing 210009, China

Correspondence should be addressed to Shiping Zhang; zhangshiping1982@gmail.com

Received 7 January 2014; Accepted 25 April 2014; Published 14 May 2014

Academic Editor: Osman Gencel

Copyright © 2014 Shiping Zhang et al. This is an open access article distributed under the Creative Commons Attribution License, which permits unrestricted use, distribution, and reproduction in any medium, provided the original work is properly cited.

The cause for deterioration of the concrete structure located in severe environment has been explored both in field and in laboratory. Serious cracking and spalling appeared upon surface of the concrete structure soon after the structure was put into service. Both alkali-aggregate reaction and freeze-thaw cycles may result in similar macro visible cracking and spalling. The possibility of alkali-aggregate reaction was excluded by both field survey and lab examination such as chemical analysis, petrographic analysis, and determination of alkali reactivity of aggregates. According to results of freeze-thaw cycles, impermeability testing, and microstructure analysis, it is deduced that the severe environmental conditions plus the relatively inferior frost resistance cause the deterioration of concrete. Usage of air entraining admixture can improve frost resistance and impermeability. Furthermore, new approaches to mitigate the deterioration of concrete used in severe environmental condition are discussed.

1. Introduction

Concrete structures are built to provide a service during a limited time period and, in some cases, the need for maintenance is foreseen [1]. However, recently durability of concrete has been a social concern due to the poor performance of concrete caused by various environmental, physical, and chemical factors such as corrosion of reinforcement bars due to carbonation or chloride ingress, freezing-thawing action, sulfate attack, alkali aggregate reaction, and so forth [2–8]. The resistance against these chemical erosions and physical deteriorations depends on the chemical composition and the microstructure of hardened cement matrix and on the environmental conditions to which the structure is exposed [9–11]. Correct understanding of the mechanism of deterioration can lead to improved specifications or construction techniques for new concrete exposed to similar condition [12].

According to statistics, most of concrete structures damaged are located in severe environment, which draws lots of attention for engineers and scientists. The temperature

in severe environment may range from -30°C in winter to 30°C during the summer; furthermore it varies from day to night sharply. The severe environment has caused serious problems for concrete structures. In the present work, a typical case was chosen to ascertain the deterioration mechanism. It is a matter of concrete materials in an airport runway. Serious cracking and spalling appeared upon surface of concrete shortly after the structure was put into service, as shown in Figure 1. The groundwater in situ is not aggressive according to geological survey by local authorities. Hence, the possibility of sulfate attack can be excluded. Since the alkali content of the cement used for the runway shoulder is a little high and the reactivity of the aggregates used is unknown, the occurrence of alkali-aggregate reaction is not eliminable. Both alkali-aggregate reaction and freeze-thaw cycles may result in similar macrostructurally visible cracking and spalling [13]. The present investigation is to identify which one is responsible for the deterioration of the concrete. Concrete cores were taken from the structure, as a reference; concrete samples were also made in laboratory. Various types of testing were carried out to characterize alkali-aggregate



FIGURE 1: Deterioration characteristic of concrete in situ (a) cracking and (b) spalling.

reaction and frost resistance. In addition, impermeability and microstructure of the concrete in question were also examined to elucidate the deterioration mechanism.

2. Samples and Test Methods

2.1. Samples. Both concrete cores and standard samples were prepared. The concrete cores were taken from actual engineering, and standard samples used for freeze-thaw testing and impermeability testing were prepared in laboratory with the same raw materials and the same mix proportion as the actual structure. The cement used for determining alkali reactivity of aggregates is ordinary Portland cement produced by Onada Corp. in Jiangsu Province, China, which meets demands of the Rapid Test Method for Determining Alkali Reactivity of Sands and Rocks (CECS48-93) ($\text{Na}_2\text{O}_{\text{eq}} = 0.53\%$). Chemical composition of the cement used for determining alkali reactivity of aggregates in lab is presented in Table 1.

2.2. Alkali-Aggregate Reaction. As well known, the coexistence of reactive aggregates, alkali, and water is prerequisite to the initiation of alkali-aggregate reaction (AAR) [14]. Map cracking, exudation of white gel, and reaction rim around aggregates are characteristic of AAR [15]. According to our field survey, there was neither map cracking nor white gel found. In addition, petrographic observations did not find reaction rim in polished section of the concrete. Accordingly, the possibility of AAR was evaluated through two aspects: alkali content of cement and reactivity of aggregates.

2.2.1. Alkali Content of Cement and Water. The experimental method and procedure for analysis of chemical composition of cement used for the runway shoulder was in accordance with Chinese National Standard GB/T 176-1996. The alkali content in water used for the concrete was detected using a type 6400A flame spectrometer.

2.2.2. Reactivity of Aggregates. The Rapid Test Method for Determining Alkali Reactivity of Sands and Rocks (CECS48-93) was chosen to assess the reactivity of aggregates.

TABLE 1: Chemical composition of the cement used for determining alkali reactivity of aggregates.

Sample	Chemical composition (wt%)						
	CaO	SiO ₂	Al ₂ O ₃	Fe ₂ O ₃	MgO	SO ₃	Na ₂ O _{eq}
Cement	63.1	22.74	6.46	3.56	1.60	0.81	0.53

The dimensions of the specimens were 10 mm × 10 mm × 40 mm, and cement to aggregate ratio was 2 : 1, 5 : 1 and 10 : 1, respectively. The samples were cured in humid air at 20°C ± 2°C for 24 h after casting. Then they were demolded, the initial length of the micro bar being measured. Afterward, the samples were autoclaved in water at 100°C for 4 h and then in 8.2% alkali solution at 150°C for 6 h. The final length of the micro bar was measured again. Aggregates are reactive if the maximum expansion of the micro bar is ≥0.1% based on the criterion specified by CECS48-93. Otherwise, aggregates are nonreactive. Besides, petrographic analysis and X-ray diffractometry of aggregates were performed using OLYMPUS BH-2 (made in Japan) and ARL X'TRA (made in USA), respectively.

2.3. Frost Resistance Testing. Rapid freezing method has been commonly used to evaluate frost resistance. The testing procedure carried out in this investigation conformed to Chinese National Standard GB/T 50082-2009. In a single cycle, the temperature of the specimens cooled from 6 to -15°C and then warmed to 6°C within approximately 2.5–3 h. Both freezing and thawing were performed in water. Since the tested cores were not standard samples in size, the relative dynamic elastic modulus failed to be examined. Standard concrete samples were made in laboratory with the same mix proportion and materials as the concrete structure. Both mass loss and loss of dynamic modulus of elasticity were checked for the standard samples.

2.4. Impermeability Testing. Impermeability of the cores from the structure was tested. Since the tested cores were not

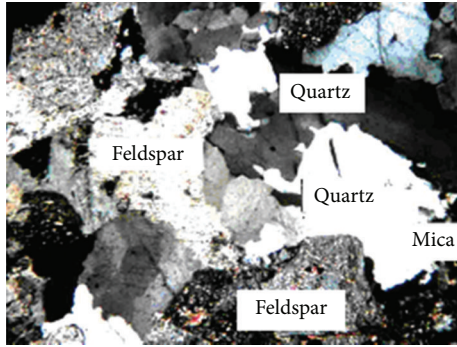


FIGURE 2: Micrographs of sands.

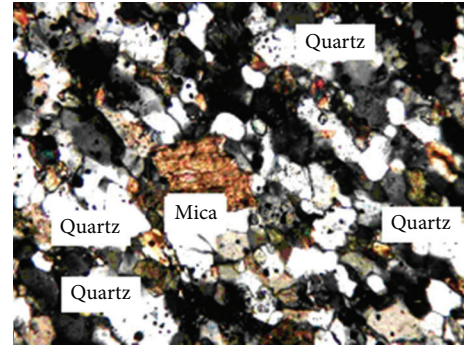


FIGURE 3: Micrographs of crushed stone.

standard samples in size, impermeability test was carried out by using an apparatus of type SS15 (made in China) originally for mortar permeability testing. Impermeability of standard samples prepared in laboratory was carried out according to GB/T 50082-2009. The samples were applied by pressurized water, and the pressure was gradually increased until the samples were penetrated by pressurized water. The maximum pressure which the sample can afford was used to evaluate the impermeability.

2.5. *Microstructure Analysis.* Polished sections of the cores taken from the structure were observed using microscope OLYMPUS XZ-2 (made in Japan). Scanning electron microscopy (SEM) (JSM 5900, made in Japan) and mercury intrusion porosimetry (MIP) (GT-60, made by Quantachrome Co., USA) were also used here.

3. Results and Discussion

3.1. *Alkali-Aggregate Reaction.* Table 2 shows chemical composition of cement used for the structure. The equivalent alkali content of the cement is calculated to be 0.62% according to the commonly recognized formula $Na_2O_{eq} = Na_2O + 0.658K_2O$, a little higher than 0.60% which is the maximum value of low-alkali cement. Table 3 presents the alkali content of water used for the structure. Apparently, the alkali content of the water is negligible. Table 4 gives testing results for alkali reactivity of aggregates. The maximum expansion of micro bars is 0.053% and 0.046% for sand and crushed stone, respectively, less than the limit of 0.10%. So, the aggregates are identified to be nonreactive according to the criterion. In order to evaluate the reactivity of aggregates, both coarse and fine aggregates were analyzed by petrographic method, and the results about that were shown in Figures 2 and 3, respectively. From petrographic analysis of aggregates, it is found that sands mainly contain quartz, feldspar, and mica. For the crushed stone, the main components are quartz and mica. Furthermore, these mineral compositions are of well crystallization, which indicates being nonreactive. Therefore, both coarse aggregates and fine aggregates are nonactive.

TABLE 2: Chemical composition of cement.

Sample	Chemical composition (wt%)						
	CaO	MgO	Fe ₂ O ₃	Al ₂ O ₃	SiO ₂	Na ₂ O _{eq}	SO ₃
Cement	61.74	1.57	3.54	5.37	21.84	0.62	2.15

TABLE 3: Chemical analysis of water.

Sample	pH	K ₂ O (%)	Na ₂ O (%)	Insoluble (mg/L)	Soluble (mg/L)
Water	6.86	0	2.3×10^{-3}	7.00	272.00

TABLE 4: Test results of alkali reactivity of aggregates.

Sample	Expansion (%)			Alkali-reactivity identification
	10:1	5:1	2:1	
Sand	0.030	0.049	0.053	Nonalkali reactive
Crushed stone	0.029	0.034	0.046	Nonalkali reactive

3.2. *Frost Resistance.* For the concrete core from practical engineering, deterioration due to freeze-thaw cycles is assessed by mass loss during freeze-thaw cycling. Figure 4 showed the mass loss of samples during freeze-thaw cycles. According to results in Figure 4, mass loss of the cores is greater than 5% after 76 freeze-thaw cycles. According to the criterion specified by GB/T 50082-2009, a sample is damaged completely when the mass loss reaches 5%. So, these concrete cores only can resist about 76 freeze-thaw cycles. For the concrete samples prepared in laboratory, deterioration due to freeze-thaw cycles is assessed by both mass loss and dynamic modulus of elasticity during freeze-thaw cycling. Figure 5 presented the freeze-thaw test results for standard samples. For number 1 sample, air entraining admixture was added. It is evident that similar to freeze-thaw test results of the cores, the mass loss of sample 2 reaches 5% in about 80 cycles. The change rate of mass loss and dynamic modulus of elasticity of standard sample 1 is much lower than that of

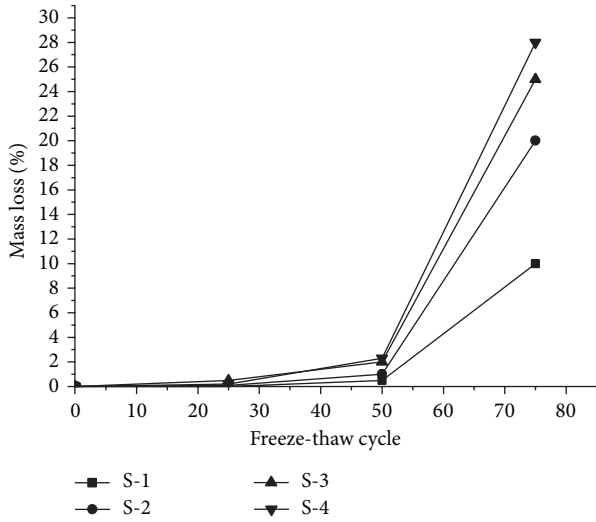


FIGURE 4: Mass loss of concrete cores after freeze-thaw cycles.

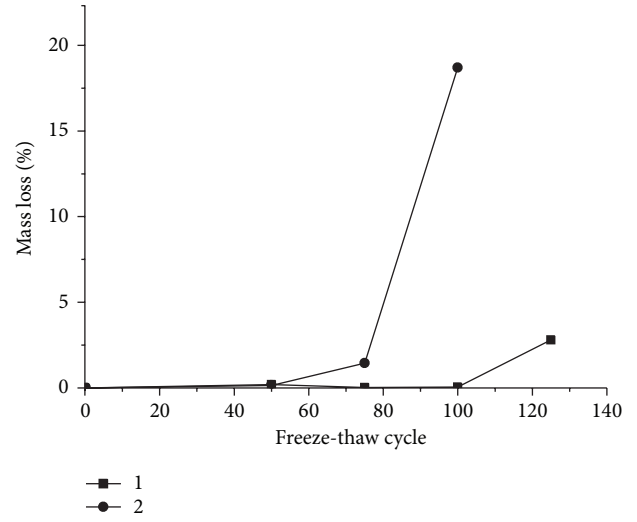
TABLE 5: Impermeability of concrete cores.

Sample	Hydraulic pressure (MPa)
S-5	0.6
S-6	0.4
S-7	0.8
1	1.3
2	0.6

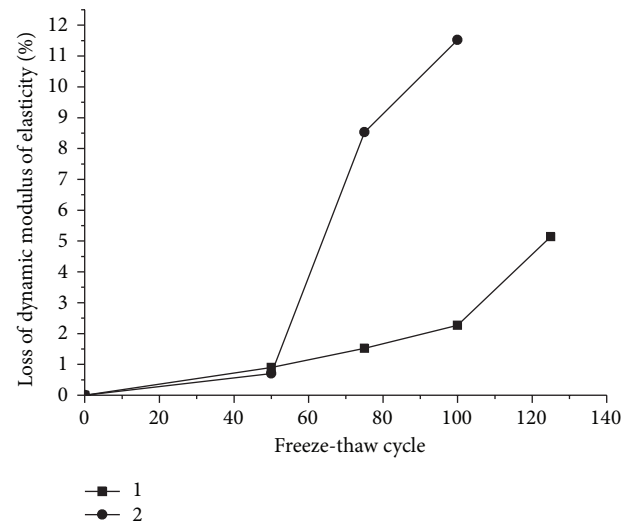
standard sample 2. In general, both of the cores taken from the structure and the standard samples without air entraining admixture made in laboratory exhibited poor frost resistance.

3.3. Impermeability Testing. During impermeability testing, the maximum pressure of samples was measured. The higher pressure sample bore, the greater impermeability concrete had. Table 5 presents testing results of impermeability of both concrete cores from project site and standard samples prepared in laboratory. It is obvious that the cores (S-5, S-6, S-7) from the actual structure exhibit poor impermeability. For standard samples made in laboratory, sample 2 which did not use air entraining admixture also presented poor impermeability, while sample 1 which contained air entraining admixture sustained almost twice hydraulic pressure as high as samples 1. Here, the only difference between sample 1 and other samples is in the usage of air entraining admixture. Therefore, the impermeability of the concrete with air entraining admixture is much better.

3.4. Microstructure Analysis. Microstructures of concrete samples from actual engineering were evaluated through polarizing microscope and SEM. Photos obtained from polarizing microscope were shown in Figure 6, and Figure 7 gave the results obtained by SEM. Observations in Figure 6(a) showed that interstice exists in the interface between mortar



(a)



(b)

FIGURE 5: Freeze-thaw test results for standard samples (a) mass loss and (b) loss of dynamic modulus of elasticity.

and aggregate. Furthermore, micro cracks also appeared in the paste, as shown in Figure 6(b). Similarly, there were also cracking and pores in mortar, as shown in Figure 7. Based on microstructure analysis, the concrete cores presented poor structure. The pore structure of cement-based materials is one of its most important characteristics and strongly influences both its mechanical properties and its durability. Table 6 presented total pore volume, porosity, and average pore diameter of three cores examined by MIP. In the MIP results, sample 1 and sample 2 stand for standard samples with and without air entraining admixture prepared in lab, respectively, while sample S means the concrete core from actual structure. It is to be noted that compared with sample 1, the total pore volume, porosity, and average pore diameter of the sample 2 and sample S are considerably higher. In addition, the sample 2 and sample S contain appreciably

TABLE 6: Pore structure of concrete cores.

Sample	Total volume (mm ³)	Porosity (%)	Average pore size (nm)	$d \geq 100$ nm (%)	$50 \text{ nm} < d < 100$ nm (%)	$d \leq 50$ nm (%)
1	38.60	8.87	47.70	28.98	18.17	52.85
S	96.80	18.64	71.20	39.27	19.20	41.53
2	92.20	17.94	83.00	44.5	16.35	39.15

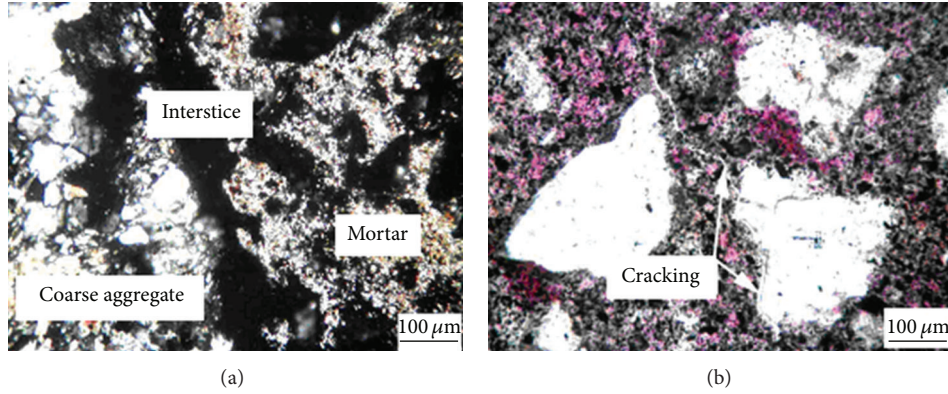


FIGURE 6: Photos of microstructure (a) interstice between coarse aggregate and mortar and (b) cracking in the mortar.

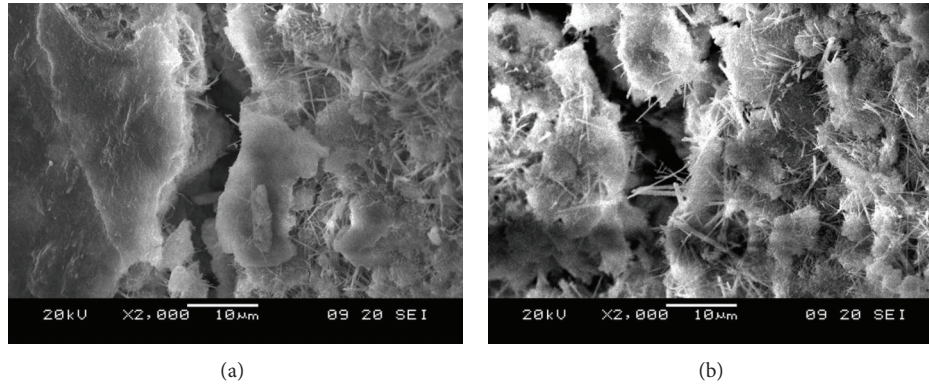


FIGURE 7: SEM images of concrete cores (a) cracking in the mortar and (b) pores in the mortar.

larger amount of pores with $d \geq 100$ nm than the sample 1, which are considered to be harmful, according to Wu and Lian [16]. Therefore, sample 1 showed relative better pore structure, and it indicated that air entraining admixture improved pore structure.

3.5. Discussion of Concrete Durability. Although alkali content in cement used for the structure exceeds the limit value 0.60% of low-alkali cement, the aggregates used are determined to be nonreactive. In addition, the characteristics of alkali-aggregate reaction such as map cracking, white gel, and reaction rim around aggregates have not been found both in field and in lab. These research findings suggest that alkali-aggregate reaction is unlikely to take place for the present case. Based on results of freeze-thaw testing and impermeability testing, it can be deduced that the concrete

cores from actual engineering present poor frost resistance and impermeability. Besides, the standard sample without air entraining admixture made in lab also showed poor frost resistance and impermeability, while the standard sample with air entraining admixture made in lab showed excellent frost resistance and impermeability. Meanwhile, according to climate data, the temperature in situ varies sharply. So, it is the severe weather conditions combined with the poor frost resistance and impermeability that bring about the deterioration of the concrete structure. To solve this problem, usage of air entraining admixture is effective.

Undoubtedly, the durability of concrete used in severe environment should be taken as a top priority. A wholly new program is currently under way in our lab. The objective of the program is to fabricate large area concrete road slabs of long service lifetime. The key point of the program is to improve the microstructure, augment the strength, and

enhance the restraining stress. The measures being taken include addition of chemical additives and expansive mineral admixtures, utilization of steel bar enforcement, and structure design. It is hoped that the ongoing research work may contribute to the solution to durability problem of concrete used in severe environment.

4. Conclusions

In order to find out the deterioration mechanism of the concrete materials used in a runway shoulder, many types of testing have been carried out, such as alkali-aggregate reaction testing, freeze-thaw cycles testing, and permeability testing. The following conclusions may be drawn from results of these investigations: the aggregates used in the concrete structure are nonreactive. Combined with other field and laboratory findings, there is little possibility of occurrence of alkali-aggregate reaction. The concrete cores from actual engineering only showed poor frost resistance and low impermeability. In addition, there were also cracking and pores in the paste of these cores through microstructure analysis. As a result, the severe environmental conditions plus the relatively inferior frost resistance cause the deterioration of the runway shoulder concrete. For the environmental condition where the actual engineering was situated, usage of air entraining admixture is an effective measure. Furthermore, new ideas and new approaches should be taken into consideration to solve the durability problem of concrete used in severe environment.

Conflict of Interests

The authors declare that they have no conflict of interests regarding the publication of this paper.

Acknowledgments

This research was supported by National Natural Science Foundation of China (no. 51108231), and Science and Technology Plan Projects of Ministry of Housing and Urban-rural Development of China (Grant no. 2013-K4-20).

References

- [1] P. M. Eduardo, "Life cycle, sustainability and the transcendent quality of building materials," *Building and Environment*, vol. 42, no. 3, pp. 1329–1334, 2007.
- [2] B. Ma, R. Dong, H. Zhu et al., "Influences of a new admixture MX on concrete durability," *Journal Wuhan University of Technology*, vol. 20, no. 1, pp. 117–120, 2005.
- [3] B. Lulu, K. Joerg, and J. C. David, "Assessment of the durability of concrete from its permeation properties: a review," *Construction and Building Materials*, vol. 15, no. 2-3, pp. 93–103, 2001.
- [4] M. Zhang and O. E. Gjør, "Effect of silica fume on pore structure and chloride diffusivity of low porosity cement pastes," *Cement and Concrete Research*, vol. 21, no. 6, pp. 1006–1014, 1991.
- [5] S. Mindess, J. F. Young, and D. Darwin, *Concrete*, Prentice Hall, New York, NY, USA, 2003.
- [6] R. L. A. Male, "Pore structure and permeability of cementitious materials," *Materials Research Society Symposium Proceedings*, vol. 137, pp. 403–410, 1988.
- [7] Y. Yun and Y. Wu, "Durability of CFRP-concrete joints under freeze-thaw cycling," *Cold Regions Science and Technology*, vol. 65, no. 3, pp. 401–412, 2011.
- [8] W. Li, W. Sun, and J. Jiang, "Damage of concrete experiencing flexural fatigue load and closed freeze/thaw cycles simultaneously," *Construction and Building Materials*, vol. 25, no. 5, pp. 2604–2610, 2011.
- [9] M. N. Haque and M. Kawamura, "Carbonation and chloride-induced corrosion of reinforcement in fly ash concretes," *ACI Materials Journal*, vol. 89, no. 1, pp. 41–48, 1992.
- [10] P. K. Metha and P. Monterio, *Concrete: Structure, Properties, and Materials*, Prentice Hall, New York, NY, USA, 1993.
- [11] H. K. Hilsdorf and J. Kropp, "Performance criteria for durability," RILEM Report 12, CRC Press, London, UK, 1995.
- [12] P. E. Grattan-Bellew, "Microstructural investigation of deteriorated Portland cement concrete," *Construction and Building Materials*, vol. 10, no. 1, pp. 3–16, 1996.
- [13] H. S. Shang and Y. P. Song, "Experimental study of strength and deformation of plain concrete under biaxial compression after freezing and thawing cycles," *Cement and Concrete Research*, vol. 36, no. 10, pp. 1857–1864, 2006.
- [14] M. Tang and M. Deng, "Recent progress of studies on alkali aggregate reaction," *Journal of Building Materials*, vol. 6, no. 1, pp. 1–8, 2003.
- [15] L. B. Mei, M. Deng, and M. S. Tang, "Advanced study on alkali-carbonate reactions in concrete," *Journal of Nanjing University of Technology*, vol. 24, no. 2, pp. 104–110, 2002.
- [16] Z. W. Wu and H. Z. Lian, *High Performance Concrete*, China Railway Press, Beijing, China, 1999.

Research Article

Application of Optimum Compaction Energy in the Development of Bricks Made with Construction Trash Soils

T. Lopez-Lara,¹ C. L. Gonzalez-Vega,¹ J. B. Hernandez-Zaragoza,¹ E. Rojas-Gonzalez,¹ D. Carreón-Freyre,² R. Salgado-Delgado,³ E. Garcia-Hernandez,³ and M. Cerca²

¹ *División de Estudios de Posgrado, Facultad de Ingeniería, Universidad Autónoma de Querétaro, Cerro de las Campanas S/N, Colonia Las Campanas, 76010 Querétaro, QRO, Mexico*

² *Laboratorio de Mecánica Multiescalar de Geosistemas, Centro de Geociencias, Universidad Nacional Autónoma de México, Boulevard Juriquilla 3001, Colonia Juriquilla, 76230 Querétaro, QRO, Mexico*

³ *División de Estudios de Posgrado e Investigación, Departamento de Ingeniería, Química y Bioquímica, Instituto Tecnológico de Zacatepec, Calzada Tecnológico 27, 62780 Zacatepec, MOR, Mexico*

Correspondence should be addressed to T. Lopez-Lara; lolte@uaq.mx

Received 8 February 2014; Accepted 17 April 2014; Published 8 May 2014

Academic Editor: Gonzalo Martínez-Barrera

Copyright © 2014 T. Lopez-Lara et al. This is an open access article distributed under the Creative Commons Attribution License, which permits unrestricted use, distribution, and reproduction in any medium, provided the original work is properly cited.

In general, bricks frequently show different densities and therefore different resistances because the compaction energy is not considered in their production. Expansive soils represent a problem for light buildings over them because of volumetric instability. A generalized solution has been to extract them and substitute them by inert soil; thus they become construction trash. So, in this work the compaction energy aspect and the use of construction trash soils in the elaboration of resistant masonry bricks of homogeneous and controlled density are a new contribution in the production of bricks of better quality. First, the soil was stabilized with CaOH which leads to a decrease in its volumetric changes. Then, they were compacted with a specific energy for obtaining an optimal and maximum controlled density to ensure an increase in strength. Our results show that two optimal compaction energies can be considered with respect to the variation of optimum moisture in masonry bricks of expansive soil stabilized with lime. The first is when the optimal humidity reaches its smallest value (integrated soil lumps) and the second is when humidity increases (disintegrated soil lumps), after reaching its lowest value. We also conclude that high compaction energy does not improve density values.

1. Introduction

Many countries in the world have to deal with the problem of expansive clays (vertisols) such as Mexico, the USA, Australia, South Africa, India, and Israel among others. In particular several regions of Mexico, for instance, in the lacustrine planes located at the states of Querétaro, Guanajuato, Michoacán, Tamaulipas, Morelos, Sonora, Baja California, Veracruz, Chiapas, and Campeche, deposits of this type of soils can be found. The constant growing of human settlements has provoked the urban stain to be extended up to agricultural lands, thus forcing to build on top of them. These soils are mainly of the expansive type and show volumetric instability due to humidity variations. Because of their expansion they bring out fissures in light constructions above them [1]. Due to this problem, these soils are replaced

by soils with inert features [2], thus remaining as trash soils. The objective of this study is to use this trash expansive soil via a composite material, soil-CaOH, to produce bricks of optimal and controlled compaction energy for masonry, which is neglected in the production of this kind of bricks.

To achieve this, the trash expansive soil was stabilized with CaOH to eliminate its volumetric changes and then it was compacted at different energies per volume (cubic meter) for controlling different densities and to obtain an optimal-controlled density and optimum moisture to assure a larger strength in the material. Then, test specimens with these densities were made and subjected to unconfined compressive tests. The compaction energy was selected to be the best reasonable strength. Thereafter, masonry bricks were subjected to tests of stress rupture and strength to first fissure.

In general, bricks frequently show different densities and therefore different resistances because the compaction energy is neglected in the production of this kind of bricks. So, the compaction energy aspect in this work is a new contribution in the production of bricks of better quality.

Therefore, after determining the ideal specific compaction energy of a lime-treated expansive soil, we will be able to use the resulting values of maximum density and optimum moisture, which can be applied with some bricks compressor. With this procedure, sustainable bricks of high and homogeneous resistance can be obtained.

2. Background

The applications of the use of soils treated with CaOH are, for example, in the construction of bed-layers of pavements, in the stabilization of dams made of earth, and as a layer for supporting shallow foundations [3]. This technique is conventional for improving expansive soils properties [4]. This is so, because the CaOH helps stop the expansion of these types of soils [5]. Earth is a cheap, ecological, and plenty material for construction. Indeed, it has been used widely in walls construction around the world, especially in developing countries [6]. About 30% of the world population lives in buildings made of earth. Near 50% of the population of developed countries, including most of the rural population, and at least 20% of urban and marginal population live in buildings where earth was used for its construction [7].

Manufacture of ceramic pieces for masonry represents a very important economical activity in some towns of Mexico and other developing countries. These pieces are preferred because of their cultural reasons, accessibility, and long history. Indeed they have been used since 4000 years ago in Egypt and they represent the first materials manufactured for buildings [8]. However, the low quality control of manufacturing of these pieces leads to strength variations, dimensions, and density. Moreover, because of its production environmental problems emerge such as a high-energy consumption as well as high emissions of carbon dioxide [9], thus causing damage to the public health [10]. This is so because wood, recycled automobile oil, coke, heavy oil, used tires, garbage, and plastics [11] are used as fuels for its production.

The study of different materials for the fabrication of pieces to substitute bricks of burned clay has been the aim of many researchers worried about the environment, the use of natural resources, and the recycling of industrial trashes. Red clay is a trash subproduct from the aluminum extraction. In this respect, there have been efforts for producing these bricks with fly ashes and a small percentage of CaOH. These pieces were tested by accelerated abrasion and considered ideal for its use as low-cost material for shelters [12].

Bricks made of fly ashes, CaOH, and calcium sulfide are one of the best alternatives for bricks of conventional burned clay. Comparative results indicate that the former are lighter in weight, last in aggressive environments, and have enough strength to be used in the construction of buildings [13].

Compressive strength increases 2.5 times when the percentage of cement is doubled from 6 to 12% in compressed

earth-cement blocks with very sandy soils. The rate of humidity absorption depends greatly on cement content. Pores size diminishes with the increase of cement content in the block [14].

Since fifty years ago, the introduction of blocks made of compressed earth was seen as an important step. These blocks are made via compression of a humid mixture of earth (90–95%) and cement (5–10%), thus forming strong and dense blocks used for walls. While their properties are well known with respect to their characteristics of initial performance, there has been little research about their durability in the long term and the deterioration due to long exposition of environmental factors [15].

Achenza and Fenu [16] reported bricks with adobe stabilized with vegetal fibers and a composite of natural polymers. It seems that the latter modified the porosity and apparent density of the bricks and improved their behavior under water action and their compressive strength too.

Soil compaction produces an increase in resistance and decreased deformability. This process is obtained with suitable techniques applied on the soil, which improves the dry specific weight decreasing its empty spaces. Therefore, there are two main factors that determine the best density of soil material: moisture and the specific energy applied.

The specific energy of soil compaction is the compaction effort applied to the soil per unit volume and is determined using the weight, height of drop, and number of blows of a hammer to compact a volume of soil placed in layers into a mold. Therefore, Proctor found a moisture entitled “optimum” that produces the maximum dry weight under a given specific compaction energy [17].

3. Tests and Experimental Methods

3.1. Geotechnical Characterization. Geotechnical characterization of the expansive soil under study was made such as gradation test, according to ASTM D 422 standard [18]. This was done to know the grain size distribution and the proportion of sizes of its constitutive particles. Then, following the ASTM 4318 standard [19], the liquid and plastic limits were determined, as well as the shrinkage limit [20]. With this information, the soil was classified by the Unified Soil Classification System (USCS) [21]. Its specific weight and specific gravity were obtained following the ASTM D 854 standard [22].

3.2. Stabilization of Soil with CaOH. For stabilization of expansive clay, three different doses of CaOH, namely, 6, 8, and 10 percent of its dry weight, were aggregated to each sample. For each dose, the plasticity limits were obtained. The aim was to find the optimal CaOH quantity for abating volumetric changes.

3.3. Application of Compaction Energies. The compacting procedure for the stabilized soil was compaction by layers with a weight falling from a controlled height (Proctor compaction procedure). The compaction energies per cubic meter were Proctor standard (600 kN-m) and modified

Proctor (2700 kN-m), following the procedures ASTM D 698 [23] and D 1557 [24], respectively. Then, higher compaction energy (4000 kN-m) was applied. Results of these tests were the determination of the maximum dried density and the optimum moisture. This procedure is supposed to increase soil density. It should be pointed out that the modified soils tests specimens had the optimal amount of CaOH, previously determined.

3.4. Unconfined Compressive Strength. Test specimens of modified soils were subjected to unconfined compression [25] at different ages (7, 14, 30, and 60 days) and the compaction energies mentioned above. This was done to define the best behavior and strength.

3.5. Fabrication of the Brick Ceramic Material. Once the dose and compaction energy were settled, bricks of 19 cm long, 10 cm width, and 5 cm height were made. Then, they were subjected to tests for determining the break modulus and the strength to first fissure [26] for comparison with commercial bricks.

4. Results

4.1. Geotechnical Properties of Soil. By gradation analysis, via dry and humid, it was determined that the soil was a material with fines, since 94.8% of its particles went through a sieve 200 (0.074 mm). The liquid limit was 70.21% and the plastic limit was 27.56%; thus the plastic index was 42.64%. From these results, the soil can be classified as high compressibility clay (CH) according to the Unified Soil Classification System (USCS), [21]. The volumetric shrinkage limit was 8.68%, specific weight of 15.68 kN/m³, and specific gravity of soil as 2.52. From the gradation via humid analysis, the percentage of particles less than 0.002 mm was 19.5%. With this data and the plasticity index, the activity index of the clay was determined as 4.5. Using the activity criteria the soil has a highly expansive potential [2].

4.2. Soil Stabilized with CaOH. Several test specimens of soil added with CaOH with different percentages in dry weight were prepared. Plasticity limits versus percentages of CaOH are shown in Figure 1. In this figure it can be observed that the plasticity limits properties are stabilized starting with 8% CaOH. Indeed, at that percentage there is little or nil variation of the liquid limit and the plastic index, even increasing the CaOH content. The natural soil corresponds to the 0% of CaOH. Moreover, the soil classification changes from CH (high compressibility clay) to ML (lime of low plasticity); thus, it has properties of a low plasticity soil, that is, little or nil volumetric change.

4.3. Application of Compaction Energies. The optimum quantity of CaOH placed in the soil composite was determined by its plasticity properties and was 8% (Figure 1). To include a broad range of energies, first this study includes two energies from two common assays of soils compaction, 600 (kN-m)/m³ at Proctor standard and 2700 (kN-m)/m³ at Proctor

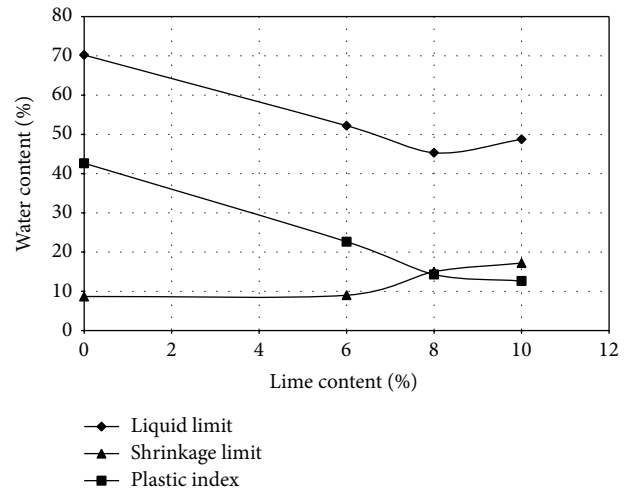


FIGURE 1: Atterberg limits versus lime content.

modified, and proposes a third higher energy value of 4000 (kN-m)/m³. After applying these three energies, we observe that the best dried density of the material corresponded to the Proctor standard energy. Then with the objective of identifying the nearest energy value, the following tests were performed between values of Proctor standard and Proctor modified energies. These were 1500, 1800, 2100, and 2400 (kN-m)/m³. Values for maximum dry density and optimum moisture content for the above conditions are shown in Table 1.

When the energy compaction of the soil increases from 600 to 2100 (kN-m)/m³, the density increases and the optimum moisture content decreases due to compression of the soil (Table 1). Then, the next increment of the compaction energy (2400 (kN-m)/m³) causes an increase in density and a sudden increase in moisture, which is likely due to dispersion of lumps of the soil which generates more smaller soil grains and therefore more contact areas surrounded by water which helps accommodate the soil. This energy causes a small final increase in its density. After 2400 (kN-m)/m³, the density tends to decrease probably due to increasing dispersion of soil aggregates into discrete units by mechanical means (increasing application of energy) [17]. Therefore additional soil dispersions generate increase of water content. This caused a poor compaction of the material (low density values) because water cannot move instantaneously under the compacting hammer blows [17].

Therefore two optimal compaction energies can be considered with respect to the variation of optimum moisture, the first when the optimal humidity reaches its smallest value and the second when it increases, after reaching its lowest value.

4.4. Strength to Unconfined Compression. Stabilized-soils tests specimens were prepared and subjected to unconfined compression, following the ASTM D 2166 standard [25]. Tests specimens were subjected to specific compaction energies of 600 (Proctor standard), 1500, 1800, 2100, 2400, 2700

TABLE 1: Compaction properties and unconfined compressive strength at different ages.

Energy/m ³ (kN-m)/m ³	Compaction data		Unconfined compressive strength (MPa)			
	Optimum moisture content (%)	Maximum dry density (kN/m ³)	7 days	14 days	30 days	60 days
600	35.00	12.74	0.78	0.97	1.06	1.41
1500	33.30	14.70	1.32	2.01	2.71	3.57
1800	31.53	15.09	1.44	2.29	3.06	4.08
2100	31.40	15.29	1.42	2.35	3.20	4.25
2400	34.20	15.39	1.63	2.62	3.57	4.74
2700	38.20	12.25	0.49	0.40	0.42	0.50
4000	37.82	12.25	0.45	0.37	0.40	0.48

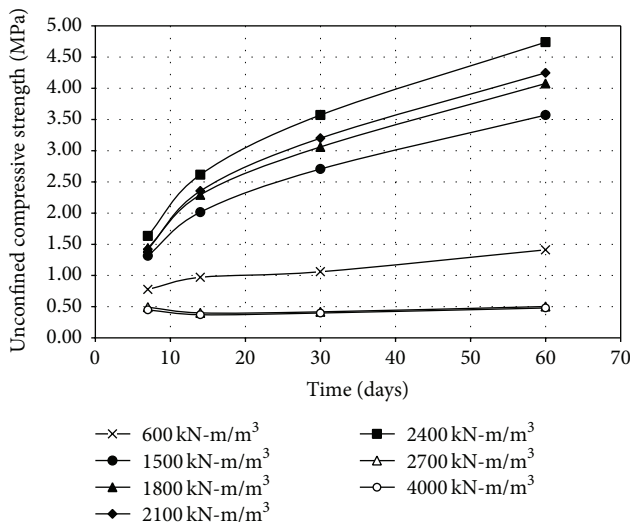


FIGURE 2: Composite strength for different specific compaction energies and ages.

(Proctor modified), and 4000 (kN-m)/m³. Results are plotted in Figure 2. Figure 2 shows that the increase in density causes increases in resistance.

From Figure 2, the best strengths were obtained with the two optimal compaction energies considered (2100 and 2400 (kN-m)/m³), the first when the optimal humidity reaches its smallest value and the second when it increases, respectively, after reaching its lowest value. This work applied the compaction effort value when the optimal humidity reaches its smallest value, 2100 (kN-m)/m³, to obtain the best dry density of the clay composite with 8% of CaOH; this is because it is more accurate to find the smallest value of moisture in similar experiments.

4.5. Rupture Stress and Fracture Stress of the Brick Ceramic Material. To determine these values, test specimens were prepared with dimensions: 19 cm long, 10 cm width, and 5 cm height, with ages of 7, 14, 30, and 60 days, and tested according to the ASTM C67 standard [26]. Results are displayed in Table 2.

TABLE 2: Rupture stress and fracture stress of the proposed brick and some commercial products.

Material	Rupture stress (MPa)	Fracture stress (MPa)
Proposed brick (7 days)	0.09	1.56
Proposed brick (14 days)	0.16	2.51
Proposed brick (30 days)	0.31	3.33
Proposed brick (60 days)	0.37	3.81
Burned clay brick	0.45	3.08
Block (cement)	0.20	5.91
“Sillar”	0.01	2.38
Adobe	0.16	1.32

From Table 2, it can be observed that the best results for the proposed brick under study were obtained at 60 days. These were compared with commercial pieces for masonry, tested under the same norm. Moreover, it can be said that the proposed brick overcame the strength of burned clay brick, “sillar,” and adobe, close to the maximum fracture stress corresponding to the brick. The “sillar” is a regional brick for construction. This is a cut material extracted from sedimentary rocks as shale.

5. Conclusions

With trash expansive clay, a brick with CaOH with optimal-controlled density could be obtained. The amount of CaOH to avoid volumetric changes on this type of soils was 8%.

We conclude that in expansive soils treated with lime two optimal compaction energies can be considered with respect to the variation of a determined optimum moisture: the first when the optimal humidity reaches its smallest value and the second when it increases, after reaching its lowest value. This probably occurs due to the continuous increase in compaction energy that causes the soil particles and humidity to achieve their best accommodation: first with intact soil particles (lumps) and then with disintegrated particles of soil, respectively. Higher compaction energy values do not improve density. The increase in density causes increases in resistance. This work applied the compaction effort value

when the optimal humidity reaches its smallest value to obtain the best dry density.

The proposed sustainable brick made of construction trash soil has a maximum controlled density and better mechanical behavior when compared to another commercial masonry pieces around the region (burned clay brick, "sillar," and adobe). In addition the mechanical properties of the composite increase with time.

Conflict of Interests

The authors declare that there is no conflict of interests regarding the publication of this paper.

References

- [1] A. Seco, F. Ramírez, L. Miqueleiz, and B. García, "Stabilization of expansive soils for use in construction," *Applied Clay Science*, vol. 51, no. 3, pp. 348–352, 2011.
- [2] F. H. Chen, *Foundations on Expansive Soils*, Elsevier Scientific, Amsterdam, The Netherlands, 1988.
- [3] N. C. Consoli, L. da Silva Lopes, and K. S. Heineck, "Key parameters for the strength control of lime stabilized soils," *Journal of Materials in Civil Engineering*, vol. 21, no. 5, pp. 210–216, 2009.
- [4] J.-L. Zheng, R. Zhang, and H.-P. Yang, "Highway subgrade construction in expansive soil areas," *Journal of Materials in Civil Engineering*, vol. 21, no. 4, pp. 154–162, 2009.
- [5] R. L. Buhler and A. B. Cerato, "Stabilization of Oklahoma expansive soils using lime and Class C Fly ash," in *Problematic Soils and Rocks and In Situ Characterization*, vol. 162 of ASCE Geotechnical Special Publication, pp. 1–10, Denver, Colo, USA, February 2007.
- [6] S. Sheweka, "Using mud bricks as a temporary solution for Gaza reconstruction," *Energy Procedia*, vol. 6, pp. 236–240, 2011.
- [7] D. Silveira, H. Varum, A. Costa, T. Martins, H. Pereira, and J. Almeida, "Mechanical properties of adobe bricks in ancient constructions," *Construction and Building Materials*, vol. 28, no. 1, pp. 36–44, 2012.
- [8] A. Lyons, *Ceramic Materials for Architects and Builders*, Butterworth-Heinemann, Oxford, UK, 3rd edition, 2006.
- [9] A. S. Muntohar, "Engineering characteristics of the compressed-stabilized earth brick," *Construction and Building Materials*, vol. 25, no. 11, pp. 4215–4220, 2011.
- [10] C. W. Bruce, A. Y. Corral, and A. S. Lara, "Development of cleaner-burning brick kilns in Ciudad Juarez, Chihuahua, Mexico," *Journal of the Air & Waste Management Association*, vol. 57, no. 4, pp. 444–456, 2007.
- [11] A. Y. Corral Avitia, A. de la Mora Covarrubias, A. D. Cota Espericueta, R. Corral Díaz, K. A. Carrasco Urrutia, and L. E. Santana Contreras, "The risk mapping as an instrument technician for the relocation of the brick industry of the municipality of Juarez, Mexico," *Revista Internacional de Contaminacion Ambiental*, vol. 26, no. 1, pp. 17–26, 2010.
- [12] A. Dass and S. K. Malhotra, "Lime-stabilized red mud bricks," *Materials and Structures*, vol. 23, no. 4, pp. 252–255, 1990.
- [13] S. Kumar, "Fly ash-lime-phosphogypsum cementitious binder: a new trend in bricks," *Materials and Structures*, vol. 33, no. 225, pp. 59–64, 2000.
- [14] B. V. V. Reddy and K. Gourav, "Strength of lime-fly ash compacts using different curing techniques and gypsum additive," *Materials and Structures*, vol. 44, no. 10, pp. 1793–1808, 2011.
- [15] A. G. Kerali, "In-service deterioration of compressed earth blocks," *Geotechnical & Geological Engineering*, vol. 23, no. 4, pp. 461–468, 2005.
- [16] M. Achenza and L. Fenu, "On earth stabilization with natural polymers for earth masonry construction," *Materials and Structures*, vol. 39, no. 285, pp. 21–27, 2006.
- [17] M. D. Braja, *Principles of Geotechnical Engineering*, Cengage Learning, United States of America, 7th edition, 2010.
- [18] "Standard Test Method for Particle-Size Analysis of Soils," ASTM D422-63, *Annual Book of ASTM Standards*, 2007.
- [19] "Standard Test Methods for Liquid Limit, Plastic Limit and Plasticity Index of soils," ASTM D4318-10, *Annual Book of ASTM Standards*, 2010.
- [20] "Standard Test Method for Shrinkage Factors of Soils by the Mercury Method (Withdrawn 2008)," ASTM D 2427-04, *Annual Book of ASTM Standards*, 2008.
- [21] "Standard Test Method for Classification of Soils for Engineering Purposes," ASTM D 2487-93, *Annual Book of ASTM Standards*, 1993.
- [22] "Standard Test Methods for Specific Gravity of Soil Solids by Water Pycnometer," ASTM D 2854-10, *Annual Book of ASTM Standards*, 2010.
- [23] "Standard Test Methods for Laboratory Compaction Characteristics of Soil Using Standard Effort (12400ft-lbf/ft³(600kN-m/m³)," ASTM D698-00a, *Annual Book of ASTM Standards*, 2000.
- [24] "Standard Test Methods for Laboratory Compaction Characteristics of Soil Using Modified Effort (56000ft-lbf/ft³(2700kN-m/m³)," ASTM D1557-12, *Annual Book of ASTM Standards*, 2012.
- [25] "Standard Test Method for Unconfined Compressive Strength of Cohesive Soil," ASTM D2166-00, *Annual Book of ASTM Standards*, 2000.
- [26] "Standard Test Methods for Sampling and Testing Brick and Structural Clay Tile," ASTM C67-13a, *Annual Book of ASTM Standards*, 2013.

Research Article

Evaluation of Relationship between Water Absorption and Durability of Concrete Materials

S. P. Zhang and L. Zong

Department of Civil Engineering and Architecture, Nanjing Institute of Technology, Nanjing 211167, China

Correspondence should be addressed to S. P. Zhang; zhangshiping1982@gmail.com

Received 6 January 2014; Revised 18 March 2014; Accepted 18 March 2014; Published 10 April 2014

Academic Editor: Juan José del Coz Díaz

Copyright © 2014 S. P. Zhang and L. Zong. This is an open access article distributed under the Creative Commons Attribution License, which permits unrestricted use, distribution, and reproduction in any medium, provided the original work is properly cited.

Environment has significant effects on the water absorption of concrete materials. This paper presents an experimental study of the influence of water absorption on the durability of concrete materials. A detailed analysis is also presented in order to establish useful relationship between them. Concrete specimens of different water absorption were prepared through different curing conditions, and results indicated that curing condition can significantly affect the surface water absorption. SEM photos also showed that different curing conditions caused different microstructure. After 28-days curing, compressive strength, permeability, sulfate attack, and chloride ion diffusion of concrete samples were investigated. As a result, both of surface sorptivity and internal sorptivity have no clear relationship with compressive strength. Results obtained also showed that only surface water absorption related to the performance of concrete including permeability, sulfate attack, and chloride ion diffusion. In addition, both impermeability and resistance to sulfate attack were linearly associated with surface sorptivity, and both correlation coefficients were not less than 0.9. Furthermore, chloride ion diffusion coefficient has exponent relation to surface water absorption with higher correlation coefficient. However, no apparent relationship was found between internal water absorption and durability like impermeability, resistance to sulfate attack, and chloride ion diffusion.

1. Introduction

Durability of concrete plays a critical role in controlling its serviceability. Furthermore, durability of concrete is mainly dependent on the capacity of a fluid to penetrate the concrete's microstructure, which was called permeability. High permeability led to the introduction of molecules that react and destroy its chemical stability [1]. Moreover, low permeability of concrete can improve resistance to the penetration of water, sulphate ions, chloride ions, alkali ions, and other harmful substances which caused chemical attack [2]. Concrete permeability had a close relationship with the characteristics of its pore structure in the cement paste and the intensity of microcracks at the aggregate-cement paste interface as well as within the paste itself [3]. Here, pore structure mainly involved volume and size of the interconnected capillary pores. As we know, the hydration reaction of cement results in a product consisting of solid and pore systems. The pore network of a cement paste matrix provides passage

for the transport of fluid into concrete and its development depends on a number of factors including the properties and composition of the concrete constituent materials, the initial curing condition and its duration, the age at testing, and the climatic exposure during drying and conditioning of the concrete [4, 5]. The temperature of curing and the duration of moist curing are the key factors for proper pore structure. The effectiveness of initial curing becomes more important when mineral admixtures like fly ash are used as partial substitution for cement in concrete. Numerous workers have reported that mineral admixtures require a relatively long curing period for the favourable pozzolanic effect on the performance of concrete to be realized [6, 7].

Sorptivity is an index of moisture transport into unsaturated specimens, and recently it has also been recognized as an important index of concrete durability [8]. During sorptivity process, the driving force for water ingress into concrete is capillary suction within the pore spaces of concrete, and not a pressure head [9]. A detailed characterisation of the pore

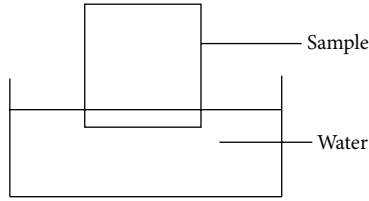


FIGURE 1: Sorptivity testing.



FIGURE 2: Permeability height of concrete.

structure of the concrete can be analyzed by many kinds of techniques, but the advanced methods are cumbersome and are neither available nor useful for daily concrete practice [3]. Sorptivity testing is also more representative of typical field conditions. Some experts have suggested that the method can also be used to measure the total pore volume of capillary and gel pores in the concrete [10]. Martys and Ferraris have shown that the sorptivity coefficient is essential to predict the service life of concrete as a structural material and to improve its performance [11]. The water absorption by immersion is also considered to be a relevant parameter about the performance of concrete. Several experimental investigations have shown that the capillary permeability is substantially affected by the curing condition [12]. Sufficient curing is essential for a concrete to provide its potential performance [13].

Theoretical relations between sorptivity and permeability are established in the literature [14, 15]. However, these relations have not been extensively evaluated experimentally. In this study, the total capillary and gel pore volume was not measured directly but was estimated using the water uptake from soaking testing. The main objective of the present work is to study the effect of water absorption on durability of concrete such as compressive strength, permeability, sulfate attack, and chloride diffusion. Within these tests, mechanical test, impermeability test, sulfate attack test, and chloride migration tests are realized. A detailed analysis is also presented in order to establish useful relationship between these parameters.

2. Materials and Methods

2.1. Materials. In experimental studies, the OPC 42.5 was used. The chemical composition of this cement is given

TABLE 1: Chemical composition of cement.

Sample	Chemical composition (%)						
	CaO	SiO ₂	Al ₂ O ₃	Fe ₂ O ₃	MgO	SO ₃	Na ₂ Oeq
Cement	63.6	23.74	5.56	3.96	1.45	0.71	0.45

TABLE 2: Mix proportions of concrete (Kg/m³).

Number	Cement	Sand	Crushed stone	Water	Admixture
A	420	635	1149	168	5.21
B	420	635	1149	189	5.21

at Table 1. The crushed stone aggregates and quartz sand with a fineness modulus of 2.4 were used in tests. The maximum particle size of aggregates is 20 mm. As a result of experiments, the specific gravities of sand and crushed stone are 2650 and 2800, respectively. Concrete admixture used was polycarboxylate water reducers.

2.2. Methods. All concrete mixtures were prepared in the laboratory. Two kinds of water to cement ratio (w/c) were used, and the detailed mixture proportions of the concrete studied are given in Table 2. $100 \times 100 \times 100$ mm cubes were cast to determine the compressive strength, respectively. Cores of $\Phi 175 \times \Phi 185 \times 150$ mm were prepared for permeability test, and $100\Phi \times 175$ mm concrete cylinders were also prepared for chloride ions diffusion testing. All specimens were cast in steel molds and compacted using a vibrating table.

In order to achieve different water absorption, specimens were subjected to different curing methods as follows: Curing a: specimens were submerged in water ($20 \pm 3^\circ\text{C}$) after demoulding until testing; Curing b: after demoulding, specimens were cured in air condition ($20 \pm 3^\circ\text{C}$, RH $90 \pm 5\%$) until testing; Curing c: specimens were cured in air condition ($20 \pm 3^\circ\text{C}$, RH $60 \pm 5\%$) until testing; Curing d: specimens were submerged in water for 7 days after demoulding and subsequently placed in air conditions ($20 \pm 3^\circ\text{C}$, RH $90 \pm 5\%$) until testing; Curing e: specimens were submerged in water for 7 days after demoulding and subsequently placed in air conditions ($20 \pm 3^\circ\text{C}$, RH $60 \pm 5\%$) until testing.

Sorptivity of concrete was evaluated by penetration height and water absorption, and the introduction of this testing method was shown in Figure 1. All of these samples were dried at 60°C for 24 h to minimize damage to the microstructure from excessive drying. For penetration height, the surface with a length of 3–5 mm of the sample was in contact with water, as shown in Figure 1. Since the surface of the sample became dark when it absorbed water, penetration height at the side of samples was observed during testing. For water absorption, the surface and middle segments were cut from samples, respectively, and thus surface water absorption and internal water absorption were also measured. Before testing, specimens were sealed on the top and sides and placed in a water bath so that the open bottom was constantly submerged in a depth of 3–5 mm. Weight of samples was measured after 4 days, and water absorption was measured.

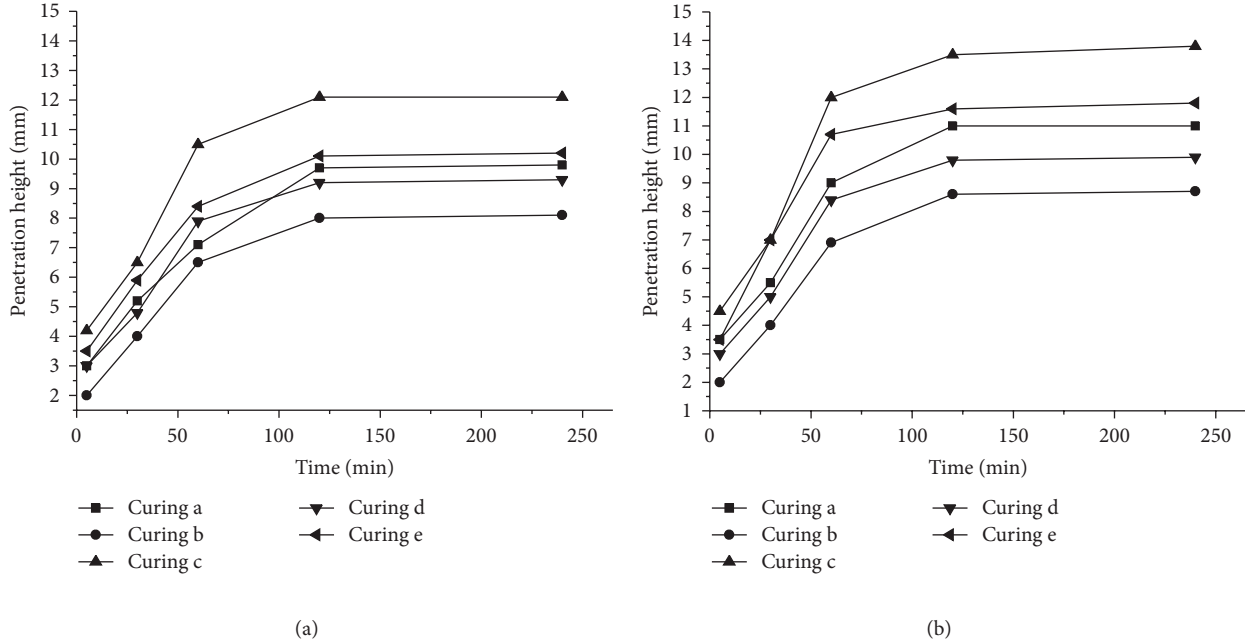


FIGURE 3: Penetration height of samples: (a) $w/c = 0.4$ and (b) $w/c = 0.45$.

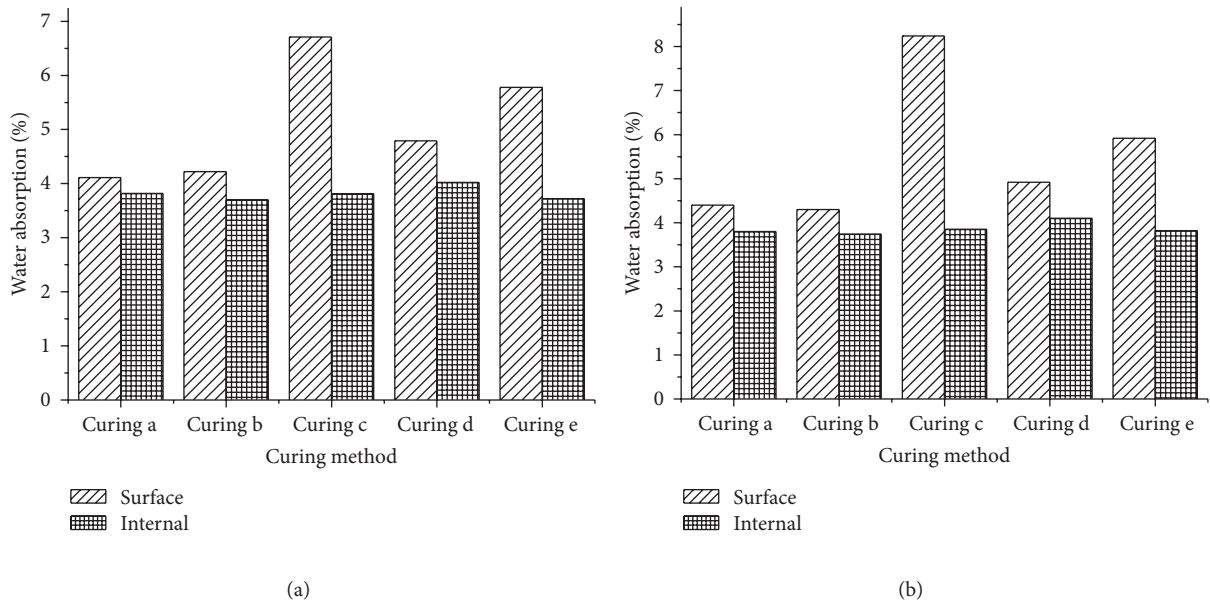


FIGURE 4: Surface and internal water absorption of samples: (a) $w/c = 0.4$ and (b) $w/c = 0.45$.

The permeability of concrete was evaluated according to Testing Code of Concrete for Port and Waterwog Engineering (JTJ 270-98). A water pressure of $1.2 \text{ MPa} \pm 0.5 \text{ MPa}$ was applied on the concrete for 24 h, and then the permeability height was measured by splitting the concrete, as shown in Figure 2. The permeability coefficient was calculated using

$$S_k = \frac{mD_m^2}{2TH}, \quad (1)$$

where S_k is the relative permeability coefficient (mm/h), D_m is the average permeability height (mm), m is the absorption of the concrete (0.03), T is the testing time (h), and H is the water pressure (mm). Resistance to sulfate attack was evaluated through dry-wet cycle testing. The specimens were kept in sulfate solution for 12 h, then dried at 60°C for 12 h, and subsequently placed in sulfate solution for 12 h in a cycle. Sodium sulfate with concentration of 5% was used. Compressive strength was measured during testing.

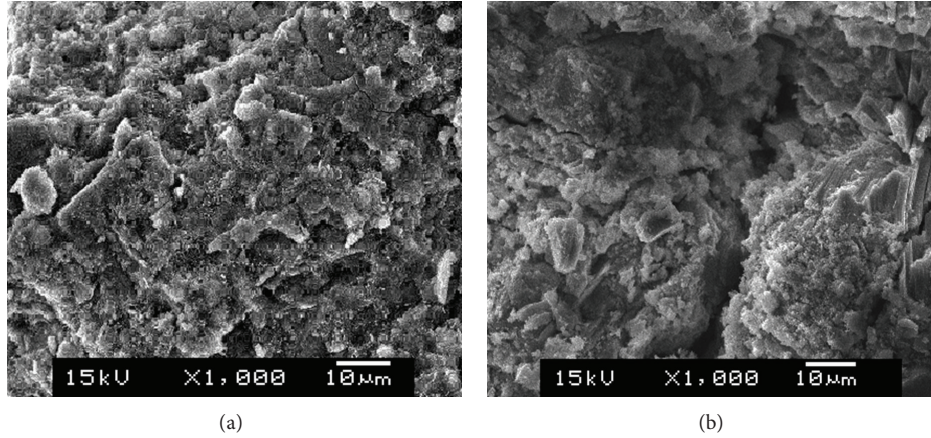


FIGURE 5: SEM photos of concrete samples: (a) condition b and (b) condition d.

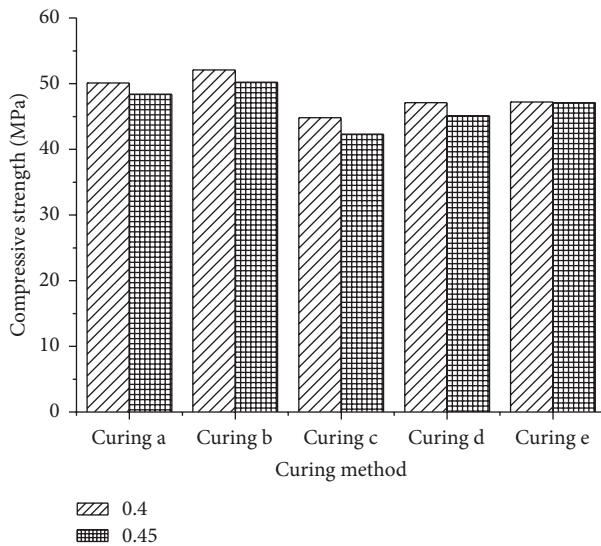


FIGURE 6: Compressive strength of samples.

Rapid migration test is a non-steady state migration using an external electrical field for accelerating chloride penetration. The test is relatively simple and rapid with the test duration in most cases being 24 hours. The concrete samples with size of 100 mm diameter and 175 mm thickness were cut into 50 mm thick slices, from surface and center of samples, respectively. A 30 V external potential was imposed across the specimen with the test surface exposing in the 10% NaCl solution and the oppose surface in the 0.3 M NaOH solution for a certain duration, then the specimen was splitted, and the penetration depth of chlorides can be measured by using a colourimetric method.

3. Results and Discussion

3.1. Water Absorption. Permeability height can be measured through soaking testing, and results about this are given in

Figure 3. It can be shown that penetration height increased apparently with time within 12 h. For different curing methods, penetration height was not the same. In contrast, the samples cured in condition b ($20 \pm 3^\circ\text{C}$, $\text{RH } 90 \pm 5\%$) showed the lowest penetration height, while the samples of Curing c presented the highest one. Samples with lower w/c also showed lower penetration height. It indicated that different curing conditions will cause different permeability of samples.

Sorption depends on both the capillary pressure and effective porosity. Capillary pressure is related to the pore size through the Young-Laplace equation, and effective porosity refers to the pore space in the capillary and gel pores. In addition, different pore size leads to different capillary pressure, and capillary pressure of concrete can be calculated by the average pore size. In order to consider surface effect, both surface water absorption and internal water absorption were investigated. Water absorption is measured by measuring the increase in mass as a percentage of dry mass. Figure 4 gives results of surface and internal water absorption. It can be seen that surface water absorption is higher than internal water absorption for all the specimens. This is due to the rapid loss of water at the cover concrete during curing. As can be expected, higher water absorption corresponds to a higher penetration height. For surface water absorption, results showed that the specimen exposed to air curing ($20 \pm 3^\circ\text{C}$, $\text{RH } 90 \pm 5\%$) exhibited low water absorption properties compared to other samples. Obviously, air condition ($20 \pm 3^\circ\text{C}$, $\text{RH } 60 \pm 5\%$) caused the highest water absorption. This may be attributed to the higher porosity of the concrete preserved in air ($20 \pm 3^\circ\text{C}$, $\text{RH } 60 \pm 5\%$). Under this curing condition, the surface concrete rapidly loses its water of hydration. On the other hand, for internal water absorption, samples exposed to different curing conditions presented similar results. So, curing methods has great influence on surface properties. For the samples with different w/c , it can be seen that surface water absorption of samples with w/c of 0.45 is only slightly higher than that of 0.4. Furthermore, there was very little difference between both samples for internal water

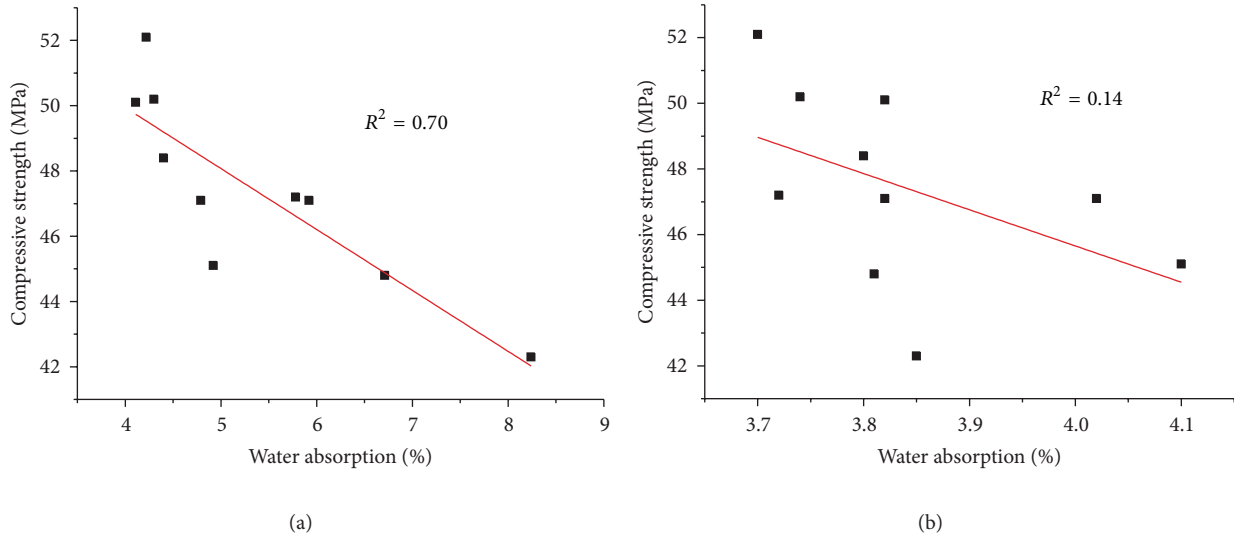


FIGURE 7: Relationship between water absorption and compressive strength: (a) surface water absorption and (b) internal water absorption.

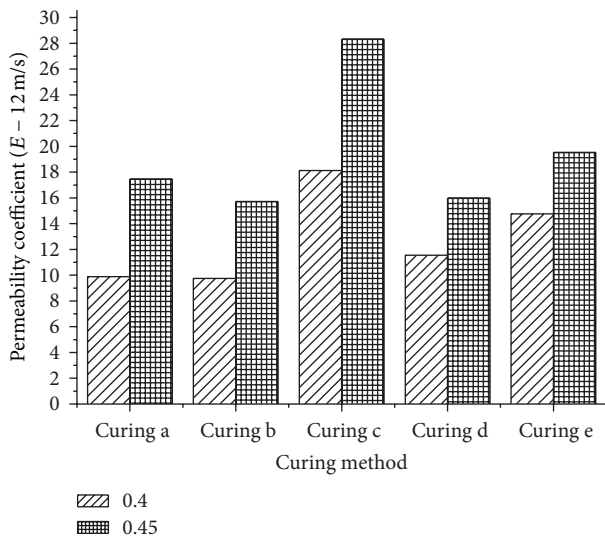


FIGURE 8: Permeability coefficient of samples.

absorption, and w/c seems to have little impact on internal water absorption. In order to investigate the influence of curing on microstructure of concrete, microstructure of concrete samples exposed to different curing conditions was also analyzed by SEM. As there was a large difference in surface water absorption, microstructure of surface concrete was further studied. Figure 5 showed photos of surface concrete obtained by SEM, and Figure 5(a) stands for the sample exposed to condition b, while Figure 5(b) stands for the sample exposed to condition d. From Figure 5, different structures can be seen. For the sample cured in condition b, the microstructure was more compact. However, for the sample cured in condition b, there were holes and loose

structure. These are consistent with the results of water absorption.

3.2. Relations between Water Absorption and Compressive Strength. After being cured for 28 days, compressive strength was measured, and Figure 6 presents results of compressive strength. Samples cured in air condition ($20 \pm 3^\circ\text{C}$, RH $90 \pm 5\%$) show highest strength, while those cured in air condition ($20 \pm 3^\circ\text{C}$, RH $60 \pm 5\%$) have lowest strength. Effects of sorptivity on compressive strength are seen in Figure 7. Figures show that both of surface sorptivity and internal sorptivity have no clear relationship with compressive strength. Although the specimens differ in surface water absorption, there is little difference in internal water absorption. Furthermore, the high surface water absorption only decreased compressive strength of cover concrete. The whole strength of concrete depends on both surface and internal structures. So, strength of concrete cannot be evaluated by water absorption.

3.3. Relations between Water Absorption and Permeability. Permeability coefficients of samples with different curing conditions were measured, and results were given in Figure 8. Relationship between permeability coefficient and water absorption was also analyzed, as shown in Figure 9. From the figures, we can see that there was no clear relationship between permeability coefficient and internal permeability coefficient. However, apparently, a linear correlation exists between permeability coefficient and surface permeability coefficient. The permeability coefficient increased with the increase in surface water absorption. As we know, both of permeability and water absorption were affected by the pore structure of cement paste, and liquid transfers from surface into interior. So, it indicated that surface water absorption provides great influence on permeability. In addition, the high correlation coefficients of 0.90 indicated that there was a significant linear correlation between permeability and

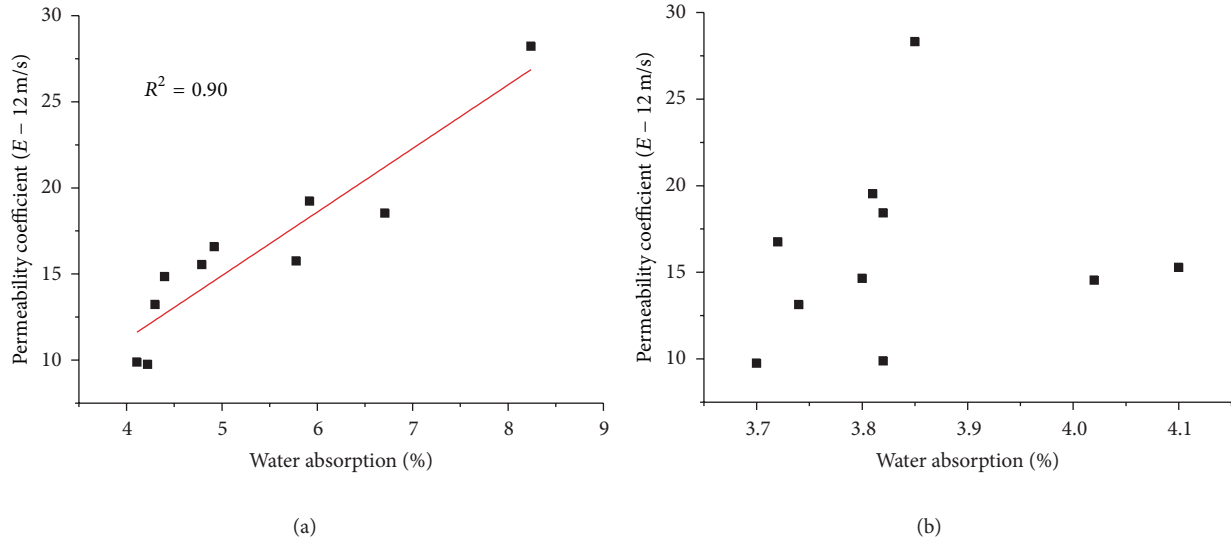


FIGURE 9: Relationship between water absorption and permeability: (a) surface water absorption and (b) internal water absorption.

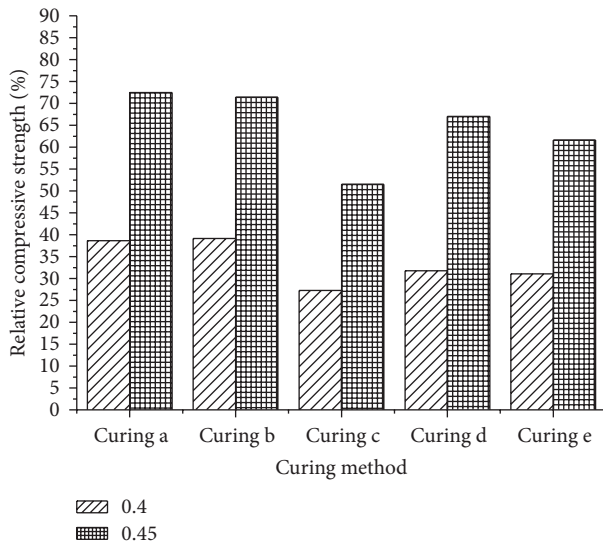


FIGURE 10: Relative strength of samples after sulfate attack.

surface water absorption. In addition, obviously, internal water absorption had little impact on permeability.

3.4. Relations between Water Absorption and Sulfate Attack. Resistance to sulfate attack is evaluated by the loss of strength. During sulfate attack testing, compressive and flexural strengths of specimens were measured after different dry-wet cycles. Relative strengths after 30 dry-wet cycles were presented in Figure 10. Based on Figure 10, it can be seen that compressive strength decreased after sulfate attack, and the sample with w/c of 0.45 showed more loss of strength than that of 0.4. High w/c led to weaker resistance to sulfate attack. Results shown in Figure 11 demonstrated the effect of water absorption on resistance to sulfate attack. Higher

relative strength indicates greater resistance to sulfate attack. It has been discussed earlier that impermeability reduced with the increasing value of surface water absorption. This characteristic was quite similar to the behavior exhibited by resistance to sulfate attack. Based on Figure 11, there was a linear correlation between surface water absorption and loss of compressive strength due to sulfate attack. In addition, loss of compressive strength showed a higher rate of decrement indicated by steep slopes of the curve. By contrast, the loss of compressive strength did not appear to depend upon internal water absorption, as shown in Figure 11(b). The relationships between two parameters were calculated and their correlation results are presented in Figure 11(a).

3.5. Relations between Water Absorption and Chloride Attack. The rapid migration test provides value of D_{Cl} , which is also under the assumption of constant chloride binding capacity during the test. D_{Cl} was deduced according to (2):

$$D_{Cl} = 2.872 \times 10^{-6} \frac{Th(x_d - \alpha\sqrt{x_d})}{t}, \quad (2)$$

$$\alpha = 3.338 \times 10^{-3} \sqrt{Th}, \quad (3)$$

where D_{Cl} is chloride ion diffusion coefficient, m^2/s ; T is average value of early and final temperature of anolyte, K; h is the height of the sample, m; x_d is the diffusion depth of chloride ion, m; t is the testing time, s; α is auxiliary variable.

Capillary absorption is an important mechanism related to the chloride ingress into concrete. Nonsaturated concrete in contact with a salt solution will absorb this solution by capillary forces [16]. Figure 12 gives the chloride ion diffusion coefficient D_{Cl} of concrete. From Figure 12, for w/c of 0.4, the chloride ion diffusion coefficient was lower, and this may be due to the higher water absorption of concrete whose w/c was 0.45. Figure 13 shows relationship between water absorption and chloride ion diffusion coefficient. Based on

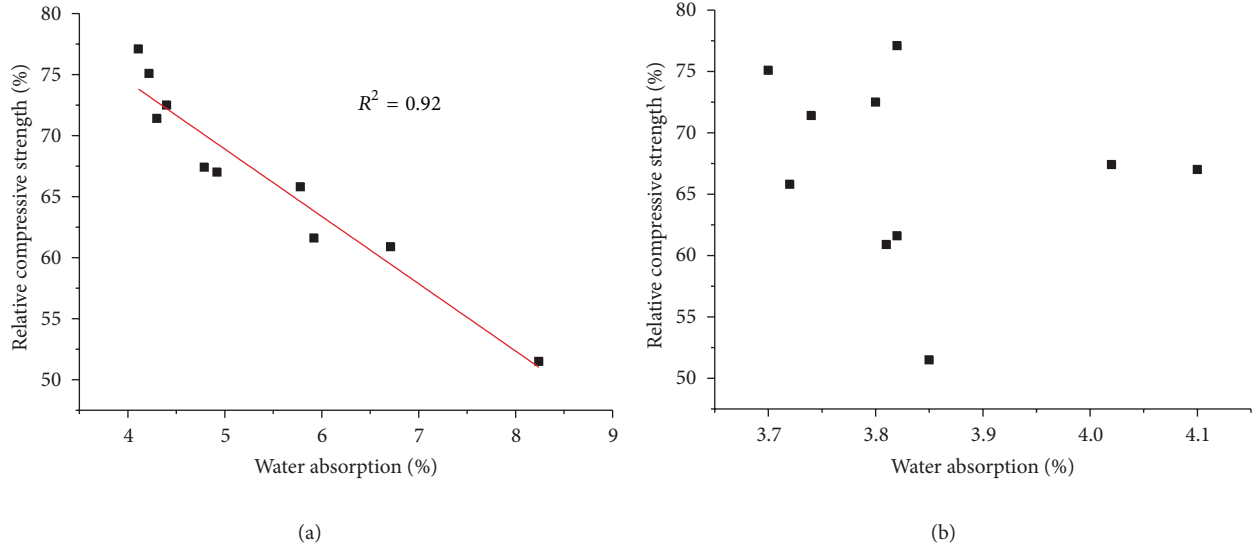


FIGURE 11: Relationship between water absorption and resistance to sulfate attack: (a) surface water absorption and (b) internal water absorption.

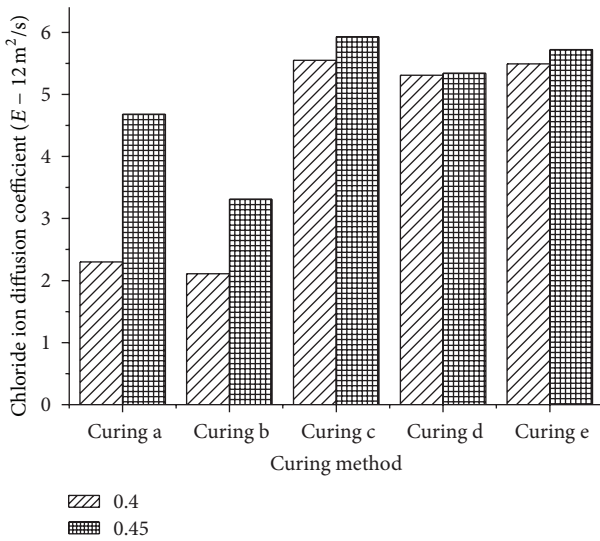


FIGURE 12: Chloride ion diffusion coefficient of samples.

the results, it can be seen that chloride ion diffusion coefficient related to water absorption surface concrete, and chloride ion diffusion coefficient increased with the water absorption. The sample with lowest absorption still showed the best resistance to chloride ion diffusion. Unlike previous results, chloride ion diffusion coefficient has exponent relation to water absorption, and the correlation coefficient is 0.91. The simultaneous action of diffusion and capillary suction thus causes a mixed transport mode. Once chloride penetrated, the initial mechanism appears to be suction when the surface is dry and chloride solution is rapidly absorbed by dry concrete. Next, diffusion dominated transport mechanism, instead of capillary movement of chloride solution. Both of

these two kinds of mechanism depended on pore structure, which was evaluated by water absorption here.

4. Conclusions

Based on the results and the discussion of mechanical performance, permeability, sulfate attack, and chloride ion diffusion of the concrete with different water absorption, the following conclusions are drawn.

Curing conditions can greatly affect the water absorption of concrete. Based on the curing conditions in this paper, the concrete which was exposed to air curing ($20 \pm 3^\circ\text{C}$, $\text{RH } 90 \pm 5\%$) exhibited low water absorption. In addition, surface water absorption was higher than internal water absorption regardless of curing conditions. Both of surface water absorption and internal water absorption had no clear relationship with compressive strength, which indicated that the strength cannot be simply evaluated by water absorption. Permeability mainly depended on the surface water absorption of concrete, and there was a significant linear correlation between permeability and surface water absorption. However, internal water absorption presented little relationships to permeability. Higher water absorption decreased resistance to sulfate attack of concrete, and the relationship between surface water absorption and resistance to sulfate attack was approximately linear. Similarly, it presented a poor correlation between internal water absorption and resistance to sulfate attack. Furthermore, chloride ion diffusion coefficient has exponent relation to surface water absorption, and the correlation coefficient is 0.91. As a whole, surface water absorption can be applied to predict some performance of concrete, including compressive strength, permeability, resistance to sulfate attack, and chloride ion diffusion.

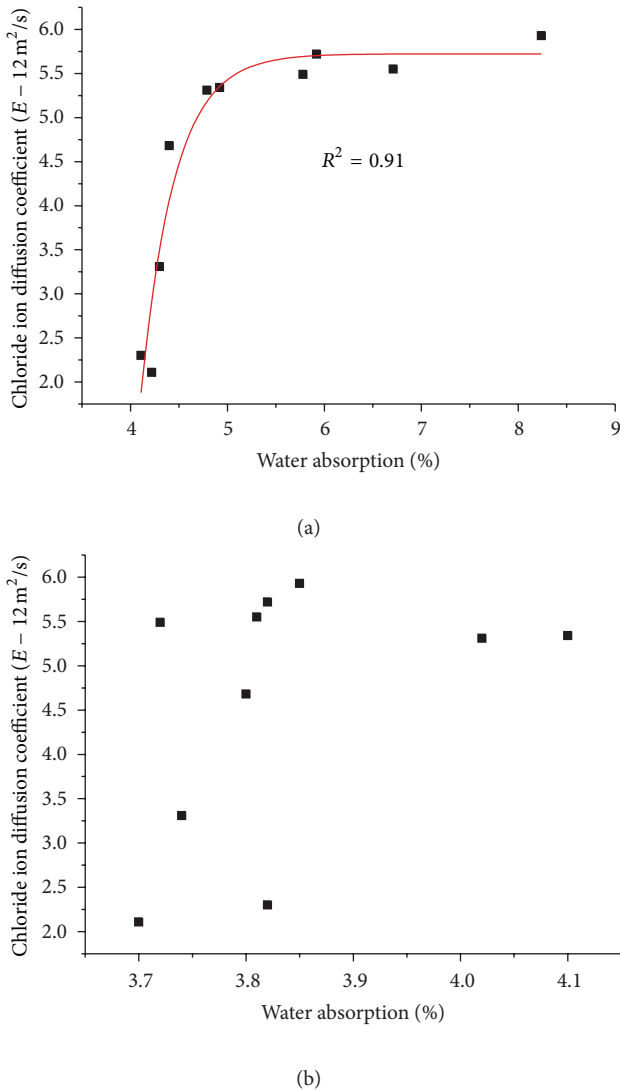


FIGURE 13: (a) Surface water absorption, and (b) internal water absorption.

Conflict of Interests

The authors declare no conflict of interests.

Acknowledgments

This research was supported by the National Natural Science Foundation of China (no. 51108231), Science and Technology Plan Projects of Ministry of Housing and Urban-Rural Development of China (Grant no. 2013-K4-20), and Project of Young Academic Backbone Teachers of Nanjing Institute of Technology.

References

[1] P. K. Mehta and P. J. M. Monteiro, *Concrete: Microstructure, Properties and Materials*, McGraw-Hill, New York, NY, USA, 2006.

- [2] A. Alhozaimy, P. Soroushian, and F. Mirza, "Effects of curing conditions and age on chloride permeability of fly ash mortar," *ACI Materials Journal*, vol. 93, no. 1, pp. 87–95, 1996.
- [3] G. De Schutter and K. Audenaert, "Evaluation of water absorption of concrete as a measure for resistance against carbonation and chloride migration," *Materials and Structures*, vol. 37, no. 273, pp. 591–596, 2004.
- [4] M. Ramli and A. A. Tabassi, "Effects of polymer modification on the permeability of cement mortars under different curing conditions: a correlational study that includes pore distributions, water absorption and compressive strength," *Construction and Building Materials*, vol. 28, no. 1, pp. 561–570, 2012.
- [5] N. Shafiq and J. G. Cabrera, "Effects of initial curing condition on the fluid transport properties in OPC and fly ash blended cement concrete," *Cement and Concrete Composites*, vol. 26, no. 4, pp. 381–387, 2004.
- [6] K. E. Hassan, J. G. Cabrera, and Y. M. Bajracharya, "The influence of fly ash content and curing temperature on the properties of high performance concrete," in *Proceedings of the 5th International Conference, Deterioration and Repair of Reinforced Concrete in the Arabian Gulf, Bahrain*, pp. 311–319, 1997.
- [7] C. Tasdemir, "Combined effects of mineral admixtures and curing conditions on the sorptivity coefficient of concrete," *Cement and Concrete Research*, vol. 33, no. 10, pp. 1637–1642, 2003.
- [8] W. P. S. Dias, "Reduction of concrete sorptivity with age through carbonation," *Cement and Concrete Research*, vol. 30, no. 8, pp. 1255–1261, 2000.
- [9] C. Hall, "Water sorptivity of mortars and concretes: a review," *Magazine of Concrete Research*, vol. 41, no. 147, pp. 51–61, 1989.
- [10] P. Mohr, *Mechanisms of improved transport phenomena in mature portland cement pavements: a macro and microstructural evaluation [Ph.D. thesis]*, University of Michigan, Ann Arbor, Mich, USA, 2004.
- [11] N. S. Martys and C. F. Ferraris, "Capillary transport in mortars and concrete," *Cement and Concrete Research*, vol. 27, no. 5, pp. 747–760, 1997.
- [12] C. Tasdemir, "Combined effects of mineral admixtures and curing conditions on the sorptivity coefficient of concrete," *Cement and Concrete Research*, vol. 33, no. 10, pp. 1637–1642, 2003.
- [13] R. P. Khatri, V. Sirivivatnanon, and L. K. Yu, "Effect of curing on water permeability of concretes prepared with normal Portland cement and with slag and silica fume," *Magazine of Concrete Research*, vol. 49, no. 180, pp. 167–172, 1997.
- [14] S. Kelham, "A water absorption test for concrete," *Magazine of Concrete Research*, vol. 40, no. 143, pp. 106–110, 1988.
- [15] M. Kaviany, *Principles of Heat Transfer in Porous Media*, Springer, New York, NY, USA, 1995.
- [16] J. Kropp, H. K. Hilsdorf, H. Grube, C. Andrade, and L. Nilsson, "Transport mechanisms and definitions editors," in *Performance Criteria for Concrete Durability*, J. Kropp and H. K. Hilsdorf, Eds., pp. 4–14, E and FN Spon, London, UK, 1995.

Research Article

Waste Tire Particles and Gamma Radiation as Modifiers of the Mechanical Properties of Concrete

Eduardo Sadot Herrera-Sosa,¹ Gonzalo Martínez-Barrera,²
Carlos Barrera-Díaz,³ and Epifanio Cruz-Zaragoza⁴

¹ *Facultad de Química, Universidad Autónoma del Estado de México, Paseo Colón Esquina Paseo Tollocan s/n, 50180 Toluca, MEX, Mexico*

² *Laboratorio de Investigación y Desarrollo de Materiales Avanzados (LIDMA), Facultad de Química, Universidad Autónoma del Estado de México, km 12 de la Carretera Toluca-Atacomulco, San Cayetano, 50200 Toluca, MEX, Mexico*

³ *Centro Conjunto de Investigación en Química Sustentable, Universidad Autónoma del Estado de México, Universidad Nacional Autónoma de México (UAEM-UNAM), Carretera Toluca-Atacomulco km 14.5, Unidad El Rosedal, 50200 Toluca, MEX, Mexico*

⁴ *Unidad de Irradiación y Seguridad Radiológica, Instituto de Ciencias Nucleares, Universidad Nacional Autónoma de México, A.P. 70-543, 04510 Mexico City, DF, Mexico*

Correspondence should be addressed to Gonzalo Martínez-Barrera; gonzomartinez02@yahoo.com.mx

Received 15 November 2013; Accepted 27 January 2014; Published 6 March 2014

Academic Editor: Osman Gencel

Copyright © 2014 Eduardo Sadot Herrera-Sosa et al. This is an open access article distributed under the Creative Commons Attribution License, which permits unrestricted use, distribution, and reproduction in any medium, provided the original work is properly cited.

In polymer reinforced concrete, the Young's modulus of both polymers and cement matrix is responsible for the detrimental properties of the concrete, including compressive and tensile strength, as well as stiffness. A novel methodology for solving such problems is based on use of ionizing radiation, which has proven to be a good tool for improvement on physical and chemical properties of several materials including polymers, ceramics, and composites. In this work, particles of 0.85 mm and 2.80 mm obtained from waste tire were submitted at 250 kGy of gamma radiation in order to modify their physicochemical properties and then used as reinforcement in Portland cement concrete for improving mechanical properties. The results show diminution on mechanical properties in both kinds of concrete without (or with) irradiated tire particles with respect to plain concrete. Nevertheless such diminutions (from 2 to 16%) are compensated with the use of high concentration of waste tire particles (30%), which ensures that the concrete will not significantly increase the cost.

1. Introduction

The final disposal of used tires is a major environmental problem. In Mexico, it is estimated that only 10% of the 30 million disposed tires are recycled. The landfills where they are disposed represent a severe risk of fire and a health hazard due to the presence of noxious fauna such as rats, cockroaches, flies, and mosquitoes which can be infectious [1, 2].

The most common method to dispose waste tires is to burn them for vapor, heat, or electricity [3, 4]. The usage of waste tires as alternative fuel in cement furnaces is

generalized across the US and Europe [5]. However, these practices result in the generation of organic and inorganic compounds such as zinc oxide (ZnO) and zinc sulfide (ZnS), in hydrocarbon gas, aromatic volatile compounds, liquids formed by heavy and light oils, and all these byproducts which are highly polluting [6].

Another approach for the application of waste tires includes hot bituminous mixes as pneumatic dust for the agglutinative modification in asphalt pavements [7–9]. This application has been more or less effective, but not enough for reducing the reserves of waste tires, since these novel technologies are more expensive than conventional methods

[10]. An alternative option is to use them as substitute of fine or coarse aggregate in concrete. Their characteristics can improve mechanical properties of concrete as strength and modulus of elasticity, instead of those achieved by sand or stone.

Concrete is one of the most important materials in the construction industry around the world, not only for its cost, but also for its properties as well as its readiness for forming before it hardens which include resistance to climate and durability, among others. However, concrete has a great impact in the environment, it requires great amounts of natural resources for its production (sand, gravel, and water), and the cement generation produces large amounts of carbon dioxide which is discharged in the atmosphere. In fact, it is estimated that cement industry is responsible for the emission of one million tons of CO₂ to the atmosphere [11].

In order to reduce the ecological impact, many efforts have been made for reducing the consumption of nonrenewable resources in the production of concrete; one of these is the production or addition of recycled materials into the mixture in substitution of the common aggregates, taking care of the final quality, that include parameters as resistance, modulus of elasticity, and durability, among others [12].

When adding particles to concrete formation, internal stresses are produced and they promote sooner cracking and subsequent failure, which can be avoided with the control of the particle sizes. Early studies pointed out that elastomeric particles can reduce propagation of cracks, show increment in tensile strength, and have capacity in energy absorption [13].

One advantage of the rubber particles is concerning to energy absorption through ultrasonic waves, in order to benefit the concrete elasticity. However, differences in the Young's modulus between rubber particles and concrete matrix, besides concentration of rubber particles into concrete, could promote great deformations when applying loads and thus progressive diminution of the mechanical properties. Other properties are concerning for concrete workability, including diminution of slump and increment of air content when increasing the elastomeric concentration, which promotes a low unit weight [14].

The use of recycled materials ensures that the product will not significantly increase in cost because is considered as waste, and there is not a specific final use for it. However, recycling of tire rubber is a practice currently industrialized which need follow the current regulations and avoid the pollution caused by a wrong disposal [15, 16].

The main aim of this study is the use of waste tire particles and gamma radiation for improvement of mechanical properties of concrete, which open several possibilities in research areas with great benefits, in order to ensure economic earnings in the context of sustainable development, by solving environmental pollution problems.

2. Experimental

2.1. Design and Manufacture of Concrete. All mixes were elaborate with Portland cement CPP-30R-RS (according to ASTM C 150 cement type II), natural sand, gravel, and water.

The objective with the mix of these components was obtained 24.5 MPa in compression strength at 28 days of curing, according to ACI 211.1 standard. Moreover, it was added waste tire particles of different sizes in function of the availability of the commercial mesh (sieve). In this case, 20 and 7 meshes correspond to 0.85 mm and 2.80 mm, respectively; thus, we have an approximate waste particle size ratio of 1 : 3.

Sieved of coarse aggregate (gravel) and fine aggregate (sand) was according to ASTM C136-06 standard. While the unit weight and the moisture content were according to ASTM C29/C29M-09 and ASTM C566-13, respectively, while the saturated surface-dry specific gravity, apparent specific gravity, and water absorption of gravel and sand were determined according to ASTM C127 and ASTM C128 standards.

Physical properties of the components are shown in Table 1. The sieve analyses of fine and coarse aggregates are shown in Tables 2 and 3.

2.2. Irradiation Procedure. Irradiation at 250 kGy of two different waste tire particle sizes (0.85 mm and 2.8 mm) was performed with an irradiator Gammabeam 651-PT loaded with ⁶⁰Co pencils, located at the Institute of Nuclear Sciences (ICN) of the National Autonomous University of Mexico. The irradiation rate was 4 kGy/h. After that the irradiated particles were mixing with concrete components, and finally the mix was casting in molds.

2.3. Mechanical Tests. Concrete specimens were tested after 28 days of curing time. Testing tolerance allowed was 28 days ± 12 hours according to ASTM C/192 M-00 standard. Compressive strength evaluation was carried out in a universal testing machine Controls 047H4 (Milano, Italy) with capacity of 2000 kN, while flexural strength was carried out in an flexural testing machine Elvec 72-4 with capacity of 10 kN. The pulse velocity evaluation was carried out with an ultrasonic pulse velocity tester Controls 58E0048 with transmitter and receiver head (54 kHz) and pulse rate of 1/s.

2.4. Mixing, Casting, and Curing Specimens. The concrete mixtures were prepared in a laboratory mixer with capacity of 265 dm³. In the first stage dry aggregates (fine and coarse), waste tire particles, and cement were mixed with addition of 85% of water. In a second stage, after mixing by one minute, 15% of water was added. Finally, all batches were mixed for a total time of 5 minutes in order to prevent fresh concrete from segregation.

After mixing, the concrete specimens were molded. For each concrete mixture, ten specimens were casting in cylindrical molds of 150 mm diameter and 300 mm height, as well as two beams of 150 × 150 × 600 mm. After 24 hours, they were placed in a controlled temperature room at 23.0 ± 2.0°C and 95% of relative humidity. Cured process was performed in accordance with ASTM C511 standard.

The component concentrations of the concrete are shown in Table 4. Regarding the manufactured concrete replacing sand by waste tire particles, two different waste tire particle sizes were used [2.8 mm (mesh 7) and 0.85 mm (mesh 20)], as

TABLE 1: Physical properties of components of concrete.

Component	Specific gravity (g/cm ³)	Water absorption (%)	Loose unit weight (kg/m ³)	Compact unit weight (kg/m ³)
Gravel	2.35	3.59	1367	1443
Sand	2.12	11.87	1278	1201
Tire rubber (2.80 mm)	1.04	—	—	—
Tire rubber (0.85 mm)	1.35	—	—	—
Cement	3.10	—	—	—
Water	1.00	—	—	—

TABLE 2: Sieve analysis of sand (fineness modulus = 3.7).

Sieve	Size (mm)	Retained (g)	% retained (individual)	% retained (cumulative)
4	4.75	81	4.07	4.07
8	2.36	212	10.66	14.74
16	1.18	285	14.34	29.07
30	0.60	402	20.22	49.30
50	0.30	671	33.75	83.05
100	0.15	312	15.69	98.74
Bottom tray		25	1.26	100.00

TABLE 3: Sieve analysis of gravel (maximum size = 40 mm).

Sieve	Size (mm)	Retained (g)	% retained (individual)	% retained (cumulative)
1	25.0	300	7.65	7.65
3/4	19.0	1200	30.61	38.27
1/2	12.5	1040	26.53	64.80
3/8	9.5	240	6.12	70.92
4	4.7	800	20.41	91.33
Bottom tray		340	8.67	100.00

well as three different concentrations of them: 10, 20, and 30% by volume. The mix code was labeled as Mix-Concentration-Mesh; for example, M10-7 specimens means “Mix with 10% of waste tire of mesh size 7.” The water/cement ratio was kept constant at 0.54.

The unit weights of concretes are shown in Figure 1. For concretes with nonirradiated waste tire particles different behaviors are observed: (a) the values decrease progressively when adding higher concentration of tire particles. The lowest value is 9% minor with respect to concrete without tire particles (namely, “control concrete” by us). (b) All concretes have lower values with respect to control concrete (1954 kg/cm³). (c) The values for concrete with waste particles of 2.8 mm are higher than those with 0.85 mm. In fact the values decrease because waste tire particles are light, and since they have porous aggregates, air content is increased in concrete mixtures generating low unit weight. This fact agrees with a previous research in which the air content in concrete increases when using bigger rubber particles [17].

In the case of concretes with irradiated waste tire particles, different behaviors are noted. (a) The values decrease when the particle concentration increase. (b) At the difference of the results for concrete with nonirradiated particles, now the higher values are for concrete with tire particles of

0.85 mm. (c) All values are bigger than those for the control concrete. The highest value is 5% higher than those for control concrete.

When adding irradiated particles, the concrete shows a reduction in measures (contractions), which was observed during the calculus of volume. With higher particle sizes lower contractions were found in consequence lower unit weight.

3. Results

3.1. Compressive Strength. Compressive strength values of concretes are shown in Figure 2. The compressive strength values vary as a function of size and concentration of waste tire particles. For concrete with nonirradiated waste tire particles, the following behaviors are observed. (a) The values decrease progressively according to the particle concentrations which increase. For control concrete, the compressive strength is 24.1 MPa, which is bigger than those for all concrete (ranging from 5.2 to 21.4 MPa); being the highest value for concrete with 10% of particles of 2.8 mm, such value is 11% lower than those for control concrete. (b) With respect to the particle size, the compressive strength values are higher for concretes with particles of 2.8 mm than those with

TABLE 4: Components of concrete (1 m³).

Mix code	Waste tire (col%)	Waste tire (kg)	Portland cement (kg)	Sand (kg)	Gravel (kg)	Water (kg)
M0	0	0	337.1	758.5	662.6	286.3
M10-7	10	36.2	337.1	596.4	758.5	278.4
M20-7	20	72.4	337.1	530.1	758.5	270.6
M30-7	30	108.7	337.1	463.8	758.5	262.7
M10-20	10	47.2	337.1	596.4	758.5	278.4
M20-20	20	94.5	337.1	530.1	758.5	270.6
M30-20	30	141.7	337.1	463.8	758.5	262.7

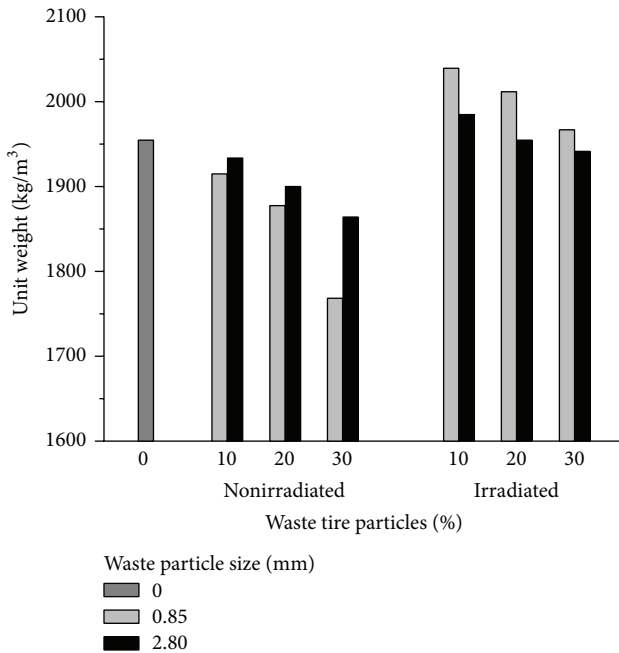


FIGURE 1: Unit weight of concrete with waste tire particles.

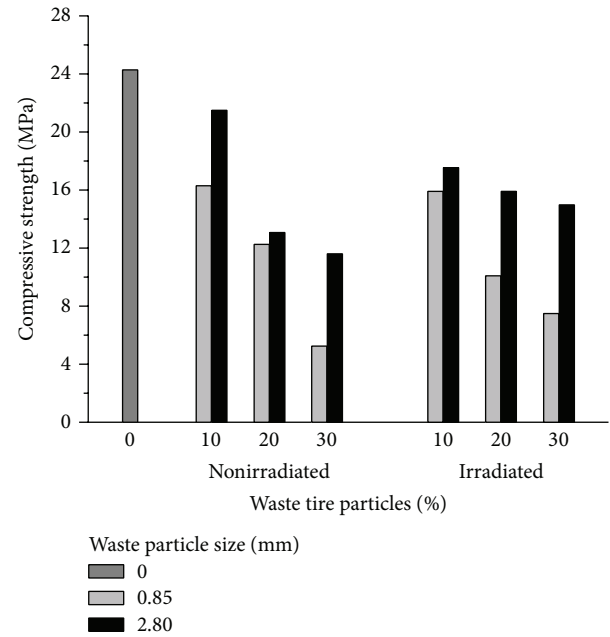


FIGURE 2: Compressive strength of concrete with waste tire particles.

0.85 mm. When increasing the waste particles concentration and adding large particles, more air content is obtained which may cause microcracking and in consequence lower compressive values.

For concrete with waste irradiated tire particles, the compressive strength values follow similar behaviors. (a) The values decrease when increasing the particle concentrations. The values range from 7.4 to 17.5 MPa; being the highest value for concrete with 10% of particles of 2.8 mm, such value is 27% lower with respect to control concrete. (b) The concretes with particles of 2.8 mm have bigger values than those with 0.85 mm. (c) The concretes with 20% or 30% of particles have higher values when comparing to concrete with nonirradiated particles. Thus, it is more convenient using bigger size particles instead of lower ones.

3.2. Splitting Tensile Strength. Splitting tensile strength values of concretes are shown in Figure 3. For concrete with nonirradiated waste tire particles, the following behaviors are observed. (a) The values decrease when increasing the

concentration of particles. The values vary from 0.7 to 1.8 MPa; being the highest value for concrete with 10% of particles of 2.8 mm, this value is 6% minor than those for control concrete. (b) Concretes with particles of 2.8 mm have higher values than those with 0.85 mm.

For concrete with irradiated waste tire particles, the splitting tensile strength also decreases when increasing the concentration of particles. The values range from 0.7 to 1.4 MPa; being the highest value for concrete with 10% of particles of 2.8 mm, it is 27% minor than those for control concrete. Moreover, higher values are seen for concrete with particles of 2.8 mm. As seen in Figure 1 for compressive strength values, in the case of tensile strength, a similar behavior is observed: the values for concrete with 20% or 30% of particles are higher than those for concrete with nonirradiated particles.

For both kinds of concrete, with irradiated or nonirradiated waste particles, the compressive and splitting tensile strength behavior is similar because the induced stresses

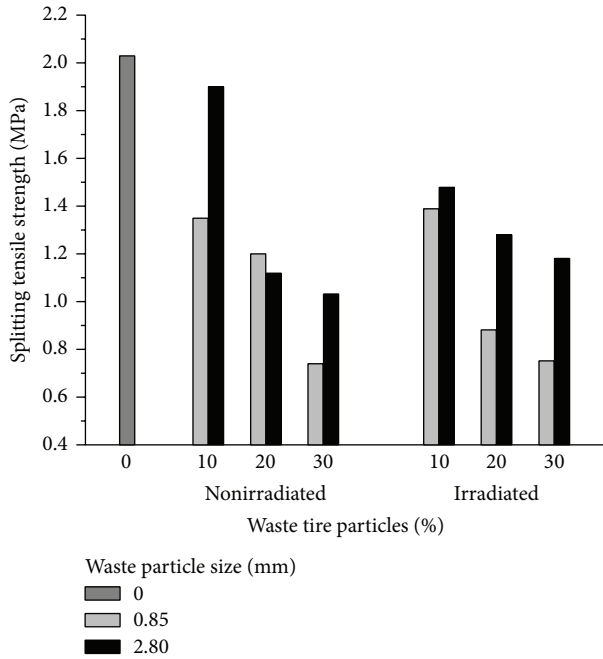


FIGURE 3: Splitting tensile strength of concrete with waste tire particles.

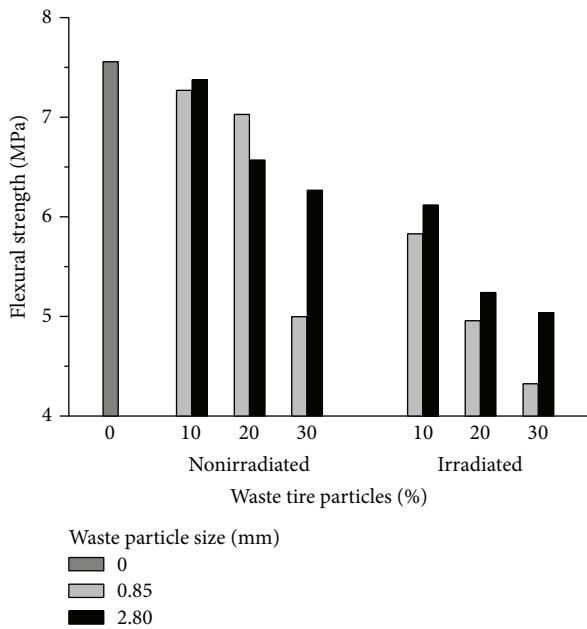


FIGURE 4: Flexural strength of concrete with waste tire particles.

generated in the specimens are of the same nature, they act in the direction of the load application axis.

3.3. Flexural Strength. The flexural strength values are shown in Figure 4. For concrete with nonirradiated waste particles, the values range from 4.9 to 7.3 MPa. The results indicate that (a) There is a progressive diminution of values when increasing the concentration of particles. The highest value is

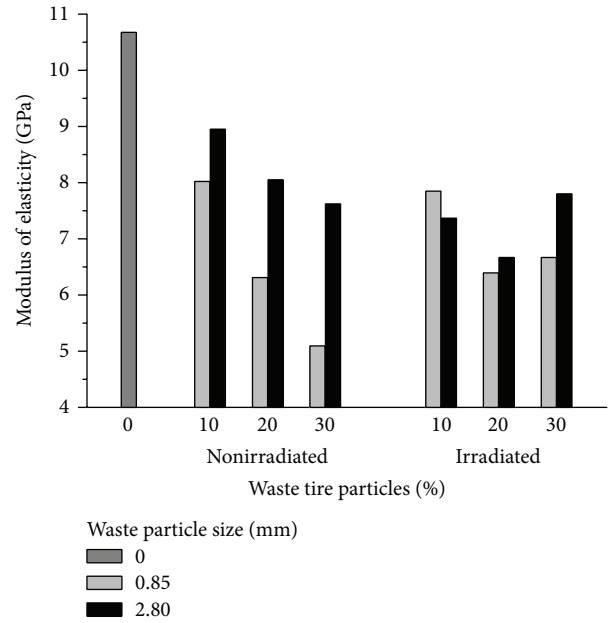


FIGURE 5: Modulus of elasticity of concrete with waste tire particles.

obtained by concrete with 10% of particles, which is 2% minor than those obtained for control concrete. (b) Variations in terms of the particle size are observed, and higher values are for concretes with 10% and 30% and particles of 2.8 mm for concrete with 20% but with particles of 0.85 mm.

For concrete with irradiated particles, the flexural strength values range from 4.3 to 6.1 MPa; such values are lower when comparing with concrete with nonirradiated particles. The flexural strength values decrease when increasing the concentration of particles; and the values are bigger for concretes with particles of 2.8 mm.

3.4. Modulus of Elasticity. The modulus of elasticity values is shown in Figure 5. The highest value corresponds to control concrete, namely, 10.6 GPa. For concrete with nonirradiated waste tire particles, the values range from 5.0 to 8.9 GPa. The highest value (obtained by concrete with 10% of particles of 2.8 mm) is 16% minor with respect to control concrete. As other mechanical features discussed in previous sections, the modulus of elasticity values follows similar behaviors. (a) The values decrease when increasing the concentration of particles. (b) Also, concrete with particles of 2.8 mm has higher modulus of elasticity values when comparing to those with 0.85 mm.

For concrete with irradiated particles, modulus of elasticity values ranges from 6.4 to 7.8 GPa, which are higher than those for concrete with nonirradiated particles. Special attention is taken on these concretes because variations in the modulus of elasticity are observed. (a) Two “stages” are identified: the first one consists in a diminution of the values for concretes with 10% and 20% of particles, and the second consists in an increment for concrete with 30% of particles. (b) In terms of the particle size, concrete with 10% of particles has the highest values when adding particles of 0.85 mm, and

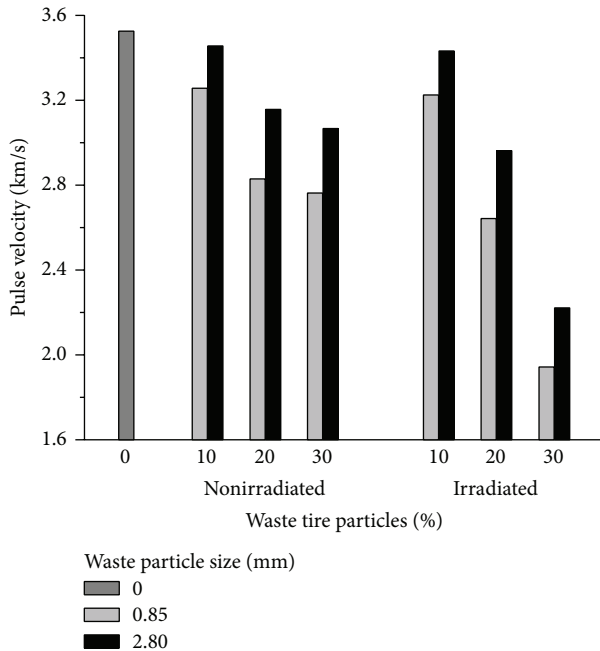


FIGURE 6: Pulse velocity of concrete with waste tire particles.

conversely highest values for concretes with 20% or 30% of particles are done when using particle sizes of 2.8 mm.

According to mechanical concepts, there is a correlation between the compressive strength and the modulus of elasticity values [18] and also between modulus of elasticity and the unit weight. In both cases, waste particles contribute to higher deformations, lower crack formation, and lower unit weights in concrete, which results in lower modulus of elasticity.

3.5. Pulse Velocity. In Figure 6 the ultrasonic pulse velocities of concrete are shown. The highest value corresponds to control concrete, namely, 3.5 km/s. For concrete with non-irradiated particles, the values range from 2.7 to 3.4 km/s; it means that the highest value is 2% minor with respect to control concrete. Moreover, the values follow the same behaviors. (a) The values decrease when increasing the concentration of waste tire particles. (b) The values are bigger for concrete with particles of 2.8 mm.

In the case of concrete with irradiated waste particles, the behavior does not change, and they follow the same behavior as concrete with nonirradiated particles.

4. Conclusions

The mechanical properties of concrete depend on the waste tire particle sizes and their concentration. Compressive and tensile strength values decrease due to waste tire particles, because they promote stress concentration zones, as well as generation of tensile stresses into concrete, resulting in a fast cracking and soon failure. Nevertheless, when applying gamma radiation to waste tire particles, in some cases, improvements on mechanical properties are found. Even so, it seems that the best option is, in all cases, for concrete with

10% of nonirradiated waste tire particles and size of 2.8 mm. Concrete with irradiated particles can support up to 30% of tire particles, making it possible to reduce the final cost of the concrete.

Conflict of Interests

The authors do not have a direct financial relation or conflict of interests with the commercial identities mentioned in this submitted paper, and the commercial trademarks such as Controls and Elvec only were reported to guarantee the reproducibility, in the same conditions, of the different tests.

Acknowledgments

The authors acknowledge the National Council for Science and Technology of México (CONACYT) for the scholarship support for Eduardo Sadot Herrera-Sosa for the achievement of this research and the Environmental Sciences Graduate Program of Universidad Autónoma del Estado de México (UAEM).

References

- [1] R. K. Dhir, M. C. Limbachiya, and K. A. Paine, *Recycling and Use of Tyres*, Thomas Telford, London, UK, 2001.
- [2] M. R. Taha, A. S. El-Dieb, and M. Nehdi, "Recycling tire rubber in cement-based material," *Concrete With Recycled Materials*, ACI Committee 555, 2008.
- [3] H. Briodsky, "The important role retreads can play in reducing the scrap tyre problem," in *Recycling and Use of Tyres*, R. K. Dhir, M. C. Limbachiya, and K. A. Paine, Eds., pp. 57–62, Thomas Telford, London, UK, 2001.
- [4] K. M. Brown, R. Cummings, J. R. Mrozek, and P. Terrebonne, "Scrap tire disposal: three principles for policy choice," *Natural Resources Journal*, vol. 41, no. 1, pp. 9–22, 2001.
- [5] R. W. Davies and G. S. Worthinton, "Use of scrap tyre as a fuel in the cement manufacturing process," in *Recycling and Use of Tyres*, R. K. Dhir, M. C. Limbachiya, and K. A. Paine, Eds., pp. 93–106, Thomas Telford, London, UK, 2001.
- [6] R. Mis-Fernandez, J. A. Azamar-Barrios, and C. R. Rios-Soberanis, "Characterization of the powder obtained from wasted tires reduced by pyrolysis and thermal shock process," *Journal of Applied Research and Technology*, vol. 6, pp. 95–105, 2008.
- [7] S. N. Amirghanian, "Utilization of crumb rubber in asphaltic concrete mixtures-south Carolinas's experience," Research Report, South Carolina Department of Transportation, 2001.
- [8] F. J. Navarro, P. Partal, F. Martínez-Boza, and C. Gallegos, "Influence of crumb rubber concentration on the rheological behavior of a crumb rubber modified bitumen," *Energy and Fuels*, vol. 19, no. 5, pp. 1984–1990, 2005.
- [9] R. G. Nelson and A. S. M. M. Hossain, "An energetic and economic analysis of using scrap tyres for electricity generation and cement manufacturing," in *Recycling and Use of Tyres*, R. K. Dhir, M. C. Limbachiya, and K. A. Paine, Eds., pp. 119–127, Thomas Telford, London, UK, 2001.
- [10] C.-T. Chiu, "Use of ground tire rubber in asphalt pavements: field trial and evaluation in Taiwan," *Resources, Conservation and Recycling*, vol. 52, no. 3, pp. 522–532, 2008.

- [11] V. M. Malhotra, "Role of supplementary cementing materials in reducing greenhouse gas emissions," in *Concrete Technology for a Sustainable Development in the 21st Century*, O. E. Gjorv and K. Sakai, Eds., pp. 226–235, E & FN Spon, London, UK, 2000.
- [12] C. Meyer, "Concrete as a green building material," in *Proceedings of the 3rd International Conference on Construction Materials (ConMat '05)*, Vancouver, Canada, 2005.
- [13] G. L. Nacif, T. H. Panzera, K. Strecker, A. L. Christoforo, and K. Paine, "Investigations on cementitious composites based on rubber particle waste additions," *Materials Research*, vol. 16, pp. 259–268, 2013.
- [14] R. Siddique and T. R. Naik, "Properties of concrete containing scrap-tire rubber—an overview," *Waste Management*, vol. 24, no. 6, pp. 563–569, 2004.
- [15] J. Karger-Kocsis, "Waste tyre rubber—what to do next?" *eXPRESS Polymer Letters*, vol. 7, p. 406, 2013.
- [16] C. R. Rios-Soberanis, S. Wakayama, T. Sakai, J. A. Rodriguez-Laviada, and E. Pérez-Pacheco, "Manufacture of partially biodegradable composite materials based on PLA-Tires powder: process and characterization," *International Journal of Polymer Science*, vol. 2013, Article ID 514951, 8 pages, 2013.
- [17] G. Skripkiunas, A. Grinys, and M. Dauksys, "Using tires rubber waste for modification of concrete properties," in *Sustainable Construction Materials and Technologies*, Y. M. Chun, P. Claisse, T. R. Naik, and E. Ganjian, Eds., pp. 85–90, Taylor & Francis, London, UK, 2007.
- [18] American Concrete Institute Committee 318: ACI 318-05/318R-05, "Building Code Requirements for Structural Concrete and Commentary," 2005.